



## City Research Online

### City, University of London Institutional Repository

---

**Citation:** Ysehak Abay, T. (2016). Reflectance photoplethysmography for non-invasive monitoring of tissue perfusion. (Unpublished Doctoral thesis, City, University of London)

This is the accepted version of the paper.

This version of the publication may differ from the final published version.

---

**Permanent repository link:** <https://openaccess.city.ac.uk/id/eprint/16923/>

**Link to published version:**

**Copyright:** City Research Online aims to make research outputs of City, University of London available to a wider audience. Copyright and Moral Rights remain with the author(s) and/or copyright holders. URLs from City Research Online may be freely distributed and linked to.

**Reuse:** Copies of full items can be used for personal research or study, educational, or not-for-profit purposes without prior permission or charge. Provided that the authors, title and full bibliographic details are credited, a hyperlink and/or URL is given for the original metadata page and the content is not changed in any way.

# Reflectance Photoplethysmography for Non-invasive Monitoring of Tissue Perfusion

Tomas Ysehak Abay

A thesis submitted to the graduate faculty  
in partial fulfilment of the requirements  
for the degree of  
Doctor of Philosophy  
in  
Biomedical Engineering



School of Mathematics, Computer Sciences & Engineering  
City, University of London

2016

*Al mio sole e alla mia luna, Eden e Matteos*

# Contents

<b>List of Figures</b>	<b>ix</b>
<b>List of Tables</b>	<b>xvii</b>
<b>Acknowledgments</b>	<b>xix</b>
<b>Declaration</b>	<b>xx</b>
<b>Abstract</b>	<b>xxi</b>
<b>Glossary of abbreviations</b>	<b>xxii</b>
<b>Publications resulting from this work</b>	<b>xxiii</b>
<b>1 Introduction</b>	<b>1</b>
1.1 Aims, objectives, and contribution of the thesis . . . . .	3
1.1.1 Aims and objectives . . . . .	3
1.1.2 Contribution of the thesis . . . . .	5
1.2 Outline of the thesis . . . . .	6
<b>2 Principles of Anatomy and Physiology</b>	<b>9</b>
2.1 Blood . . . . .	9
2.1.1 Blood structure and functions . . . . .	10
2.1.2 Haemoglobin and haemoglobin derivatives . . . . .	10
2.1.3 The respiratory system and gas exchange . . . . .	12
2.1.4 The respiratory system . . . . .	12
2.1.5 Gas exchange . . . . .	13

2.1.6	Oxyhaemoglobin dissociation curve . . . . .	14
2.2	The Cardiovascular System . . . . .	17
2.2.1	The arterial circulation . . . . .	17
2.2.2	The capillaries . . . . .	20
2.2.3	The venous circulation . . . . .	21
2.3	Summary . . . . .	23
<b>3</b>	<b>Review on noninvasive techniques for the <i>in vivo</i> monitoring of blood perfusion and oxygenation</b>	<b>24</b>
3.1	Photoplethysmography & Pulse Oximetry . . . . .	25
3.2	Near Infrared Spectroscopy . . . . .	26
3.3	Laser Doppler Flowmetry . . . . .	28
3.4	Ultrasound Doppler Flowmetry . . . . .	31
3.5	Transcutaneous PO <sub>2</sub> and PCO <sub>2</sub> . . . . .	34
3.6	Gastric Tonometry (capnography) and Sublingual Capnometry . . . . .	35
3.7	White light reflectance spectrophotometry . . . . .	36
3.8	NADH fluorescence and Palladium-Porphyrin phosphorescence . . . . .	37
3.9	Imaging of the microcirculation . . . . .	40
3.10	Clinical assessments and temperature gradients . . . . .	42
3.11	Summary . . . . .	43
<b>4</b>	<b>Photoplethysmography &amp; Pulse Oximetry</b>	<b>44</b>
4.1	Principles of Photoplethysmography . . . . .	44
4.2	Components of the photoplethysmogram . . . . .	47
4.2.1	Alternated PPG component . . . . .	47
4.2.2	Continuous PPG component . . . . .	48
4.3	Photoplethysmography measurement modalities . . . . .	49
4.3.1	Transmission Photoplethysmography . . . . .	49
4.3.2	Reflectance Photoplethysmography . . . . .	50
4.4	Clinical and Research applications of PPG . . . . .	51
4.4.1	Heart rate . . . . .	51
4.4.2	Respiration rate . . . . .	52
4.4.3	Photoplethysmography as indicator of perfusion . . . . .	54
4.4.4	Continuous arterial blood pressure . . . . .	55
4.4.5	PPG for cardiovascular assessment . . . . .	56

4.4.6	PPG from alternative measurement locations . . . . .	58
4.4.7	Non-contact PPG, imaging, and smartphones applications . . . . .	59
4.5	Pulse oximetry . . . . .	61
4.5.1	Principles of pulse oximetry . . . . .	62
4.5.2	Clinical applications of pulse oximetry . . . . .	66
4.5.3	Pulse Co-oximetry . . . . .	67
4.5.4	Venous saturation . . . . .	68
4.6	Limitations of PPG and Pulse Oximetry . . . . .	68
4.7	Summary . . . . .	69
<b>5</b>	<b>Principles and applications of Near Infrared Spectroscopy</b>	<b>71</b>
5.1	Principles of Near Infrared Spectroscopy . . . . .	72
5.1.1	The Modified Beer-Lambert law . . . . .	76
5.2	NIRS Measurement Techniques . . . . .	77
5.2.1	Time Resolved Spectroscopy . . . . .	77
5.2.2	Phase Modulated Spectroscopy . . . . .	78
5.2.3	Continuous wave NIRS . . . . .	80
5.2.4	Spatially Resolved Spectroscopy . . . . .	81
5.3	Penetration depth and origins of NIRS signal . . . . .	84
5.3.1	Penetration depth of NIRS signal . . . . .	84
5.3.2	Origins of the NIRS signal . . . . .	85
5.4	Clinical and research applications of NIRS . . . . .	86
5.4.1	Cerebral perfusion, oxygenation and blood flow . . . . .	87
5.4.2	Muscle perfusion and oxygenation . . . . .	88
5.4.3	NIRS in critical care and perioperative monitoring . . . . .	91
5.4.4	Functional Near Infrared Spectroscopy (fNIRS) . . . . .	93
5.5	Limitations and open challenges of NIRS . . . . .	95
5.6	Summary . . . . .	98
<b>6</b>	<b>Design and Development of a Reflectance Photoplethysmography Sen- sor</b>	<b>99</b>
6.1	Optical components . . . . .	99
6.1.1	Light Emitting Diodes . . . . .	100
6.1.2	Photodiode . . . . .	102
6.2	Electrical design of the Reflectance PPG probe (RPS1) . . . . .	103

6.2.1	Printed Circuit Board design . . . . .	103
6.2.2	Printed Circuit Board manufacturing . . . . .	104
6.3	Mechanical structure . . . . .	106
6.3.1	Mechanical structure design . . . . .	106
6.3.2	Mechanical structure manufacturing . . . . .	108
6.4	Evaluation of the Reflectance PPG sensor . . . . .	109
6.4.1	Photoplethysmographic signals . . . . .	109
6.4.2	Temperature tests . . . . .	110
6.5	RPS1-2 and RPS3 sensors development . . . . .	112
6.5.1	Larger emitter-detector separation distance . . . . .	113
6.5.2	Further miniaturisation . . . . .	113
6.6	Finger reflectance PPG sensor . . . . .	114
6.7	Summary . . . . .	116
<b>7</b>	<b>Evaluation of a Research Photoplethysmography Processing System for the assessment of tissue perfusion and oxygenation</b>	<b>118</b>
7.1	Research photoplethysmography system: ZenPPG . . . . .	119
7.2	LEDs currents time multiplexing . . . . .	120
7.2.1	LEDs time multiplexing . . . . .	120
7.2.2	Microcontroller . . . . .	122
7.2.3	Voltage Reference Circuits . . . . .	123
7.2.4	Evaluation of LEDs time multiplexing and voltage reference . . .	124
7.3	Current Source Board . . . . .	124
7.4	Transimpedance Amplifier Board . . . . .	126
7.4.1	Evaluation of the Transimpedance Amplifier . . . . .	128
7.5	Demultiplexing and Sample & Hold . . . . .	131
7.5.1	Evaluation of time demultiplexing and Sample & Hold . . . . .	134
7.6	Power board and external connections . . . . .	135
7.7	Summary . . . . .	137
<b>8</b>	<b>Development of a Virtual Instrument for signal acquisition &amp; the application of the modified Beer-Lambert law to PPG</b>	<b>138</b>
8.1	Introduction to LabVIEW . . . . .	139
8.2	Analogue to Digital conversion set-up . . . . .	139

8.3	Development of a Virtual Instrument for physiological signals acquisition and control of light intensities . . . . .	140
8.3.1	Acquisition of PPG signals from ZenPPG . . . . .	141
8.3.2	Display of acquired signals and indicators . . . . .	143
8.3.3	Control and monitoring of ZenPPG's light intensities . . . . .	144
8.3.4	Arterial oxygen saturation estimation from PPG signals . . . . .	146
8.3.5	Signal acquisition from commercial devices . . . . .	146
8.3.6	Measurements file saving and protocol timers . . . . .	148
8.4	Application of the modified Beer-Lambert law to Photoplethysmography	149
8.5	Summary . . . . .	153

**9 Investigation of photoplethysmography, Near Infrared Spectroscopy, laser Doppler flowmetry and pulse oximetry for assessing perfusion and oxygenation changes during vascular occlusions 154**

9.1	Introduction . . . . .	155
9.2	Measurements set-up, protocols and data analysis . . . . .	157
9.2.1	Measurement system . . . . .	157
9.2.2	Subjects and investigation set-up . . . . .	158
9.2.3	Investigation protocols . . . . .	159
9.2.4	Data analysis & statistics . . . . .	160
9.3	Results . . . . .	161
9.3.1	Haemoglobin concentration changes from PPG signals . . . . .	163
9.3.2	Assessment of correlation and trending between PPG and NIRS	169
9.3.3	Slopes from haemoglobin concentration changes . . . . .	170
9.3.4	Haemoglobin oxygenation changes from PPG signals . . . . .	176
9.3.5	Estimation of arterial oxygen saturation from PPG signals . . . . .	176
9.3.6	Comparison of TOI, Flux, Perfusion Index and SpO <sub>2</sub> during protocol 1 . . . . .	177
9.3.7	Comparison of TOI, Flux, Perfusion Index and SpO <sub>2</sub> during protocol 2 . . . . .	180
9.3.8	Changes in finger PPG Optical Densities during vascular occlusion challenges . . . . .	182
9.3.9	Dynamic changes in TOI, nTHI and Optical Densities during vascular occlusions challenges . . . . .	183
9.4	Summary . . . . .	185

<b>10 Photoplethysmography and Near Infrared Spectroscopy perfusion and oxygenation changes at the forehead during a bed tilting protocol</b>	<b>187</b>
10.1 Introduction . . . . .	188
10.2 Measurements set-up, protocols and data analysis . . . . .	190
10.2.1 Measurement system . . . . .	190
10.2.2 Subjects and investigation set-up . . . . .	190
10.2.3 Investigation protocol . . . . .	191
10.2.4 Data analysis & statistics . . . . .	193
10.3 Results . . . . .	194
10.3.1 Haemoglobin concentration changes estimated from PPG . . . . .	195
10.3.2 Assessment of correlation and trending between PPG and NIRS . . . . .	198
10.3.3 Haemoglobin oxygenation from PPG signals . . . . .	198
10.3.4 Influence of large vasculature on haemoglobin concentrations estimation by PPG . . . . .	200
10.3.5 Influence of large vasculature on haemoglobin oxygenation estimation by PPG . . . . .	204
10.3.6 Influence of large vein on SpO <sub>2</sub> estimation by PPG . . . . .	205
10.4 Summary . . . . .	206
<b>11 Investigation of Photoplethysmography and Near Infrared Spectroscopy during an induced thermal stress</b>	<b>209</b>
11.1 Introduction . . . . .	210
11.2 Measurements set-up, protocols and data analysis . . . . .	211
11.2.1 Measurement system . . . . .	211
11.2.2 Subjects and investigation set-up . . . . .	211
11.2.3 Investigation protocol . . . . .	213
11.2.4 Data analysis & statistics . . . . .	213
11.3 Results . . . . .	214
11.3.1 Haemoglobin concentration changes estimated from PPG . . . . .	214
11.3.2 Assessment of correlation and trending between PPG and NIRS . . . . .	218
11.3.3 Comparison between haemoglobin concentrations from finger and ear canal . . . . .	219
11.3.4 Comparison of muscle and brain TOI and nTHI during exposure to cold . . . . .	222
11.4 Summary . . . . .	225

<b>12 Discussion</b>	<b>227</b>
<b>13 Conclusion</b>	<b>238</b>
<b>A Multiplexing/demultiplexing code implementation</b>	<b>241</b>
<b>B NIRO 200NX Specifications</b>	<b>245</b>
<b>References</b>	<b>246</b>

## List of Figures

2.1	Red blood cell's shape, haemoglobin molecule, and haeme. . . . .	11
2.2	Structure of the alveoli inside the lungs and diffusion of gases between air in the alveoli and red blood cells through the respiratory membrane. . . . .	13
2.3	Cycle of internal and external respiration. . . . .	15
2.4	Oxygen-haemoglobin dissociation curve. . . . .	16
2.5	The systemic circulation. . . . .	18
2.6	Major systemic arteries in the human body. . . . .	19
2.7	Schematic illustration on the succession of arteries, arterioles, capillaries, venules and veins. . . . .	21
2.8	Major systemic veins in the human body. . . . .	22
3.1	Red and infrared PPG signals acquired from the index finger of a healthy volunteer. . . . .	26
3.2	Cerebral near infrared spectroscopy measurement. . . . .	27
3.3	Doppler shift occurring in laser Doppler flowmetry. . . . .	29
3.4	Montecarlo simulation of the spatial distribution of laser Doppler flowmetry measurements. . . . .	30
3.5	Doppler shift of ultrasound wave propagating in tissue and ultrasound Doppler measurement from the radial artery of a healthy subject. . . . .	33
3.6	White light reflectance spectra acquired from the skin of the back of the hand (a) and a white light reflectance spectrophotometry sensor applied on the surface of a breast flap (b). . . . .	38

3.7	NADH video fluorimetry of a pig's heart during clamping of the left coronary artery and NADH fluorimetry signals from a dog's heart during hypoxia and ischaemia. . . . .	39
3.8	OPS and SDF images of the sublingual microcirculation. . . . .	41
3.9	Laser Doppler Imaging acquisition of a skin graft on the nose. . . . .	42
4.1	Original and flipped photoplethysmogram and features of the photoplethysmogram. . . . .	46
4.2	Distribution of light absorption and attenuation in photoplethysmography. . . . .	47
4.3	Raw PPG signals acquired from the finger of a healthy subject. . . . .	48
4.4	Configuration of transmission photoplethysmography. . . . .	50
4.5	Configuration of reflectance photoplethysmography. . . . .	51
4.6	Time domain and frequency domain heart rate estimation from PPG. . . . .	52
4.7	Effect of respiration on PPG signals. . . . .	53
4.8	Example of arterial blood pressure measurement from a healthy subject. . . . .	56
4.9	Changes in compliance measured by PPG and Pulse Transit Time as a function of age for different locations. . . . .	57
4.10	Insertion of optical fibres in the skull and PPG recordings from the brain. . . . .	59
4.11	Non-contact PPG measurements from a subject. . . . .	60
4.12	Schematic of the Hewlett Packard ear oximeter. . . . .	62
4.13	Absorption spectra of oxygenated and deoxygenated haemoglobin in the red and infrared regions. . . . .	63
4.14	Absorbance of infrared and red light with varying oxygen saturation. . . . .	64
4.15	PPG parameters used for the calculation of the ratio of ratios. . . . .	65
4.16	Pulse oximeter calibration curve. . . . .	66
5.1	Absorption spectrum of oxygenated haemoglobin, deoxygenated haemoglobin and Cytochrome Oxidase in the near-infrared range. . . . .	73
5.2	Effects of scattering on the light propagation through a medium. . . . .	76
5.3	Example of Temporal Point Spread Function (TPSF) measured in the brain. . . . .	79
5.4	Simulation of the light attenuation and phase shift of modulated incident light in Phase Resolved Spectroscopy for different scattering coefficients. . . . .	79
5.5	SRS measurement and schematic of a multidistance SRS sensor. . . . .	83

5.6	Changes in relative and absolute haemoglobin concentrations and tissue oxygenation measured by NIRS at the brachioradialis during total occlusion. . . . .	84
5.7	Model representing light penetration in NIRS muscle measurements for high and low adipose tissue content. . . . .	86
5.8	Changes in cerebral oxygen saturation during clamping in carotid endarterectomy. . . . .	88
5.9	Changes in oxygenated, deoxygenated, and total blood volume measured by NIRS during cuff-induced ischaemia and venous occlusion. . .	89
5.10	Decline rate of HbO <sub>2</sub> during arterial occlusion at both rest and after exercise. . . . .	90
5.11	Changes in haemoglobin concentrations and tissue oxygen saturation during sequential, increasing muscle's contractions, and ischaemic occlusion. . . . .	91
5.12	Example of NIRS muscle imager. . . . .	92
5.13	Changes in NIRS parameters during venous and arterial thrombosis in flaps postoperative monitoring. . . . .	93
5.14	Different types of functional NIRS measurements and their timeline. . .	94
6.1	Diagram showing the PPG sensor and the PPG processing system. . .	100
6.2	Mechanical drawings of the red and infrared LEDs of the RPS1 PPG sensor. . . . .	101
6.3	Mechanical drawings of the TEMD5010X01 photodiode employed in the PPG sensor RPS1. . . . .	102
6.4	Reflectance PPG sensor (RPS1) PCB footprint and 3D model. . . . .	105
6.5	3D model views of the RPS1 PPG sensor's case and cover. . . . .	106
6.6	Exploded views and assembly views of the RPS1 PPG sensor's 3D model.	107
6.7	Drawing of the mechanical structure of the PPG sensor RPS1. . . . .	108
6.8	Final manufactured RPS1 PPG sensor. . . . .	109
6.9	Red and infrared raw PPG traces acquired from the RPS1 sensor. . . .	110
6.10	First temperature test on the RPS1 sensor's surface. . . . .	112
6.11	Second temperature test on the RPS1 sensor's surface. . . . .	113
6.12	Final RPS1-2 manufactured sensor. . . . .	114
6.13	3D model views and components of the RPS3 PPG sensor. . . . .	115
6.14	Picture of the final manufactured RPS1 and RPS3 PPG sensors. . . . .	115

6.15	Manufactured finger reflectance PPG sensor. . . . .	116
6.16	Red and infrared PPG signals acquired from the finger reflectance sensor.	117
7.1	Block diagram of the ZenPPG architecture. . . . .	119
7.2	Generic light switching in pulse oximetry or NIRS. . . . .	120
7.3	MC14052BD multiplexer connection schematic, truth table, and outputs vs. logical controls. . . . .	121
7.4	ATTiny2313-20SU I/O ports lines in ZenPPG. . . . .	122
7.5	Voltage reference circuit for the first (a) and second (b) channel of ZenPPG. . . . .	123
7.6	Reference voltages and multiplexer output at 1 V and 2 V. . . . .	125
7.7	Modified Howland current source in ZenPPG. . . . .	126
7.8	Basic transimpedance amplifier circuit . . . . .	127
7.9	Transimpedance amplifier with compensation feedback capacitor . . . . .	127
7.10	Transimpedance amplifier output in ZenPPG. . . . .	129
7.11	ZenPPG's transimpedance amplifier output for different feedback capacitor values. . . . .	130
7.12	MC14052BD demultiplexer connections schematic in ZenPPG. . . . .	131
7.13	Illustration of the input, outputs, and logical controls of the demultiplexer during two consecutive cycles. the . . . . .	132
7.14	Illustration of the input, outputs, and logical controls of the demultiplexer during a single cycle. . . . .	133
7.15	Sample and hold circuit in ZenPPG. . . . .	134
7.16	Sample and hold circuit, low-pass anti-aliasing filter and voltage follower (buffer). . . . .	135
7.17	Transimpedance amplifier output and demultiplexer clocks. . . . .	135
7.18	Evaluation of the sample and hold circuit with sine waves and simulated PPG signals. . . . .	136
7.19	ZenPPG system's front panel (a) and ZenPPG with two PPG sensors connected (b) . . . . .	137
8.1	Block Diagram of the Virtual Instrument (VI) developed for acquisition of PPG and NIRS signals. . . . .	141
8.2	Front Panel of the Virtual Instrument (VI) developed for acquisition of PPG and NIRS signals. . . . .	142

8.3	DAQ Assistant VI, split signals function and separated signals in the VI.	143
8.4	Filter Express VI and signal display chart. . . . .	144
8.5	LEDs driving current control and monitor in the VI. . . . .	145
8.6	SpO <sub>2</sub> calculation in the VI. . . . .	147
8.7	Acquisition, calibration and display of signals from commercial devices and NIRS TOI analogue outputs calibration line and equation. . . . .	148
8.8	Save measurements and timers in the VI. . . . .	150
8.9	Front panel of the running VI acquiring PPG and NIRS signals from a healthy subject. . . . .	151
9.1	Measurement system set-up and placement of PPG, NIRS, and LDF sensors on the forearm . . . . .	159
9.2	Example of PPG, NIRS, laser Doppler, and pulse oximetry signals ac- quired from a volunteer. . . . .	162
9.3	Infrared AC PPG signal acquired from forearm and fingers. . . . .	162
9.4	Example of relative haemoglobin concentrations changes estimated by PPG and NIRS. . . . .	163
9.5	Mean ( $\pm$ SD) changes in relative haemoglobin concentrations estimated from PPG and NIRS during venous occlusion in the first protocol. . . .	164
9.6	Mean ( $\pm$ SD) changes in relative haemoglobin concentrations estimated from PPG and NIRS during total occlusion in the first protocol. . . . .	165
9.7	Mean ( $\pm$ SD) changes in relative haemoglobin concentrations during the second protocol. . . . .	166
9.8	Bland & Altman plots and analysis of the haemoglobin concentrations estimated from PPG against the reference NIRS method during the first protocol. . . . .	168
9.9	Bland & Altman plots and analysis of the haemoglobin concentrations estimated from PPG against the reference NIRS method during the second protocol. . . . .	169
9.10	Four quadrant plots between $\Delta$ HbO <sub>2</sub> , $\Delta$ HHb, and $\Delta$ tHb estimated from PPG and NIRS during venous and total occlusion in the first protocol.	171
9.11	Four quadrant plots between deoxygenated haemoglobin estimated from PPG and NIRS during the second protocol. . . . .	172
9.12	Four quadrant plots between oxygenated haemoglobin estimated from PPG and NIRS during the second protocol. . . . .	173

9.13	Four quadrant plots between total haemoglobin estimated from PPG and NIRS during the second protocol. . . . .	174
9.14	Example of the slope of the regression lines on $\Delta\text{HHb}$ and $\Delta\text{Hb}_{Diff}$ during venous and total occlusions. Box and whisker plots of the slopes from $\Delta\text{HHb}$ and $\Delta\text{Hb}_{Diff}$ , estimated by both PPG and NIRS, during venous and total occlusion. . . . .	175
9.15	Mean changes in $\Delta\text{Hb}_{Ratio}$ during the first and the second protocol (b).	177
9.16	Bland and Altman comparison plots between the $\text{SpO}_2$ estimated from custom-made finger PPG, custom-made forearm PPG, and standard finger pulse oximeter. . . . .	178
9.17	Mean changes in TOI, nTHI, nPI, $\text{SpO}_2$ , and nFlux during the first protocol. . . . .	179
9.18	Mean changes in TOI, nTHI, nPI, $\text{SpO}_2$ , and nFlux during the second protocol. . . . .	182
9.19	Mean changes ( $\pm\text{SD}$ ) in optical densities during the first protocol. . . .	183
9.20	Box and whisker plot of the changes in optical densities during the second protocol. . . . .	184
9.21	Slope changes for TOI, nTHI and optical densities during the first and second protocol. . . . .	185
10.1	Positioning of the PPG and NIRS sensors on the forehead and investigation set-up . . . . .	192
10.2	Example of PPG, arterial blood pressure and NIRS signals acquired from one volunteer. . . . .	194
10.3	Mean changes ( $\pm\text{SD}$ ) in mean arterial pressure (MAP) during the tilting protocol. . . . .	195
10.4	Mean changes ( $\pm\text{SD}$ ) in $\Delta\text{HbO}_2$ , $\Delta\text{HHb}$ , and $\Delta\text{tHb}$ from the forehead estimated by PPG and NIRS during bed tilting. . . . .	196
10.5	Bland & Altman plots and analysis of the haemoglobin concentrations estimated from the second PPG sensor (PPG-2) against the reference NIRS method during the bed tilting protocol. . . . .	197
10.6	Four quadrant plots between $\Delta\text{HbO}_2$ , $\Delta\text{HHb}$ , and $\Delta\text{tHb}$ estimated from the second PPG sensor (PPG-2) and NIRS during the bed tilting protocol.	198
10.7	Mean changes ( $\pm\text{SD}$ ) of $\Delta\text{Hb}_{Ratio}$ during the bed tilting protocol. . . .	199

10.8	Changes in $\Delta\text{Hb}_{\text{Ratio}}$ , TOI, and nTHI in all volunteers during the bed tilting protocol. . . . .	200
10.9	Mean changes ( $\pm\text{SD}$ ) in $\text{HbO}_2$ , HHb, and tHb from the forehead estimated by the two PPG sensors. . . . .	202
10.10	Box and whiskers plots of the mean changes in $\text{HbO}_2$ , HHb, and tHb estimated from both PPG sensors during baseline, tilting, and recovery. . . . .	203
10.11	Bland & Altman plots of the deoxygenated haemoglobin ( $\Delta\text{HHb}$ ) estimated from the PPG sensor on the large vein and the PPG sensor distant from large vasculatures on the forehead during the three stages of the bed tilting protocol. . . . .	203
10.12	Box and whiskers plots of the mean changes in $\Delta\text{Hb}_{\text{Ratio}}$ estimated from the PPG sensor on the large vein and the PPG sensor distant from large vasculatures on the forehead during the three stages of the bed tilting protocol. . . . .	204
10.13	Bland & Altman plots of $\Delta\text{Hb}_{\text{Ratio}}$ estimated from the PPG sensor on the large vein and the PPG sensor distant from large vasculatures on the forehead during the three stages of the bed tilting protocol. . . . .	205
10.14	Bland & Altman plots of $\text{SpO}_2$ estimated from the PPG sensor on the large vein and the PPG sensor distant from large vasculatures on the forehead during baseline. . . . .	206
10.15	Mean changes in $\text{SpO}_2$ estimated from the PPG sensor placed on top of the large vein and the PPG sensor positioned distant from large vasculatures during the bed tilting protocol. . . . .	206
10.16	Five seconds traces of infrared AC PPG signals acquired from the PPG sensor on top of the large vein and distant from large vasculature during the three stages of the bed tilting protocol. . . . .	207
11.1	Placement of PPG, NIRS and LDF sensors on the forearm and the PPG ear canal sensor. . . . .	212
11.2	Example of PPG, NIRS, laser Doppler flowmetry and skin temperature signals acquired from one subject during the investigation protocol. . . . .	215
11.3	Example of $\Delta\text{HbO}_2$ , $\Delta\text{HHb}$ , and $\Delta\text{tHb}$ estimated from finger (PPG) and forearm (NIRS) of four subjects during cold exposure. . . . .	216
11.4	Box and whiskers plot of the means of $\Delta\text{HbO}_2$ , $\Delta\text{HHb}$ , and $\Delta\text{tHb}$ measured at the finger by PPG during cold exposure. . . . .	217

11.5	Box and whiskers plot of the means of $\Delta\text{HbO}_2$ , $\Delta\text{HHb}$ , and $\Delta\text{tHb}$ measured from the forearm by NIRS during cold exposure. . . . .	217
11.6	Box and whiskers plot of the means of normalised Flux and skin temperature during cold exposure. . . . .	218
11.7	Four-quadrant plots between $\Delta\text{HbO}_2$ , $\Delta\text{HHb}$ , and $\Delta\text{tHb}$ estimated from PPG (finger) and NIRS (forearm) during cold exposure and recovery.	219
11.8	Example of $\Delta\text{HbO}_2$ , $\Delta\text{HHb}$ , and $\Delta\text{tHb}$ estimated from ear canal (PPG) and forehead (NIRS) of four subjects during cold exposure. . . . .	220
11.9	Box and whisker plot of the changes in oxygenated haemoglobin estimated from finger and ear canal during exposure to cold. . . . .	221
11.10	Box and whisker plot of the changes in deoxygenated haemoglobin estimated from finger and ear canal during exposure to cold. . . . .	221
11.11	Box and whisker plot of the changes in total haemoglobin estimated from finger and ear canal during exposure to cold. . . . .	222
11.12	Box and whisker plot of the changes in perfusion index estimated from finger and ear canal during exposure to cold. . . . .	223
11.13	Mean changes in TOI in all volunteers during the protocol. . . . .	224
11.14	Mean changes in nTHI in all volunteers during the protocol. . . . .	224

# List of Tables

6.1	Optical and electrical characteristics of the red wavelength LED (KP-2012SRC-PRV) at 25 °C . . . . .	101
6.2	Optical and electrical characteristics of the infrared wavelength LED (KP-2012 SF4C) at 25E . . . . .	101
6.3	Optical and electrical characteristics of the photodiode (TEMD5010X01) at 25 °C . . . . .	103
8.1	Extinction coefficients of oxygenated and deoxygenated haemoglobin at 660 nm (red) and 880 nm (infrared). . . . .	153
9.1	Mean changes ( $\pm$ SD), in mM·cm, of relative haemoglobin concentrations changes estimated by PPG and NIRS during baseline, venous occlusion, and total occlusion. . . . .	165
9.2	Mean changes ( $\pm$ SD) in $\Delta$ HbO <sub>2</sub> , $\Delta$ HHb, and $\Delta$ tHb estimated by both PPG and NIRS during the second protocol. . . . .	167
9.3	Correlation coefficients between PPG and NIRS haemoglobin concentrations during the second protocol. . . . .	170
9.4	Mean changes in $\Delta$ Hb <sub>Ratio</sub> during the second protocol and correlation coefficients $r$ between $\Delta$ Hb <sub>Ratio</sub> and TOI during the second protocol. . .	176
9.5	Mean changes ( $\pm$ SD) in TOI, nTHI, nFlux, nPI, and SpO <sub>2</sub> during the second protocol. . . . .	181
10.1	Mean changes ( $\pm$ SD), in mM·cm, of relative haemoglobin concentrations changes estimated by PPG and NIRS during baseline, tilting, and recovery.197	

10.2	Mean changes ( $\pm$ SD), of $\Delta$ Hb <sub>Ratio</sub> , TOI and nTHI during the bed tilting protocol. . . . .	200
10.3	Mean absolute errors (MAE) between haemoglobin concentrations estimated from the two PPG sensors during the bed tilting protocol. . . . .	203
11.1	Mean changes ( $\pm$ SD), of TOI measured at the forehead and forearm during the cold exposure protocol. . . . .	223
11.2	Mean changes ( $\pm$ SD), of nTHI measured at the forehead and forearm during the cold exposure protocol. . . . .	225

# Acknowledgments

I am deeply grateful to my supervisor Prof. Kyriacou. Since the start of this experience, he guided me with patience and he has always been extremely supportive in all aspects. His motivational boosts and the passion he transmits have helped me seeing things easier than I thought. Thank you!

Thanks to my co-supervisor Dr Triantis. In these four years, he has always been present for suggestions or simply for a chat.

Thanks to Dr Constantino Carlos Reyes-Aldasoro for his helpful suggestions in these years and the pleasant conversations in Italian.

Thanks to Dr Phillips for always been supportive since the period of my MSc at City.

Thanks to my friend and companion of PPG adventures Karthik Budidha. He has helped me since the start of the PhD. Some ideas in this thesis have originated from our long conversations, either in front of a coffee, a beer or on the phone.

Thanks to Kamran and Victor for pushing me to do more and more at the best that I could. They both always made time to teach or suggest. In particular, thanks to Kamran for the many suggestions he gave me during the last couple of years.

Thanks to all my friends, but in particular to Patrice and Fai for supporting me every day. The many nice meals, drinks, and moments that we shared helped me re-charging the batteries when I needed it most.

Thanks to all the friends and colleagues of the Biomedical Engineering Research Centre at City University of London, but in particular to my dear friend Mario, Meha, Michelle, Haneen, Loukas, and John.

I want to thank all the colleagues, students, and friends who volunteered in the studies.

Finally, I want to thank my family for their love and support. In particular, my parents who made great sacrifices to make sure I received the education that they could never get.

# Declaration

I hereby declare that the work presented in this thesis is my own work. Any idea, result, or illustration originating from other subjects' work has been acknowledged in the text by referencing to the original author. This thesis has never been published or submitted elsewhere for obtaining an academic degree or professional qualification.

I grant power of discretion to the Librarian at City University of London to allow the thesis to be copied in whole or in part without further reference to the author. This permission covers only single copies made for study purposes, subject to normal conditions of acknowledgement.

Tomas Ysehak Abay

# Abstract

Monitoring blood perfusion and oxygenation changes is of vital importance and for this reason many different techniques have been developed over the decades. Photoplethysmography (PPG) is an optical technique that measures blood volume variations in vascular tissue and it is well known for its utilisation in pulse oximetry for the estimation of arterial blood oxygen saturation ( $SpO_2$ ). In pulse oximetry, mainly the pulsatile component of the signal (AC PPG) is used while the continuous DC component is mostly excluded. Near Infrared Spectroscopy (NIRS) is another optical technique that measures changes in the concentration of oxygenated ( $\Delta HbO_2$ ), deoxygenated ( $\Delta HHb$ ), and total haemoglobin ( $\Delta tHb$ ) from the variations in light attenuations at different wavelengths.

The main motivation of this research is to explore the capability of Photoplethysmography in assessing tissue perfusion and oxygenation similarly as NIRS. The hypothesis underlining this research is that the DC component of the PPG signal contains information on the overall absorbed light and this part of the PPG signal, acquired at least two wavelengths, may be used to obtain  $\Delta HbO_2$ ,  $\Delta HHb$ , and  $\Delta tHb$  as performed in NIRS. Therefore, DC PPG attenuations may be related to haemoglobin concentrations by the modified Beer-Lambert law (MBLL). In order to investigate this, novel reflectance, custom-made PPG sensors and measurement systems, including advanced signal processing algorithms, have been developed for the acquisition and analysis of raw PPG signals (AC + DC) from different anatomical locations.

Three *in vivo* studies on healthy volunteers were carried out in order to investigate if  $\Delta HbO_2$ ,  $\Delta HHb$ , and  $\Delta tHb$  estimated from PPG could indicate changes in blood perfusion and oxygenation. The studies consisted of vascular occlusions on the forearm, negative bed tilting, and whole body cold exposure. Raw PPG signals were acquired from different locations such as the forearm, fingers, and forehead, whereas simultaneous NIRS signals were used as a reference. The results showed that  $\Delta HbO_2$ ,  $\Delta HHb$ , and  $\Delta tHb$  could be effectively estimated from PPG signals. These parameters indicated the changes in blood volumes and/or oxygenation, whereas comparison with NIRS signals showed good levels of correlation and trending. These promising results showed that DC PPG signals could be used to monitor changes in blood perfusion and oxygenation, extending the range of applications of Photoplethysmography.

# Glossary of Abbreviations

<b>AC PPG</b>	PPG Pulsatile Component
<b>ABP</b>	Arterial Blood Pressure
<b>ADC</b>	Analogue to Digital Converter (Conversion)
<b>CO<sub>2</sub></b>	Carbon Dioxide
<b>DAQC</b>	Data Acquisition Card
<b>DC PPG</b>	PPG Continuous Component
<b>DPF</b>	Differential Pathlength Factor
<b>FaO<sub>2</sub></b>	Functional Saturation
<b>fNIRS</b>	Functional Near Infrared Spectroscopy
<b>FrO<sub>2</sub></b>	Fractional Saturation
<b>HbO<sub>2</sub></b>	Oxygenated Haemoglobin
<b>HHb</b>	De-oxygenated (Reduced) Haemoglobin
<b>IR</b>	Infrared
<b>LDF</b>	Laser Doppler Flowmetry
<b>LED</b>	Light emitting Diode
<b>MAE</b>	Mean Absolute Error
<b>MAP</b>	Mean Arterial Pressure
<b>MBLL</b>	Modified Beer-Lambert Law
<b>NIRS</b>	Near Infrared Spectroscopy
<b>nTHI</b>	Normalized Tissue Haemoglobin Index
<b>O<sub>2</sub></b>	Oxygen
<b>PI</b>	Perfusion Index
<b>PMS</b>	Phase Modulated Spectroscopy
<b>PPG</b>	Photoplethysmography
<b>SaO<sub>2</sub></b>	Arterial Oxygen Saturation (Blood analysis)
<b>SD</b>	Standard Deviation
<b>SpO<sub>2</sub></b>	Arterial Oxygen Saturation (Pulse oximetry)
<b>SRS</b>	Spatially Resolved Spectroscopy
<b>tHb</b>	Total Haemoglobin
<b>TOI</b>	Tissue Oxygenation Index (NIRS)
<b>TRS</b>	Time Resolved Spectroscopy
<b>VI</b>	Virtual Instrument

# Publications resulting from this work

## Journals

Abay, T.Y. and Kyriacou, P.A., 2015. Reflectance photoplethysmography as noninvasive monitoring of tissue blood perfusion. *IEEE Transactions on Biomedical Engineering*, 62(9), pp.2187-2195.

Abay, T.Y. and Kyriacou, P.A., 2016. Comparison of NIRS, laser Doppler flowmetry, photoplethysmography, and pulse oximetry during vascular occlusion challenges. *Physiological measurement*, 37(4), p.503.

## Conference Proceedings

Abay, T.Y. and Kyriacou, P.A., 2014, August. Investigation of photoplethysmography and Near Infrared Spectroscopy for the assessment of tissue blood perfusion. In *2014 36th Annual International Conference of the IEEE Engineering in Medicine and Biology Society* (pp. 5361-5364). IEEE.

Abay, T.Y. and Kyriacou, P.A., 2015, August. Accuracy of reflectance photoplethysmography on detecting cuff-induced vascular occlusions. In *2015 37th Annual International Conference of the IEEE Engineering in Medicine and Biology Society (EMBC)* (pp. 861-864). IEEE.

Budidha, K., Abay, T.Y. and Kyriacou, P.A., 2015, August. Investigation of photoplethysmography, laser Doppler flowmetry and near infrared spectroscopy during induced thermal stress. In *2015 37th Annual International Conference of the IEEE Engineering in Medicine and Biology Society (EMBC)* (pp. 6417-6420). IEEE.

## Abstracts

Abay, T.Y., Budidha, K. and Kyriacou, P.A., 2015, October. Assessment of Blood Flow, Blood Volume and Haemoglobin concentrations by Photoplethysmography during induced hypothermia. *International Symposium of Innovations and Applications of Monitoring Perfusion, Oxygenation and Ventilation (IAMPOV)*, Tokyo Japan.

Budidha, K., Abay, T.Y. and Kyriacou, P.A., 2015, October. Comparison of cerebral blood flow auto regulation with peripheral blood flow autoregulation using photoplethysmography. *International Symposium of Innovations and Applications of Monitoring Perfusion, Oxygenation and Ventilation (IAMPOV)*, Tokyo Japan.

Shafqat, K., Abay, T.Y., Budidha, K. and Kyriacou, P.A., 2015, October. Empirical Mode Decomposition of NIRS signals for assessment of cerebral and muscle thermoregulation. *International Symposium of Innovations and Applications of Monitoring Perfusion, Oxygenation and Ventilation (IAMPOV)*, Tokyo Japan.

## **Presentations**

Some of the results presented in this thesis were presented by Prof. Kyriacou as a keynote lecture entitled “Assessing Tissue Oxygenation and Perfusion Utilising Reflectance PPG and NIRS” at the *International Symposium of Innovations and Applications of Monitoring Perfusion, Oxygenation and Ventilation (IAMPOV)*, Tokyo Japan.

# Chapter

# 1

## Introduction

Photoplethysmography (PPG) is a noninvasive optical technique that measures blood volume changes [1]. In PPG, light is shone in tissue and the backscattered light is measured by a photodetector. When light travels through the tissue, it is reflected, scattered, and absorbed. In PPG, the photodetector collects the light that is absorbed in tissue and the resulting signal represents the absorption changes due to variations in blood volume [1]. The signal produced by the photodetector is called photoplethysmogram and contains information on the blood light absorption. The photoplethysmogram comprises of two main components. The alternated component AC is synchronous with the cardiac cycle and is represented by the cyclical variations in arterial blood volumes [1–3]. The systole, when the arteries fill with blood, corresponds to high light absorption, whereas during diastole, light is absorbed minimally. These alternated variations in high and low absorption are then reflected in the signal. The second component of the photoplethysmogram is an almost-constant DC offset. This DC component represents the total incident light and expresses the light absorption by static structures such as non-pulsatile arterial blood, venous blood, skin, and bones [1–3]. This DC component is represented in the photoplethysmogram as an offset on which the AC PPG component rides on top [1].

Due to its synchronicity with the cardiac cycle, the AC PPG component has attracted most of the interest. The component can be used to estimate heart rate, but most importantly, it is used to calculate arterial oxygen saturation ( $SpO_2$ ). Since the AC

---

PPG component represents arterial blood pulsations, it can be used to isolate arterial blood from other light absorbers, and then estimate continuously SpO<sub>2</sub> without the need of calibrations [4, 5]. The technique is known as pulse oximetry and is performed by shining light at two wavelengths (red and infrared) and recording the light absorption at these two wavelengths [4]. From the spectroscopic properties of oxygenated and deoxygenated blood, and by applying calibration curves, the SpO<sub>2</sub> can be estimated from the AC PPG components at two wavelengths [4–6]. Pulse oximetry has been having a huge impact in clinical practice since it allowed to measure arterial oxygen saturation noninvasively and continuously [3]. In this context, the AC PPG has gained most of the attention and the DC component has not been playing any major role, except being used for the normalization of the AC PPG in the SpO<sub>2</sub> calculation [7, 8]. Also, the success of pulse oximetry, as an application of the AC PPG component, has overshadowed the rest of the signal. Except this, the most significant use of the DC PPG is the estimation of the respiration rate from the slow frequency variations of this component [1, 9, 10].

Near Infrared Spectroscopy (NIRS) is another optical technique in which light in the near-infrared region of the spectrum (700-1100 nm) is shone in tissues. Light in this region of the spectrum is used in NIRS due to its high scattering and low absorption properties, allowing a deep penetration in tissues. Light at multiple wavelengths is shone in the tissue and the attenuation of light at this different wavelength is used to estimate changes in the concentration of oxygenated ( $\Delta\text{HbO}_2$ ), deoxygenated ( $\Delta\text{HHb}$ ), and total haemoglobin ( $\Delta\text{tHb}$ ) [11]. The modified Beer-Lambert law (MBLL) is used in NIRS to express  $\Delta\text{HbO}_2$ ,  $\Delta\text{HHb}$ , and  $\Delta\text{tHb}$  from light attenuations [11, 12]. Usually, changes in these parameters are expressed as relative changes from baseline, but absolute concentrations can also be determined by Time Resolved Spectroscopy or Phase Modulated Spectroscopy [11, 13]. If the measures of absolute concentrations are obtained, the oxygenation of the tissue can be expressed as the ratio of oxygenated over the total haemoglobin [13]. The technique provides the ability to assess changes in tissue blood perfusion and oxygenation *in vivo*. This ability of the technique has attracted significant interests among clinicians and researchers, and NIRS has been used for monitoring blood perfusion and oxygenation changes in different scenarios.

As the reader could notice, PPG and NIRS share some common characteristics. Both techniques shine light into tissue and they usually adopt similar technology for emission

and detection of light (light emitting diodes and photodiode). PPG signals are often used at two wavelengths for the estimation of  $SpO_2$ . This requires the fast, intermittent switching of light, as performed in NIRS for obtaining spectroscopic information on light attenuations at different wavelengths. The main difference between the techniques is in how the signals are processed. PPG (pulse oximetry) uses the pulsatile component of the signals for estimation of  $SpO_2$  and uses the continuous DC for normalisation. Contrarily, NIRS excludes any pulsatile component and uses the overall incident light (DC) for the determination of light attenuation changes. The light attenuations are then used to express changes in oxygenated ( $\Delta HbO_2$ ), deoxygenated ( $\Delta HHb$ ), and total haemoglobin ( $\Delta tHb$ ).

## 1.1 Aims, objectives, and contribution of the thesis

The DC component of the PPG signal contains vital information on the overall light absorption in tissue. Therefore, dual-wavelength DC PPGs may be used to extract spectroscopic information on the haemoglobin content in the sampled volume. The DC PPG is already measured in all PPG/pulse oximetry systems, and it is often acquired at two wavelengths (red and infrared). Therefore, by taking into consideration the different optical properties of oxygenated and deoxygenated haemoglobin, the DC PPGs acquired at red and infrared may be used to express changes in light attenuations, and the MBLL may be applied to extract  $\Delta HbO_2$ ,  $\Delta HHb$ , and  $\Delta tHb$ .

### 1.1.1 Aims and objectives

The primary aim of this thesis is to investigate the feasibility of using the DC component of the PPG signal to infer relative changes in oxygenated ( $\Delta HbO_2$ ), deoxygenated ( $\Delta HHb$ ), and total haemoglobin ( $\Delta tHb$ ), and use these parameters to assess changes in blood perfusion. In particular, it is intended to apply NIRS processing techniques in order to extract  $\Delta HbO_2$ ,  $\Delta HHb$ , and  $\Delta tHb$  from dual-wavelength PPG signals. In order to achieve this aim, the fulfilment of the objectives listed below is required.

- Design and develop reflectance PPG sensors and couple them to a research processing system capable of acquiring dual-wavelength and raw PPG signals (AC+DC).

- Set up physiological measurement systems for the simultaneous acquisition of multiple signals such as PPG and NIRS.
- Apply NIRS processing techniques such as the MBLL to extract  $\Delta\text{HbO}_2$ ,  $\Delta\text{HHb}$ , and  $\Delta\text{tHb}$  from dual-wavelength PPG signals.
- Perform *in vivo* studies on healthy volunteers in which changes in perfusion are induced by different procedures (e.g. vascular occlusions, bed tilting, etc.) and in different measurement locations (e.g. forearm, forehead, etc.).
- Apply appropriate statistical and signal processing techniques in order to evaluate whether  $\Delta\text{HbO}_2$ ,  $\Delta\text{HHb}$ , and  $\Delta\text{tHb}$  estimated from PPG were able to detect the changes in perfusion induced and compare these changes with reference NIRS measures (e.g. mean and standard deviation, correlation, etc.).

In addition to the primary aim, the *in vivo* studies mentioned above allow the investigation of some secondary aims.

- Examine the simultaneous response of different noninvasive optical techniques to vascular occlusions on the forearm. This can be performed by the acquisition of additional physiological signals such as laser Doppler flowmetry and pulse oximetry, simultaneously to the PPG and NIRS measurements. Signal analysis and statistical tests can be then used to assess the changes in several physiological parameters during different degrees of vascular occlusions.
- Investigate whether the presence of a large vessel underneath the PPG sensor may cause errors in the estimation of haemoglobin concentration changes by PPG. In order to analyse this, a PPG sensor placed on top of a large vessel on the forehead will be compared to another identical PPG sensor (reference) placed in a vessel-free area on the forehead. Statistical comparisons between the haemoglobin concentrations estimated from the two PPG sensors can reveal any difference in the measurements due to the positioning of the sensor.
- Investigate any difference in perfusion between peripheral and more central locations measured by PPG and NIRS during a whole-body cold exposure study. Such comparison can be performed by comparing the changes in PPG perfusion

measurements between the finger and ear canal, and between NIRS perfusion measurements at the forearm (muscle) and the head (cerebral). It is hoped that the results may reveal whether PPG and NIRS can be used to assess blood flow autoregulation during cold exposure.

### 1.1.2 Contribution of the thesis

Using the PPG/pulse oximeter signals to estimate  $\Delta\text{HbO}_2$ ,  $\Delta\text{HHb}$ , and  $\Delta\text{tHb}$  could open up to new interesting uses of the PPG. The number of parameters extracted from the PPG signals, usually  $\text{SpO}_2$  and heart rate, can then be increased further without the need of any additional instrumentation. Such an achievement could establish PPG as a technique for assessing multiple parameters, such as global oxygenation through  $\text{SpO}_2$  and regional perfusion through the measurement of  $\Delta\text{HbO}_2$ ,  $\Delta\text{HHb}$ , and  $\Delta\text{tHb}$ . At the same time, other parameters such as perfusion index and heart rate could also be estimated from the PPG signal. This research aims to push the current limits of PPG signal processing, which nowadays is predominately used for the measurement of  $\text{SpO}_2$ . This additional analysis of the PPG signal could offer new insights on the technique and extend its current range of applications. Furthermore, the comparison between  $\Delta\text{HbO}_2$ ,  $\Delta\text{HHb}$ , and  $\Delta\text{tHb}$  estimated by both PPG and NIRS would contribute on exploring similarities and differences between these two techniques in different conditions and measurement locations. Examining the effects of large vasculature on haemoglobin concentrations by PPG (and  $\text{SpO}_2$ ) is complementary to the primary aim of this thesis, as well as directly contributing to the existing body of knowledge on the placement of PPG/pulse oximetry sensors.

The comparison of different noninvasive optical techniques during vascular occlusions would provide a unique setting to analyse the simultaneous responses of several perfusion parameters measured by different modalities. Whereas some of these techniques have been investigated alone, a similar comparison that includes NIRS, laser Doppler flowmetry, PPG and pulse oximetry has not been previously performed and it can contribute to the current knowledge on these techniques. In addition, the use of different degrees of occlusions could provide a comparative assessment of the behaviour of these modalities during partial vascular occlusions.

## 1.2 Outline of the thesis

After introducing the aims of the thesis, this section presents the outline and contents of the chapters in the thesis.

Chapter 2 introduces some basic principles of physiology. The composition and functions of blood will be described, with a particular emphasis on haemoglobin and its roles in the transport of oxygen. The gas exchange at the pulmonary level, between the lungs and blood, will be explained, as well as the exchange of oxygen and carbon dioxide at the tissue levels. The cardiovascular system will be briefly described as well. The chapter will then conclude by describing the structure of the systemic circulation, composed by arteries, veins, and capillaries.

Chapter 3 presents a review of techniques used to monitor blood perfusion and oxygenation in tissue. The chapter aims at providing an overview of the current state of the art in techniques and technologies used in both research and clinical settings. The principles, applications, and limitations of the different techniques will be briefly described and discussed in this chapter.

Chapter 4 presents in more details the principles of photoplethysmography and pulse oximetry. The description of how blood volume changes are measured in photoplethysmography will be described, along with the origins and composition of the signal. The clinical applications of photoplethysmography will also be briefly introduced. The second part of the chapter will conclude by presenting the principles and applications of pulse oximetry.

Chapter 5 will introduce Near Infrared Spectroscopy (NIRS). The chapter will begin by describing the physical principles used in NIRS. In particular, the modified Beer-Lambert law will be presented as being used in NIRS to infer haemoglobin concentrations changes in tissue. Different typologies of NIRS instruments such as Continuous Wave NIRS and Spatially Resolved Spectroscopy will be briefly described. A review of the main clinical and research applications of NIRS will be presented, and some of the limitations will be discussed at the end of the chapter.

Chapter 6 describes the design and development of reflectance photoplethysmographic

sensors that were used in the *in vivo* studies presented in this thesis. Particular attention will be given to the RPS1 sensor, which was designed to acquire PPG signals from the forearm and forehead. The optical components selected (light emitting diodes and photodiode) will be described, as well as the electrical and mechanical design of the sensor. The evaluation of the sensor, along with thermal tests will also be discussed in the chapter. The development of other versions of the reflectance PPG sensor will be described at the end of the chapter, along with a reflectance finger PPG sensor that was used to acquire signals from the fingers.

Chapter 7 presents the evaluation of a reflectance PPG processing system that was used to drive the PPG sensors described in Chapter 6. This chapter reviews the functionalities of such PPG system, including light multiplexing (switching), current-to-voltage conversion, and time demultiplexing. The main components of the system will be described, along with their evaluation.

Chapter 8 describes the development of a software application to acquire physiological signals from custom-made and commercial devices. The software application was also developed to display in real time the acquired signals and save the measurements for post-acquisition analysis. The second part of this chapter plays a central role in this thesis, as it will propose the application of the modified Beer-Lambert to PPG signals for the determination of haemoglobin concentration changes.

Chapter 9, Chapter 10, and Chapter 11 will present the *in vivo* studies carried out to investigate the feasibility of using relative haemoglobin concentrations from PPG signals to assess changes in blood perfusion and oxygenation in different physiological settings. Chapter 9 will describe a study where changes in blood perfusion were induced by different levels of vascular occlusions in the forearm. Relative haemoglobin concentrations of oxygenated ( $\Delta\text{HbO}_2$ ), deoxygenated ( $\Delta\text{HHb}$ ), and total haemoglobin ( $\Delta\text{tHb}$ ) were estimated from dual wavelength forearm PPG signals and compared with the same parameters estimated by forearm NIRS. The settings of this study also allowed investigating the simultaneous behaviour of different optical techniques during vascular occlusions. Therefore, the second part of Chapter 9 will also present comparative results between different modalities such as NIRS, laser Doppler flowmetry, photoplethysmography, and pulse oximetry during vascular occlusions.

Chapter 10 will present the second *in vivo* study, consisting of a bed tilting protocol. PPG and NIRS sensors were attached on the forehead of healthy volunteers and a bed was tilted at -30 deg. The PPG and NIRS responses were acquired simultaneously and the relative haemoglobin concentrations estimated by the two techniques were compared. A second PPG sensor was placed on top of a large vein in order to analyse the effects of large vasculature on the PPG signals.

Chapter 11 illustrates results from a whole-body cold exposure. Healthy volunteers were exposed to a cold temperature (10 °C) and PPG and NIRS signals were recorded simultaneously. The relative haemoglobin concentrations from finger and ear canal PPG were compared with forearm and forehead NIRS measurements. In addition, any difference in perfusion between finger and ear canal was analysed by comparing the relative haemoglobin concentrations estimated from the two PPG locations.

Finally, Chapter 12 and Chapter 13 will conclude the thesis by discussing the main findings from the *in vivo* studies, the limitations, and suggestions for future work.

# Chapter 2

## Principles of Anatomy and Physiology

The human body needs oxygen to survive. Without the supply of oxygen, the cells in our body will not be able to perform their metabolic action. The respiratory and cardiovascular systems have the function of providing oxygen to the tissues in our body. In this chapter, a brief overview on the anatomy and physiology relevant for this work will be presented. In particular, the composition of blood and its main functions will be introduced, along with the exchange and transport of oxygen and carbon dioxide by the blood. The cardiovascular system, which composes the dense net of vessels responsible for carrying blood in the human body, will also be described. This chapter aims at introducing the basic principles of blood perfusion and oxygenation, but the subjects are however vast and, for a more detailed description, the reader could refer to anatomy and physiology textbooks such as [14–16].

### 2.1 Blood

Blood is a tissue in fluid form in the human body and composes around 8 % of the total body weight [14, 16]. The main function of blood is the transportation of oxygen ( $O_2$ ), other nutrients, and hormones to the tissues, and the removal of waste products (e.g. carbon dioxide,  $CO_2$ ) from the tissues [14–16]. The blood also plays an important role in the maintenance of the correct levels of pH and temperature in the body and for repairing injuries [14–16]. The work presented in this thesis focuses on measuring the

oxygenation status of the blood in tissues, thus, a particular attention will be dedicated to the properties and functions of the blood involved in the transport of oxygen and CO<sub>2</sub> in blood.

### 2.1.1 Blood structure and functions

Blood is a connective tissue in which living cells are dispersed in a largely water-composed fluid called plasma [14]. Blood can be decomposed by centrifugation to separate plasma from the living cells (or formed elements). Of the whole blood, 55 % is composed of plasma, less than 1 % is composed of white blood cells and platelets, and 44-45 % is composed of erythrocytes (or red blood cells) [14]. These percentages, however, may vary depending on the gender or the health status of a subject [14]. White blood cells mainly provide protection and immunity against infections and diseases [14, 15], platelets prevent blood loss by repairing injuries (coagulation), and red blood cells transport nutrients and waste products of metabolism [14, 15].

Red blood cells (RBC) compose the great majority of blood cells and they are produced in the red bone marrow [14, 15]. The main function of RBCs is the transport of oxygen to the tissues [14]. As shown in Figure 2.1, RBC have a biconcave shape (diameter of 7-8  $\mu\text{m}$ ), which increases the surface available for carrying oxygen molecules [14]. Also, red blood cells can carry the CO<sub>2</sub> produced by tissues after utilising the oxygen. Due to the absence of a nucleus, the RBCs have a low metabolic activity [14]. One of the main properties of the red blood cells is their colour appearance when they are bounded to O<sub>2</sub> or CO<sub>2</sub>. Arterial blood, rich in O<sub>2</sub>, has a bright red colour, whereas venous blood, with poor O<sub>2</sub> content, presents a dark red colour [15]. This physical property is exploited in several measuring techniques such as pulse oximetry and near infrared spectroscopy for the determination of blood oxygenation. Red blood cells transport oxygen or carbon dioxide by the haemoglobin, a protein with high gas-binding capacity [15].

### 2.1.2 Haemoglobin and haemoglobin derivatives

Haemoglobin is a protein present in most vertebrates, which gives the red blood cells the ability to transport oxygen. Each haemoglobin molecule is composed of a globin

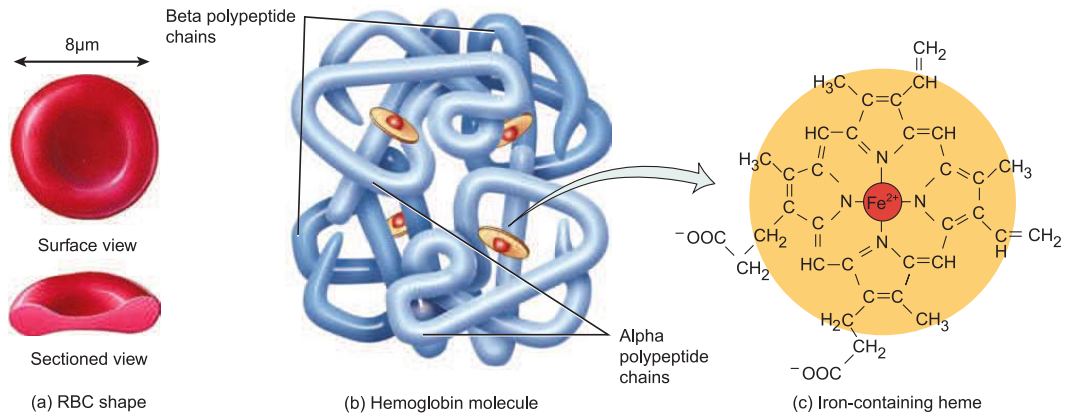


**Figure 2.1:** Red blood cell's shape (a), haemoglobin molecule (b), and haeme (c). The red blood cell presents a biconcave shape with a diameter of 7-8  $\mu\text{m}$ . The haemoglobin molecule has two  $\alpha$  chains and two  $\beta$  chains. Each chain is bound to a single haeme. The haeme has an iron ion in the centre dedicated to binding with the oxygen molecule. Figure reproduced from [14].

protein, which comprises of four polypeptide chains (two  $\alpha$  chain and two  $\beta$  chain) [14,17]. To each of these chains, a non-protein pigment called haeme, is bonded. Each haeme has an iron ion at the centre, which is responsible for binding to a single oxygen molecule [14,15]. Then, the overall haemoglobin molecule contains four iron ions with an overall capacity to bind four oxygen molecules to each haemoglobin molecule [14]. Figure 2.1 illustrates the structure of a haemoglobin molecule. When gas exchange takes place in the lungs, the iron ions bind with an oxygen molecule and, after being transported by the red blood cells, oxygen will be released in the tissue through the systemic capillaries [14,15]. When the oxygen is released, the haemoglobin molecule is able to collect part of the  $\text{CO}_2$  produced by the tissue by amino-acids in the globin part of the haemoglobin molecule, while the majority of  $\text{CO}_2$  is transported in blood by dissolving in the plasma [14,15]. The  $\text{CO}_2$  is then released in the lungs, where it will be expelled by exhalation [14].

Haemoglobin is present in human blood in different forms, defined as haemoglobin derivatives [17]. The most common haemoglobin derivatives are oxyhaemoglobin and deoxyhaemoglobin (or oxygenated and deoxygenated haemoglobin) [17]. Oxyhaemoglobin is a haemoglobin molecule bonded with oxygen, whereas the deoxyhaemoglobin is not bonded to oxygen [17]. Usually, these are the only forms of haemoglobin present in the human blood and they alternate each other in the transport of  $\text{O}_2$  and  $\text{CO}_2$  to and from the tissues. Haemoglobin derivatives which have lost the capacity to bind with oxygen are defined as dyshaemoglobins [17]. An example of dyshaemoglobin is carboxyhaemoglobin, in which the iron ion has reversibly bound with carbon monoxide [17].

The haemoglobin is also responsible for regulation of the blood flow. When in certain situation nitric oxide (NO) is produced by the vessel's endothelium, it binds with haemoglobin. If the tissue requires more oxygen than what is supplied by the blood flow, NO is released, causing vasodilation of the capillaries [14]. This dilation mechanism enhances the amount of blood (oxygen) delivered to the tissue [14]. For instance, when blood flow is restricted by vascular occlusion, capillaries vasodilate and, as soon as flow is restored, an abnormal (hyperaemic) blood flow takes place [18].

### **2.1.3 The respiratory system and gas exchange**

#### **2.1.4 The respiratory system**

The respiratory system is the structure in human body involved in the transport of oxygen into the lungs and in the exchange of oxygen from the lungs into the blood. The functions of the respiratory system can be divided in pulmonary ventilation and respiration. Pulmonary ventilation, divided in inhalation and exhalation, is the mechanical process of moving air in and out of the lungs. The respiration, which is the exchange of oxygen and carbon dioxide between lungs and blood, takes place in the alveoli inside the lungs.

The respiratory system, divided by upper and lower respiratory system, is composed of nasal cavity, oral cavity, pharynx, larynx, trachea, bronchi, lungs, and alveoli [14]. The principal functions of these structures are the filtration, humidification, and direction of air into the lungs. The lungs are organs placed in the thorax cavity and are responsible for the gas exchange with blood. Inhalation is an active action in which the thorax cavity expands and, by the lower pressure created in the lungs, air fills into the lungs [14]. During exhalation, which is a passive movement created by the relaxation of the muscles involved in the ventilation, air is expelled from the lungs [14].

Inside the lungs, small balloon-shape structures called alveoli collect the inhaled air. Several alveoli are grouped in a structure called alveolar sac, in which the alveolus share the same air conduit [14]. Around each alveolar sac, there is a dense net of blood vessels called pulmonary capillaries, where the exchange of gases between the air in the alveolus and the blood in these capillaries takes place [14]. The regions between

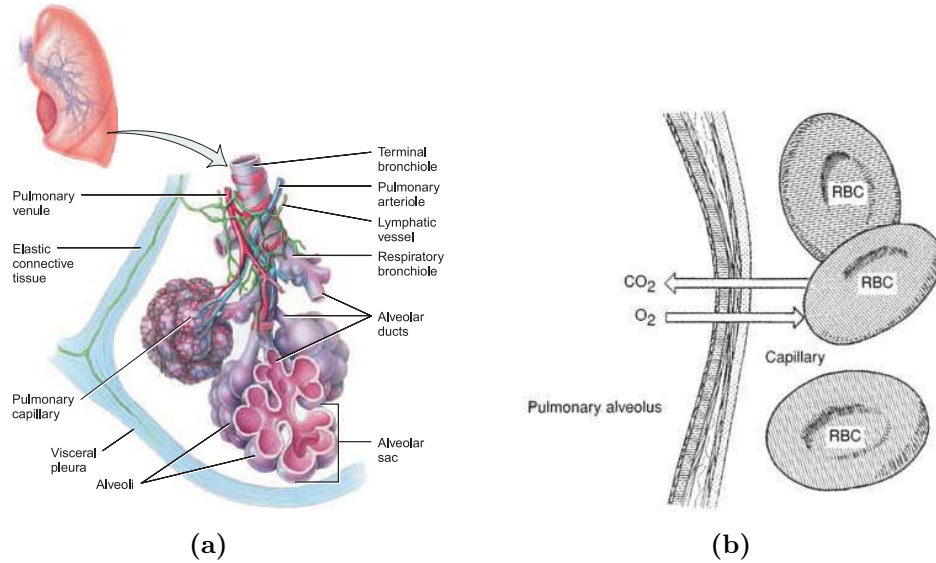


**Figure 2.2:** Structure of the alveoli inside the lungs and diffusion of gases between air in the alveoli and red blood cells through the respiratory membrane. (a) Inside the lungs, alveoli are grouped in alveolar sacs. The alveolar sacs are surrounded by a dense net of pulmonary capillaries where gas exchange between air and blood takes place. Figure reproduced from [14] (b) The gases diffuse through the respiratory membrane, dividing the alveolus and the capillaries. Oxygen ( $O_2$ ) diffuses from the alveolus into the capillaries blood, where it binds to the red blood cells (RBCs). RBCs release carbon dioxide ( $CO_2$ ) inside the alveolus, where it is expelled by exhalation. Figure reproduced from [20].

the pulmonary capillaries and the alveolus walls constitute the respiratory membrane, across which  $O_2$  and  $CO_2$  are exchanged [14, 15]. Figure 2.2a shows the structure of the alveoli and the pulmonary capillaries, which surround each alveolar sac.

### 2.1.5 Gas exchange

As mentioned earlier, the exchange of gases (i.e.  $O_2$  and  $CO_2$ ) between air and blood takes place between the alveoli and the pulmonary capillaries surrounding them. This exchange of gases is controlled by the diffusion law (or Fick's law) [19]. This states that the rate of diffusion of a gas through a barrier is directly proportional to the concentration of the gas and inversely proportional to the area of the barrier [19]. Considering that the concentration, or solubility of a gas in a solution, is directly proportional to the partial pressure of the gas (i.e. the partial pressure is defined as the pressure at which a gas is present in a solution) [14], gases will diffuse from solutions in which they are present in high partial pressure to solutions at lower partial pressures [14, 15]. The large number of alveolus in the lungs (i.e. 300 million) [14] increases the area of the alveolar barrier (respiratory membrane), increasing further the rate of diffusion [19].

The exchange of gases inside the lungs is called external respiration [14, 15]. The pulmonary capillaries receive the deoxygenated blood from the venous circulation, which collects deoxygenated blood from the tissues after these have extracted the oxygen required for their metabolism [14, 15]. Therefore, this blood has a low  $O_2$  content (previously extracted by the tissues) and a high  $CO_2$  content (a waste product of cellular metabolism) [14, 15]. When deoxygenated blood reaches the alveolus, the  $CO_2$ , which is in higher concentration (partial pressure) in the blood compared to the alveolus, diffuses inside the alveolus through the respiratory membrane [14, 15]. Simultaneously,  $O_2$ , which is present in higher concentration (partial pressure) in the lungs compared to deoxygenated blood, diffuses into the blood. This exchange of  $O_2$  and  $CO_2$ , between alveolar air and the blood in the pulmonary capillaries, is represented in Figure 2.2b. After this exchange, the blood exiting the pulmonary capillaries has a high  $O_2$  and a lower  $CO_2$  content [14, 15] and it is directed to the left side of the heart, which will push it towards the tissues by the arterial circulation [14].

A similar, but reversed process takes place in the systemic capillaries at the tissue level and it is defined as internal respiration [14]. Arterial blood entering the systemic capillaries is rich in  $O_2$  and has a low  $CO_2$  content [14, 15]. Across the systemic capillaries, the tissues have low  $O_2$  and a high  $CO_2$  concentration because the tissues' cells continuously use  $O_2$  for their metabolism and they produce  $CO_2$  as a waste product [14, 15]. When arterial blood reaches the systemic capillaries,  $O_2$  diffuses from the capillaries into the interstitial fluid and then it reaches the cells. At the same time,  $CO_2$  diffuses from the tissue into the capillaries' blood [14, 15]. Once this exchange takes place, blood with high  $CO_2$  and low  $O_2$  content enters the venous circulation when it will be redirected to the right side of the heart, where it will be pushed towards the lungs. Figure 2.3 shows a diagram of the internal and external respiration cycle in the body.

### 2.1.6 Oxyhaemoglobin dissociation curve

Haemoglobin binds with oxygen in the pulmonary capillaries and releases oxygen to the tissue at the systemic capillaries. The haemoglobin's ability of binding with oxygen molecules is directly controlled by the partial pressure of oxygen in solution ( $PO_2$ ) [14]. In the presence of high  $PO_2$ , haemoglobin is fully bonded with oxygen (i.e. fully saturated or high saturation), whereas a low  $PO_2$  causes the haemoglobin to be only

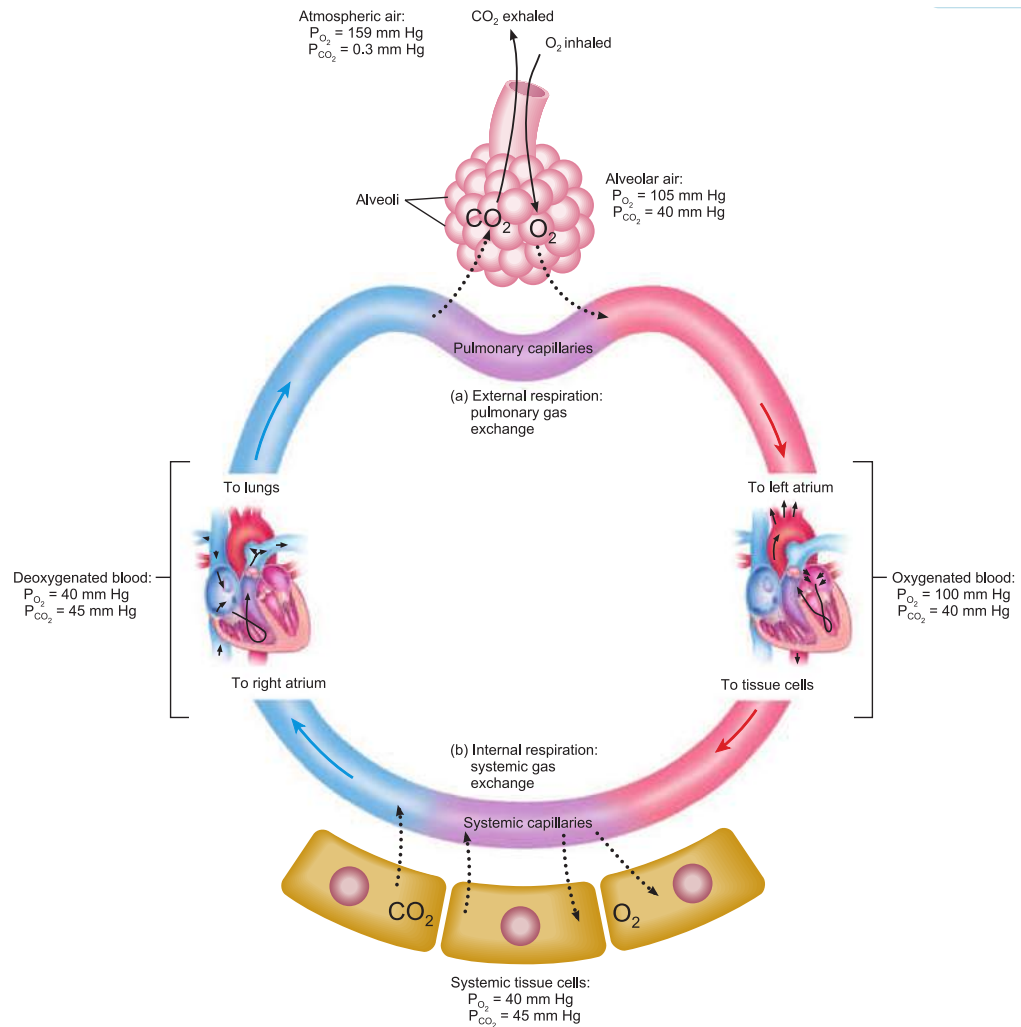


**Figure 2.3:** Cycle of internal and external respiration. After the gases exchange in the alveoli, the blood with high oxygen ( $O_2$ ) partial pressure (and low carbon dioxide ( $CO_2$ )) is directed to the heart. The left side of the heart pushes the oxygenated blood through the tissues by the arterial circulation (in red). In the systemic capillaries, the tissues extract the  $O_2$  for their metabolism and release  $CO_2$  as a waste product. The deoxygenated blood (low  $O_2$  and high  $CO_2$ ) is redirected towards the heart by the venous circulation (in blue). The right side of the heart pushes the deoxygenated blood towards the lungs, where it will be oxygenated again and  $CO_2$  will be removed by exhalation. Figure reproduced from [14]

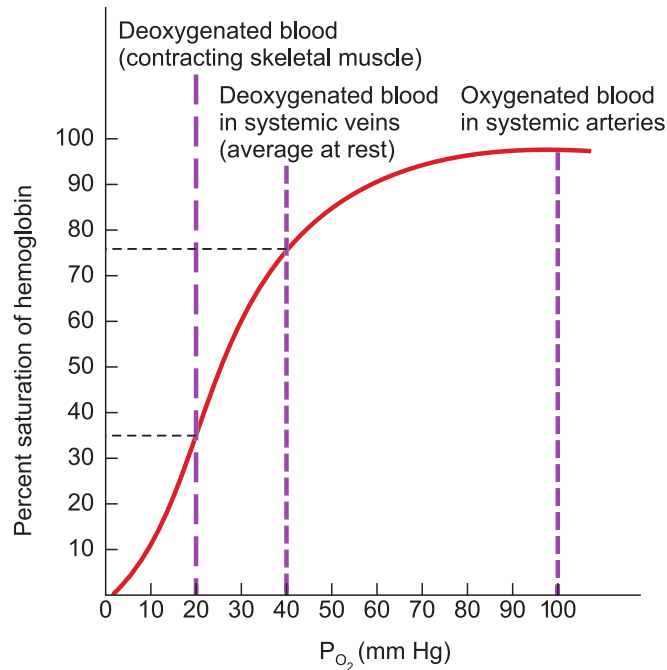


**Figure 2.4:** Oxygen-haemoglobin dissociation curve. At high oxygen partial pressure ( $PO_2$ ), the haemoglobin is highly saturated, while at low  $PO_2$ , the haemoglobin is partially saturated. Arterial blood, with a high  $PO_2$  is fully saturated ( $\approx 100\%$ ), whereas deoxygenated venous blood, at lower  $PO_2$ , is partially saturated ( $\approx 75\%$ ). When the tissue (muscle) is contracting, more oxygen is consumed, with a further decrease in  $PO_2$  and saturation. Figure reproduced from [14]

partially bonded with oxygen (i.e. low saturation) [14]. This relationship is described by the oxygen-haemoglobin dissociation curve as showed in Figure 2.4.

In the pulmonary capillaries, where oxygen is present in high  $PO_2$ , the haemoglobin binds easily with oxygen and is fully (or almost entirely) saturated ( $\approx 100\%$  saturated). In the systemic capillaries, the  $PO_2$  is lower, causing the haemoglobin to not hold the oxygen, and easily releasing it to the tissues by diffusion [14]. In the arteries, the  $PO_2$  is high and the haemoglobin is fully saturated ( $\approx 100\%$  saturation), whereas, in the venous circulation, after oxygen has been released to the tissue,  $PO_2$  drops to around 40 mmHg, creating a lower saturation ( $\approx 75\%$ ) [14]. This means that, in normal conditions, approximately 25 % of oxygen transported by the haemoglobin is actually released and used by the tissue [14].

Certain factors affect the relationship between  $PO_2$  and haemoglobin saturation (or oxygen-haemoglobin affinity). Temperature, pH (acidity), and partial pressure of  $CO_2$  ( $PCO_2$ ) can vary how haemoglobin binds with oxygen, shifting the oxygen-haemoglobin curve [14]. A higher pH, lower blood  $PCO_2$ , or lower temperature can shift the curve to the left, with an increased oxygen-haemoglobin affinity. On the other side, a lower pH,

higher  $\text{PCO}_2$ , or higher temperature decrease the oxygen-haemoglobin affinity, shifting the curve to the right [14].

## 2.2 The Cardiovascular System

The cardiovascular system is the dense net of vessels responsible for transporting nutrients and waste products (e.g.  $\text{O}_2$  and  $\text{CO}_2$ ) inside the body. The right side of the heart pushes deoxygenated blood towards the lungs for gas exchange, whereas the left side of the heart pushes oxygenated blood towards the tissues for the extraction of nutrients in the systemic capillaries. A complex system of tubes (blood vessels) connects the heart, tissues, and lungs, with the aim of transporting the blood (systemic circulation). Figure 2.5 schematically illustrates the structure of the systemic circulation, where the arteries, veins, and the previously introduced systemic capillaries are the main components. The following sections describe the structure and functions of arteries, veins and systemic capillaries.

### 2.2.1 The arterial circulation

Arteries are responsible for transporting and distributing oxygenated blood from the heart to the tissues [14]. Arteries branch from the left side of the heart (left ventricle) and divide into elastic and muscular arteries. Figure 2.6 shows the major arteries of the human body and how they branch from the heart to the tissues. Elastic arteries, as implied by the name, are elastic vessels that, due to their thin walls composed of elastic fibres, have the ability to stretch. Elastic arteries (also known as *conducting arteries*) are the largest arteries in the human body and are also the first arteries branching from the heart (e.g. aorta and pulmonary track) [14]. Their elastic structure allows to resist to the high blood pressure at the heart's exits and to propel the blood forward towards the tissues. The initial pressure necessary to move the blood is provided by the left ventricle's pressure, whereas the elastic arteries, by stretching and recoiling, give the necessary inertia for the blood to move onwards [14].

Elastic arteries branch to medium-sized, more muscular arteries also known as muscular arteries [14]. Muscular arteries continue to branch towards the tissues (or organs)

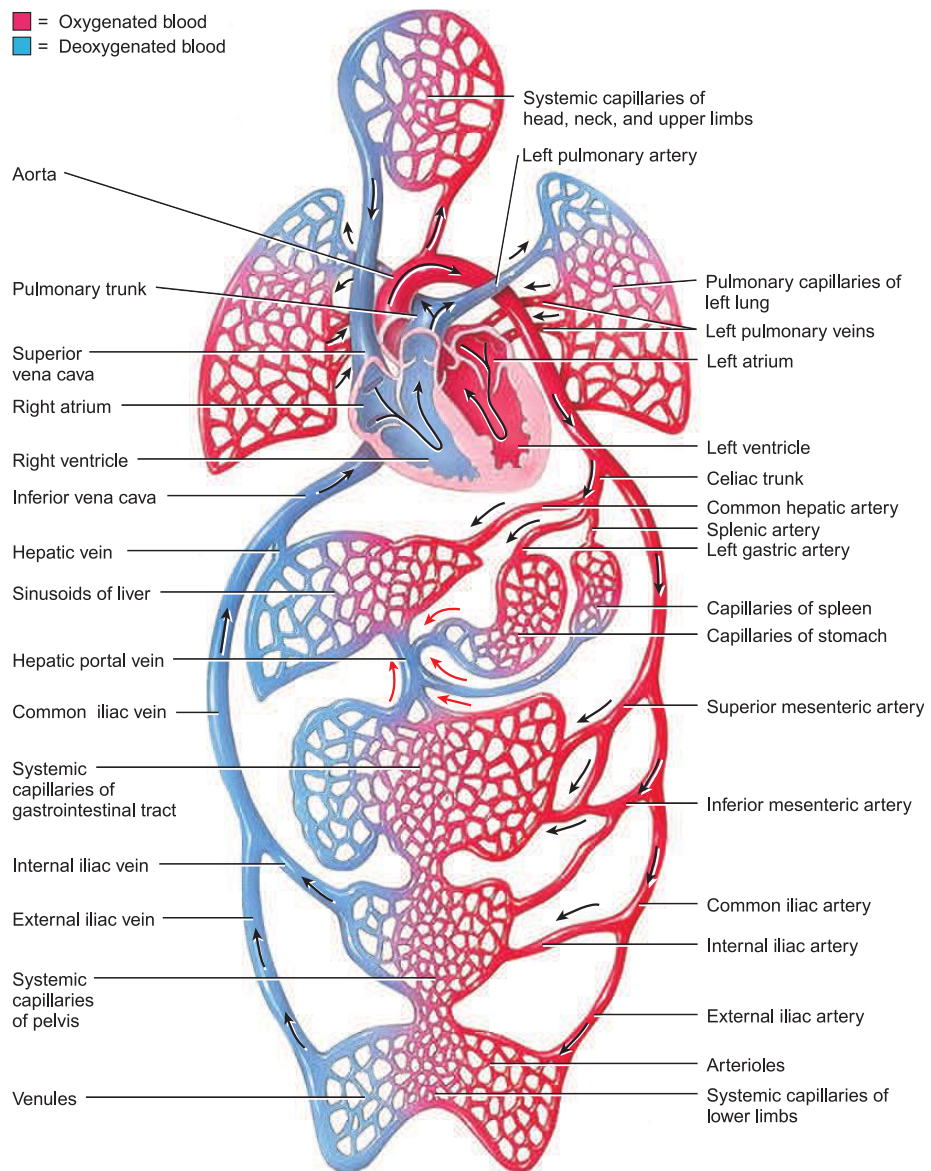


**Figure 2.5:** The systemic circulation. The newly oxygenated blood from the pulmonary capillaries reaches the left side of the heart, where it is pushed towards the tissues. The arteries (in red colour) transport the oxygenated blood to the systemic capillaries, where oxygen is released in the tissues. The veins (in blue colour) transport the deoxygenated blood back to the right side of the heart, where it is pushed towards the lungs for being oxygenated again. Figure reproduced from [14].

and their wall can be relatively thick since it is composed of smooth muscle. This muscular structure gives the ability to vasodilate (increase diameter) or vasoconstrict (decrease diameter) [14]. Muscular arteries, also called *distributing arteries*, are present in different sizes down to 0.5 mm, and the lack of elastic fibres prevent them to recoil as the elastic arteries [14]. Vasodilation and vasoconstriction of muscular arteries are controlled by stimulation of the sympathetic fibres innervating the smooth muscles of the vessels. An increased sympathetic stimulation initiates vasoconstriction, whereas a decreased stimulation causes vasodilation [14].

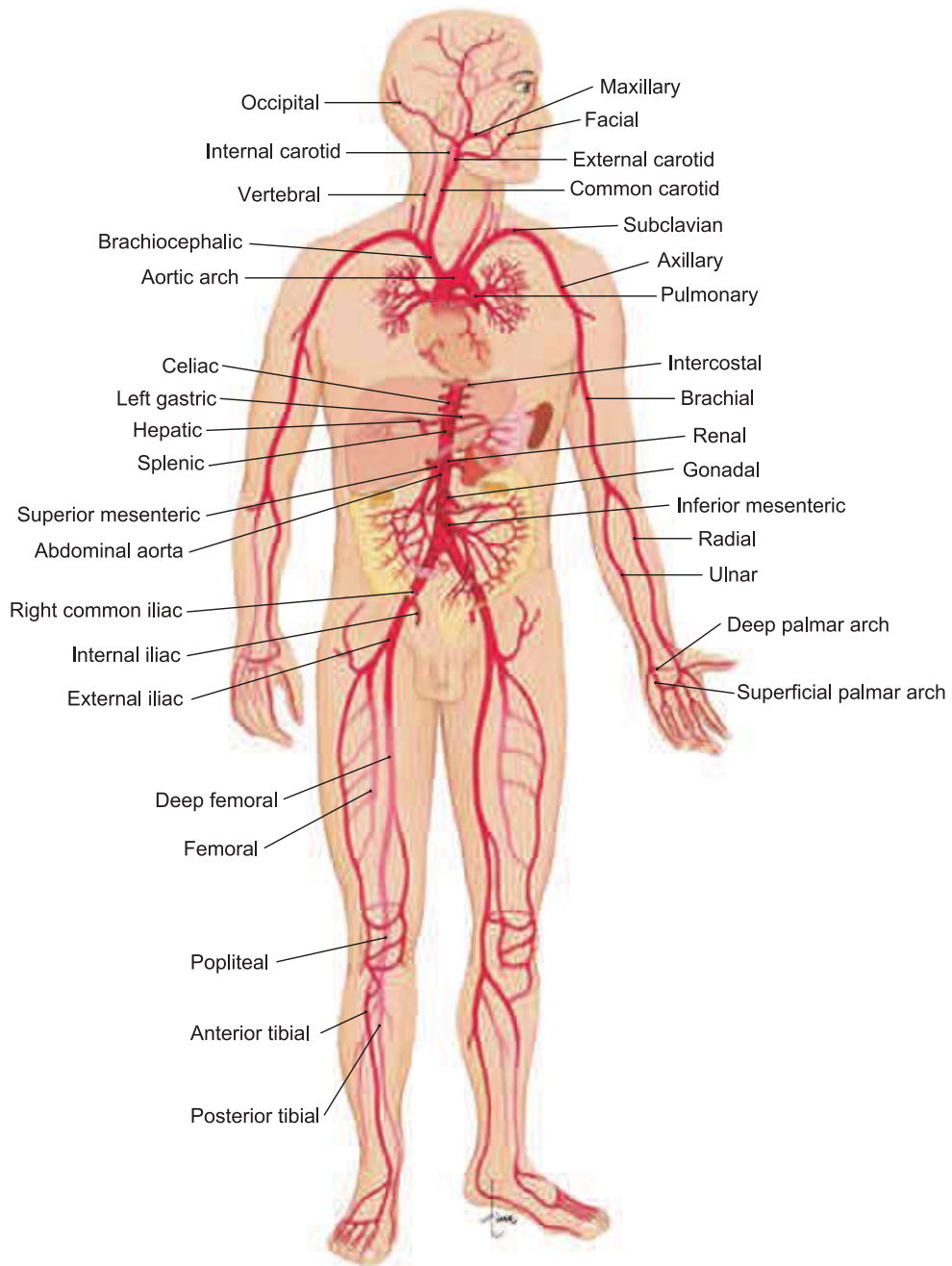


**Figure 2.6:** Major systemic arteries in the human body. Figure reproduced from [15].

### 2.2.2 The capillaries

Arteries have the main function of conducting blood from the heart to the systemic capillaries, where the extraction of oxygen from the tissues takes place.

Arteries connect to the capillaries through small blood vessels called arterioles. By contracting or dilating, the arterioles regulates blood flow to the capillaries (blood flow is also controlled by pre-capillary sphincters) [14–16]. The contraction/dilation of the arterioles directly acts on the vascular resistance and the consequent blood pressure (i.e. increase in vascular resistance cause an increase in blood pressure, whereas a decrease in vascular resistance make the blood pressure to drop) [14].

After passing through the arterioles, the oxygenated blood from the arteries enters the systemic capillaries [14,15]. Capillaries are the smallest blood vessels in the body, they have a thin wall for diffusion of substances through it, and they connect the arterial inflow to the venous outflow (see Figure 2.5). As shown in Figure 2.7, each systemic (or tissue) capillary bed is composed of a net of capillaries which ramifies from arterioles to venules. This dense net of vessels increases the surface available for the diffusion of oxygen into the tissues and it can be more extensive for tissues with a higher metabolic demand [14,15].

Different types of capillaries are present in the human body and they vary in the vessel's structure and their location [14,15]. The blood flow through the capillaries is not only mechanically regulated by pre-capillaries sphincters and arterioles, but it is also regulated by endothelial chemical substances (e.g. nitric oxide, NO) that control the vasodilation or vasoconstriction of capillaries [14].The blood flow in the extensive capillaries net is also known as *microcirculation* [14]. The exchange of nutrients between blood and tissues takes place by diffusion, as explained in subsection 2.1.5. After the exchange of nutrients and waste products between capillaries blood and tissues, the deoxygenated blood enters the venous circulation (venules and veins) in order to be transported back to the heart [14,15].

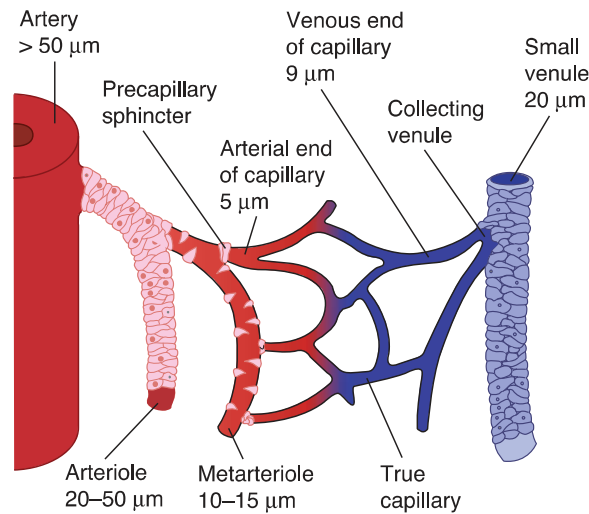


**Figure 2.7:** Schematic illustration on the succession of arteries, arterioles, capillaries, venules and veins. Figure reproduced from [16].

### 2.2.3 The venous circulation

After the exchange of  $O_2$  and  $CO_2$  in the capillaries, deoxygenated blood moves towards the venous circulation. Before entering the veins, blood from capillaries passes through intermediate vessels known as venules [14]. As showed in Figure 2.7, venules are tiny vessels and are also called post-capillary venules. These blood vessels are involved in the exchange of nutrients and white cell migrations, thus playing an effective part in the functions of the microcirculation [14].

Venules continue to enlarge until reaching the veins. Veins are large vessels transporting the blood back to the right side of the heart. Figure 2.8 shows the major systemic veins present in the human body. Like arteries, veins are not involved in the exchange of nutrients between blood and tissues. Veins are composed of thinner walls compared to arteries, they are extensible, but they cannot support high blood pressures like the arteries (venous blood pressure is significantly lower than arterial pressure) [14]. Veins usually accompany arteries, but often more than one vein is paired to each artery [14].

The return of blood to the heart through the veins is a passive action. Return of blood is achieved by the heart's action, contraction of limb muscles, and the negative pressure

created in the thoracic cavity during ventilation [14]. Back-flow of blood towards the capillaries is controlled by valves inside the veins, which allows the blood to move in the heart's direction while preventing the blood from flowing in the opposite direction due to gravity [14,15]. The greatest amount of blood at any given time (approximately 64 %) is in the venous circulation, making this part of the circulation to act as a blood

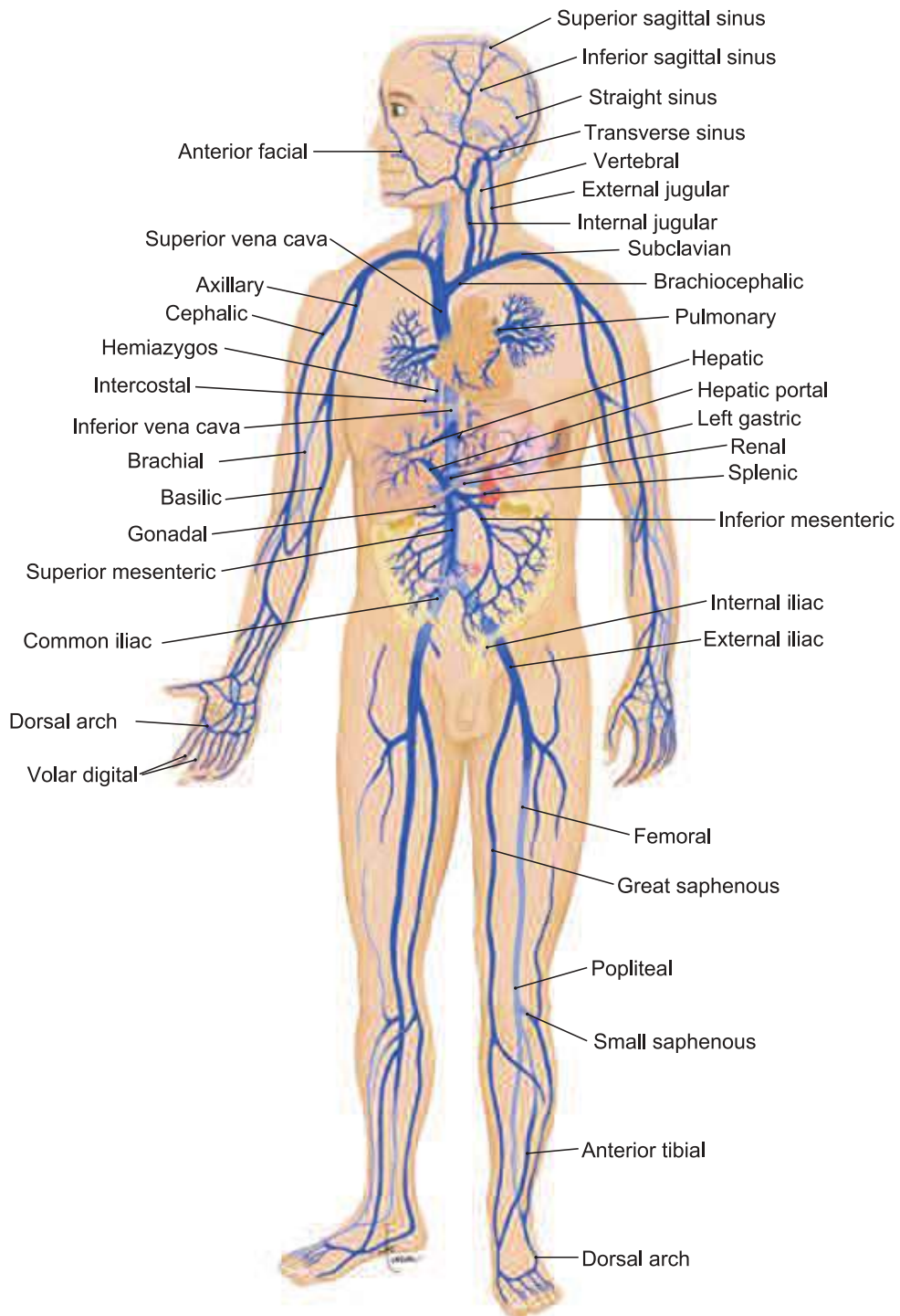


Figure 2.8: Major systemic veins in the human body. Figure reproduced from [15].

reservoir for the redirection of blood in situations when tissues demand higher blood flows (e.g. exercise or haemorrhage) [14, 15].

## **2.3 Summary**

In this chapter, a brief overview of the anatomy and physiology related to this work was presented. The structure of blood and its functions as a carrier of nutrients such as oxygen have been described, with a particular focus to the role of red blood cells and haemoglobin in the transport of oxygen and the removal of carbon dioxide from tissues. Also, the process of exchange of oxygen and carbon dioxide in the lungs and tissues (lungs-blood and blood-tissues) has been briefly introduced. The cardiovascular system has been presented as the group of blood vessels (arteries, capillaries and veins) responsible for transporting blood to tissues and releasing the necessary nutrients to the tissues in the body. The concepts introduced in this chapter should form the necessary basis of anatomy and physiology for the following chapters, where technologies and techniques for measuring blood flow, blood volumes, and blood oxygenation will be presented.

# Chapter 3

## **Review on noninvasive techniques for the *in vivo* monitoring of blood perfusion and oxygenation**

As described in the previous chapter, blood carries oxygen and nutrients to the tissues for their functioning. Therefore, monitoring of blood perfusion and oxygenation in tissues is of vital importance in clinical practice, and over the last decades, several techniques have been developed for the noninvasive assessment of these parameters. In this chapter, an overview of some techniques used for *in vivo* monitoring of blood perfusion and oxygenation will be presented. Techniques such as Laser Doppler flowmetry, Ultrasound Doppler or traditional clinical assessments will be introduced in the following sections of this chapter. Each of the techniques presented in this chapter occupies extensive branches of clinical monitoring, but their fundamental principles, measured parameters, and main applications will be briefly described in order to illustrate the current state of the art in the noninvasive monitoring of blood perfusion and oxygenation. Photoplethysmography and Near Infrared Spectroscopy will be presented in this chapter as well, but they will be explored in more depth in Chapter 4 and Chapter 5.

### 3.1 Photoplethysmography & Pulse Oximetry

Photoplethysmography (PPG) is a noninvasive optical technique used to measure blood volume changes and forms the basis of pulse oximetry [3]. PPG exploits the light absorption properties of tissues when light is emitted in a tissue and it will be described in details in Chapter 4. The light emitted in PPG is absorbed by structures within the tissue and the backscattered and absorbed light is detected by a photodetector. Moving structures within the tissue generate an intermittent absorption, while static components will cause a relatively constant absorption. The detected light in PPG is therefore composed of an alternated component (AC) and a constant component (DC). The AC component represents the arterial blood, which changes volume in synchrony with the cardiac cycle (systole and diastole) [1, 2, 9]. The DC component is resulting from the constant light absorption of static structures such as venous blood and surrounding tissue [1, 3, 9].

An example of this signal is illustrated in Figure 3.1, with AC and DC PPG signals, at both red and infrared wavelengths, acquired from the finger of a healthy volunteer. From this figure, the two components of the signal can be distinguished, with the DC component being the slowly varying part of the signal (offset) and the AC PPG overriding on top. The two components can then be separated by appropriate filtering. The PPG signal has found many applications such as heart rate and respiration estimation [1, 9], but the main application of the technique remains pulse oximetry [1].

Pulse oximetry is a technique used to monitor noninvasively and continuously arterial blood oxygen saturation ( $\text{SpO}_2$ ) [3, 4]. The technique exploits the optical absorption properties of oxygenated and deoxygenated blood and the PPG signal [4]. When PPG signals can be acquired at two wavelengths (red and infrared), the relationship between the signal amplitudes at red and infrared is directly proportional to the arterial oxygen saturation [4]. By applying calibration curves extracted from healthy volunteers, the  $\text{SpO}_2$  expressed in percentage can be estimated from the red and infrared PPG signals [3]. Since its first implementation in the 70's, pulse oximetry has revolutionised medicine by providing continuous and noninvasive measurement of arterial saturation [1, 4]. The technique is currently used in many clinical settings and it is a mandatory instrument during induction of anaesthesia [1, 3, 4].

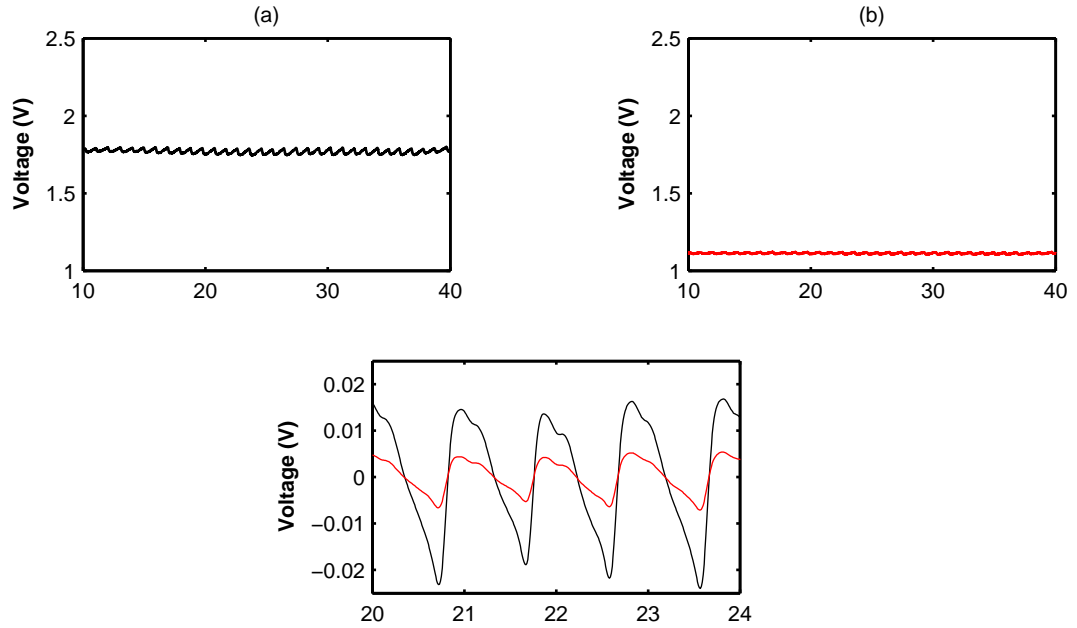


**Figure 3.1:** Red and infrared PPG signals acquired from the index finger of a healthy volunteer. (a) and (b) are respectively the infrared (black trace) and red (red trace) raw PPG signals (AC+DC). A small pulsatile AC PPG component is superimposed on a slowly varying DC PPG component. The DC component, representing the general light absorption by the tissue, is higher in the infrared wavelength than the red (greater light absorption by the red wavelength). (c) shows the same signals filtered and inverted. The DC component has been filtered out and only the red and infrared AC PPGs (red and black trace respectively) are plotted against each other. From the signals in (c), the arterial oxygen saturation ( $SpO_2$ ) can be estimated.

As mentioned above, photoplethysmography will be the core of the research work presented in this thesis. For this reason, a more detailed description of the technique will be provided in the next chapter, where the principles and applications of photoplethysmography and pulse oximetry will be provided.

## 3.2 Near Infrared Spectroscopy

Near Infrared Spectroscopy (NIRS) is an optical technique used for the noninvasive and continuous monitoring of perfusion and oxygenation in tissues. In NIRS, near infrared light is shone into tissues and the changes in light absorption are used to infer relative changes in oxygenated ( $HbO_2$ ) and deoxygenated haemoglobin (HHb). Near infrared light (700-1000 nm) is used in NIRS due to low absorption and high scattering properties of light in this part of the spectrum, causing the light to penetrate deep into tissues [12, 21–23].

NIRS bases its principles on the Beer-Lambert Law (BLL) and it will be further de-

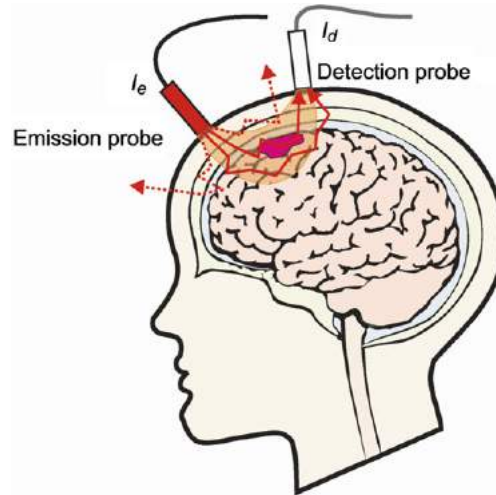


**Figure 3.2:** Cerebral near infrared spectroscopy measurement. Near-infrared light is emitted transcutaneously into the brain, passing through the skull. Light undergoes absorption and scattering before being detected by a photodetector. The detection probe collects spectral information from the superficial cerebral tissue and transforms it into haemoglobin concentration changes and cerebral oxygen saturation. Figure reproduced from [24].

scribed in Chapter 5. Briefly, the BLL correlates the changes in light attenuations to the concentrations of chromophores (i.e. light absorbing structures) present in the solution [11,12,24]. Therefore, by applying light into a solution (tissue) and observing the changes in light attenuations, the changes in concentrations of the chromophores present in the tissue can be determined [11]. By assuming that the only chromophores changing concentration in tissue are  $\text{HbO}_2$  and HHb, and assuming constant scattering, changes in  $\text{HbO}_2$  and HHb concentrations can be estimated from the light attenuations detected by a photodetector [11,24]. For the estimation of  $\text{HbO}_2$  and HHb, a system of at least two equations should be solved. By applying near infrared light at least two different wavelengths, the BLL can be solved for  $\text{HbO}_2$  and HHb [11,24]. This method, however, only estimates relative changes in concentrations from a baseline, whereas, for the estimation of absolute concentrations, the pathlength travelled by light or the absorption and scattering characteristics of the tissue should be known [11,12,22–24]. Techniques such as Time Resolved Spectroscopy or Phase Resolved Spectroscopy allow the estimation of absolute concentrations of  $\text{HbO}_2$  and HHb and they will be described later in Chapter 5. Once absolute concentrations of  $\text{HbO}_2$  and HHb are determined, or by applying other computational techniques, an oxygenation index can be calculated from the ratio  $\text{HbO}_2 / (\text{HbO}_2 + \text{HHb})$  [11–13,24].

Due to the high penetration depth reached by NIRS in tissues and the relative transparency of bones (e.g. skull) to the near infrared light, the technique has been exten-

sively applied to monitor perfusion and oxygenation changes in the brain [12, 13]. An example of cerebral NIRS measurement is depicted in Figure 3.2. NIRS has also been widely used to study muscles' metabolism during rest and during exercise [13, 24]. The technique is continuously attracting interest for its ability to monitor organs' perfusion and oxygenation and some of the technique's applications are shock and trauma medicine [25], surgery [22, 25], flap monitoring [26, 27], splanchnic perfusion monitoring [22], as well as mapping of the brain (imaging) [24] and brain functional studies.

### 3.3 Laser Doppler Flowmetry

Laser Doppler Flowmetry (LDF) is an optical technique used for the noninvasive measurement of blood flow in skin and organs. The technique's name originates from the Doppler shift, which relates the change in frequency of electromagnetic waves after they have interacted with a moving object [28]. When light is emitted into a tissue, the photons undergo reflection and scattering after interacting within the tissue's structure; but when light hits a moving object such as a red blood cell, a shift in frequency (Doppler shift) between the emitted and detected light appears [28, 29]. This shift in frequency is directly related to the speed of the moving object [28, 29] and the general relationship between the shift in frequency and the speed is described by Equation 3.1.

$$\Delta f = f_e - f_d = \frac{2v \cdot \sin \alpha}{\lambda} \quad (3.1)$$

Where  $f_e$  is the emitted frequency,  $f_d$  is the detected frequency,  $v$  is the velocity (speed) of the moving object,  $\alpha$  is the angle between the light beam and the normal to the object's direction of motion, and  $\lambda$  is the wavelength of the light beam. For this to hold, the light source is considered stationary with respect to the moving object.

When light is shone into a tissue (microcirculation), the interaction between light and moving red blood cells causes a Doppler shift in the detected light [28–30]. However, in real situations, photons in tissues undergo more than one scattering event and multiple shifts in frequency, with a resulting shift in frequency being the linear sum of the single shifts [29].

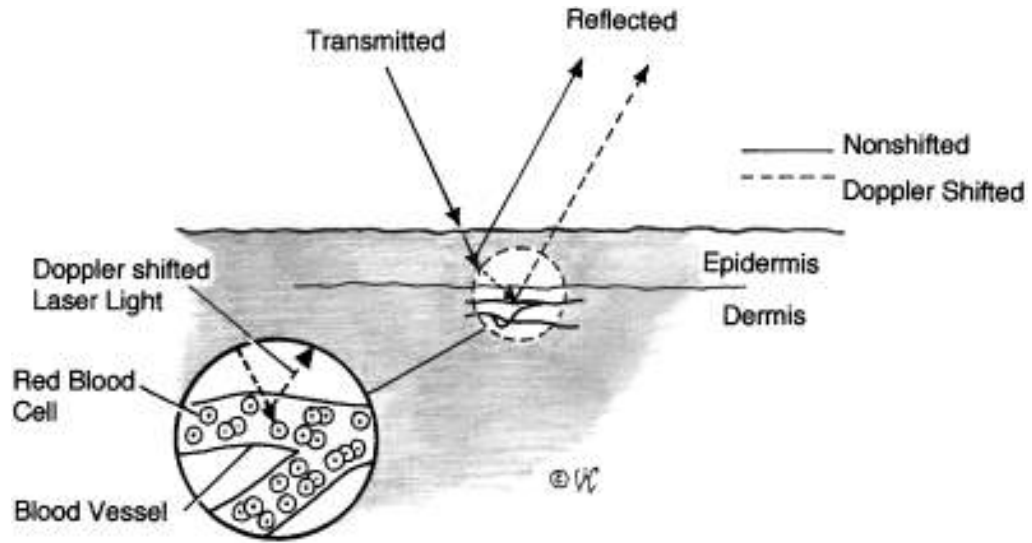


**Figure 3.3:** Doppler shift occurring in laser Doppler flowmetry. The transmitted light inside the tissue reflects onto red blood cells in the blood vessels. Interaction with red blood cells causes a Doppler shift in the reflected light. A portion of the light that does not interact with moving objects is reflected without being Doppler-shifted. Figure reproduced from [28].

In order to be able to detect the shift in frequency between emitted and detected light, a monochromatic and coherent light source such as a laser light beam is used in LDF measurements. Laser light is used as it is centred to a specific wavelength  $\lambda$  (monochromatic), is a coherent light beam, and it can be emitted at a specific frequency [28]. Once the light beam enters a tissue, photons are scattered by both stationary objects (e.g. skin, tissues, and vessels) and moving objects (blood cells) [28–30]. As shown in Figure 3.3, reflection of light on stationary objects does not create a shift in frequency in the reflected light, whereas light interaction with moving objects (red blood cells) generates a frequency shift in the reflected light. When the reflected light beams, at both shifted and non-shifted frequencies, impinge on the photodetector, they create a beat in frequency [28–30]. Laser Doppler instruments process these beats in frequency to have an estimation of red blood cells velocity [28]. This generated beat, however, is the combination of the frequency shifts generated by objects moving in all directions, making impossible to distinguish the direction of motion [30]. Different techniques may be used to process this beat in frequency, but all of them generate a voltage signal, which is usually transformed to a unit-less parameter known as *Flux* [28, 29]. As described in (Equation 3.2), the Flux is directly proportional to the product of red blood cells' concentration ( $[RBC]$ ) and the red blood cells' velocity ( $v_{RBC}$ ) [28–30].

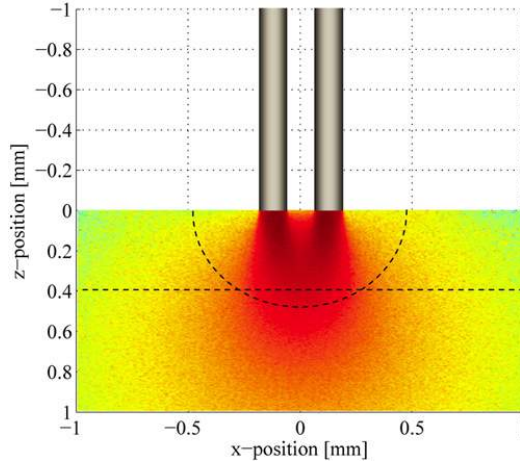


**Figure 3.4:** Montecarlo simulation of the spatial distribution of laser Doppler flowmetry measurements. Measurement depth (0.39 mm) and volume ( $0.23 \text{ mm}^3$ ) are marked respectively with horizontal and hemispheric dotted lines. Fibres separation distance was set at 0.25 mm, whereas the emission wavelength was 780 nm. Figure reproduced from [33].

$$Flux \approx [RBC] \times v_{RBC} \quad (3.2)$$

Laser light sources (helium-neon gas or laser diodes) are adopted along with optic fibres to transport the light to the surface of the tissue [30,31]. Very close to the emitting fibre (usually less than 1 mm apart), another fibre is deployed to transport the backscattered light to a photodetector, which will convert the detected light into a voltage signal for being processed [28,30]. This signal from the photodetector contains an alternated (AC) and a stationary (DC) component. The AC component contains frequency information generated from the interaction with moving objects (frequency shift), whereas the DC component represents the light attenuation from non-moving structures [30]. Both AC and DC are processed by the instrumentation for extracting information on RBCs' flow and unwanted noise [30]. The wavelength of the emitted laser beam is usually selected between the red and near-infrared part of the spectrum [28–31], in order to increase the sensitivity of the instrument to red blood cells' motion over other moving objects (e.g. white blood cells) [29]. LDF measurements do not penetrate tissues in depth and they typically interrogate a limited part of the superficial anatomical regions, with a penetration depth between 1 and 2 mm [28, 30, 31]. This penetration depth is dependent on the type of tissue, the specific light wavelength used and the emitter-detector separation distance [28, 30–33]. Figure 3.4 illustrates an example of Montecarlo simulation of the spatial distribution (penetration depth and volume) of an LDF measurement.

Laser Doppler flowmetry has found a multitude of applications for the noninvasive monitoring of blood flow. The main application of LDF is the continuous monitoring of skin blood flow changes and the assessment of the status of the microcirculation by analysing the response to a vascular occlusion [31, 34]. Among the numerous applications, the technique has been used for diagnosis of peripheral arterial or venous disorders [31, 34], flaps and grafts monitoring [28, 31, 35, 36], assessment of endothelial function [34], skin diseases and tumours [28], skin ulcers and burns [28]. LDF has also been investigated for the measure of changes in blood flow directly from organs such as the brain [37, 38] and the liver [39].

Although it has been widely used for monitoring blood flow in different settings, Laser Doppler flowmetry suffers from some limitations. The estimated Flux is presented in arbitrary units, it is not predictable nor reproducible [28, 29], and it has an inter- and intra-subject variability [29]. Therefore, the users should observe the results as changes from a baseline (trends) rather than absolute values of Flux [29, 36]. LDF does not provide an indication of the direction of motion [30] and there is no actual knowledge of the penetration depth [29, 40]. The technique is also considerably sensitive to minimum pressures applied on the sensor [40] or to movement artefacts [28, 29, 40]. Finally, laser Doppler measurements do not have an absolute zero, because of the residual signal (biological zero) that is measured even after complete occlusion of arterial and venous circulation [28, 29]. It was also previously reported that LDF measurements alone may not be sufficient for distinguishing between venous and arterial occlusions [36, 41].

### **3.4 Ultrasound Doppler Flowmetry**

The Doppler effect introduced in Section 3.3 is not used with laser light only, but it can be applied to ultrasound waves as well. Ultrasound Doppler flowmetry is a noninvasive technique, which applies the Doppler principle to ultrasound waves for the measurement of blood flow. Sound waves are mechanical waves that propagate through a medium such as air, liquid or tissue, and are usually known for constructing sounds like voices or music [42]. Sound waves propagate through a medium in a certain frequency and waves propagating at a frequency between 20 Hz to 20 kHz can be detectable by the human ear [42]. Ultrasound waves used for medical application have propagating

frequencies comprised between 2 MHz and 40 MHz [42], thus far beyond the audible range of the human ear. Ultrasound waves are used in medical applications for their ability to propagate through tissues noninvasively and for the capability of providing information from their interaction with structures within the tissues.

When ultrasound waves are emitted in tissue, they undergo reflection with stationary objects, whereas a Doppler shift in frequency is generated from the interaction with moving structures such as blood. Reflection is created when the waves travelling in the medium interact with a second medium with different acoustic characteristics [42]. Part of the original wave is reflected backwards, while a portion continues to diffuse through the second medium. This principle is used in ultrasound imaging techniques, but is rather discarded in ultrasound Doppler flowmetry, which processes the shift in frequency for assessing blood flow [42]. Similarly to laser Doppler flowmetry, the change in frequency in the detected sound wave is proportional to the velocity of the moving object and their relationship is described by Equation 3.3 [42].

$$\Delta f = f_d - f_e = \frac{2f_e v \cos \theta}{c} \quad (3.3)$$

Where  $\Delta f$  is the shift in frequency,  $f_d$  is the detected shifted frequency,  $f_e$  is the original emitted frequency,  $v$  is the velocity of the moving object,  $\theta$  is the angle between the sensor and the direction of motion, and  $c$  is the speed of sound in the medium [42]. The Doppler effect of ultrasound waves for motion of blood in a vessel is also graphically depicted in Figure 3.5a. Differently from light beams, ultrasound waves are able to maintain their directionality. Therefore, changes in frequency detected yield the direction of motion, with a positive shift if the object is moving towards the sensor and a negative shift in case the object is moving away [42]. Thus, the technique is able to provide information on blood flow moving towards the sensor (forward flow) and flow moving away from the sensor (reverse flow) [42]. In ultrasound Doppler flowmetry, the Doppler shift is then used to infer a flow signal (spectral Doppler) which will be proportional to the velocity and direction of blood's motion. Figure 3.5b shows an example of ultrasound Doppler readings (spectral Doppler) acquired from the radial artery of a healthy subject. If the angle  $\theta$  at which the sensor is held (with respect to the direction of blood flow) is known, the blood velocity can also be estimated from the spectral Doppler signal by solving Equation 3.3 [42].

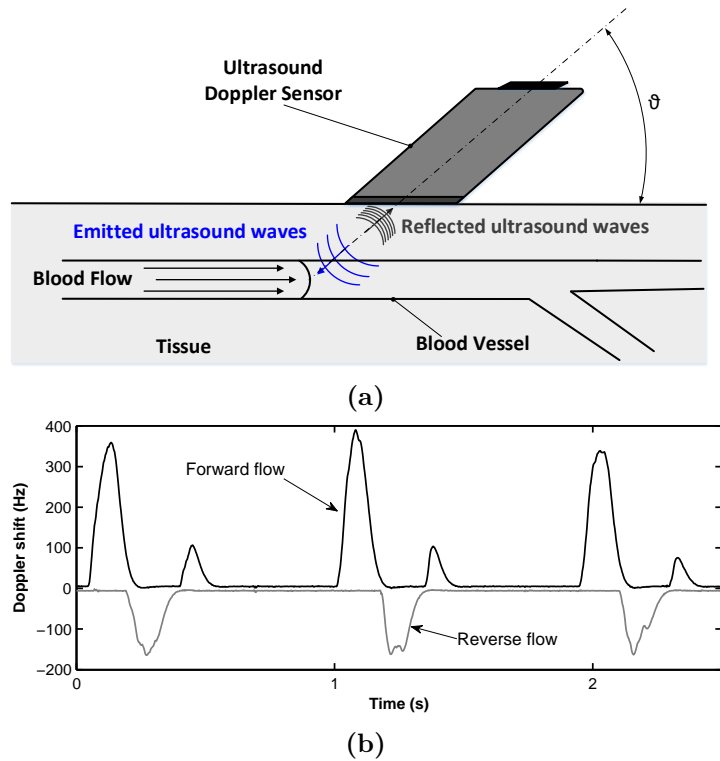


**Figure 3.5:** Doppler shift of ultrasound wave propagating in tissue and ultrasound Doppler measurement from the radial artery of a healthy subject. (a) A sensor, inclined with an angle  $\theta$ , emits ultrasound waves into a tissue. The emitted ultrasound waves impinge on the moving blood in the vessel and, after experiencing Doppler shift, the reflected waves return to the sensor. (b) Ultrasound Doppler measurements acquired from the radial artery of a healthy subject. The forward flow (black trace) generates a positive Doppler shift, while a smaller reverse flow (grey trace) is noticed from the negative Doppler shift. The sensor was held opposite to the direction of blood movement as in (a).

Ultrasound Doppler flowmetry sensors have limited dimensions and they can be easily held by the examiner. The sensors usually comprise of both emitting and detecting elements. Ultrasound waves are generated and detected by plates composed of a piezoelectric material. Piezoelectric materials produce mechanical vibrations proportional to the intensity and frequency of the voltage at which they are supplied and, inversely, generate a proportional voltage when mechanically strained [43]. The detecting element transforms the reflected waves into voltages in order to be processed by the instrumentation [42,43]. Emission and detection can be performed by the same piezoelectric plate in pulsed waves ultrasound Doppler flowmetry [42].

Ultrasound Doppler is widely used for the measurement of blood flow and velocity in arteries and veins [42], as well as for the diagnosis of vascular pathologies [42]. Hand-held and implantable Doppler sensors are often used to monitor flaps perfusion [36,44], whereas transcranial Doppler systems can be used to monitor cerebrovascular blood flow [45].

### 3.5 Transcutaneous PO<sub>2</sub> and PCO<sub>2</sub>

As previously mentioned in subsection 2.1.6, the partial pressures of oxygen (PO<sub>2</sub>) and carbon dioxide (PCO<sub>2</sub>) play an important role in the ability of haemoglobin in transporting oxygen to tissue. Therefore, monitoring the PO<sub>2</sub> and PCO<sub>2</sub> can provide an indication of the quality of oxygen delivery to tissues. The noninvasive monitoring of PO<sub>2</sub> and PCO<sub>2</sub> can be performed by Clark's electrodes. These PO<sub>2</sub>/PCO<sub>2</sub> sensors are based on the property of noble metals, which reduce when they enter into contact with oxygen [43, 46]. The electrodes are composed by an anode (reference) and a cathode, which reduce and oxidise when in contact with oxygen, generating a current proportional to the concentration of oxygen [43, 46]. Both the anode and cathode are placed behind a permeable membrane, which filtrates oxygen from the high-pressure environment (skin) to the zero pressure environment (membrane) [43, 46]. The same principle is used for measuring PCO<sub>2</sub> as well [34]. Clark's electrodes can be in form of a needle or transcutaneous (surface) sensors [34, 46]. In the first configuration, the electrode is inserted through the skin, while in the latter the sensor is placed transcutaneously on the skin's surface [34, 46]. When placed transcutaneously, the sensor heats the skin to 43-45 °C, facilitating the oxygen to diffuse through the skin and into the sensor's chamber, where the process of cathode-oxygen-reduction takes place [34]. Another application of Clark's electrode is in catheters to be placed directly in tissues [46].

Clark's electrodes are used in newborn infants because their thinner skin facilitates the diffusion of oxygen through the skin [34]. The sensors can also be applied directly to organs such as intestine and muscles [46]. Clark's electrodes present several limitations, which contributed to their low acceptance in clinical environments. The insertion of needles can cause tissue damages and does not guarantee a spatially homogeneous measurement, causing incorrect PO<sub>2</sub>/PCO<sub>2</sub> readings [46, 47], the technique has a small penetration depth (15-20 μm) [46, 47], and it requires continuous calibration and long times to reach equilibrium [34, 43].

### 3.6 Gastric Tonometry (capnography) and Sublingual Capnometry

In cases of hypoperfusion or hypoxia, the tissue is deprived of the correct amount of oxygen necessary for its metabolism. In this mismatch between oxygen delivery and oxygen demand,  $\text{CO}_2$  accumulates and it diffuses through tissues. Gastric Tonometry (GT) and Sublingual Capnometry are measurement techniques that estimate the partial pressure of  $\text{CO}_2$  ( $\text{PCO}_2$ ) in order to detect situations of deprived oxygen delivery [47].

In gastric tonometry, a nasogastric tube is inserted into the gastric mucosa, with the aim of monitoring  $\text{PCO}_2$  in this location as an early indicator of perfusion or metabolic mismatches [47]. The tip of the catheter has a saline solution-filled balloon for the determination of changes in pH. After 30 or 90 min of equilibration, the  $\text{PCO}_2$  in the gastric mucosa is in equilibrium with the air in the balloon. By measuring the arterial Bicarbonate ( $\text{HCO}_3^-$ ) the Henderson-Hasselbalch equation can be used in order to calculate the mucosal pH, which, in turn, is an indicator of acidosis (i.e. anaerobic metabolism in the case of oxygen deprivation) [46, 47]. This approach, however, produces some flaws and a modification of the technique has been introduced, consisting on the direct measure of  $\text{PCO}_2$  by a conventional air-filled capnometer [47]. This also allows for more frequent measures of  $\text{PCO}_2$  gradients instead of the less frequent pH [46, 47].

Sublingual capnometry (SC) is a less invasive and quicker method to assess  $\text{CO}_2$  accumulation in tissues [46, 47]. SC adopts fibre optics to transport light to a sensor placed between the tongue and the mouth mucosa [34, 48]. The sensor is composed of a permeable membrane through which the  $\text{CO}_2$  diffuses. On the opposite side of the membrane, a fluorescent dye solution is continuously illuminated by a fibre optic [34, 48]. If the  $\text{PCO}_2$  on the other side of the membrane is high, the gas diffuses through the membrane and an increase in  $\text{CO}_2$  causes the dye to produce fluorescence (i.e. energy process that causes photons to be absorbed and re-emitted at a different wavelength) [34, 48]. The re-emitted light is proportional to the  $\text{CO}_2$  concentration and is then processed to quantify the  $\text{PCO}_2$  [34, 48].

GT and SC have been demonstrated to be reliable indicators of states of deprived oxy-

gen delivery in septic patients, anaerobic metabolism (acidosis), indicator of splanchnic perfusion, and Multiple Organ Failure syndrome [34, 46–48]. Moreover, SC has been demonstrated to be a more reliable indicator of hypoperfusion in septic shock patients compared to blood lactate levels [47]. However they present different limitations such as incorrect theoretical assumptions [46, 47], long times to perform a measurement (GT) [46], necessity of gas calibrations and blood gas analysis [34], non-continuous measurements [46, 48], discrepancies in the indication of regional or global oxygen deprived states [46, 47], scattered results depending on the specific application [46–48], as well as difficulties in the interpretation of the results [48].

### 3.7 White light reflectance spectrophotometry

White light reflectance spectrophotometry (WLRS) is an optical technique that exploits the reflection and absorption properties of oxygenated and deoxygenated haemoglobin in order to measure a haemoglobin oxygenation index (HOI) in tissues. In WLRS, white light is applied to a tissue, but instead of acquiring only a few discrete number of wavelengths as in pulse oximetry or NIRS, the entire spectrum range is emitted and recorded from the tissue [49, 50]. The emitted spectrum may vary between different instruments, but it usually ranges between 502 and 630 nm [49, 50]. The light source is a lamp emitting white light, whereas an interference band-pass rotating filter is used for the selection of discrete wavelengths in the 502-630 nm range, with about 2 nm resolution (64 wavelengths) [49, 50]. This process guarantees the emission of a spectrum of wavelengths in the visible region and it is performed at high speed (100 spectra per second). Optical fibres are usually dedicated for the emission and transportation of the reflected light from the tissue [49, 50].

The detected reflected spectra provides information on the wavelength-dependent reflection (absorption) of blood in the tissue. From this, concentrations of oxygenated ( $\text{HbO}_2$ ) and deoxygenated haemoglobin (HHb) can be extracted. For the calculation of  $\text{HbO}_2$  and HHb concentration, a mathematical process, relating light absorption and scattering to concentration is used [50]. The acquired absorption at several wavelengths (e.g. 64 wavelengths) are correlated to the concentrations of  $\text{HbO}_2$  and HHb in tissue [49, 50]. An example of the detected spectra by WLRS is depicted in Fig-

ure 3.6a. The concentrations estimated by this method are, however, relative to the basic amount of scattering, which is unknown. Nevertheless, this is not taken into account for the calculation of oxygenation as the common scattering factor is ruled out as in Equation 3.4.

$$HOI = \frac{HbO_2}{HbO_2 + HHb} \quad (3.4)$$

This process consents the determination of haemoglobin oxygenation from the mixed spectra, but correction procedures are required to correct the collected spectra from noise [49]. Before each measurement a black and a white reference spectra need to be acquired for the correction of the mixed spectra acquired [49, 50].

The short separation distance between fibres and the limited penetration depth of white light cause the technique to not be able to penetrate deep into tissues, thus providing the assessment of only superficial structures (1 mm or less in depth) [51, 52]. Due to the flexibility of transmitting and detecting light by optic fibres, WLRS has been mainly applied to measure oxygenation and perfusion in the gastrointestinal tract [49, 51, 53]. Reflectance sensors have also been used and showed good results for transcutaneous measurements such as flaps perfusion monitoring [52, 54]. For instance, Figure 3.6b shows the application of a WLRS sensor on a breast flap.

### 3.8 NADH fluorescence and Palladium-Porphyrin phosphorescence

NADH (Nicotinamide Adenine Dinucleotide) is a molecule involved in the cellular metabolism of the mitochondria. In this process, NADH is oxidised to  $NAD^+$  as result of the reaction with oxygen for the production of ATP [46]. In situations of hypoxia, less oxygen is delivered to the mitochondria, failing the oxidisation of NADH into  $NAD^+$ , and consequent accumulation of the reduced NADH in tissues [46, 55]. Therefore, monitoring of NADH accumulation can give an indication of a decrease in oxygen transport to a tissue [46]. Like haemoglobin, NADH presents two main absorption peaks at 250 nm and between 320-380 nm, while  $NAD^+$  does not absorb light in the

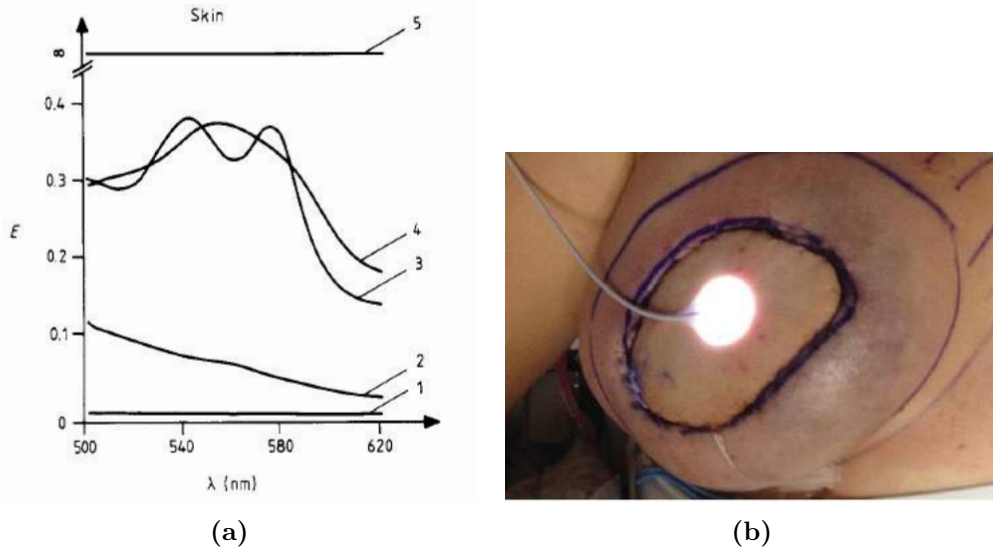


**Figure 3.6:** White light reflectance spectra acquired from the skin of the back of the hand (a) and a white light reflectance spectrophotometry sensor applied on the surface of a breast flap (b). In (a), (1) is the reflectance spectrum from the white standard, (3) and (4) are respectively the intracapillary spectrum of haemoglobin and the spectrum of deoxygenated haemoglobin during arterial occlusion, (2) is the reflectance spectrum from the skin during vascular occlusion on the forearm, and (5) is the spectrum of the black standard. The figure was reproduced from [50]. In (b) a white reflectance spectrophotometry sensor is applied transcutaneously on the surface of a breast flap for postoperative monitoring of flaps oxygenation (figure reproduced from [54]).

range 320-380 nm [46,55]. Therefore, by monitoring light absorption in the 320-280 nm range, only NADH absorption can be monitored, neglecting  $\text{NAD}^+$  [55]. Also, NADH absorption in the 320-380 nm range causes fluorescence in the 420-480 nm range [46,55]. Thus, by applying light at 360 nm and detecting changes in fluorescence intensity (e.g. photomultiplier tubes, fluorometer, or video cameras), accumulation of NADH in tissues can be monitored [46,55]. The technique can be added to microscopy and it can be incorporated in catheters for *in vivo* measurements. Figure 3.7a shows images from a NADH fluorescence video acquisition from myocardial tissue during clamping of the left coronary artery. In addition to image/video acquisition, the technique can also be applied to acquire trend signals of NADH fluorescence (Figure 3.7b) [55]. *In vitro* and *in vivo* studies showed the ability of the technique to detect changes in NADH accumulation due to hypoxia (i.e. reduce oxygen content) or ischaemia (i.e. blood flow) [55]. Although the technique can provide trend images and signals on NADH accumulation [55], the quantification of NADH still remains an open challenge [46,55].

Phosphorescence is a similar process to fluorescence. In phosphorescence, light is absorbed and released by a substance after the application of a pulse of light. Palladium-Porphyrin (PP) is a water-soluble compound, which can be injected intravenously. PP presents a quenching property when it is illuminated by light. This quenching effect is

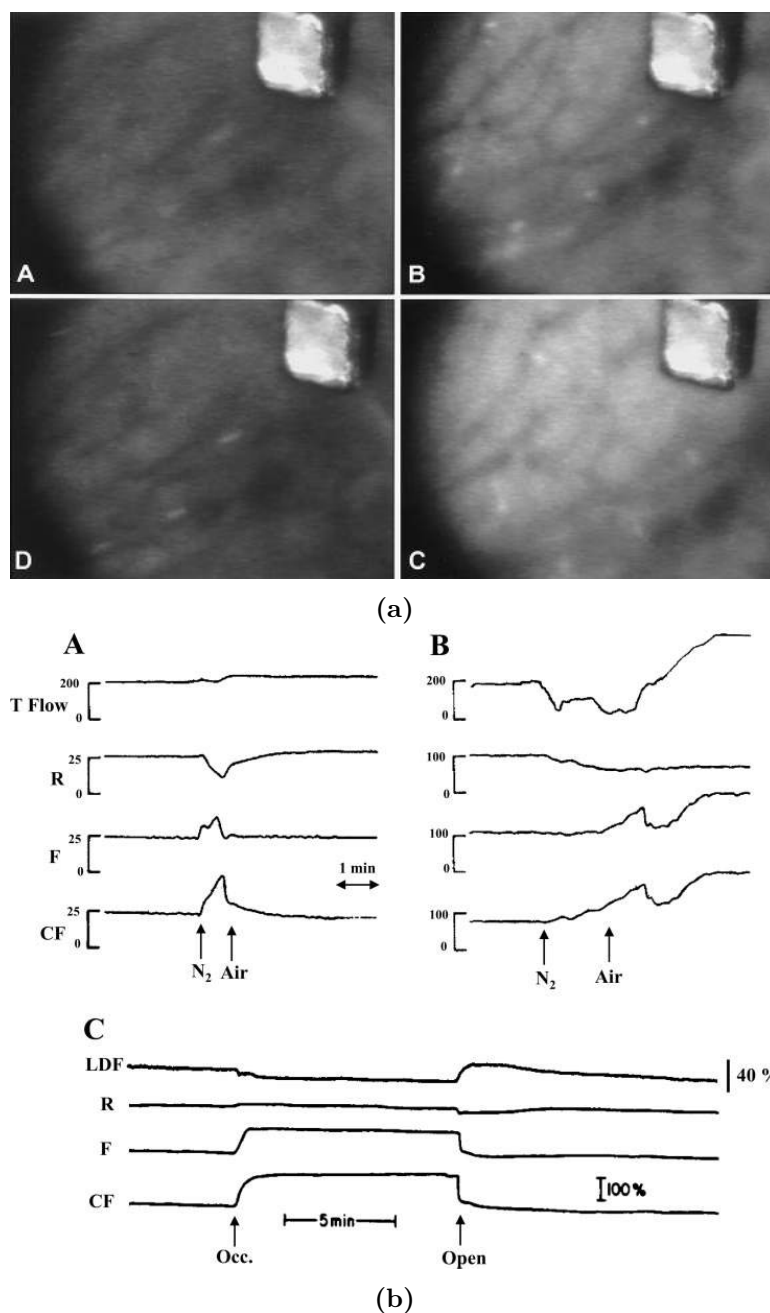


**Figure 3.7:** NADH video fluorimetry of a pig's heart during clamping of the left coronary artery (a) and NADH fluorimetry signals from a dog's heart during hypoxia and ischaemia (b). In (a), baseline image (A) shows normal blood flow. After 30 seconds (B), fluorescence increases until reaching maximum fluorescence after 3 minutes of occlusion (C). When blood flow is restored (D), fluorescence returns to baseline. Figure reproduced from [46]. In (b), changes in fluorescence during hypoxaemia are represented in A and B. When a hypoxic mixture (N<sub>2</sub>) is administered, fluorescence (NADH concentration) increases. When a normoxic air mixture (Air) is administered, fluorescence returns to baseline. Similar behaviour can be observed during induced ischaemia (C). Fluorescence increases after occlusion (Occ.) and when blood flow is restored (Open), fluorescence returns to baseline. Figure reproduced from [55].

dependent on the oxygen presence in the solution and the decay time is proportional to the concentration of oxygen present [46]. Thus, by injecting PP intravenously and applying a pulse of light, the measurement of the quenching decay time by a Photomultiplier Tube is possible, and the oxygen tension (or partial pressure) can be calculated by computing this decay time [46]. Both NADH fluorescence and PP phosphorescence are non-invasive methods that are able to provide information on oxygenation of microvascular compartments. They do not need to be in contact with the tissue, thus can be applied to moving organs and incorporated in microscopes [46].

### 3.9 Imaging of the microcirculation

Imaging of the microcirculation offers the possibility to visually check the perfusion of capillaries. Orthogonal Polarization Spectra, Sidestream Dark Field, Laser Doppler Imaging and Laser Speckle imaging offer this possibility.

Orthogonal Polarization Spectra (OPS) is a microcirculation monitoring technique in which filtered and polarised light is applied to the tissue [47, 56, 57]. The light beam is then focused by a lens in order to be applied to a tissue area of around 1 mm in diameter [56]. Polarised light is preserved in reflection and scattering, but after more than ten scattering events, it becomes depolarised [56]. If the light emerging from the tissue is detected by a charge-coupled device camera after passing through a depolarization analyser, the detection of reflected light originating from only deep structures is guaranteed [47, 57]. By filtering wavelengths in the interested absorption range of haemoglobin (e.g. at 548 nm) only structures absorbing in that range can be visualised (i.e. blood vessels) [56, 57]. However, this wavelength has to be carefully selected to balance the absorption and scattering properties of tissues' structures [56].

Sidestream Dark Field (SDF) is another imaging technique, which utilises the scattering properties of tissues. A ring-shaped light source, with LEDs mounted on the external ring, emits green light into the tissue (i.e. the haemoglobin's isobestic point at 530 nm is usually used as emission wavelength). At the centre of the sensor ring, a lens is used for the collection of the backscattered light. Only the light reaching the deep structures of the tissue and scattering within the tissue (i.e. changing direction) is reflected to the lens (and the detecting system), while light reflection at the surface is

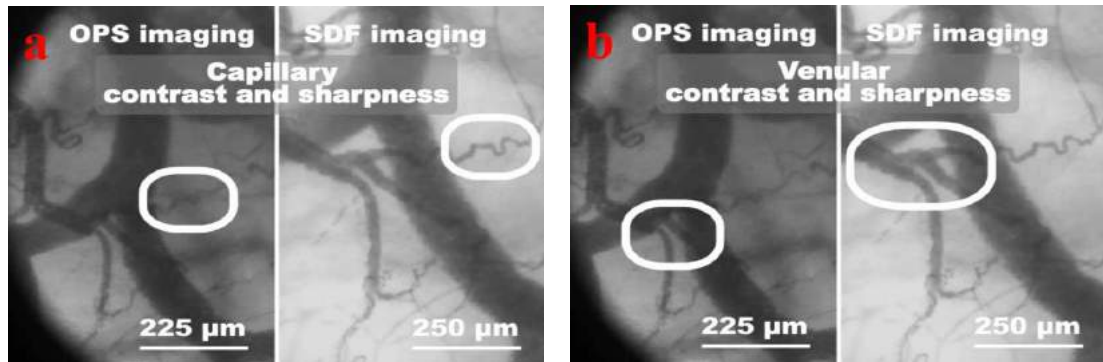


**Figure 3.8:** OPS and SDF images of the same sublingual microcirculation. The images acquired by SDF appeared to have a higher contrast and sharpness for both capillary and venular details. Figure reproduced from [58].

neglected [58]. The backscattered light is then acquired by a CCD video camera with acquisition rate synchronous to the pulse light emission [57, 58]. Images acquired by both SDF and OPS can be analysed by image or video processing techniques in order to estimate several parameters for the assessment of the microcirculation status (e.g. vessel density, dimensions, blood flow, etc.) [47, 56–58]. Both OPS and SDF comprise of a sensor that can be handheld by the examiner and they have been used for imaging the circulation in several tissues such as sublingual tissue, skin, brain, liver, and lungs [57]. An example of OPS and SDF images of the sublingual microcirculation can be seen in Figure 3.8. The techniques also have some limitations such as patient or examiner’s movement artefacts and the lack of standards for image analysis [47, 57].

Laser Doppler flowmetry was previously described in Section 3.3. A relatively recent development in laser Doppler measurements is laser Doppler Imaging (LDI or LDPI) [28, 47, 57]. LDI extends the principle of the single point, time changing laser Doppler flowmetry to a laser Doppler perfusion image of a region of interest [57]. This non-contact imaging technique depends on the acquisition of multiple laser Doppler measurements from an area, for the creation of a perfusion image in which regions with different blood flows are classified into a colour-coded image [28, 29, 59, 60]. An example of LDI images acquired from a skin graft can be seen in Figure 3.9. The advantage of the technique is its ability to provide an instantaneous look at the perfusion in an area without any contact with the tissue [28, 47, 57]. LDI has been mainly employed to acquire images of blood perfusion from the skin [28, 47, 57], but the technique was also investigated in organs such as bowel, colon and brain [47, 57]

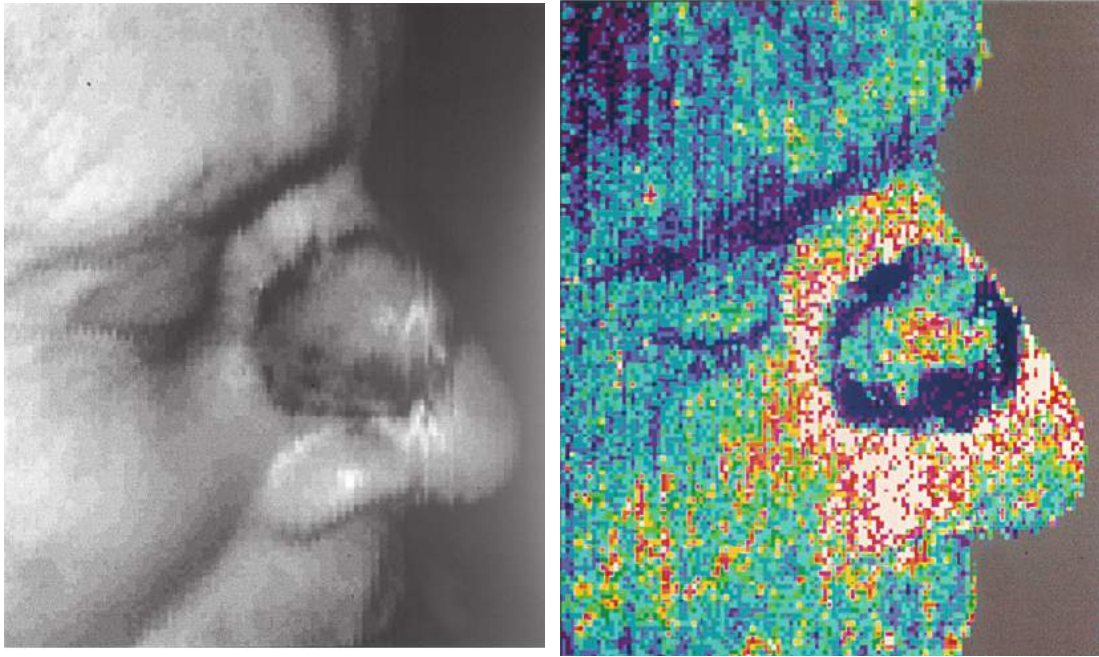


**Figure 3.9:** Laser Doppler Imaging acquisition of a skin graft on the nose. Black areas indicate a poor perfusion, while red and white areas indicate a high blood flow in those regions (increased blood flow around the skin graft). Figure reproduced from [28].

### 3.10 Clinical assessments and temperature gradients

Tissues exhibiting a poor perfusion tend to assume a pale colour and a visual assessment of the skin colour may give a preliminary indication of the perfusion status [34, 61, 62]. A simple measurement that clinicians use, as an adjunct for visual assessments, is the Capillary Refill Time (CRT) [34]. Application of pressure on the surface of a tissue causes the emptying of capillaries and the change into a pale colour. The CRT is the measurement of the time that the tissue employs to return to its original colour after the pressure is released (i.e. capillaries refilling with blood) [34, 63]. A CRT  $< 2$  s usually indicates adequacy of perfusion, while a CRT  $> 4.5$  s may indicate a poor blood perfusion [34, 61]. Although being quick, relatively simple to use, and not requiring any particular instrumentation, the method is qualitative rather than quantitative, it has an intra- and inter-observer variability, it depends on the subject's age, and it can vary with gender [34, 64]. Also, the method relies on the ambient light conditions and the applied pressure, and it can be affected by administration of vasoactive drugs [61, 63, 64]. In order to overcome some of these limitations, automated methods such as digitally videography and photoplethysmography were recently investigated for the accurate measure of CRT [63, 65].

One of the main roles of the microcirculation is maintaining a correct body temperature (thermoregulation) [61]. When perfusion is reduced, skin temperature drops, most commonly at the extremities. Assessing the skin temperature is one of the quickest methods for the identification of hypoperfusion status and it can be qualitatively performed by touching the patient's skin or by measuring the skin temperature by means of a sensor [34, 61]. Instead of measuring the temperature from a single location, a more efficient method is the measurement of temperature gradients between two locations, as these may better indicate the onset of temperature variations [61]. The changes in the differences in temperature between two locations (e.g. central-to-toe or forearm-to-fingertip) or between ambient and peripheries can reliably indicate changes in temperature (perfusion) that are independent of fluctuations in ambient room temperature [34, 61]. Temperature gradients have been investigated in circulatory shock or hypovolaemic patients, post-surgery or post-resuscitation patients, and for flaps perfusion monitoring. The results, however, vary and there is no consensus on the relationship between temperature gradients and global haemodynamic variables or patient's outcomes [34, 36, 44, 61]. Also, the application of the technique in critically ill or surgical patients poses a contradicting limitation, due to the administration of anaesthetic drugs, which often suppress the thermoregulatory activity in these patients [34].

### 3.11 Summary

This chapter presented a brief overview of some techniques adopted for *in vivo* measurements of blood perfusion and oxygenation. Several parameters measured by the techniques presented in this chapter directly or indirectly relate to blood flow, blood volumes, blood oxygenation or metabolism. Among the techniques presented in this chapter, Photoplethysmography and Near Infrared Spectroscopy have been briefly described. These two techniques play a central role in the research work presented in this thesis, and separate chapters describing these techniques in more detail are deemed necessary. Therefore, the next chapter will focus on describing the principles and applications of photoplethysmography and pulse oximetry.

## Photoplethysmography & Pulse Oximetry

In the last chapter, photoplethysmography and pulse oximetry have been briefly introduced. This chapter describes in more details the principles and main applications of photoplethysmography and pulse oximetry. The two techniques are strongly linked and, sometimes, even confused and mixed. Pulse oximetry is an application of photoplethysmography, and, due to its enormous success, it has overshadowed the latter. In some cases, the greater popularity of pulse oximetry has even led to mention photoplethysmography in the literature as the *pulse oximeter waveform*. However, in this chapter, the two techniques will be described and defined separately. The first part of the chapter will introduce the principles and applications of photoplethysmography, while the second part will be dedicated to pulse oximetry. Some of the limitations are mentioned throughout the chapter, while other major limitations and open challenges are discussed at the end of this chapter.

### 4.1 Principles of Photoplethysmography

Photoplethysmography (PPG) is an optical technique that exploits the optical absorption of tissues to express variations in blood volume. The action of pumping blood by the heart can be divided into two periods known as systole and diastole. Systole is the period when blood has just been ejected by the heart's left ventricle. During systole, the arteries extend due to the high pressure exerted by the arterial blood.

This pressure increases until reaching a maximum and decreases before the next pulse. When the pressure starts to decrease, the diastolic phase begins. In diastole, the pressure decreases until reaching a minimum, corresponding to the minimal distension of arteries.

Photoplethysmography exploits the changes in light absorption during the cardiac cycle between systole and diastole. The first major developments of the technique have been attributed to Hertzman, who observed that the light passing through biological tissue underwent cyclic changes in intensities [66]. A similar and more pragmatic example of this phenomenon can be observed by placing one finger over a strong cold white source. The light intensity passing through the finger can be seen oscillating due to the changes in arterial blood (i.e. systole-diastole).

In photoplethysmography, a light beam is emitted by means of laser diodes or light emitting diodes (LED). When light interacts with tissue, complex mechanisms like reflection, scattering, and absorption take place. The latter has the strongest impact on PPG measurements, while reflection and scattering are mostly neglected. When a sensitive photodetector like a photodiode or phototransistor is used to detect the light exciting the tissue, a physiological signal can be measured. This signal is known as photoplethysmogram and its main feature is the alternating intensity, reflecting the cardiac cycle. During systole, the increase in arterial blood is measured in the photoplethysmogram as a decrease in light intensity due to greater absorption (i.e. increased quantity of blood underneath the sensor). During diastole, the blood in the arteries reach its minimal presence and this corresponds to a decreased absorption measured by the photodetector. A raw photoplethysmogram acquired from a finger is depicted in Figure 4.1, along with the main characteristics of the signal. The figure also shows the flipped version of the signal, which is performed in order to resemble the photoplethysmogram to the arterial blood pressure (ABP) waveform. The reversed signal is often displayed in pulse oximeters along with the arterial oxygen saturation and heart rate. This flipping process is important to mention, but the flipped signal is almost always used when referring to the photoplethysmogram. The flipped version of the signal has gained recognition because an increase in the signal corresponds to an increase in blood volume and *vice versa*. The photoplethysmogram can be roughly divided into two stages. The initial stage is the upslope coinciding with the systole phase of the cardiac cycle. In this stage, the signal increases until reaching a maximum. The

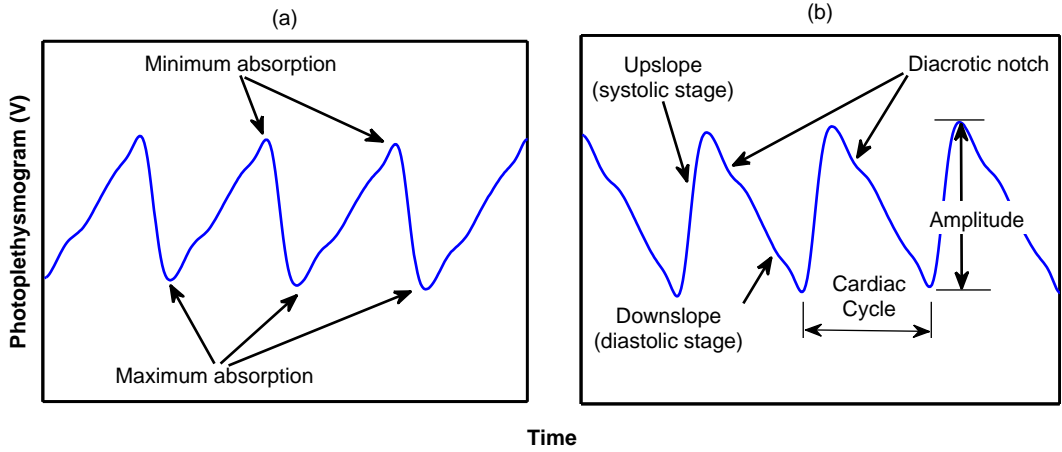


**Figure 4.1:** Original (a) and flipped (b) photoplethysmogram and features of the photoplethysmogram. In (a), the original photoplethysmogram represents the absorption cycles measured directly by the photodetector. The minima correspond to maximal absorption (systole), while the maxima are the minimal absorption points (diastole). In (b), the original photoplethysmogram is conventionally flipped. The upslopes and downslopes correspond respectively to systolic and diastolic stages respectively. The dicrotic notch is present in healthy volunteers during the diastolic stage. The pulse amplitude can be considered as the difference between the maximum and the minimum within one cardiac cycle.

second stage corresponds to the diastolic phase and appears as a decrease of the signal (downslope). In the diastolic phase, an inflexion, known as the dicrotic notch, can be observed [1].

From a more physical point of view, the generation of the photoplethysmogram can be attributed to the Beer-Lambert law, which states that the intensity of the detected light  $I$  is proportional to the concentration of the substance  $c$  and the distance travelled by the light beam  $d$ .

$$I = I_0 \exp^{\varepsilon cd} \quad (4.1)$$

Where  $I_0$  is the emitted light intensity and  $\varepsilon$  is the specific extinction coefficient (or molar absorptivity) of the substance, expressing the absorption properties of the substance. During the cardiac cycle, the amount (concentration) of blood in the measurement area changes over time and the distance travelled by light varies due to the distension of the arteries. The continuous cycle of systole and diastole, causing both variations in blood volume and arteries diameters, generates the change in the detected light intensity expressed by the photoplethysmogram. Furthermore, the different direction of red blood cells during systole and diastole could cause changes in the light reflection, thus contributing to the overall signal [1, 6, 67].

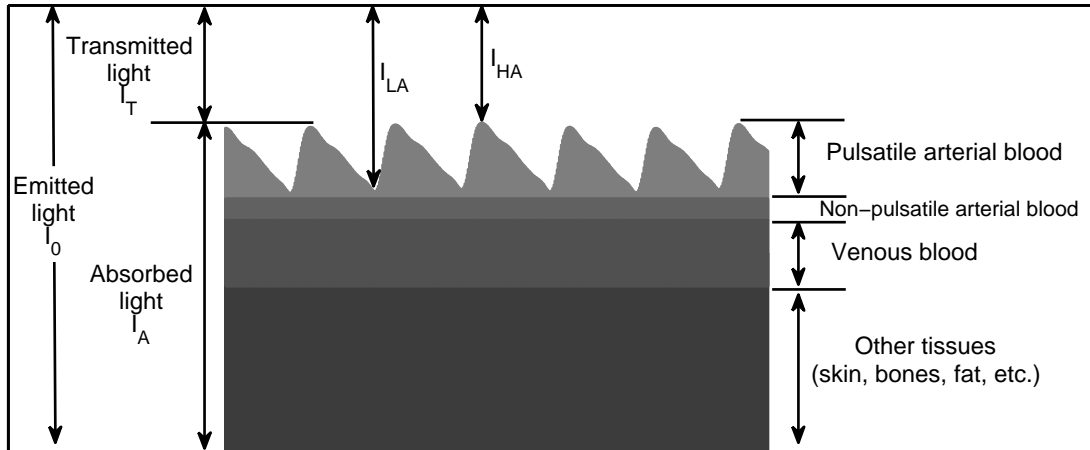


**Figure 4.2:** Distribution of light absorption and attenuation in photoplethysmography. Part of the emitted light  $I_0$  is absorbed by the tissue ( $I_A$ ), whereas the transmitted light  $I_T$  is measured by the photodetector.  $I_T$  undergoes cycles of maximal ( $I_{HA}$ ) and low absorption ( $I_{LA}$ ) due to the pulsation of arterial blood. This alternation of absorption constitutes the alternated AC component of the photoplethysmogram. Other tissue's structures constantly absorb light, the most significant being non-pulsatile arterial blood, venous blood, skin, and bones. The figure was re-drawn from [8].

## 4.2 Components of the photoplethysmogram

Although the photoplethysmogram is widely known for the measurement of arterial blood volume changes, the signal is not solely composed by the contribution of arterial blood. Light interacts with several tissue structures and these interactions are then represented in the photoplethysmogram. A schematic representation of the contribution of different tissue structures is shown in Figure 4.2. From that figure, the signal can be divided into two components: alternated (AC) and continuous (DC).

### 4.2.1 Alternated PPG component

The alternated AC component (from this point, AC PPG) represents the changes in blood volume due to the pulsation of arteries and resembles the shape of the arterial blood pressure waveform [68]. An example of AC PPG is illustrated in Figure 4.1. The component is characterised by the continuous oscillations representing the systolic and diastolic phases, thus synchronous with the cardiac cycle. The AC PPG component varies from subject to subject, having distinct features for each subject [69] and when it is measured from different locations (e.g. finger, forehead, ear) [1, 69].

The AC PPG is often mistaken as the only component of the PPG signal and can be used for different applications. The primary utilisation of the AC PPG is the

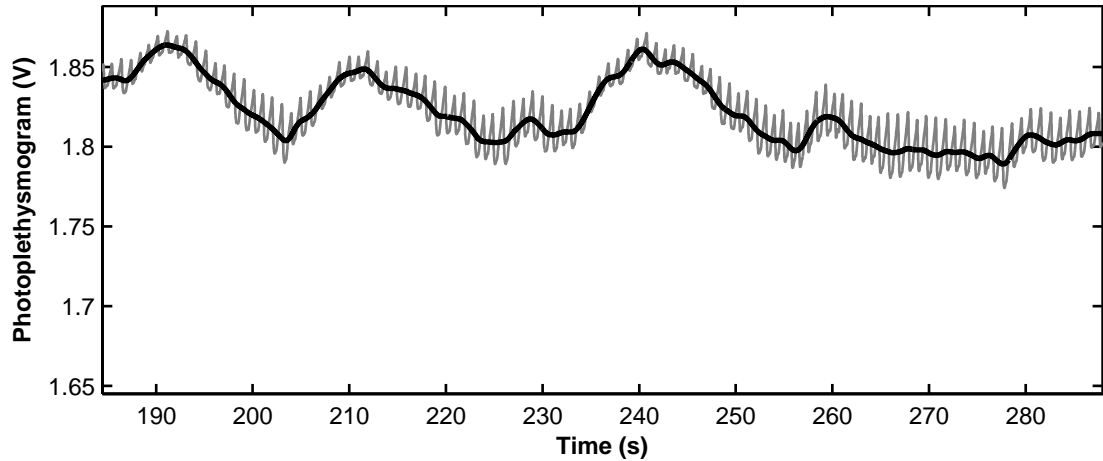


**Figure 4.3:** Raw PPG (AC + DC) signals acquired from the finger of a healthy subject. The small pulsatile AC component (in grey) overrides on a slow-varying continuous DC component (black line).

estimation of arterial oxygen saturation by pulse oximetry, which will be described in Section 4.5. By representing the arterial pulsations during the cardiac cycle, the component is also widely used for the estimation of the heart rate or it can be used to assess arrhythmias [1,9]. The amplitude of the component varies on the vascular status of the arteries; for instance, diminishing during vasoconstriction or increasing during vasodilation [9].

#### 4.2.2 Continuous PPG component

The AC PPG component constitutes only 1-2 % of the total light detected [67]. As can be seen from Figure 4.2, the greater proportion of light absorption originates from the light interaction with other tissue structures other than the pulsating arterial blood. Relatively static structures such as non-pulsatile arterial blood, venous blood, skin, and bones dominate absorption, thus creating an offset of the photoplethysmogram, known as DC component [1, 2, 67, 68]. Figure 4.3 shows an example of raw PPG (AC + DC) acquired from the finger of a healthy subject. The pulsating AC component overrides over a slowly varying DC component, which reflects the (relatively constant) absorption of structures other than the pulsating arterial blood.

Although the DC PPG component is usually filtered out or used for normalisation in conventional PPG processing systems (i.e. pulse oximeters display only the pulsatile AC PPG component), it contains valuable physiological information. The DC PPG component represents the amount of blood volume under the sensor, thus can provide

information on blood pooling (or flowing) under the sensor [1,2]. The DC PPG oscillates at low frequencies, synchronously with respiration [1, 2, 67, 68]. This effect is created by variations in the resistance of venous blood flow, caused by the changes in the intrathoracic pressure during ventilation [2, 67]. The respiratory-induced variations represent venous blood motion and, by applying similar methods used in pulse oximetry, they have been proposed for the estimation of venous oxygen saturation from PPG signals (see subsection 4.5.4). Other spontaneous oscillations at lower frequencies than the respiration can also be extracted from the DC PPG component. These very low-frequency oscillations occur in the range 0.01-0.5 Hz and they have been related to regulation mechanisms mediated by a sympathetic nervous system such as Mayer waves [2], blood pressure regulation [2], or thermoregulation [1, 2].

### 4.3 Photoplethysmography measurement modalities

As mentioned earlier, photoplethysmography requires a light emitter and a photodetector. Often, light emitting diodes (LEDs) and photodiodes are used for this purpose. Compared to other light sources, LEDs have the advantage of being smaller, produce less noise, can be switched ON/OFF at faster rates, they are inexpensive, produce less heat and have a long operating life [1, 2, 6]. LEDs and photodiodes can be of small size and they can be easily incorporated directly into PPG probes [1]. Optic fibres can also be employed in PPG measurements to transport the light to and from the tissue. However, this solution is more fragile, but allows using the technique in the presence of Magnetic Resonance Imagers (MRI) [6]. Depending on the configuration of light emitters and photodetectors, there are two modalities by which PPG measurements can be performed, known as transmission and reflectance mode [1].

#### 4.3.1 Transmission Photoplethysmography

In transmission mode, the light emitter and photodetector are placed parallel to each other on each side of the tissue [1, 2, 67, 68, 70]. An example of the transmission mode is depicted in Figure 4.4, in which light is transmitted through the tissue, from one side to the other. This configuration, however, can only be applied to small extremities

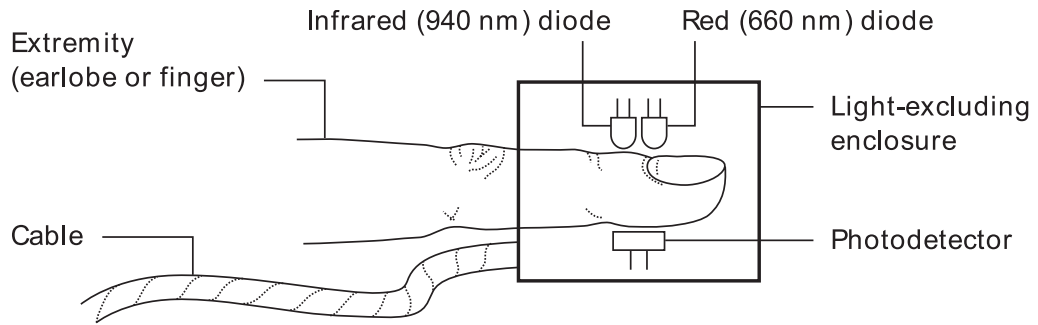


**Figure 4.4:** Configuration of transmission photoplethysmography. The light emitters (diodes) and the photodetector are placed opposite to each other across the tissue (finger). An enclosure protects from ambient light interference, while a cable connects the optical components to the processing unit. In this figure, two light emitters, red and infrared, are used for pulse oximetry. Figure reproduced from [6].

such as fingers or earlobe and requires a small pressure to hold the sensor in place [1, 2, 6, 70]. Measurements across thicker tissues may suffer from greater absorption, with the shortcoming of producing smaller and noisier signals.

### 4.3.2 Reflectance Photoplethysmography

For other measurement locations, the reflectance mode is more suitable [2]. In reflectance mode, the light emitter and photodetector are positioned on the same surface of the tissue [1, 2, 67, 68, 70]. Due to light scattering in tissue, the emitted light is back-reflected in a banana-shaped path to the same planar surface as the light emitter, where the photodetector receives the reflected light from the tissue [68, 70].

An example of reflectance mode is depicted in Figure 4.5, showing the position of the light emitters and the photodetector. This measuring mode has been used for PPG measurements from several locations such as fingers, forehead, or forearm [2, 6, 70], but it requires a good contact between the sensor and the skin, in order to avoid movement artefacts and ambient light interference [1]. Reflectance sensors are usually attached to the skin by means of double-sided adhesives, and PPG measurements acquired in reflectance mode contain a more significant contribution of venous blood due to the absence of pressure (i.e. transmission mode exert some pressure on the tissue, thus collapsing the venous blood) [68]. Also, PPG measurements acquired in reflectance mode usually provide a lower signal when compared to the transmission mode [71].

The reflectance PPG measurement mode has been primarily used in the research carried out in this thesis. This modality has been selected since it can be used to acquire signals

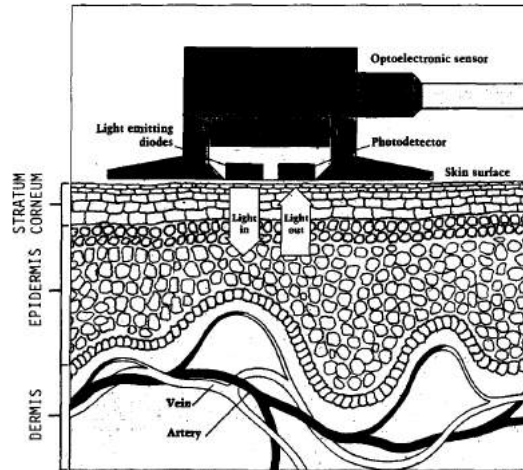


**Figure 4.5:** Configuration of reflectance photoplethysmography. The light emitter (light emitting diode) and the photodetector are positioned on the same plane, side by side. The backscattered light returns to the photodetector after travelling across the different structures of the tissue and interacting with the blood vessels. The enclosure protects from ambient light interference and allows the attachment of the sensor on the skin. Figure reproduced from [71].

from almost any location in the body, whereas the transmission mode is limited to the fingers and earlobes. Later in this thesis, the design and development of reflectance PPG sensors used for this research will be described in Chapter 6.

## 4.4 Clinical and Research applications of PPG

The previous sections introduced the principles of photoplethysmography. This section aims at reviewing briefly the main applications of photoplethysmography. Pulse oximetry will not be introduced at this point since a separate section will be dedicated to describing pulse oximetry.

### 4.4.1 Heart rate

The pulsatile component of the photoplethysmogram is synchronous with the cardiac cycle, thus information on the heart rate frequency can be estimated from the AC PPG [1]. Two methods can be used to extract the heart rate from PPG, one being in the time domain and the second in the frequency domain. In the time domain, the period between two successive beats yields the beat-to-beat heart rate, whereas in the frequency domain the cardiac frequency (usually around 1 Hz) is extracted from the

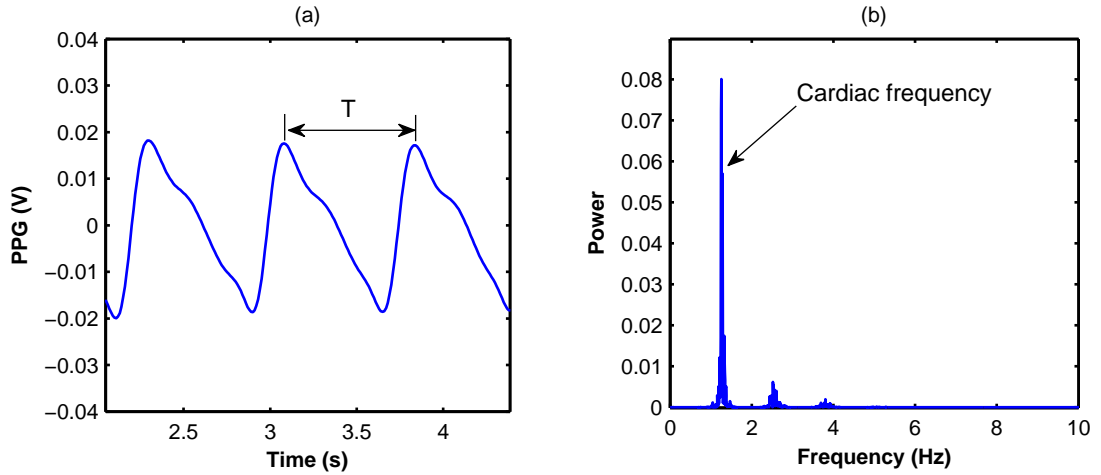


**Figure 4.6:** Time domain (a) and frequency domain (b) heart rate estimation from PPG. (a) In the time domain, the beat-to-beat period  $T$  is calculated from the time locations of the PPG signal. (b) In the frequency domain, the peak of the cardiac frequency is extracted from the power spectra of the signal. The spectrum refers to 10 seconds of the same signal presented in (a). The period  $T$  in (a) is 0.79 s, while the peak of the cardiac frequency is at 1.25 Hz (the smaller peaks at higher frequencies are harmonics). The time and frequency domain result respectively in a heart rate of 75.9 beats/min and 75 beats/min.

power spectra of the signal. Figure 4.6 illustrates how both methods estimate the heart rate.

The heart rate estimated from PPG signals is obviously a fundamental haemodynamic parameter and it is usually showed along with the arterial oxygen saturation in pulse oximeters [1]. The heart rate can be estimated from PPG acquired from different locations, but the finger, forehead, and wrist have been reported as more reliable than other locations (i.e. finger, forehead, and wrist showed less respiratory-induced variations in the PPG signals) [72]. The PPG signals can be used along with ECG to find possible arrhythmias [9], while the beat-to-beat variability of PPG signals can be used to obtain information on heart rate variability [70]. Recently, Grubb et al. investigated the neonate's forehead as a location of heart rate estimation and showed good agreement with ECG measurements. The authors proposed the forehead PPG since it offers several advantages over other conventional methods (e.g. ECG or stethoscope) [73]. Although the heart rate can be extracted from PPG measurements, the main challenge remains the validity of PPG-derived heart rate in the presence of movements [1].

#### 4.4.2 Respiration rate

As mentioned in the previous sections, the photoplethysmogram contains spontaneous, respiratory-induced fluctuations. These fluctuations appear in the DC component of

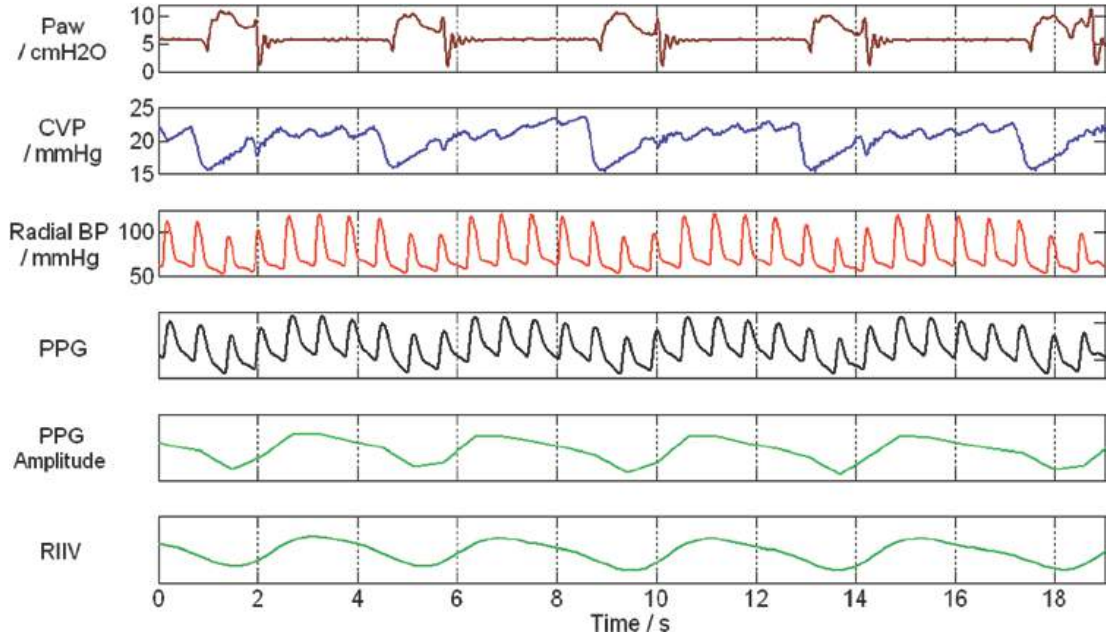


**Figure 4.7:** Effect of respiration on PPG signals. Measurements acquired from a spontaneously breathing subject. Positive airway pressure (PaW) was used as an aid in ventilation. Central venous pressure (CVP) was measured by a jugular catheter and the arterial blood pressure (Radial BP) was measured from a radial catheter. The PPG (fourth from the top) was acquired from a finger PPG sensor. PPG Amplitude (fifth from the top, in green) is the interpolation of the PPG peaks, while the RIIV (bottom) was obtained by low pass filtering the PPG signal. Figure reproduced from [10].

the signal and their origins are still under debate [1, 2, 9, 10, 72]. The changes in venous flow resistance due to intrathoracic pressure variations, with the corresponding changes in stroke volume and cardiac output, are considered the first cause of these modulations, but respiration-synchronised mediation of the sympathetic nervous system has been advocated as an additional source [10]. These low-frequency oscillations are easily visible during positive pressure ventilation and can increase in amplitude after blood withdrawal or haemorrhage [9]. Due to the synchrony with the respiration, these fluctuations have been defined as respiratory-induced intensity variations (RIIV) and they can be used to derive respiratory rates from the photoplethysmogram [1, 9, 10]. Depending on the specific filtering, the respiration-induced fluctuations can be fully separated from the pulsatile component, thus appearing only in the DC component of the PPG signals [10]. The forehead, ear, and forearm have been indicated as best locations to measure RIIV, due to a greater presence of venous blood in these locations and the method of attachment (i.e. transmission sensors can compress the venous blood underneath the sensor) [72, 74].

The use of the PPG signal for estimation of respiration rates can offer several advantages over traditional methods for monitoring respiration, avoiding the use of additional, and sometimes bulkier, sensors [10]. Respiration is an important physiological parameter

and monitoring this with a PPG/pulse oximetry sensor can have several applications such as anaesthesia and sleep/neonatal apnoea [1].

#### 4.4.3 Photoplethysmography as indicator of perfusion

As mentioned earlier the AC component of the photoplethysmogram is synchronous with the cardiac cycle, thus representing the pumping action of the heart. This arterial component can be therefore used for the assessment of the blood supply to the tissue. Changes in the AC PPG directly reflect variations in the blood volume supplied to the region. During cuff-induced occlusions, the AC PPG decreases or, during full arterial occlusion, completely disappear. Different studies have been performed on this aspect and showed how the PPG can be used in situations of compromised perfusion [75–77]. However, the use of AC PPG alone for assessing perfusion should be cautious. Firstly, the AC PPG represent volume changes of pulsatile blood and it does not assess the oxygen delivery to the tissue (i.e.  $\text{oxygen delivery} = \text{blood flow} \times \text{oxygen content}$ ) [75]. Secondly, this component only represents the pulsatile arterial blood volume in the measured area, whereas the venous component is neglected during filtering of the signal. Thirdly, the presence of arterial pulsations does not preclude adequacy of perfusion, which can be compromised by venous occlusion as well [75]. Even if decreased during occlusion of the venous outflow, the pulsatile component is still present or it significantly drops after a long period of time. In this regard, previous studies showed that the AC PPG started to decrease drastically only at occlusion pressures close to 100 mmHg, much after occlusion of the venous circulation [75–77]. Furthermore, the AC PPG amplitude physiologically varies due to sympathetic activity or small temperature changes in normal conditions, thus significant variations may be identified only after some time before the complication occurred.

The DC component of the photoplethysmogram seems to be more reliable for indication of perfusion changes and it can provide important information when the AC component may not be sufficient like in venous congestion. In 1940, Hertzman and Dillon were the first to report changes in the DC PPG component for blood volumes variations due to venous congestion, with an unaffected pulsatile component [78]. Almond et al. compared the DC PPG recordings from the finger with laser Doppler flowmetry and strain-gage plethysmography during vascular occlusions at different arm positions. The

DC PPG significantly changed during the occlusions, indicating the changes in blood flow perfusion [79]. Later on, Galla et al. studied the response of the DC PPG in animal flaps in order to investigate the feasibility of distinguishing between venous and arterial occlusion. The DC PPG showed different responses during the two occlusions, with the signal increasing during arterial occlusion, whereas decreasing during venous occlusion [41].

A more recent advancement in PPG processing is the calculation of the perfusion index (PI). The index is calculated from infrared PPGs as the percentage ratio of the amplitude of the pulsatile AC component and the DC level ( $PI = AC/DC \times 100 \%$ ). The index is nowadays displayed in modern pulse oximeters along with the photoplethysmogram and it is believed to reflect changes in perfusion [70, 80].

Lima et al. investigated the relationship between PI and clinical measures of perfusion such as capillary refill time and central-to-toe temperature gradients in healthy volunteers and critically ill patients. A positive relationship was found between changes in peripheral PI and changes in central-to-toe temperature in critically ill patients. From the study population, a cut-off value of 1.4 for PI measurements was considered as an indicator of abnormal perfusion [80]. The perfusion index measured at the neonates' foot was also correlated with blood flow and oxygen delivery derived from NIRS measured at the calf [81]. Van Genderen et al. demonstrated that changes in the perfusion index were able to indicate the onset mild hypovolaemia during low body negative pressure [82]. The perfusion index can be used to differentiate between high and low severity illness in neonates (cut-off PI = 1.24) [83], as well as to detect changes in perfusion after harvesting of the radial artery for coronary artery bypass [84].

#### 4.4.4 Continuous arterial blood pressure

Photoplethysmography can be used for the measurement of beat-to-beat arterial blood pressure (ABP) [85]. The method is based on the unloading of the finger arterial walls, combining both optical (photoplethysmography) and mechanical principles (occlusion). In these instruments, the optical components measuring infrared PPGs are enclosed in a finger cuff. At the beginning of the measurement, this cuff inflates in steps, correlating the inflation pressure to AC and DC PPG signals acquired from the

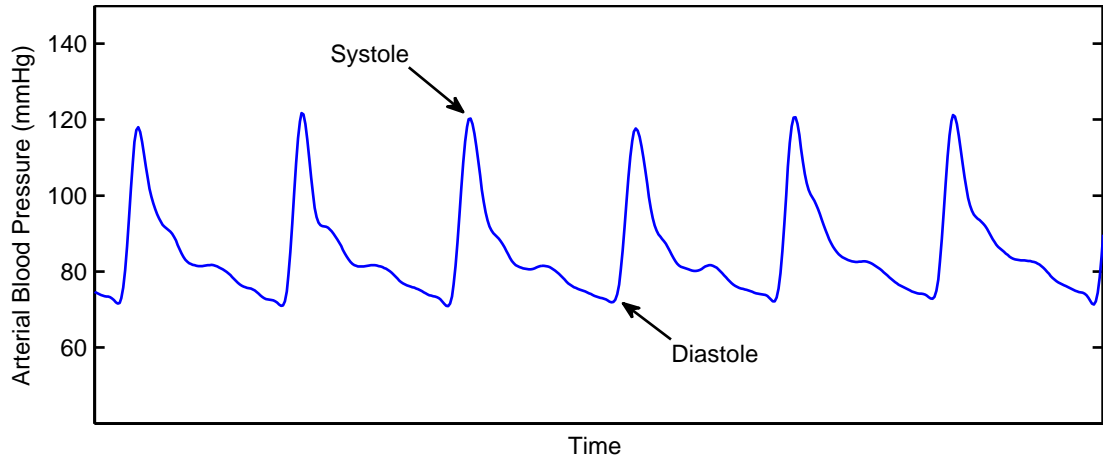


**Figure 4.8:** Example of arterial blood pressure measurement from a healthy subject. The maximum point of the curve represents the maximal pressure reached during systole, while the minimum pressure point corresponds the diastolic pressure.

optical sensor. This step-wise calibration allows identifying the pressure at which the finger cuffs will measure the ABP at the finger and small adjustments are performed at regular intervals during the measurement [85]. In some instruments, this initial calibration is also performed with the aid of a cuff placed on the forearm [86]. To determine its accuracy, the method was compared against reference invasive (radial artery catheters) and noninvasive measures (auscultation) of blood pressure, showing good levels of agreement [85–87]. However, the main advantage of the method is the ability to track beat-to-beat arterial blood pressure changes in a noninvasive and continuous manner. Figure 4.8 shows an example of continuous beat-to-beat ABP measurements on a healthy volunteer.

#### 4.4.5 PPG for cardiovascular assessment

Vascular compliance is the ability of a vessel to adapt to variations in pressure by changing its volume. In mathematical form, the compliance  $C$  can be defined as the ratio between changes in volume and pressure ( $C = \Delta V / \Delta P$ ). Compliance was previously assessed by strain-gage plethysmography ( $\Delta V$ ) and invasive intra-arterial pressure measurements [88]. Shelley et al. introduced the concept of using the AC PPG amplitude variations to measure volume changes  $\Delta V$  per changes in pressure  $\Delta P$ , thus assessing alterations in vascular compliance or vascular tone. By plotting  $\Delta V$  traces (PPG) against  $\Delta P$ , a loop is created, which slope is proportional to vascular tone/compliance. As showed in Figure 4.9a, the method could be used to track changes in compliance

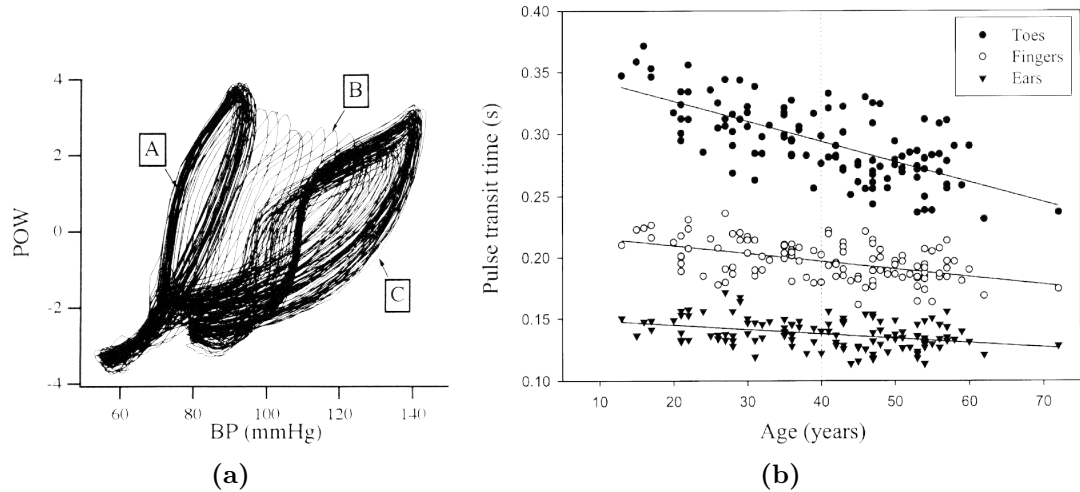


**Figure 4.9:** Changes in compliance measured by PPG (a) and Pulse Transit Time as a function of age for different locations (b). In (a), changes in amplitude of the AC PPG component (POW) are plotted against changes of blood pressure (BP). Compliance is represented by the slope of the loops. In this example, baseline measurements (A) change at 60 s (B) and 120 s (C) after injection of phenylephrine. Figure reproduced from [88]. In (b), PTT measured at different locations (finger, toe, and earlobe) are plotted against age. PTT values are proportional to the distance from the heart and decrease in PTT with age indicates the increased arterial stiffness. Figure reproduced from [89].

after the administration of a vasoconstrictor [88].

The photoplethysmogram can also be used to assess arterial stiffness [1]. With increasing age, the morphology of the pulsatile AC component change and they can be used to assess stiffness of the arterial vessels [89]. Also, with increased stiffness, the velocity of blood in the arteries increases. By measuring the time it takes for the pulse wave to travel from the heart to the PPG measurement location (e.g. finger or toes), the arterial stiffening can be assessed. This parameter is known as Pulse Transit Time (PTT) and is measured from the time difference between simultaneous ECG (ventricular ejection) and PPG measurements (arterial pulse) [89]. If the distance from the heart and the PPG measurement location is known, the velocity of arterial blood, Pulse Wave Velocity (PWV) can also be obtained. Figure 4.9b shows PTT measurements from fingers, toes, and earlobe as function of age. As can be seen from the figure, the PTT is proportional to the distance travelled and decreases with increasing age (arterial stiffness).

PPG has attracted some interests for the assessment of fluid responsiveness. Fluid Responsiveness (FR) is the ability of the cardiovascular system to adapt to intravascular volume administration and assessing FR can help guiding fluid resuscitation in critical patients [69]. The main parameter involved during volume administration is the stroke volume (SV). The photoplethysmogram gives an indication of periodic changes in SV

due to the increase in intrathoracic pressure in respiration, reflected in the DC component of the PPG, as well as in amplitude changes of the pulsatile component [69]. Therefore, the PPG could provide a noninvasive tool to guide fluid resuscitation. During mechanical ventilation, the oscillations in the PPG signal are more visible and change accordingly during intravascular volume changes such as bleeding (hypovolaemia) [90] or volume administration [91].

#### 4.4.6 PPG from alternative measurement locations

With the technological advancements in the last decades, optical components have smaller sizes, allowing the miniaturisation of PPG sensors. For this, various measurement locations have been investigated other than the more conventional positions such as fingers, earlobe or forehead.

The oesophagus was investigated as a location for PPG measurements by Kyriacou. The rationale behind is that PPG measurements from this location will be less affected by vasoconstriction than extremities, with the ability to estimate the arterial oxygen saturation more effectively from vulnerable patients. By means of a tiny reflectance PPG sensor, good quality PPGs were acquired from the lumen of the oesophagus in cardiothoracic surgery patients, burned patients, and neonates [3, 92]. To overcome the limitations of PPG measurements under poor perfusion due to vasoconstriction, the ear canal was also investigated as a new location for PPG measurements. The ear canal, being supplied by branches of the carotid artery, demonstrated to provide more stable PPG signals than fingers during hand immersion in ice and whole body hypothermia [93, 94].

In order to monitor perfusion of splanchnic organs, PPG signals were also acquired from the small and large bowel [95, 96] or the surface of the colon [97]. A very interesting application is the measurement of PPG from the spinal cord tissue or from the cerebral cortex. Through a cranial bolt used in for intracranial pressure monitoring, the PPG signal can be measured from the cerebral cortex by means of optic fibres [98]. This approach could provide the ability to monitor intracranial blood volume changes and estimate cerebral arterial oxygen saturation from subjects with head injuries or neurosurgery patients [98]. Figure 4.10 shows the insertion of the fibre optics into the

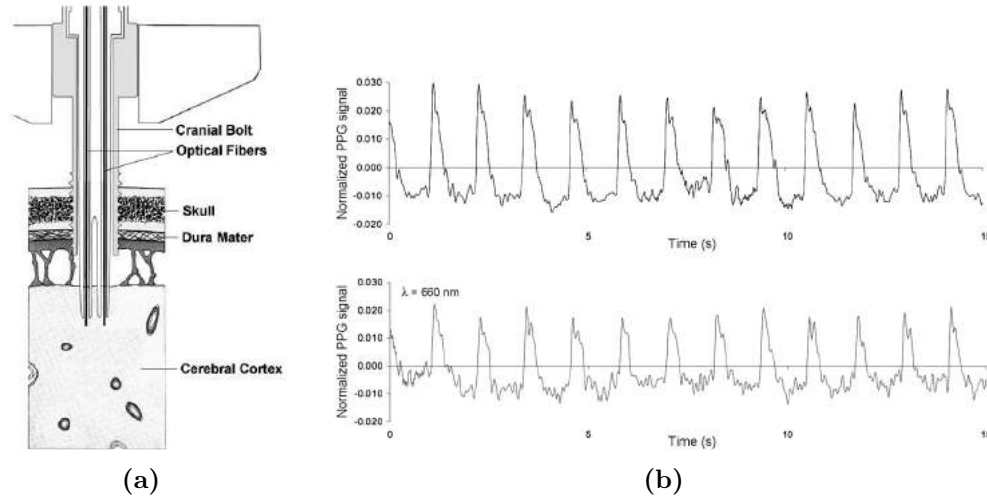


**Figure 4.10:** Insertion of optical fibres in the skull (a) and PPG recordings from the brain (b). (a) The cranial bolt is inserted in the brain through a hole in the skull with the optical fibres running in the middle. (b) Top trace: infrared PPG; bottom trace: red wavelength PPG. Figure reproduced from [98].

brain bolt and PPG recordings acquired from the brain.

Photoplethysmography has been investigated for the intra- and post-operative monitoring of surgical flaps [99–102]. Being noninvasive, harmless, and inexpensive, the technique could be a suitable method to monitor postoperative complications in these tissues. However, extensive clinical studies are still needed to determine the ability of photoplethysmography to detect reliably vascular complications in flaps.

#### 4.4.7 Non-contact PPG, imaging, and smartphones applications

One of the most attractive new implementation of the PPG technique is the possibility to acquire non-contact PPG measurements. This can be achieved by acquiring video sequences (frame) of the backscattered light from the tissue by means of a camera positioned at a distance greater than 1 m [103,104]. Light sources of the wavelength of interest can be used to illuminate the tissue under examination [104] or ambient white light can be used as well [103]. The acquired images can either be used from the entire area, to obtain a map of the signal intensity or can be used to extract the PPG signal from a specific region of interest. Briefly, the processing of these time-frames involves selecting a spot measurement area and performing a spatial averaging of the pixels of interest. From the time variations in the intensity of these pixels, the PPG signal can then be obtained [103]. From non-contact PPG measurements, heart rate and/or respiration can be obtained without contact with the subject and this offers the

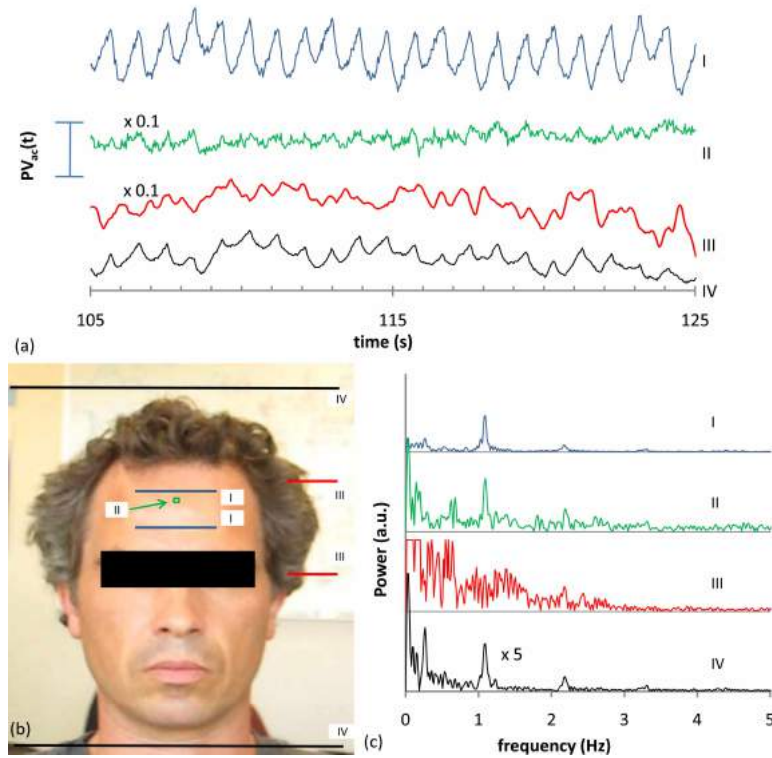


**Figure 4.11:** Non-contact PPG measurements from a subject. In (a), the PPG signals are extracted from four region of interest I-IV showed in (b). The power spectra of the signals extracted from the four regions are shown in (c). The measurements have been acquired with white ambient light. The signals in (a) represent the green channel (RGB) of the video frames. Figure reproduced from [103].

potential for monitoring these parameters from vulnerable patients [103].

PPG has also attracted the interests of smartphone manufacturers. Some new smartphones are equipped with built-in technology that allows measuring the user's heart rate based on PPG measurements. Also, several applications have been developed for the same purpose. The light source can be a dedicated LED or the camera's flashlight and the PPG signal is recorded from the smartphone's camera. The principle of non-contact PPG has also been implemented for smartphone or tablet applications such as Vital Signs Camera by Philips N.V., in which the PPG signal can be acquired from the front camera of the smartphone for estimation of heart rate and respiration without any contact with the subject. The introduction of PPG technology in smartphones could pave the way to a future in which each person would have a photoplethysmograph in their pockets.

## 4.5 Pulse oximetry

The determination of oxygen content in blood is of vital importance in clinical settings. Usually, this is achieved by withdrawing blood samples and analysing them *in vitro* in the laboratory. One of the major parameters of interests in oxygen blood analysis is the arterial oxygen saturation ( $SaO_2$ ) or functional saturation ( $FaO_2$ ). The calculation of this parameter is showed in Equation 4.2 and expresses the content of oxygenated haemoglobin  $HbO_2$  over the full amount of haemoglobin (expresses as the sum of oxygenated and deoxygenated haemoglobin  $HHb$ ). As explained in Chapter 2, haemoglobin plays an important role in the oxygen metabolism of tissue by transporting oxygen to the tissues (oxygenated haemoglobin) and collecting waste products of the metabolism (deoxygenated haemoglobin). Therefore,  $SaO_2$  is a fundamental parameter since it represents the quantity (in percentage) of oxygen being delivered to the tissue.

$$SaO_2 = FaO_2 = \frac{[HbO_2]}{[HbO_2] + [HHb]} \times 100\% \quad (4.2)$$

However, blood samples analysis have some limitations such as intermittent blood samples withdrawal, invasiveness, and it requires some minutes for the analysis. This method, which is the gold standard for blood oxygenation measurements, is still used in clinical practice and it was the only method available before *in vivo* and continuous oxygenation measurements became available.

Before the arrival of pulse oximetry, the device for *in vivo* determination of arterial saturation was an ear oximeter firstly developed by Wood and Geraci in 1949 and later modified by Hewlett-Packard in the early 1970s [4]. The device is depicted in Figure 4.12 and consisted of an earpiece sensor emitting light at eight wavelengths. By measuring the light attenuations at different wavelengths and comparing them with reference light beams, the instrument was applying a spectroscopic method for the determination of  $HbO_2$  and  $HHb$ , and therefore  $SaO_2$  [4,6]. Although being efficient, the instrument had some limitations such as instrumentation and sensor bulkiness, it was limited to and required heating of the ear, slight changes in position during the measurement could cause inaccuracies, as well as intermittent calibrations [4–6, 105]. It was later that Dr Aoyagi, while he was working on cardiac output measurements, noticed a pulsatile

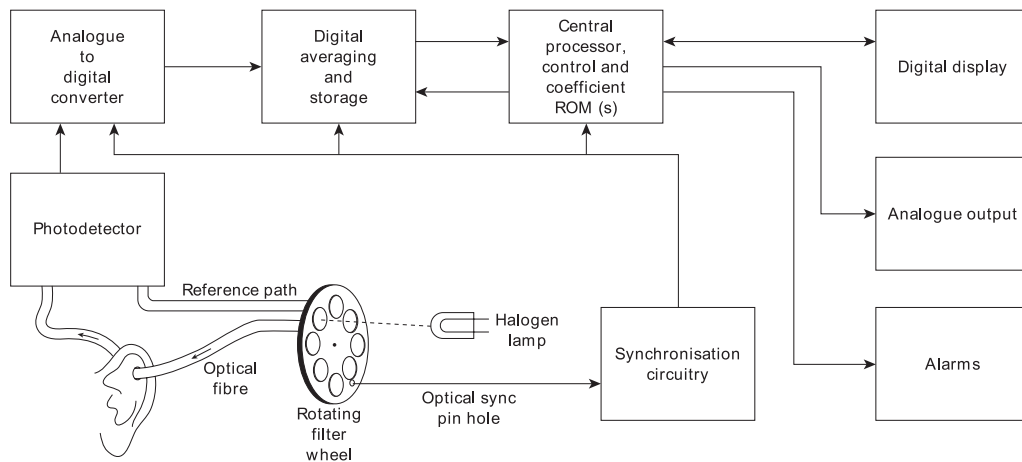


**Figure 4.12:** Schematics of the HP Packard ear oximeter. Figure reproduced from [6].

component in the signal measured by the Wood's ear oximeter. This signal was initially considered as an interference, but later Aoyagi realised that this pulsatile component did not have any effect in the calculation of  $\text{SaO}_2$ , but instead it could be effectively used to isolate the arterial blood for oxygen saturation measurements [5]. After presenting his first results at a conference in 1974, he was relocated without being able to continue his work. A decade later, the first pulse oximeters incorporating Aoyagi's principles were commercially available [5].

### 4.5.1 Principles of pulse oximetry

The function of pulse oximetry is based on the absorption properties of blood at two wavelengths, more specifically red and infrared. Figure 4.13 shows the absorption spectra of oxygenated and deoxygenated haemoglobin. As it can be seen from the graph, oxygenated haemoglobin absorbs less light in the red region (600-700 nm), while it absorbs more light in the infrared region (800-1000 nm) of the spectrum. This inversion of absorption takes place after the isobestic point (800-810 nm), where the two haemoglobin species absorb light equally [6,8]. The figure also indicates the absorption of oxygenated and deoxygenated haemoglobin at the two wavelengths mostly used in pulse oximetry, 660 nm for red and 940 nm for infrared. The red wavelength is mostly used at 660 nm, while a source between 810 to 1000 nm can be used for infrared light, with the main criterion that oxygenated and deoxygenated haemoglobin at the two wavelengths have different or, even better, inverted absorption (see Figure 4.13) [7].

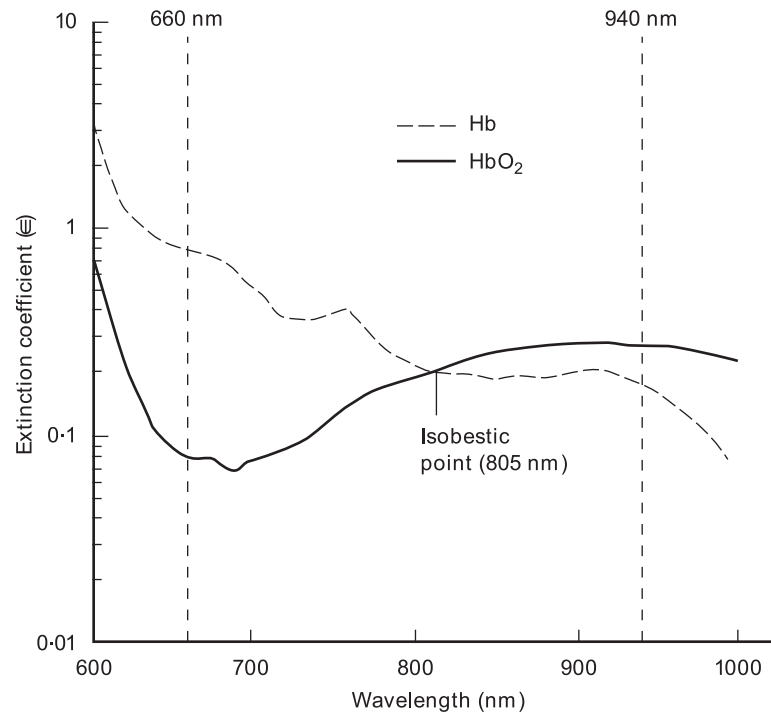


**Figure 4.13:** Absorption spectra of oxygenated ( $\text{HbO}_2$ ) and deoxygenated ( $\text{Hb}$ ) haemoglobin in the red and infrared regions. The two wavelengths commonly used in pulse oximetry (660 nm and 940 nm) are depicted as well. In the red region,  $\text{HbO}_2$  has a lower absorption than  $\text{Hb}$ . In the infrared region, after the isobestic point, the absorption of the two haemoglobin species is inverted. Figure reproduced from [6].

If light at two wavelengths is emitted in the tissue, these different absorption properties of blood can be exploited to obtain information on the quantity of oxygenated and deoxygenated haemoglobin. This principle was used in the Wood's ear oximeter and consisted in the application of the Beer-Lambert law to obtain the concentrations of oxygenated and deoxygenated haemoglobin in blood (the Beer-Lambert law is used in Near Infrared Spectroscopy and it is extensively explained in Chapter 5). This method, however, did not discriminate between arterial and venous blood, and it required frequent calibrations and a reference light intensity. The intuition of Aoyagi to use the pulsatile component of the signal allowed to isolate the arterial blood and to use a method that did not require frequent calibrations or a reference [5, 7].

Figure 4.14 shows the light absorbance at red (600 nm) and infrared light (940) for a blood sample with varying oxygen saturation. At high saturations ( $> 80\%$ ), red light is absorbed more than infrared light, while at low saturations ( $< 80\%$ ) the absorption is inverted. This relationship between oxygen saturation and absorption at red and infrared light is the fundamental principle used in pulse oximetry. In particular, this absorption at red and infrared is expressed as a ratio and related empirically to the oxygen saturation [4, 7, 8].

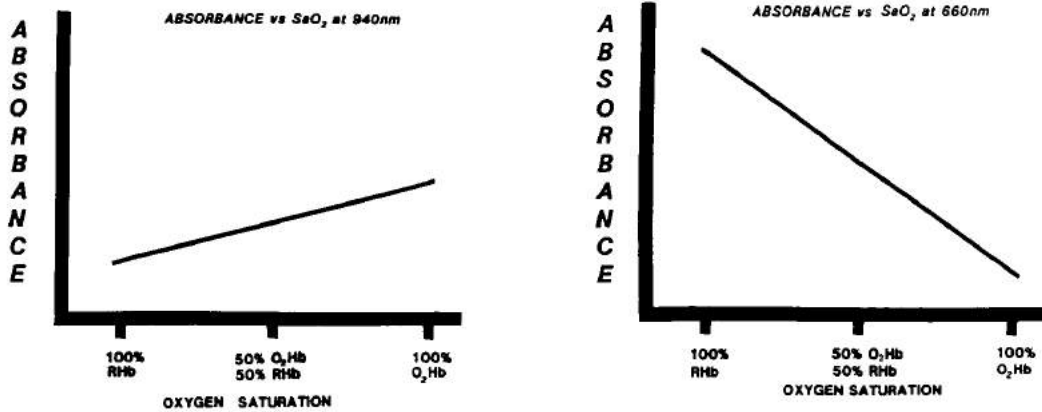


**Figure 4.14:** Absorbance of infrared (left side) and red (right side) light with varying oxygen saturation ( $\text{SaO}_2$ ). On the left side plot, infrared light (940 nm) has a greater absorption at high saturations than low saturation. On the right side plot, red light (660 nm) has a lower absorption at high saturation than at low saturation. Measurements obtained by varying the ratio of oxygenated/deoxygenated haemoglobin in a blood sample and keeping total haemoglobin constant. Figure reproduced from [7].

The pulsatile component of the PPG signal at red and infrared is used to express the absorption ratio. This ratio  $R$  is known as *Ratio of Ratios* and expresses the relationship between red absorption  $\alpha(\lambda_R)$  and infrared absorption  $\alpha(\lambda_{IR})$  [7,8]. By using this ratio, information on the incident light is no longer required as in the Wood's ear oximeter, but only relative changes in absorption between red and infrared are used [4,7].

$$R = \frac{\alpha(\lambda_R)}{\alpha(\lambda_{IR})} \quad (4.3)$$

The ratio  $R$  can be calculated from red and infrared PPG signals in different methods. Here, the derivative method will be illustrated, while the other methods are described in details in [8]. The ratio or ratios  $R$  in the derivative method can be expressed as:

$$R = \frac{AC_R/DC_R}{AC_{IR}/DC_{IR}}. \quad (4.4)$$

Where  $AC_R$  and  $AC_{IR}$  are the amplitude of the pulsatile component of the signals at red and infrared respectively, and  $DC_R$  and  $DC_{IR}$  are respectively the mean light absorptions at red and infrared. These parameters are illustrated in Figure 4.15, where  $AC$  is considered the difference between the maximum and minimum of the pulsatile component during the cardiac cycle, while the  $DC$  is the average absorption [4,7,8]. The  $AC$ s and  $DC$ s are directly dependent on the incident light intensity, thus dividing

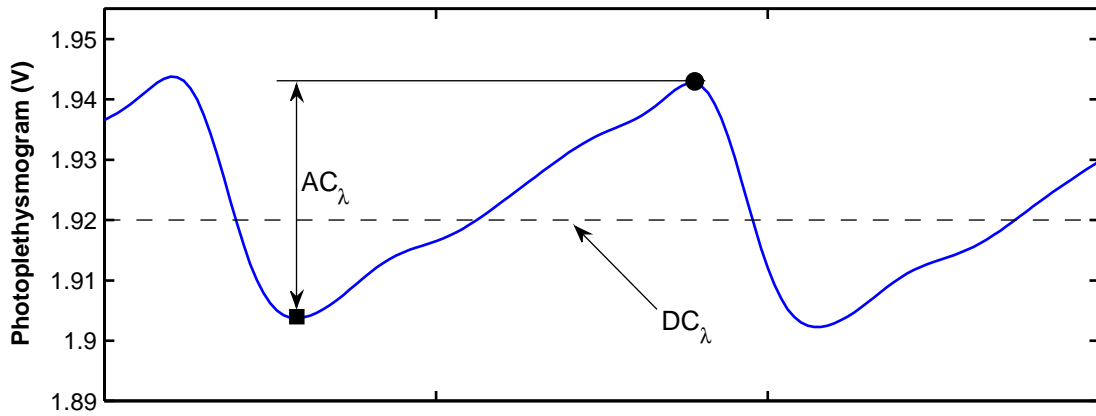


**Figure 4.15:** PPG parameters used for the calculation of the ratio of ratios. The AC amplitude at a generic wavelength  $\lambda$  is obtained from the difference between lower (circle) and maximum absorption (square) during the cardiac cycle. The DC is the average light intensity. These two parameters are extracted from red and infrared wavelength for the calculation of the ratio of ratios  $R$  in Equation 4.4.

the ACs to the DCs provides a corrected pulsatile component  $AC$  that is not dependent on the incident light [4, 7].

The ratio of ratios  $R$  is related to arterial oxygen saturation by empirical curves obtained from healthy volunteers. These calibrations are performed by varying the inspired fraction of oxygen in order to change the  $SaO_2$ . The  $SaO_2$  is measured by standard devices such as Co-oximetry (gold standard) and the measured ratio  $R$  is then related to  $SaO_2$  measurements [4, 7, 8]. Figure 4.16 shows the empirical calibration curve of pulse oximeters, relating  $SaO_2$  to the ratio  $R$ . Due to the impossibility to desaturate the subjects  $< 80\%$ , the calibration is performed for a  $SaO_2$  range between  $80\%$  and  $100\%$  and the curve is then extrapolated for a full range  $0-100\%$  [106]. Due to the fact that the calibration curves are extrapolated for low saturation values, the accuracy of pulse oximeters cannot be guaranteed for saturations  $< 70-80\%$  [106].

Once the calibration curve has been obtained, the ratio of ratios  $R$  can be used to calculate the arterial oxygen saturation  $SpO_2$  by using the equation of the calibration curve. The typical linear equation for the calibration curve in Figure 4.16 is depicted in Equation 4.5. For fully oxygenated blood ( $SpO_2 = 100\%$ ) the ratio or ratios  $R$  is about  $0.4$ , while for a ratio  $R = 1$ , corresponding to the same relative absorption of red and infrared light, the  $SpO_2$  is equal to  $85\%$ . These principles of pulse oximetry allow the noninvasive and continuous estimation of arterial oxygen saturation from red and infrared PPG signals. Pulse oximetry had a significant impact on clinical monitoring and it is now widely used in the hospitals around the world. The next section will briefly describe some of the main applications of pulse oximetry.

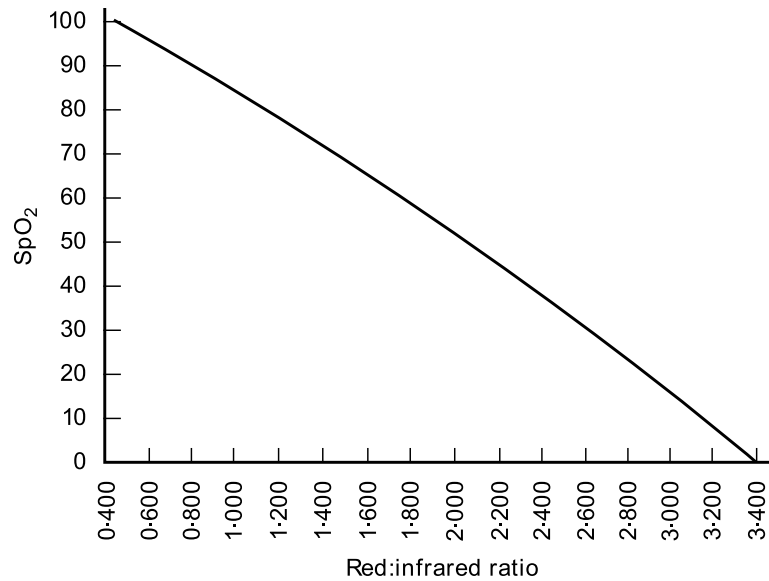


**Figure 4.16:** Pulse oximeter calibration curve. The ratio-of-ratios  $R$  is on the x-axes, while the arterial saturation  $SpO_2$  is on the y-axes. Figure reproduced from [6].

$$SpO_2 = 110 - 25 \cdot R \quad (4.5)$$

## 4.5.2 Clinical applications of pulse oximetry

Pulse oximetry has revolutionized clinical care by providing continuous and noninvasive measurements of arterial oxygen saturation ( $SpO_2$ ). Pulse oximeters are commonly used in anaesthesia and are mandatory during induction of anaesthesia [3, 4, 6]. Pulse oximetry can be used for the detection of oxygen-deprived status such as hypoxaemia [106–108]. The technique is used also in emergency medicine or intensive care [3, 6, 106] and in the identification of respiratory complications/diseases (e.g. obstructive pulmonary disease, asthma, etc.) [4, 6, 108]. Pulse oximetry can be used in neonatal care to monitor foetus oxygenation during labour [3, 4] or to detect apnoea in neonates [4].

Pulse oximetry probes are usually applied at extremities such as fingers or toes (in particular in neonates). However, these locations may suffer from vasoconstriction, degrading the quality of the PPG signal. More central locations such as the forehead and the earlobe appear to be less susceptible to vasoconstriction and may indicate  $SpO_2$  desaturations earlier than extremities [109–111]. Other locations such as oesophagus and ear canal have also been investigated and demonstrated that the  $SpO_2$  from these locations is less affected by vasoconstriction compared to extremities [3, 93].

Very recently, Verkruysse et al. and Shao et al. reported some results on the calibration of non-contact pulse oximetry [112, 113]. These are based on the principles of non-contact PPG measurements and the results may lead to an interesting future, where  $SpO_2$  will be measured without the necessity of attaching a single sensor to the patients.

### 4.5.3 Pulse Co-oximetry

One of the assumptions of pulse oximetry is that the only haemoglobin species in blood are oxygenated and deoxygenated haemoglobin. If other dyshaemoglobins such as carboxyhaemoglobin (HbCO) or methaemoglobin (MetHb) are present in the blood, pulse oximetry may not be able to distinguish them, giving inaccurate  $SpO_2$  measurements [6]. Carboxyhaemoglobin is a haemoglobin molecule that has bound reversibly with carbon monoxide [17]. In the red region of the spectrum, HbCO has very similar absorption to  $HbO_2$ , making it impossible to distinguish between the two and causing false  $SpO_2$  readings, in which HbCO has been mistaken by  $HbO_2$  [4, 6]. In healthy subjects, HbCO does not constitute a major concern, but higher concentrations of HbCO can be present in smokers or in carbon monoxide poisoning [6]. Co-oximeters are able to overcome this limitation by using at least four wavelengths for the determination of  $HbO_2$ , HHb, HbCO, and MetHb [4, 6]. Then, the oxygen saturation known as fractional saturation can be expressed as the percentage ratio of  $HbO_2$  over the full haemoglobin content [4].

$$FrO_2 = \frac{HbO_2}{HbO_2 + HHb + HbCO + MetHb} \quad (4.6)$$

Pulse oximeter manufacturers have recently proposed the solution of this limitation of pulse oximetry, by providing an instrument, known as Pulse CO-oximeter, capable of measuring the content of HbCO and MetHb in blood. The Pulse Co-oximeter uses eight wavelengths instead of the conventional two and some studies demonstrated that it can be used as a screening test for detection of abnormal levels of HbCO and MetHb [114].

#### 4.5.4 Venous saturation

As mentioned earlier, the DC component of the PPG signal contains respiratory-induced, low-frequency oscillations. These are believed to represent blood volume changes due to respiration. It has been proposed that these oscillations could be used to estimate venous oxygen saturation, similarly to AC pulsations for arterial oxygen saturation. If these low-frequency DC oscillations are isolated, a ratio  $R_v$  could be calculated as done with the ratio  $R$ . From  $R_v$ , the venous oxygen saturation  $SvO_2$  can then be estimated. Studies evaluating this method demonstrated that  $SvO_2$  was significantly lower than arterial  $SpO_2$ , thus possibly providing venous saturation measures [115,116]. However, challenges still remain such as validation against standard measures of venous saturation and irregular breathing.

## 4.6 Limitations of PPG and Pulse Oximetry

Although photoplethysmography and pulse oximetry have found many applications in clinical monitoring, they have some limitations that are worth mentioning.

- *Movement artefacts and sensor positioning.* Photoplethysmography suffers from movement artefacts and these should be avoided during the measurement. Reflectance PPG sensors need to be attached properly on the skin and any detachment could cause ambient light interference. Pulse oximetry measurements can be affected by movement artefacts, but if the sensor returns in place,  $SpO_2$  measures are restored. If the movements are periodic, these can cause the generation of pulsation of extra-arterial tissues with relative erroneous  $SpO_2$  readings. Advancements in signal processing in modern pulse oximetry allow for movement artefact correction [108,117]. If the pulse oximeter sensor is not properly applied to the tissue, mismatches in the red and infrared absorptions (penumbra effect) could cause  $SpO_2$  false readings [6,117].
- *Compromised peripheral perfusion.* Pulse oximetry measurements acquired from peripheral locations such as the fingers may be affected by vasoconstriction caused by compromised perfusion [4,108,114]. During such perfusion states, the quality

of the PPG signal degrades and SpO<sub>2</sub> measurements may not be accurate [108, 114, 117].

- *Pulse oximeters calibration.* Pulse oximetry does not measure directly arterial oxygen saturation, but it relates the measured ratio R to empirical calibrations. These calibrations, however, are performed on healthy adult subjects [106, 114] and may not be valid for a diverse population such as critically ill patients or neonates [114].
- *Dyshaemoglobins.* As mentioned earlier, dyshaemoglobin such as carboxyhaemoglobin and methaemoglobin can cause inaccurate SpO<sub>2</sub> readings [6, 106, 117]. Conventional pulse oximetry could not overcome this limitation, while pulse co-oximetry appears to be able to isolate the contribution of dyshaemoglobin [114].
- *Venous pulsations.* Pulse oximetry relies on the pulsatile nature of arterial blood, assuming that venous blood does not pulsate. In certain circumstances such as changes in positions, the venous blood may pulsate. In these situations, pulse oximeters are unable to distinguish between venous and arterial blood, giving lower SpO<sub>2</sub> values [4, 6, 117].
- *Skin pigmentation, intravenous dyes and finger nail polish.* Due to changes in the relative absorptions at red and infrared wavelengths, skin pigmentation, intravenous dyes and fingernail polish can cause errors in SpO<sub>2</sub> readings [108, 117].
- *Venous congestion.* As mentioned earlier, the AC PPG alone may not be adequate for the identification of venous congestions. In this regard, pulse oximetry suffers from the same (related) limitation. SpO<sub>2</sub> readings during venous occlusion may still take some time before they indicate the onset of venous congestion or they may still remain in the normoxic range [75–77, 118].

## 4.7 Summary

In summary, this chapter described the principles of photoplethysmography and pulse oximetry. The main clinical and research applications of the two techniques have also

been reviewed, along with some of the limitations and open challenges. The next chapter will present an overview of the principles and applications of another noninvasive optical technique, Near Infrared Spectroscopy.

## Principles and applications of Near Infrared Spectroscopy

Near Infrared Spectroscopy (NIRS) is a noninvasive optical technique that measures haemoglobin concentrations and oxygenation changes in tissues. The technique exploits the transparency of tissues to the near-infrared region of the light spectrum (700-1000 nm) in order to penetrate deep into tissues. Near Infrared Spectroscopy was introduced among other techniques in Chapter 3, whereas the current chapter presents a more detailed overview. The principles of the technique will be described, along with the different typologies of Near Infrared Spectroscopy instruments and their application. The modified Beer-Lambert law, used in Near Infrared Spectroscopy to infer haemoglobin concentration changes, will be introduced and discussed in this chapter. Finally, the limitations and the open challenges of the technique will also be reported. This chapter is presenting the potentials that the technique offers by monitoring haemoglobin concentrations and oxygenation changes. In this regard, the work in this thesis explores the feasibility of using photoplethysmography for monitoring haemoglobin concentration changes as performed in NIRS. Therefore, after presenting the principles of photoplethysmography in the previous chapter, this chapter aims at presenting the principles and the advantages of *in vivo* Near Infrared Spectroscopy monitoring.

## 5.1 Principles of Near Infrared Spectroscopy

Near Infrared Spectroscopy (NIRS) is an opto-technique, which relies on the application of the Beer-Lambert Law to measure haemoglobin concentrations and oxygenation in tissue [11]. The first *in vivo* NIRS study has been related to Jobsis, who observed that it was possible to monitor changes in haemoglobin oxygenation and Cytochrome (Cyt aa3) reduction by applying light in the spectral range of 700-1300 nm (i.e. near-infrared) through the cats' cranium, humans' cranium, and dogs' myocardium. Jobsis successfully demonstrated that the technique was able to monitor changes from normoxia to anoxia states from these organs. With that study, Jobsis showed the possibility of monitoring continuously and non-invasively the oxygenation states of haemoglobin, Cyt aa3, and blood volume, founding the basis for in-vivo NIRS [21].

Light interaction in tissue is composed of light absorption by chromophores and by absorption and light scattering. Visible light, between 450-700 nm, is strongly attenuated due to high absorption, being unable to penetrate more than 1 cm into tissues [12]. The near-infrared region of the light spectrum is between 700 and 1100 nm and light absorption in this range is relatively low, creating a zone of relative transparency in tissues [12, 21]. In this part of the spectrum, there are three major chromophores: oxygenated haemoglobin ( $\text{HbO}_2$ ), deoxygenated haemoglobin (HHb), and reduced or oxidised forms of Cytochrome Oxidase (CtOx) [11,12,119]. As introduced in Chapter 2, haemoglobin is responsible for the transport of oxygen in blood and for the release of oxygen into tissues, whereas CtOx is an enzyme involved in the electron chain of oxygen metabolism in cells [11]. These chromophores have the peculiarity of changing their light absorption properties depending on their oxygenation state [11, 12, 119]. Each chromophore has an absorption spectrum, in which the absorption of light is expressed as a function of wavelength. The absorption spectra of  $\text{HbO}_2$ , HHb, and CtOx in the near-infrared region are presented in Figure 5.1, where their different wavelength-dependent absorption characteristics in the near-infrared region are described by the curves. The isobestic point (between 800-810 nm) is the only point in the spectrum where deoxygenated haemoglobin and oxygenated haemoglobin have the same absorption characteristics (i.e. extinction coefficient). NIRS uses the different absorption properties of these chromophores to quantify their concentrations in tissues. The principle used is based on the application of the Beer-Lambert law. Although some NIRS

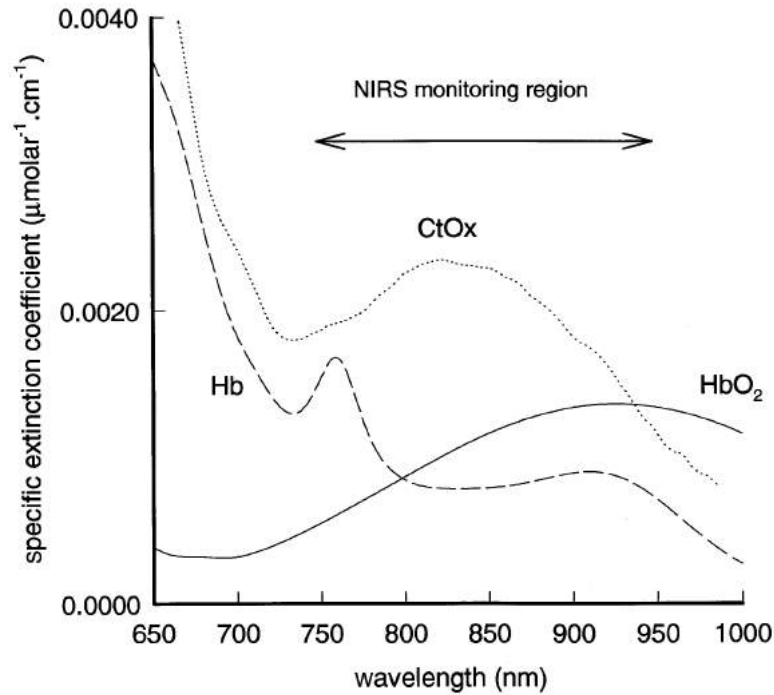


**Figure 5.1:** Absorption spectrum of oxygenated haemoglobin ( $\text{HbO}_2$ ), deoxygenated haemoglobin (Hb) and Cytochrome Oxidase (CtOx) in the near-infrared range. The absorption is expressed as specific extinction coefficient. Figure reproduced from [119].

instruments allow the additional estimation of CtOx, this chapter will mainly focus on the determination of oxygenated and deoxygenated haemoglobin only.

The Beer-Lambert law relates the absorption of light passing through a solution to the concentration of the chromophores present in the solution and the pathlength travelled by light [11,24]. Initially, Lambert described the decrease in light intensity as dependent on the distance travelled by the light beam as in Equation 5.1.

$$I = I_0 \exp^{-\mu l} \quad (5.1)$$

Where  $I_0$  is the intensity of the light applied to the substance,  $I$  is the measured transmitted and light intensity,  $\mu$  is the absorption coefficient, expressing the substance's light absorption (in  $\text{cm}^{-1}$ ), and  $l$  is the distance travelled by the light beam. Later on, Beer contributed to the concept by stating that decrease of light intensity is also due to the concentration of light absorbers in the substance. Therefore, the absorption coefficient  $\mu$  can be expressed as  $\mu = \varepsilon \times c$  and Equation 5.1 becomes:

$$I = I_0 \exp^{-\varepsilon cl}. \quad (5.2)$$

Where  $I_0$  is the intensity of the light applied to the substance,  $I$  is the measured transmitted light intensity,  $\varepsilon$  is the specific extinction coefficient (or molar absorptivity) of the substance,  $c$  is the chromophore concentration and  $l$  is the distance travelled by the light in the substance [11, 12, 17, 24]. The specific extinction coefficient  $\varepsilon$  describes the relationship between absorption properties of a substance (or chromophore) and the light wavelength (see Figure 5.1). As shown later, the extinction coefficient plays a determinant role in distinguishing two substances from each other (e.g. oxygenated and deoxygenated haemoglobin) [11, 17].

By reordering Equation 5.2 and applying the logarithm, the equation can be expressed as:

$$A = \ln \left( \frac{I_0}{I} \right) = \varepsilon \cdot c \cdot l. \quad (5.3)$$

The left side of the equation represents the light attenuation  $A$  (in natural logarithm), also known as optical densities (OD), and directly relates to the concentration of the light absorbers [11]. Equation 5.3 has been reported in both natural and base 10 logarithms, but in this work the natural logarithm convention will be used.

If the substance is composed of the mixture of multiple chromophores, the additive property of the extinction coefficients allows expressing the total light attenuation  $A$  as the linear sum of the contribution of each chromophore's concentration as showed in Equation 5.4.

$$A = (\varepsilon_1 \cdot c_1 + \varepsilon_2 \cdot c_2 + \dots \varepsilon_n \cdot c_n) \cdot l. \quad (5.4)$$

This generalised equation can be also described in terms of the light wavelength  $\lambda$ .

$$A_\lambda = (\varepsilon_{1\lambda} \cdot c_1 + \varepsilon_{2\lambda} \cdot c_2 + \dots \varepsilon_{n\lambda} \cdot c_n) \cdot l. \quad (5.5)$$

Where  $A_\lambda$  is the light attenuation at the wavelength  $\lambda$ ,  $\varepsilon_{n\lambda}$  is the extinction coefficient of substance  $n$  at wavelength  $\lambda$ , and  $c_n$  is the concentration of substance  $n$ . Equation 5.5 is an equation with  $n$  unknowns (i.e. chromophores concentrations). In order to solve this, at least  $n$  equations are required. By applying light at different wavelengths ( $\lambda_1, \lambda_2, \dots, \lambda_n$ ), at which the chromophore's extinction coefficients differ, Equation 5.5 will become an exactly determined system [17].

$$\begin{aligned}
 A_{\lambda_1} &= (\varepsilon_{1\lambda_1} \cdot c_1 + \varepsilon_{2\lambda_1} \cdot c_2 + \dots \varepsilon_{n\lambda_1} \cdot c_n) \cdot l \\
 A_{\lambda_2} &= (\varepsilon_{1\lambda_2} \cdot c_1 + \varepsilon_{2\lambda_2} \cdot c_2 + \dots \varepsilon_{n\lambda_2} \cdot c_n) \cdot l \\
 &\vdots \\
 A_{\lambda_n} &= (\varepsilon_{1\lambda_n} \cdot c_1 + \varepsilon_{2\lambda_n} \cdot c_2 + \dots \varepsilon_{n\lambda_n} \cdot c_n) \cdot l
 \end{aligned} \tag{5.6}$$

By using multi-component analysis, the system of equations in Equation 5.6 can be solved in order to estimate the concentrations of the chromophores. This principle is used in NIRS for the estimation of the concentration of oxygenated HbO<sub>2</sub> and deoxygenated haemoglobin HHb. For the calculation of these two chromophores, Equation 5.5 is applied at least at two wavelengths in the near-infrared region. These two wavelengths are usually selected on opposite sides with respect to the isobestic point of the haemoglobin absorption spectra (i.e. 800-810 nm). Wavelengths are often selected at both sides of the isobestic point of the spectra because HbO<sub>2</sub> and HHb have opposite absorption properties and, therefore, considerably different extinction coefficients  $\varepsilon$  (see Figure 5.1). A minimum of two wavelengths is required for the estimation of HbO<sub>2</sub> and HHb, but additional wavelengths can be used, particularly if other chromophores' concentrations such as CtOx should be derived [11]. For the specific purpose of calculating the concentrations of HbO<sub>2</sub> and HHb by NIRS, the system in Equation 5.6 transforms to:

$$\begin{aligned}
 A_{\lambda_1} &= (\varepsilon_{HbO_2\lambda_1} \cdot [HbO_2] + \varepsilon_{HHb\lambda_1} \cdot [HHb]) \cdot l \\
 A_{\lambda_2} &= (\varepsilon_{HbO_2\lambda_2} \cdot [HbO_2] + \varepsilon_{HHb\lambda_2} \cdot [HHb]) \cdot l.
 \end{aligned} \tag{5.7}$$

Where  $A_{\lambda_1}$  and  $A_{\lambda_2}$  are the light attenuations at wavelengths  $\lambda_1$  and  $\lambda_2$  respectively,  $\varepsilon_{HbO_2\lambda_1}$  and  $\varepsilon_{HHb\lambda_1}$  are respectively the extinction coefficients of HbO<sub>2</sub> and HHb at wavelength  $\lambda_1$ ,  $\varepsilon_{HbO_2\lambda_2}$  and  $\varepsilon_{HHb\lambda_2}$  are respectively the extinction coefficients of HbO<sub>2</sub>

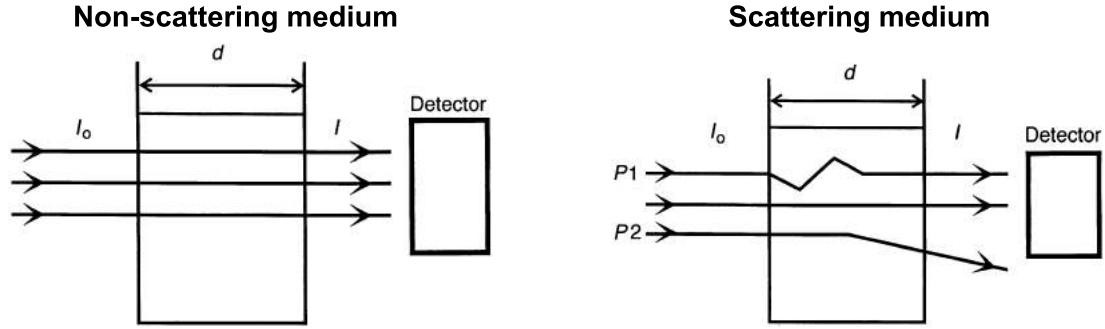


**Figure 5.2:** Effects of scattering on light propagation through a medium. In the non-scattering medium the emitted light beam with intensity  $I_0$  does not undergo scattering and the detected beam  $I$  is only attenuated due to absorption. The light path length travelled by light corresponds to the thickness of the sample. A different behaviour can be noticed in the scattering medium. The light undergoes scattering in the sample, causing a prolonged light path length as well as the dispersion of some of the emitted light (i.e.  $P_2$ ), which does not reach the detector. Figure reproduced from [12].

and HHb at wavelength  $\lambda_2$ ,  $[HbO_2]$  and  $[HHb]$  are the concentrations of oxygenated and deoxygenated haemoglobin, and  $l$  is the pathlength travelled by light. Equation 5.7 assumes that  $HbO_2$  and  $HHb$  are the only chromophores present in the solution, which does not hold for tissues, where other absorbers such as lipids, melanin, and myoglobin could contribute to the overall light absorption. Later in the chapter, the approach used in NIRS to deal with this assumption will be described.

### 5.1.1 The Modified Beer-Lambert law

The Beer-Lambert law described so far is based on the assumption that light only undergoes absorption. However, this assumption is not valid in tissues, where near-infrared light attenuation due to scattering dominates compared to absorption (roughly 80 % scattering vs. 20 % absorption) [12, 23]. The first implication on the use of the Beer-Lambert law in presence of scattering is the impossibility of quantitatively determining the actual light attenuation, since some part of the scattered light will not reach the detector. [12]. Secondly, multiple scattering in tissue causes an increase of the pathlength travelled by light [11, 12]. Figure 5.2 visually represents both these scattering effects.

The modified Beer-Lambert law (MBLL) takes into account of the effects of scattering in tissues, by transforming Equation 5.5 in:

$$A_\lambda = (\varepsilon_{1\lambda} \cdot c_1 + \varepsilon_{2\lambda} \cdot c_2 + \dots \varepsilon_{n\lambda} \cdot c_n) \cdot d \cdot DPF + G. \quad (5.8)$$

Where  $DPF$  is the Differential Pathlength Factor, expressing the increase of the light path length due to scattering and relating the emitter-detector separation distance  $d$  to the effective pathlength travelled by light ( $l = d \times DPF$ ) [11, 12, 23]. The factor  $G$  is a scattering factor, which expresses both the nature and the geometry of the tissue [11].

The DPF is a unit-less, wavelength-dependent coefficient [119] and it can be measured by Time Resolved Spectroscopy (time of flight) or Phase Modulated Spectroscopy (both described later in this chapter) [120, 121]. The DPF is dependent on the type of tissue [120, 121] and gender [120, 121], but a constant range was found for emitter-detector distances  $d > 2.5$  cm [120]. The mean DPF values measured by Time Resolved Spectroscopy for the adult forearm ( $DPF = 3.59$ ), neonate head ( $DPF = 3.85$ ), and adult head ( $DPF = 5.93$ ) are still used nowadays for quantification of  $HbO_2$  and  $HHb$  concentrations by NIRS.

Since the invention of NIRS, several measurement techniques have been introduced for the quantification of the concentrations of  $HbO_2$  and  $HHb$ . These techniques, which differ in their measurements principles, will be briefly described in the next sections.

## 5.2 NIRS Measurement Techniques

### 5.2.1 Time Resolved Spectroscopy

Time Resolved Spectroscopy (TRS), also known as Time domain NIRS, is an NIRS technique that allows the solution of the modified Beer-Lambert and determination of absolute concentration values of  $HbO_2$  and  $HHb$ . The technique determines the optical properties of the tissue by observing the temporal distribution of light in tissue (time of flight).

In TRS, a small impulse of coherent light is emitted to the tissue. The impulse lasts a few tens of picoseconds and is produced by means of lasers [24, 119, 122]. Light is emitted to and collected from the tissue by optical fibres. The detected light is collected by a photomultiplier in photon-counting mode, which orders the photons by their time of arrival [119]. This detected signal is defined as Temporal Point Spread Function (TPSF) and presents the distinctiveness of being “delayed, broadened, and

attenuated” with respect to the emitted impulse of light [122]. Figure 5.3 shows an example of TPSF measured from the brain. The TPSF contains information on the temporal light propagation into the tissue due to light path length (time delay and broadening), the attenuation due to absorption and scattering (attenuation, tail’s slope, and broadening) [122]. Once the TPSF has been obtained, the median intensity (50th percentile) is extrapolated for the determination of the average arrival time of the photons [11, 123]. Once this time  $t_m$  has been determined from the TPSF, the light path length  $L$  can be calculated (knowing the speed of light in vacuum  $c$  and the refractive index of the tissue  $n$ ).

$$L = \frac{c \cdot t_m}{n}. \quad (5.9)$$

Also, the diffusion equation, expressing the light reflectance in function of time and space, can be used to estimate the absorption and scattering properties of the tissue ( $\mu_a$  and  $\mu'_s$ ) [24, 122]. Once the time of flight and relative light pathlength have been derived, the TPSF can be measured at different wavelengths (at least two) [122]. The absorption and scattering properties of the tissue at several wavelengths can be extrapolated by fitting the measured TPSF (i.e. temporal and spatial information) and the solution to the diffusion equation [24, 122]. Once  $\mu_a$  and  $\mu'_s$  are obtained, absolute concentrations of HbO<sub>2</sub> and HHb can be calculated from the modified Beer-Lambert law [11, 24, 122].

### 5.2.2 Phase Modulated Spectroscopy

Phase Modulated Spectroscopy (PMS) or Intensity Modulated Spectroscopy is an NIRS measurement technique that exploits the intensity and, more particularly, the phase shift that light experiences in tissues. When light, modulated in both frequency and intensity, is emitted into tissues, it undergoes constant attenuation in continuous intensity (DC) and in the alternated component (AC), as well as a phase shift in the AC component [11, 24]. This is showed in the simulation presented in Figure 5.4, where a modulated incident light is constantly attenuated in both DC and AC components, while it undergoes a phase shift as well. The attenuation in DC and AC increases with increasing scattering  $\mu'_s$ . Therefore, the detected light  $I$  can be expressed in the form of the DC and AC detected signals (respectively  $I_{DC}$  and  $I_{AC}$ ):

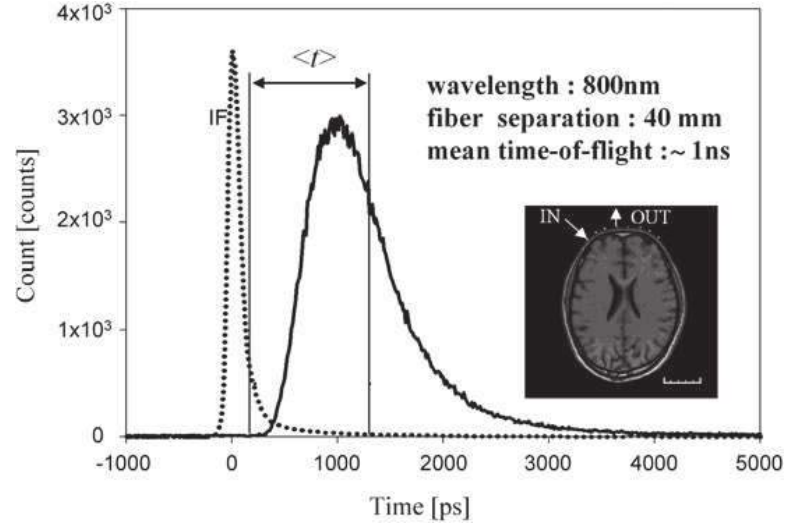


**Figure 5.3:** Example of Temporal Point Spread Function (TPSF) measured in the brain. The emitted impulse (dotted line) lasts only a few picoseconds and it is centred at the zero point on the time scale. The detected photons are detected and ordered on their arrival time, forming the TPSF curve (continuous line). The TPSF is attenuated in intensity and broadened in time due to absorption and scattering. The time delay  $t$  is the mean time of arrival of the photons, used for estimating the mean light path length by Equation 5.9. Figure reproduced from [24]

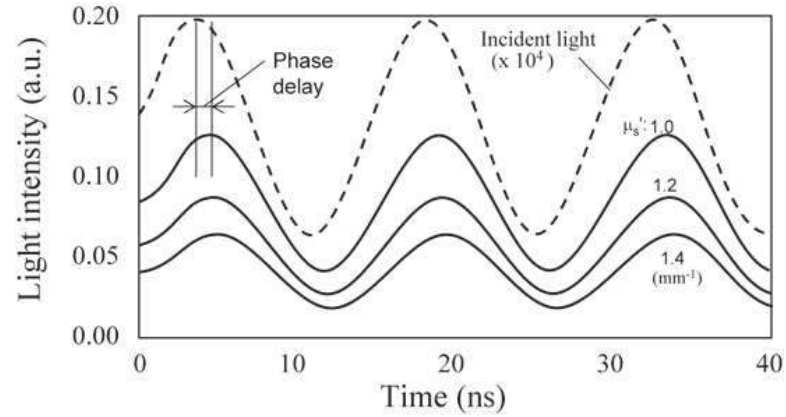


**Figure 5.4:** Simulation of the light attenuation and phase shift of modulated incident light in Phase Modulated Spectroscopy for different scattering coefficients. The modulated incident light (dashed line) is attenuated in both continuous and alternated component (continuous lines). The attenuations increase with increasing scattering  $\mu_s'$ . Also, the detected light intensities experience a delay (shift) in frequency. Figure reproduced from [24].

$$I = I_{DC} + I_{AC} \cdot (2\pi f_e t + \phi). \quad (5.10)$$

Where,  $f_e$  is the modulation frequency of the emitted light,  $\phi$  is the shift in frequency, and  $t$  is time.

In PMS, a phase and intensity modulated light (usually in the radio frequencies) is emitted to the tissue and the measured attenuations and frequency shift are used to estimate the light path length and the absorption and scattering properties of the tissue [11,24,119]. The light path length  $L$  can be estimated from the shift in frequency

$\phi$ , the modulating frequency  $f_e$ , the refractive index of the tissue  $n$ , and the speed of light in vacuum  $c$  [11].

$$L = \frac{\phi \cdot c}{2 \cdot f_e \cdot n} \quad (5.11)$$

The absorption and scattering properties of the tissue  $\mu_a$  and  $\mu'_s$  are estimated in PMS by solving a derivation of the diffusion equation [11,24]. With this method, the AC and DC detected intensities, along with the phase shifts are measured from two detectors placed close to each other. The measurement of these variables at two locations allows to fit these in a light diffusion model, in order to extract  $\mu_a$  and  $\mu'_s$  [11,24,119]. Once  $\mu_a$  and  $\mu'_s$  are derived at least two wavelengths, absolute concentrations of HbO<sub>2</sub> and HHb can be calculated from the modified Beer-Lambert law [11].

### 5.2.3 Continuous wave NIRS

Continuous wave (CW) NIRS instruments are the earlier versions of the NIRS instruments [119]. As the name suggests, continuous light intensities are emitted in the tissue by means of laser diodes or light emitting diodes (LED). The backscattered light is then detected by a photodiode or photomultiplier tube [11,24,119].

CW NIRS instruments ignore the originally emitted intensity, requiring the adoption of a different approach for the solution of the MBLL in Equation 5.8. The differential solution of the MBLL is used in CW NIRS, consisting in representing the changes in attenuation from the baseline (start of the measurement) instead of the absolute attenuation. These changes in attenuation are then related to relative changes in concentrations of HbO<sub>2</sub> and HHb. Therefore, the differential version of Equation 5.8, for HbO<sub>2</sub> and HHb becomes:

$$\begin{aligned} \Delta A_{\lambda_1} &= (\varepsilon_{HbO_2\lambda_1} \cdot \Delta[HbO_2] + \varepsilon_{HHb\lambda_1} \cdot \Delta[HHb]) \cdot d \cdot DPF + \Delta G \\ \Delta A_{\lambda_2} &= (\varepsilon_{HbO_2\lambda_2} \cdot \Delta[HbO_2] + \varepsilon_{HHb\lambda_2} \cdot \Delta[HHb]) \cdot d \cdot DPF + \Delta G. \end{aligned} \quad (5.12)$$

Where,  $\Delta A_{\lambda_n}$  is the light attenuation change at wavelength  $\lambda_n$ ,  $\Delta[HbO_2]$  and  $\Delta[HHb]$

are the relative changes from the baseline of  $\text{HbO}_2$  and  $\text{HHb}$ , and  $\Delta G$  are the changes in scattering. The changes in attenuation  $\Delta A_{\lambda_n}$  are expressed as  $\ln\left(\frac{I(0)}{I(t)}\right)$ ; with  $I(0)$  being the light intensity at the baseline (or start of the measurement) and  $I(t)$  is the light intensity throughout the measurement. This allows relating the changes in light attenuation to the changes in concentrations of  $\text{HbO}_2$  and  $\text{HHb}$ . The DPF can be utilised from TRS or PMS measurements previously acquired from different tissues [120]. If the DPF cannot be derived from the literature, the changes in concentration  $\Delta[\text{HbO}_2]$  and  $\Delta[\text{HHb}]$  can be expressed as relative to the path length in  $\text{mM} \cdot \text{cm}$  (concentration  $\times$  optical path length).

In order to solve the system of equations in Equation 5.12, few assumptions should be made. Firstly, it should be assumed that  $\text{HbO}_2$  and  $\text{HHb}$  are the only chromophores changing concentration throughout the short measurement. Secondly, assuming that the scattering factor  $G$  is constant during the measurement allows to rule out the scattering contribution ( $\Delta G = 0$ ), and then solving the system for at least two wavelengths. These assumptions can be valid for the relatively short NIRS measurements, in which the tissue's optical properties are assumed constant. Furthermore, the method assumes that the detected light attenuation is only due to haemoglobin concentrations. Other absorbers such as myoglobin or lipids could be considered constant for the measurement duration. However, for prolonged measurements (several hours) or during muscle contraction (possible change in myoglobin) the CW NIRS methods may suffer the influence of other absorbers in tissue.

The CW NIRS measurements are highly sensitive, fast, economical, and the adopted technology (LEDs/photodiodes) offers a greater level of flexibility, simplicity, and miniaturisation when compared to TRS or PMS instruments [24].

#### 5.2.4 Spatially Resolved Spectroscopy

Spatially Resolved Spectroscopy (SRS) is an extension of CW NIRS that allows the estimation of tissue oxygenation (often known as TOI,  $\text{StO}_2$ , or  $\text{rSO}_2$ ). In SRS, the optical properties of the tissue are derived from the spatial distribution of light attenuation with respect to the photodetectors' distance. When two photodetectors are placed close to each other, the detected light intensities emitted from a single source

(i.e. in reflectance configuration) yield information on the optical properties of the tissue measured. By solving the diffusion approximation for a highly scattering medium ( $\mu_a \ll \mu'_s$ ), the attenuation  $A$ , with respect to the photodetectors' distance  $\rho$ , can be expressed as follows:

$$\frac{\partial A}{\partial \rho} = \frac{1}{\ln 10} \cdot \left( \sqrt{3 \cdot \mu_a \cdot \mu'_s} + \frac{2}{\rho} \right). \quad (5.13)$$

Equation 5.13 can be solved by approximating  $\mu'_s$  as constant in the near-infrared region ( $\mu'_s = k$ ). By doing this, the equation can be solved to determine the absorption term  $k \cdot \mu_a$  [124]. However, the scattering coefficient  $\mu'_s$  varies slightly with the wavelength and a scaling factor  $h$  can be introduced to consider the wavelength dependence of  $\mu'_s$  (i.e.  $h$  is the normalised slope of  $\mu'_s$  with respect to  $\lambda$ ). Thus, the factor  $k \cdot \mu_a$  can be calculated from Equation 5.13.

$$k \cdot \mu_a(\lambda) = \frac{1}{3 \cdot \mu'_s(\lambda)} \cdot \left( \ln 10 \cdot \frac{\partial A}{\partial \rho} - \frac{2}{\rho} \right)^2; \text{ With: } \mu'_s(\lambda) = k \cdot (1 - h \cdot k) \quad (5.14)$$

By applying light at least two wavelengths, the absorption coefficients  $k \cdot \mu_a(\lambda)$  can be obtained at different wavelengths. By considering that  $\mu_a = \varepsilon \times c$ , a solvable system of equation can be created.

$$\begin{aligned} k \cdot \mu_a(\lambda_1) &= \varepsilon_{HbO_2\lambda_1} \cdot k \cdot [HbO_2] + \varepsilon_{HHb\lambda_1} \cdot k \cdot [HHb] \\ k \cdot \mu_a(\lambda_2) &= \varepsilon_{HbO_2\lambda_2} \cdot k \cdot [HbO_2] + \varepsilon_{HHb\lambda_2} \cdot k \cdot [HHb] \end{aligned} \quad (5.15)$$

From the system of equations above, the relative concentrations of oxygenated and deoxygenated haemoglobin  $k \cdot [HbO_2]$  and  $k \cdot [HHb]$  can be obtained [11, 124].

Even though absolute concentrations of HbO<sub>2</sub> and HHb cannot be obtained by SRS, the relative concentrations  $k \cdot [HbO_2]$  and  $k \cdot [HHb]$  can be used to calculate the Tissue Oxygenation Index (TOI).

$$TOI = \frac{k \cdot [HbO_2]}{(k \cdot [HbO_2] + k \cdot [HHb])} \times 100(\%) \quad (5.16)$$

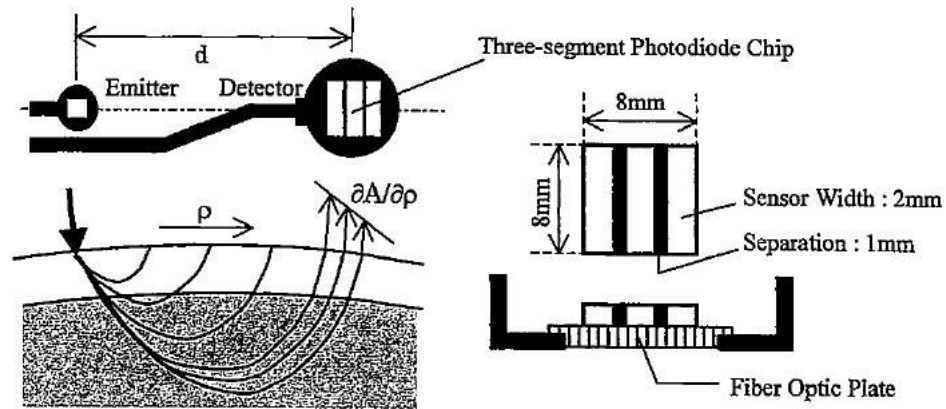


**Figure 5.5:** SRS measurement and schematic of a multi-distance SRS sensor. The emitter shines light into the tissue and three detectors, placed close to each other, measure the light attenuation  $A$  as a function of their distance  $\rho$  from the emitter. Figure reproduced from [124].

The TOI is expressed in percentage and represents the haemoglobin oxygenation saturation of the sampled volume of tissue. Equation 5.16 expresses the tissue oxygen saturation measured in the SRS case, but the same formula can be applied to TRS or PMS absolute measurements of  $\text{HbO}_2$  and  $\text{HHb}$ . Figure 5.5 shows an example of SRS measurement and sensor, where three photodetectors are placed close to each other for the measurement of  $\frac{\partial A}{\partial \rho}$ .

Due to the multi-distance approach and the derivation of the measurement relative to the two detectors, the SRS is considered less susceptible to the superficial structures within the light-path. When applied on the forehead for the monitoring of cerebral oxygenation, SRS-derived TOI demonstrated to be affected by clamping of the internal carotid artery, while there were no changes and no association with LDF measures when the external carotid was clamped [125].

Depending on the device manufacturers, TOI is also referred in the literature as  $\text{StO}_2$  or  $\text{rSO}_2$ , but the acronym TOI will be used throughout this thesis in order to avoid confusion to the reader.

Figure 5.6 shows a collection of NIRS measurements acquired by CW, PMS and SRS during vascular occlusions on the forearm. The CW NIRS instrument expressed the changes in relative units of concentration ( $\mu\text{M} \cdot \text{cm}$ ), the PMS device estimated the absolute concentrations, and the SRS derived the tissue oxygenation index TOI.

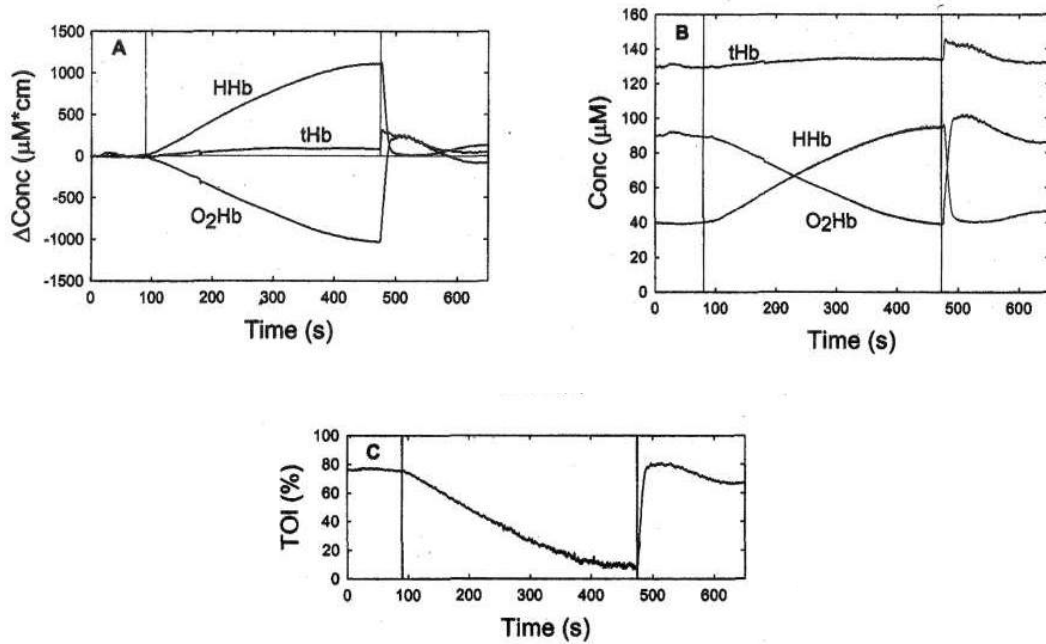


**Figure 5.6:** Changes in relative and absolute haemoglobin concentrations and tissue oxygenation measured by NIRS at the brachioradialis during total occlusion. (A) Changes in relative concentrations of oxygenated (O<sub>2</sub>Hb), deoxygenated (HHb), and total haemoglobin (tHb) measured by a continuous wave NIRS instrument. (B) Changes in absolute concentrations of O<sub>2</sub>Hb, HHb, and tHb measured by a phase modulated NIRS instrument. (C) Tissue oxygenation index (TOI) measured by a spatially resolved spectroscopy instrument. All measurements were acquired from the brachioradialis during vascular occlusion at 250 mmHg, occluding both veins and arteries. Vertical lines indicate the duration of the occlusion. In (A) and (B), the increases in HHb and tHb indicate the engorgement of the venous circulation, while the drop in O<sub>2</sub>Hb is due to the occlusion of the arterial inflow. Figure reproduced from [13].

After describing the principles of NIRS and the different typology of NIRS measurements, the following sections will provide an overview of the different clinical and research applications of NIRS. However, before introducing the applications of NIRS, it is necessary to discuss the penetration depth of NIRS measurements and the origin of the NIRS signals, which still remain among the main topics of debate in NIRS research.

## 5.3 Penetration depth and origins of NIRS signal

### 5.3.1 Penetration depth of NIRS signal

NIRS is been known for its great ability to penetrate deep into tissues. The technique has been initially applied on neonates' head because the light could be shone from one side of the head to the other (i.e. transmission mode). The same cannot be generally applied to adult's head due to the greater head's diameter and scalp/skull thickness. Therefore, the technique is almost always applied in reflectance mode, with

both emitter and detector on the same side of the tissue. When in reflectance mode, NIRS light diffuses in tissue in a banana-shaped arc. The penetration depth of this light beam is dependent on the specific wavelength used (i.e. absorption and scattering are wavelength-dependent) and the emitter-detector separation distance. For separation distances greater than 2.5 cm, Van der Zeer et al. found that the DPF measured by TRS was constant, indicating that this value is the minimum suggested distance to obtain a penetration depth constantly proportional to the emitter-detector separation distance [120]. Although increasing the separation distance increases the penetration depth, it also causes a decrease in the overall signal quality due to high absorption. Thus, a separation distance greater than 5 cm should be avoided in NIRS measurements [22]. The quality of the signal for larger separation distances can be improved by increasing the light intensities, but this may cause overheating of the tissue. The typology of tissue affects the penetration depth due to different scattering and absorption properties (i.e. absorption is inversely proportional to the DPF, while scattering is directly proportional) and different fat thickness [120, 121, 126]. For instance, NIRS seems to penetrate more on the head (DPF = 5.93) than the muscle (DPF = 3.59), due to higher scattering in cerebral tissue [120]. Overall, the effective penetration depth of NIRS measurements is difficult to predict, it can only be simulated by Monte Carlo simulations, and it may vary on the measurement type (TRS, PMS, or other), wavelengths, instrumentation, or the complexity of the simulation model [24, 119]. For these reasons, the exact prediction of tissue penetration is still under debate and it cannot be quantified for each single measurement. However, it is common practice to consider the penetration depth to be between one-half and one-third of the actual emitter-detector separation distance [13, 22, 23, 127]. For instance, when an NIRS sensor with an emitter-detector separation distance of 4 cm is used, the penetration depth of the measurement can be considered to be roughly between 1.33 and 2 cm.

### 5.3.2 Origins of the NIRS signal

Due to the deep penetration, NIRS signals are believed to originate from the tissues' microcirculation. Large vessels such as arteries and veins are considered to affect NIRS measurements, mainly because light is strongly absorbed by these structures [13]. Therefore, the NIRS signal represents a mixed sample volume composed by arterioles, capillaries, and venules [12, 13, 22, 128, 129]. The structural composition of tissues un-

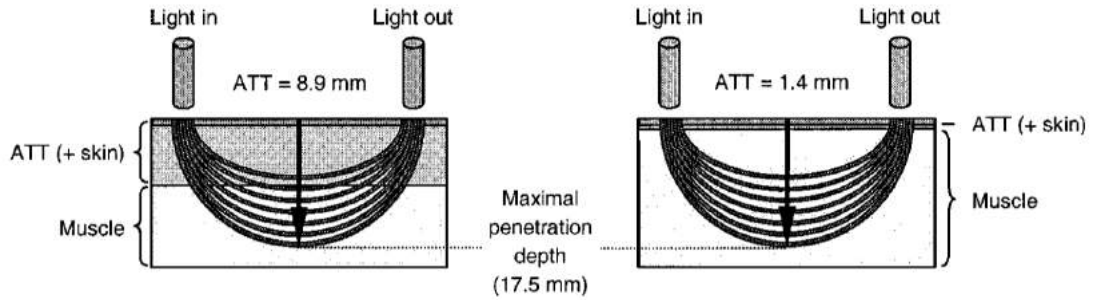


**Figure 5.7:** Model representing light penetration in NIRS muscle measurements for high and low adipose tissue content. Light diffuses in tissue in a banana-shape arc and the maximum penetration depth is about half of the emitter and detector distance (in this figure, the separation distance is 3.5 cm). In the case of high adipose tissue content, only 49 % of the signal passes through the muscle. In situations of a normal or low adipose tissue content, most of the light (92 %) passes through the muscle. Figure reproduced from [127].

der normal conditions yields the contribution of arterial-venous blood [22, 23, 129]. For instance, cerebral tissue is mostly composed of venous blood (30 % arterial blood and 70 % venous blood) [22]. Generally, the partitioning of the microcirculation is 10 % arterioles, 20 % capillaries, and 70 % venules [128, 129]. Due to the mixed nature of the NIRS sampled volume, the tissue oxygen saturation measured by NIRS (Equation 5.16) represents a mixed saturation between arterial and venous blood. This saturation tends to follow the venous saturation and it has the advantage of indicating a balance between oxygen supply and oxygen consumption of tissue [13, 23, 129]. This also explains why the tissue saturation measured by NIRS is always lower than the arterial oxygen saturation  $\text{SpO}_2$  measured by pulse oximetry. NIRS does not discriminate between arterial blood, capillaries, and venous blood, whereas pulse oximetry assesses only the arterial blood by filtering the pulsatile component of the signal [12, 129].

## 5.4 Clinical and research applications of NIRS

The previous sections described the principles of NIRS. The technique has found many clinical and research applications and this section wants to overview some of these. Although NIRS is relatively new compared to other traditional physiological measurements, the technique has been investigated for a multitude of applications and these are covered in the extensive literature on the subject. This section offers an overview of some of the main applications of NIRS.

### 5.4.1 Cerebral perfusion, oxygenation and blood flow

NIRS monitoring of changes in cerebral haemoglobin oxygenation saturation (cerebral oximetry) is considered the primary application of NIRS, with a significantly vast literature. The reason for the focus of NIRS on cerebral monitoring is the ability of near-infrared light to penetrate the skull, thus allowing the monitoring of cerebral perfusion and oxygenation transcutaneously and noninvasively.

In surgery, cerebral NIRS monitoring (cerebral oximetry) can provide valuable information in situations when cerebral perfusion may be compromised. Cerebral oximetry demonstrated to improve patients' clinical outcomes when cerebral oxygen saturation was monitored and restored during coronary artery bypass [22]. Cerebral oximetry was also found to detect desaturations and changes in perfusion during different scenarios such as aortic dissection, deep hypothermic circulatory arrest, and carotid endarterectomy [22]. In this context, desaturations greater than 25 % or an absolute saturation less than 45 % correlated with poor postoperative outcomes [25]. During carotid endarterectomy, a sudden drop in TOI greater than 13 % indicated the clamping of the internal carotid [130].

Decreases in cerebral oxygen saturation were found to be correlated with hypoxic events in adults and pre-term neonates [131, 132], whereas oscillations in the inspired fraction of oxygen  $> 3$  % reflected variations in the NIRS cerebral oxygen saturation measured in neonates [133].

By using oxygen as a tracer and the Fick's principle, cerebral blood flow (CBF) and volume (CBV) can be derived from NIRS measurements [23, 134]. CBF can be calculated from the increase in  $\text{HbO}_2$  or  $\text{HbdD}$  ( $\text{HbdD} = \text{HbO}_2 - \text{HHb}$ ) concentrations after a sudden increase in inspired fraction of oxygen ( $\text{FiO}_2$ ), whereas CBV can be determined from the change in  $\text{HbO}_2$  (or  $\text{HbdD}$ ) after a slow change in  $\text{FiO}_2$  [134]. The cerebral NIRS signals can also be used to assess vasomotor reactivity during breath holding in healthy volunteers and to distinguish between healthy, smokers, and stroke patients [135]. Changes in cerebral NIRS signals can also indicate gravitational changes caused by head-up or head-down bed tilting [136].

Frequency domain analysis of cerebral NIRS signals can provide important informa-

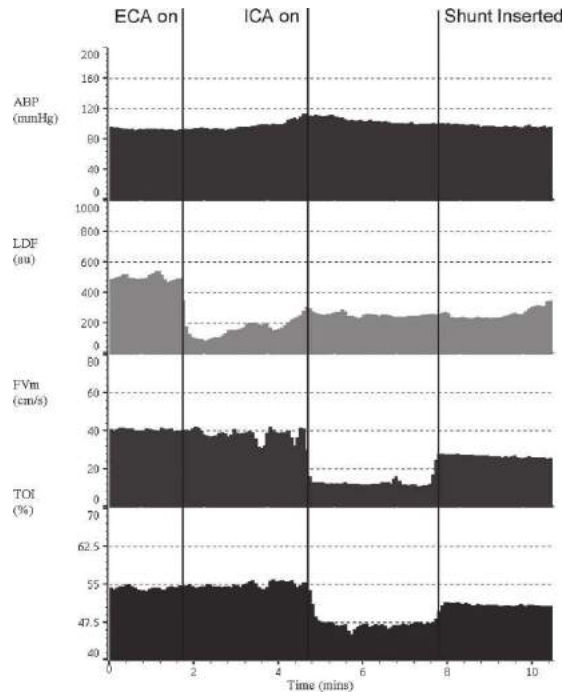


**Figure 5.8:** Changes in cerebral oxygen saturation (TOI) during clamping in carotid endarterectomy. External carotid clamping (ECA) causes the forehead laser Doppler signal (LDF) to drop, whereas TOI and transcranial Doppler flow (FVm) do not vary. Contrary, clamping of the internal carotid artery (ICA) generates a drop in both TOI and FVm, whereas LDF remains constant. When the carotid shunt is inserted, TOI and FVm return to values close to the baseline. Arterial blood pressure (ABP), measured via a catheter in the radial artery, remains mostly stable throughout the procedure. Figure reproduced from [130]

tion related to stimulation, vasomotion, or cerebral autoregulation. Low and very low-frequency oscillations in NIRS variables demonstrated to be related to functional visual activation and hypercapnia [137]. Differences in low-frequency oscillations of HbO<sub>2</sub> and TOI were also found during posture changes between supine, standing, and sitting positions, whereas there were no significant changes in the variables between the different positions [138]. During haemorrhage, low-frequency oscillations of cerebral TOI were correlated with autoregulation indexes from transcranial Doppler, thus indicating cerebral autoregulation [139].

#### 5.4.2 Muscle perfusion and oxygenation

Monitoring muscle perfusion and oxygenation noninvasively may be challenging due to the depth at which muscles lay from the surface of the skin. NIRS provides the means for monitoring perfusion and oxygenation changes in muscle. Hampson and Piantadosi pioneered the NIRS monitoring of skeletal muscle. In their earlier paper, Hampson and Piantadosi demonstrated that changes in forearm's skeletal muscle could be monitored by NIRS. An NIRS sensor was placed on the skin, above the left forearm

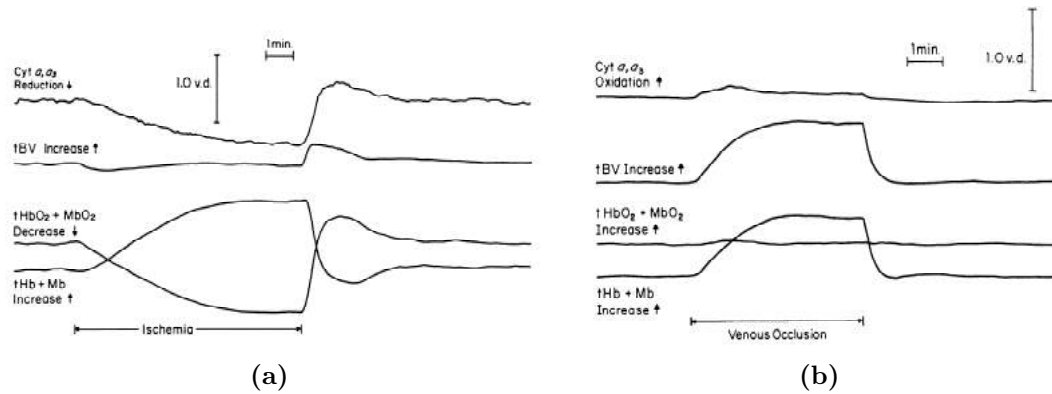


**Figure 5.9:** Changes in oxygenated (tHbO<sub>2</sub>), deoxygenated (tHb), and total blood volume (tBV) measured by NIRS during cuff-induced ischaemia (a) and venous occlusion (b). In (a), occlusion of both arterial and venous vasculatures (ischemia) causes a decrease in tHbO<sub>2</sub> and a simultaneous increase of tHb, while the total blood volume (expressed as the sum of tHbO<sub>2</sub> and tHb) does not change. At the release of occlusion, the variables return to baseline after a hyperaemic shoot. In (b), venous occlusion causes an increase in tHb and total blood volume tBV, while tHbO<sub>2</sub> remains unchanged. The ischemic occlusion lasted for 8 minutes, whereas venous occlusion was performed for 5 minutes. The concentration of cytochrome oxidase *Cyta, a<sub>3</sub>* is depicted along with the haemoglobin concentrations. Figure reproduced from [140].

musculature (brachioradialis) and vascular occlusions were produced by inflating a cuff placed around the left arm. The trends in the changes of HbO<sub>2</sub> and HHb indicated that it was possible to distinguish between forearm ischaemia (i.e. occlusion of both venous and arterial vasculature) and venous occlusion in the forearm. As showed in Figure 5.9, ischaemia caused a rapid decrease of HbO<sub>2</sub> and an increase in HHb. Contrarily, the venous occlusion produced an increase in HHb only. The authors also verified that the changes were mostly originating from the muscle, since the PO<sub>2</sub> measured on the skin and the NIRS signals from the control forearm did not vary [140]. The methods introduced by Hampson and Piantadosi are still used nowadays to assess muscle activity and they are often used as a primary *in vivo* test for NIRS instrumentation [141–143].

The changes in NIRS signals measured from muscle can also be used to assess the muscle's oxygen metabolism *in vivo*, at rest and during exercise. Muscle oxygen consumption (VO<sub>2</sub>) can be assessed by analysing the rate of changes in NIRS haemoglobin concentrations during induction of vascular occlusions. The rate at which HbD, defined as  $HbD = HbO_2 - HHb$ , or HbO<sub>2</sub> only, changes during total occlusion was found to correlate with muscle's VO<sub>2</sub> and was able to indicate a greater VO<sub>2</sub> for muscles during exercise than at rest [144–147]. Figure 5.10 shows an example of the rate of HbO<sub>2</sub> measured by Hamaoka et al. during both rest and exercise. VO<sub>2</sub> can also be estimated from the rate of increase in HHb concentration during venous occlusion [148], but it may be less reproducible compared to the total occlusion method [147]. Muscle blood flow may additionally be assessed from NIRS signals by analysing the rate of increase

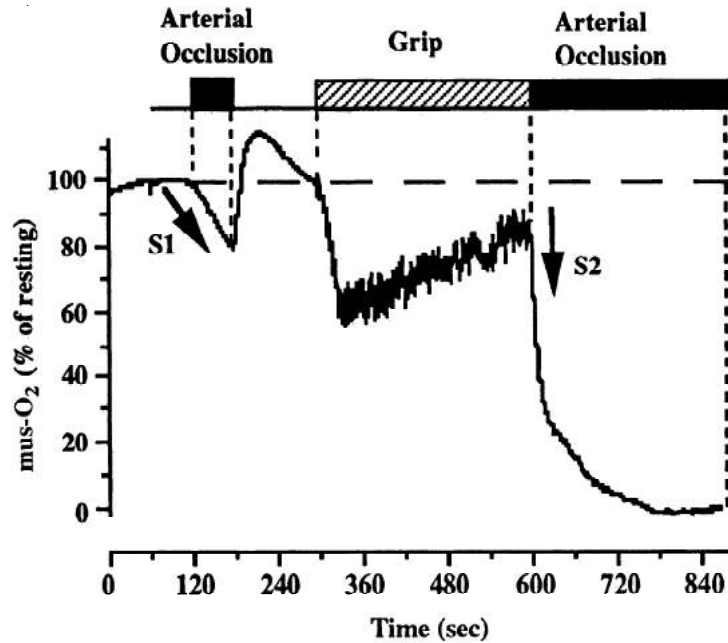


**Figure 5.10:** Decline rate of HbO<sub>2</sub> during arterial occlusion at both rest and after exercise (grip). NIRS measurement was performed from the finger flexor muscles. An arterial occlusion at rest was followed by a grip exercise and another occlusion quickly after the muscle's exercise. The oxygen consumption of the muscle was calculated from the slope of the change during occlusion. The slope was significantly steeper after exercise, indicating an increased oxygen consumption. Figure reproduced from [146]

of tHb ( $tHb = HbO_2 + HHb$ ) during venous occlusion [148,149].

During muscle exercise, the haemoglobin concentrations measured from muscles vary consistently with the metabolic demand of the tissue. Muscular workload usually causes a decrease in HbO<sub>2</sub> and a simultaneous increase in HHb, which indicate the elevated oxygen demand (HbO<sub>2</sub>) and oxygen consumption (HHb) [141,150–152]. The decrease in total haemoglobin indicates the blood flow/oxygen supply occlusion due to the increased intramuscular pressure in contracting muscles [153]. Also, as showed in Figure 5.11, the tissue oxygen saturation measured at the muscle can indicate deoxygenation due to muscle exercise [141,152]. The tissue oxygen saturation index, representing the balance between oxygen supply and oxygen consumption, provides important insights into the muscle metabolism during exercise. The slope of decline in tissue oxygen saturation during contraction represents the increased oxygen demand and consumption of the muscle. The difference between the minimum value during contraction and baseline values indicates the oxygen demand in relation to the oxygen supply. At the end of the exercise, the increase of saturation, with respect to the baseline, indicates a greater oxygen supply than the actual oxygen demand by the tissue [153]. Changes in HbO<sub>2</sub> and HHb measured by NIRS during exercise were compared to lactate levels in blood, observing a good correlation between lactate accumulation in blood and the point of

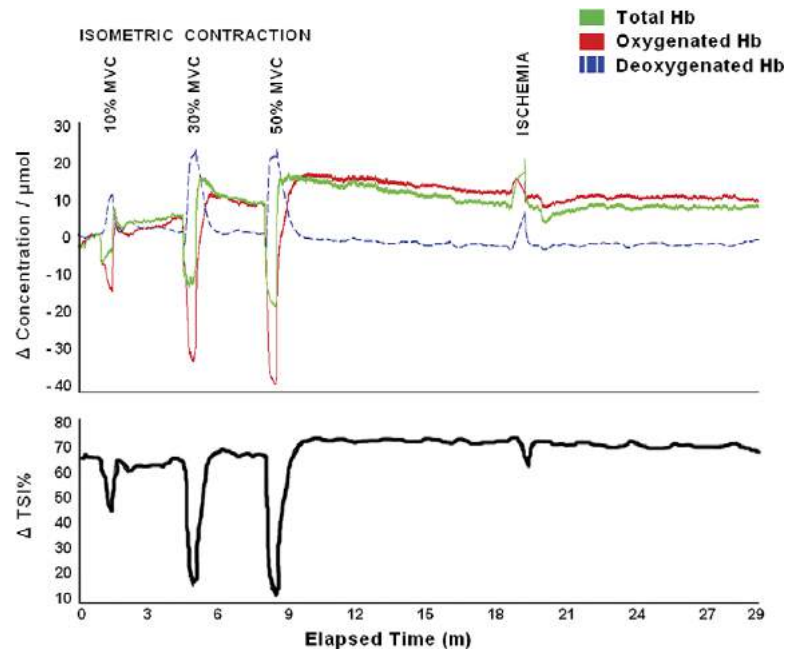


**Figure 5.11:** Changes in haemoglobin concentrations and tissue oxygen saturation during sequential, increasing muscle's contractions, and ischaemic occlusion. Measurements were performed by placing the NIRS sensors on the flexor digitorum superficialis. The workload was increased in 10 %, 30 %, and 50 % of the maximal voluntary contraction (MVC). Along with changes in haemoglobin concentrations, the changes in tissue oxygen saturation (TSI) indicates the muscle's deoxygenations. After few minutes of rest, ischaemia is produced by inflating a cuff placed on the arm (occlusion pressure of 250 mmHg). Figure reproduced from [141].

inflexion of  $\text{HbO}_2$  and HHb during exercise [154].

A fascinating advancement in monitoring muscle oxygenation/metabolism by NIRS is the multichannel approach, also known as NIRS imager. By placing different emitters and detectors over a wide area and analysing the optical attenuation at different wavelengths, it is possible to reconstruct an image of perfusion/oxygenation in muscles. The created image(s) represents the spatial and temporal changes of haemoglobin concentrations in the measured area [155]. Figure 5.12 shows an example of NIRS-muscle-imaging during contractions of the thigh muscles.

### 5.4.3 NIRS in critical care and perioperative monitoring

NIRS can be adopted to monitor perfusion and oxygenation in critical care and for perioperative assessment. Monitoring peripheral tissue oxygen saturation (TOI) in these patients may help clinicians in guiding therapy and detect hypoperfusion events that may be undetected by conventional macrocirculation parameters (e.g. blood pressure) [25, 129]. The rationale behind this approach is the possibility of monitoring early compensatory mechanisms that will change peripheral perfusion to protect cen-

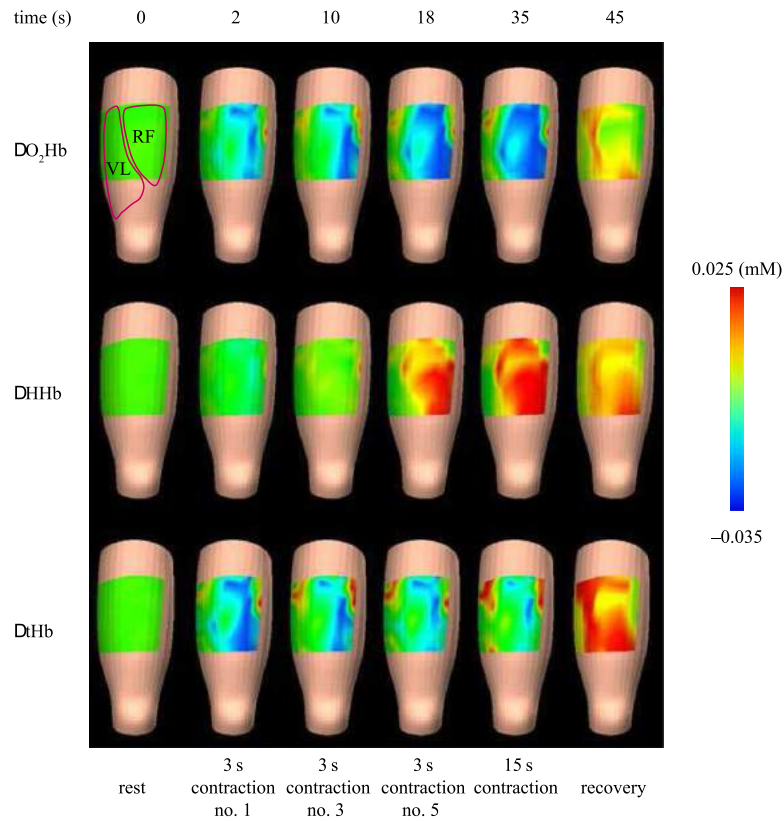


**Figure 5.12:** Example of NIRS muscle imager. The changes in concentration of oxygenated ( $DO_2Hb$ ), deoxygenated (DHHb), and total haemoglobin (DtHb) are represented in time and space. A colour-map is used to classify the amount of concentration change in the measured area. The image represent sequential contractions of the thigh muscles. Figure reproduced from [155].

tral organs such as the brain [25]. The TOI values measured at the thenar eminence demonstrated to discriminate between no-shock and severe shock patients, whereas a  $TOI > 75\%$  can be considered an indicator of survival after trauma [25].

However, the absolute values of TOI can vary between subjects, thus several efforts have been made to analyse the response of NIRS variables during a vascular occlusion test (VOT), rather than the absolute values of TOI. Girardis et al. measured the blood flow and oxygen consumption from the increase rates of total haemoglobin and deoxygenated haemoglobin respectively during venous occlusion. The NIRS parameters measured from the brachioradialis of septic patients were significantly different from the non-septic and control groups, while the absolute values of TOI were similar among all groups [156]. In a similar approach, Gomez et al. analysed the dynamics of TOI and total haemoglobin changes during a VOT in an attempt of discriminate between trauma patients and healthy subjects. Significant differences were observed between trauma patients and controls in the recovery rate of TOI and total haemoglobin at the release of an over-systolic occlusion. Again, there was no difference in TOI baseline

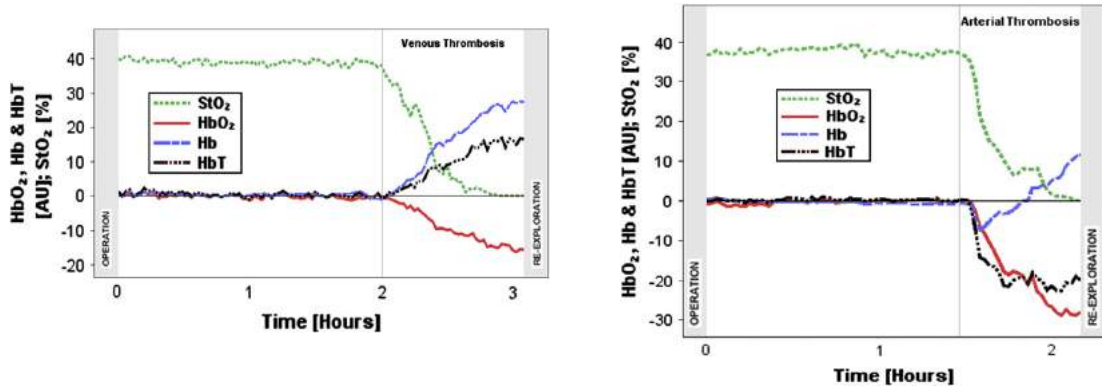


**Figure 5.13:** Changes in NIRS parameters during venous and arterial thrombosis in flaps postoperative monitoring. Left side plot: venous thrombosis. Right side plot: arterial thrombosis. During venous thrombosis, deoxygenated (Hb) and total haemoglobin (HbT) increase, while oxygenated haemoglobin (HbO<sub>2</sub>) drops along with the tissue oxygen saturation (StO<sub>2</sub>). During arterial thrombosis, similar trends take place, but with total haemoglobin dropping and StO<sub>2</sub> falling more rapidly than venous occlusion. Figure reproduced from [27].

values between the two groups [157]. In an animal model of induced shock (28 % of blood loss), Beilman et al. found that changes in TOI measured on the leg, on the stomach, and on the liver were highly correlated with traditional measures of oxygen delivery [158].

NIRS can be adopted for the perioperative flap monitoring in plastic surgery. Earlier animal studies demonstrated the ability of the technique to indicate changes in haemoglobin concentrations due to venous and arterial occlusion [26, 159]. The technique has been later investigated in human flaps for the identification of postoperative complications. NIRS was able to indicate all the occurrences of venous and arterial occlusions, with the ability to differentiate between venous or arterial occlusion (see Figure 5.13) [27].

#### 5.4.4 Functional Near Infrared Spectroscopy (fNIRS)

The NIRS technique can also be applied for the analysis of haemoglobin concentration changes as an indication of brain activation. The haemoglobin changes are usually defined as Blood Oxygenation Level Dependent (BOLD) and the technique is known as Functional NIRS (fNIRS). In cerebral fNIRS, the changes in haemoglobin concentrations yield information on the activation of regions in the brain [160]. In single-point cerebral fNIRS, the sensors are attached on the forehead and the changes in haemoglobin concentrations indicate the activation of frontal areas in the brain. In order to distinguish the responses, a stimulus such as a mental task, problem-solving,

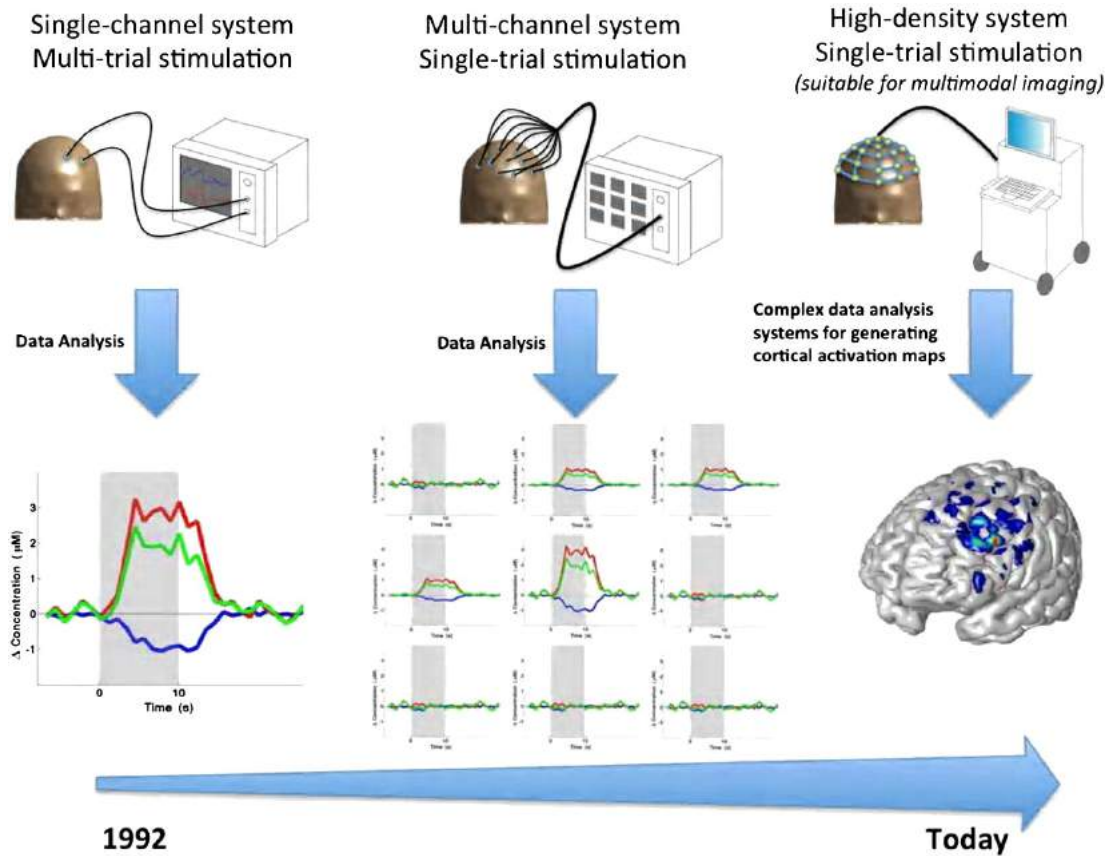


**Figure 5.14:** Different types of functional NIRS (fNIRS) measurements and their timeline. The first fNIRS instruments (left side) were measuring cerebral activation from the haemoglobin changes acquired from single pairs of light emitters and detectors. The second typology (middle) measured activations at different locations simultaneously. In these instruments, the changes in haemoglobin concentrations were observed upon application of a stimulus (grey areas in the plots at the bottom). Nowadays (right side), by using multiple combinations of different pairs of emitters and detectors, a colour map of the activated areas can be obtained by sophisticated signal processing techniques. Figure reproduced from [160].

visual/auditory triggers, or others are applied on the investigated subject. Functional activation is then assessed from the response of  $\text{HbO}_2$  and  $\text{HHb}$  following the stimuli. The technique was studied to assess the differences in neurological or psychiatric disorders such as Alzheimer's disease, schizophrenia, or epileptic patients, and comparison between fMRI and fNIRS showed good correlation in the haemodynamic changes related to functional activation [160]. Also, if multiple pairs of light emitters and detectors are used, a spatial distribution (i.e. mapping) of the activation areas can be obtained [160]. In this approach, head-caps with optodes placed in a configuration similar to EEG are worn by the subject and light attenuations from multiple pairs are processed to obtain a colour map of the haemodynamic changes. Figure 5.14 depicts a schematic representation of the different fNIRS modalities.

## 5.5 Limitations and open challenges of NIRS

Even though NIRS has found many applications, the technique still suffers from some limitations. For this, several open challenges still exist and it is hoped that future developments in technology and computation techniques would contribute overcoming these drawbacks. Some of the main limitations and open challenges of NIRS are listed below.

- *Relative haemoglobin concentrations.* Continuous wave NIRS instruments are able to provide only relative haemoglobin concentrations from an arbitrary time point, usually baseline [11,161,162]. These can still be used for intervention studies, but only Time Resolved and Phase Modulated instruments are capable of determining absolute haemoglobin concentrations.
- *DPF wavelength-dependence.* In order to fully quantify the relative changes in haemoglobin concentrations by CW NIRS, the DPF needs to be used, with the assumption that scattering is constant during the measurement. Usually, a single DPF value is used, based on the type of tissue from which the measurements are acquired (e.g. forearm or head). It is assumed that this value is equal at the different wavelengths at which the modified Beer-Lambert law is used to infer haemoglobin concentrations. However, the DPF, being related to scattering, is wavelength-dependent [119]. This approach used in CW NIRS could introduce some errors, which could only be eliminated if the DPF at each specific wavelength used is calculated.
- *Other chromophores.* NIRS assumes that the only light absorbers (chromophores) within the light path are oxygenated and deoxygenated haemoglobin. This assumption can hold under certain conditions in which only blood changes are considered [11, 22, 25]. Cytochrome oxidase can be neglected due to the low contribution in the overall light absorption, while the effect of other haemoglobin derivatives such as carboxyhaemoglobin is usually ignored. In muscle NIRS, Myoglobin cannot be distinguished from haemoglobin due to the overlapping of the substances' spectra and the contribution of myoglobin to the signal is still under debate [13,25,129]. In order to take this into consideration, muscle-NIRS studies often report their results as mixed haemoglobin-myoglobin changes.

- *Extra cerebral/muscle tissue contributions.* The contribution of extracerebral/muscle tissues such as skin and adipose tissue has been under debate for several years [13, 22, 161]. When light is emitted and detected transcutaneously, it crosses several layers of tissues before entering the cerebral cortex or muscles. This can cause NIRS measurements to be affected by skin blood flow or volume changes [162]. A multi-distance approach, in which the signal passing through only superficial layers is subtracted from the total light beam traversing the entire tissue, could solve the problem [161]. However, this method is not always used and, single-distance CW, TRS and PMS instruments collect light that passes through other layers of tissue. The indexes estimated by Spatially Resolved Spectroscopy seem to provide isolation from superficial layers of tissues [125].
- *Tissues heterogeneities.* NIRS assumes that the portion of tissue interrogated by the light beam is homogeneous [161]. In presence of oedemas or focal changes in haemoglobin concentrations, this assumption may not hold [22, 163].
- *Standardization.* The continuous development of commercial and research NIRS instruments in the last decades has created a lack of standardisation in the field. Currently, available NIRS devices differ in peak emission wavelengths, the number of wavelengths, the emitter-detector separation distances, the algorithms, the measured areas, etc. Therefore, the comparison between different studies or instruments is rather difficult [161, 162]. For instance, *in vivo* and *in vitro* comparison between different NIRS commercial monitors revealed differences in the absolute values of tissue oxygen saturation between the devices [164, 165]. Also, if the comparison within NIRS instruments is difficult, the NIRS technique cannot be fully validated *in vivo* with a gold-standard measure of perfusion or oxygenation [166]. In this regard, more *in vitro* studies like Hyttel-Sorensen et al. and Suzuki et al. are still needed to validate the haemoglobin concentrations measured by NIRS instruments with gold-standard measures of haemoglobin concentrations [124, 166]. Although the lack of standardisation and discrepancies in absolute values, NIRS devices have demonstrated to be valuable tools for trend monitoring.
- *Absolute values of tissue oxygen saturation.* Baseline absolute values of tissue oxygen saturation suffer from inter-subjects variability, due to different tissues' com-

position and arterial-venous partitioning between subjects [22, 167, 168]. Therefore, it has been suggested of using TOI as a trend indicator and cautiously use its absolute values.

- *Movement artefacts.* As any other optical technique, NIRS suffers from movement artefacts [161, 162] and subject's movements should be minimised during the measurements. Although being susceptible to movement artefacts, the technique can still be used for assessing oxygen metabolism in contracting muscles. By using the multi-distance approach, movement artefacts could be minimised [161]. NIRS sensors need a good attachment on the skin, but sensors may detach from the skin, with possible light interferences and consequent inaccuracies [161, 162, 167].
- *Bulkiness.* One of the main strengths of NIRS is the ability to penetrate in deep tissues such as brain and muscle. This, however, can be only be achieved by a large separation distance between light emitter and detector. A separation distance  $> 2.5$  cm is suggested for NIRS measurements [23]. Therefore, NIRS sensors can have bulky dimensions and usually require an adequately large measurement area on the skin. While this can be acceptable on large muscles or other tissue surfaces, some measurement locations such as flaps may not satisfy the spatial requirements for NIRS sensors.

TRS and PMS devices require large instrumentation for their functioning, making their transportation and portability rather difficult [161]. For this reason, these instruments are often used in research rather than at the patient's bedside. Hopefully, the technological developments in the future may allow the miniaturisation of these instruments, with the possibility of exploiting their potential in clinical settings [161].

- *Costs.* Finally, another important limitation of the technique is its elevated costs, particularly when compared to other technologies such as photoplethysmography, pulse oximetry, or laser Doppler flowmetry [25, 36, 44]. The costs of NIRS, added to the other drawbacks listed above, limits their wide adoption in a clinical environment.

## 5.6 Summary

This chapter presented an overview of Near Infrared Spectroscopy. The principles of the technique, the different NIRS instruments, and the main applications of NIRS have been presented. The modified Beer-Lambert law for the determination of haemoglobin concentration changes in NIRS was introduced and discussed. This will be introduced again in Chapter 8, where its application to PPG signals will be described. The method was then investigated in a series of studies described in Chapter 9, Chapter 10, and Chapter 11, in which photoplethysmographic signals were acquired from different body locations. The next chapter will describe the design and development of reflectance photoplethysmographic sensors that were used in the investigations.

## Design and Development of a Reflectance Photoplethysmography Sensor

This thesis explores the capability of photoplethysmography in providing information about perfusion and oxygenation other than the conventional PPG signals and the arterial oxygen saturation ( $SpO_2$ ). In order to investigate this, reflectance PPG signals were acquired from the forearm, finger, and forehead of healthy volunteers in different physiological conditions and NIRS principles were applied to the signals. This chapter describes the design, development, and manufacturing of custom-made reflectance PPG sensors for the acquisition of PPG signals from those locations. The evaluation of these sensors is also presented. Later, in Chapter 7, the research PPG processing system used to drive these sensors will be presented as well.

### 6.1 Optical components

Optical modalities such as PPG, NIRS or laser Doppler flowmetry use light emitters to shine light into living tissue and acquire the backscattered light by means of a photodetector(s). The quantity, typology, and placement of light emitters and photo-detector depend on the specific technique, or may vary depending on the anatomical location where the sensor will be placed on. The PPG sensors that were developed were dual-wavelength PPG sensors, comprising of red and infrared LEDs for light emission and a single photodiode to detect the backscattered light. Figure 6.1 shows a simplified block

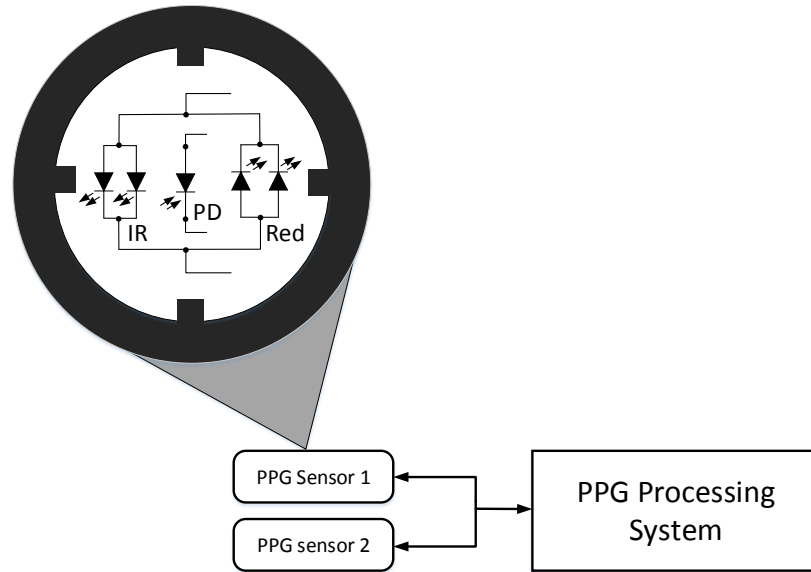


**Figure 6.1:** Diagram showing the PPG sensor and the PPG processing system. The processing system drives the sensors and processes the signals from the detected. Within the sensors, two red and two infrared (IR) LEDs emits light, while a photodiode (PD) detects the backscattered light from the tissue.

diagram of the PPG system used in this thesis. The system is composed of reflectance PPG sensor(s) and a processing system. The PPG processing system drives the LEDs and acquires the light intensities from the photodiode. The sensor comprises of two red LEDs, two infrared LEDs, and a single photodiode. In this section, the properties of the chosen LEDs and photodiode are presented, while the following sections will describe the electrical and mechanical development of the PPG sensors.

### 6.1.1 Light Emitting Diodes

The red wavelength light sources selected for the RPS1 PPG sensor were two chip surface mounting LEDs (KP-2012SRC-PRV, Kingbright, Taiwan). The low-power consumption red LEDs measured  $2.0 \text{ mm} \times 1.25 \text{ mm} \times 1.1 \text{ mm}$  ( $L \times W \times H$ ).

The two infrared emitters were two chip surface mounting LEDs as well (KP-2012 SF4C, Kingbright, Taiwan), with dimensions of  $2.0 \text{ mm} \times 1.25 \text{ mm} \times 1.1 \text{ mm}$  ( $L \times W \times H$ ). Figure 6.2 shows the mechanical drawings of the red and infrared LEDs, while the electrical and optical characteristics are summarized in Table 6.1 for the red LED and Table 6.2 for the infrared LED.

The selection of the two light sources at different emission wavelengths presents two

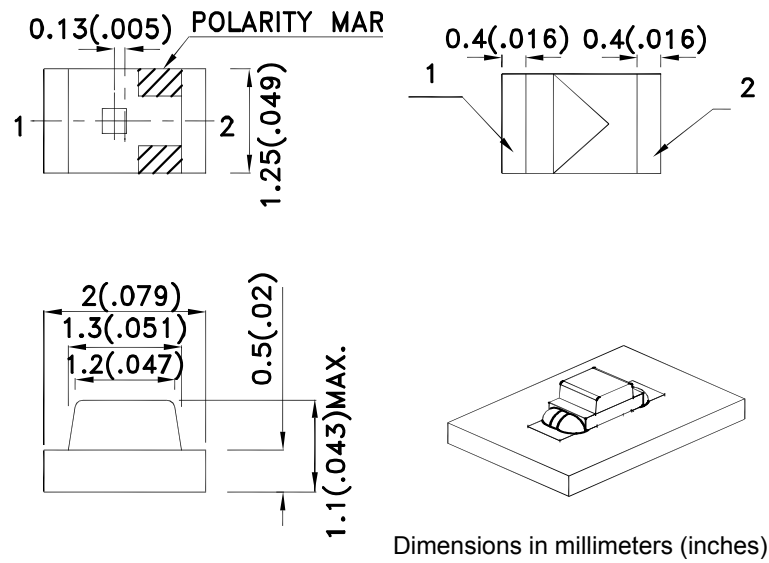


**Figure 6.2:** Mechanical drawings of the red and infrared LEDs of the RPS1 PPG sensor

**Table 6.1:** Optical and electrical characteristics of the red wavelength LED (KP-2012SRC-PRV) at 25 °C

Optical/Electrical characteristics at 25 °C	
Parameter	Value
Forward Voltage ( $I_F=20$ mA)	1.85 (2.5 max.) V
Reverse current ( $V_R=5$ V)	10 $\mu$ A
Capacitance	45 pF
Peak spectral wavelength ( $I_F=20$ mA)	660 nm
Spectral Bandwidth ( $\Delta \lambda_{1/2}$ ) ( $I_F=20$ mA)	20 nm
Power dissipation	75 mW
Peak forward current	155 mA
Reverse voltage ( $V_R$ )	5 V
Operating temperature	-40 to +85 °C

**Table 6.2:** Optical and electrical characteristics of the infrared wavelength LED (KP-2012 SF4CV) at 25 °C

Optical/Electrical characteristics at 25 °C	
Parameter	Value
Forward Voltage ( $I_F=20$ mA)	1.3 (1.6 max.) V
Reverse current ( $V_R=5$ V)	10 $\mu$ A
Capacitance	90 pF
Peak spectral wavelength ( $I_F=20$ mA)	880 nm
Spectral Bandwidth ( $\Delta \lambda_{1/2}$ ) ( $I_F=20$ mA)	50 nm
Power dissipation	80 mW
Peak forward current	1.2 A
Reverse voltage ( $V_R$ )	5 V
Operating temperature	-40 to +85 °C

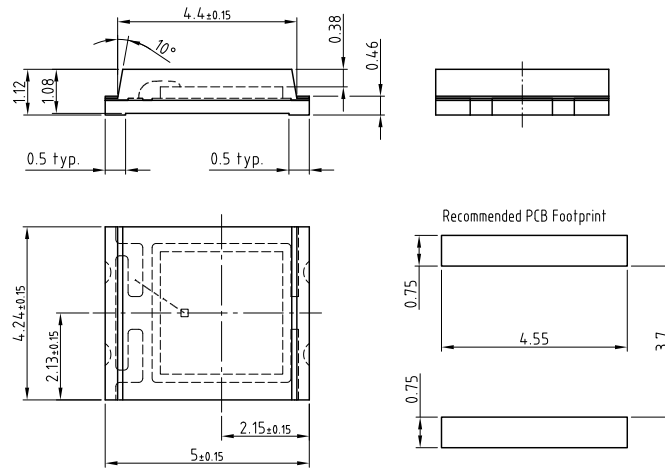


**Figure 6.3:** Mechanical drawings of the TEMD5010X01 photodiode employed in the PPG sensor RPS1

main advantages. In the first place, these two wavelengths (red and infrared) were chosen as these are commonly used in pulse oximetry to estimate arterial oxygen saturation ( $\text{SpO}_2$ ). Thus, if two photoplethysmography signals at red and infrared are acquired from a tissue, the  $\text{SpO}_2$  can be estimated as described in subsection 4.5.1. Secondly, the acquisition of PPG signals (or more generally, any optical signals) at two wavelengths permits also the application of the Beer-Lambert law to estimate the concentration changes of two light absorbers such as oxygenated and reduced haemoglobin. As showed previously in Chapter 5, these two chromophores absorb light differently and measuring absorption at two different light wavelengths permits to calculate their relative or absolute concentrations.

### 6.1.2 Photodiode

The photodiode adopted in the PPG sensor RPS1 was a surface mount PIN photodiode (TEMD5010X01, Vishay Intertechnology Inc. USA). The TEMD5010X01 is a high speed and high sensitive photodiode with dimensions of 5 mm  $\times$  4.24 mm  $\times$  1.12 mm (L $\times$ W  $\times$ H). The photodiode can detect visible and near infrared light and its large active area (i.e. 7.5 mm<sup>2</sup>) makes it suitable for low-intensity light applications such as PPG signal detection. Figure 6.3 shows the mechanical drawing of the TEMD5010X01, whereas Table 6.3 summarizes its optical and electrical characteristics.

**Table 6.3:** Optical and electrical characteristics of the photodiode (TEMD5010X01) at 25 °C

Optical/Electrical characteristics at 25 °C	
Parameter	Value
Forward Voltage ( $I_F=50$ mA)	1 (1.3 max.) V
Breakdown Voltage ( $I_R=100$ $\mu$ A)	60 V
Reverse Dark Current ( $V_R=10$ V)	2 (30 max.) nA
Diode Capacitance ( $V_R=0$ V)	70 pF
Reverse light current ( $V_R=5$ V, $\lambda=950$ nm)	45(55) $\mu$ A
Angle of half sensitivity	$\pm 65$ deg
Range of spectral bandwidth	430-1100 nm
Rise time ( $V_R=10$ V, $\lambda=920$ nm)	100 ns
Fall time ( $V_R=10$ V, $\lambda=920$ nm)	100 ns
Operating temperature range	-40 to +100 °C

## 6.2 Electrical design of the Reflectance PPG probe (RPS1)

Figure 6.1 shows the diagram of the reflectance PPG sensor (RPS1) and its driving/processing system. The main components of the sensor are the light sources (LEDs) and photodetector (photodiode), while the processing system is responsible for supplying the driving currents for the LEDs and for processing the signal generated by the photodiode. The PPG sensors used in this work were designed and manufactured to conform to the PPG processing system described in Chapter 7. This section describes the electrical design of the reflectance PPG sensor.

### 6.2.1 Printed Circuit Board design

In order to provide mechanical support and electrical connections for the LEDs and photodiode presented in Section 6.1, Printed Circuit Board (PCB) technology was adopted. PCBs are copper-based sheets on which pads and tracks can be designed in order to allocate and connect electronic components. In order to use a PCB for the optical components described in Section 6.1, the PCB was designed in Altium Designer (Altium Ltd, Australia). Altium Designer is a PCB-design software, which allows the full customization of PCBs's tracks and pads.

The PCB had a circular shape, with a diameter  $d = 20$  mm, in order to facilitate contact with such anatomical regions such as the forearm and forehead. Different shapes (e.g. rectangular or square) or a larger diameter could have caused a rather difficult attachment to the skin, particularly on curved surfaces. The PCB for the sensor was designed

in order to allocate the required optical components and connections to the PPG processing system. Figure 6.4a shows the PCB footprint for the RPS1 sensor. The pads were designed for the placement of the LEDs and photodiode presented in Section 6.1, as suggested by the manufacturers. The PPG signal amplitude in reflectance mode is a trade-off between separation distance and LEDs driving current. Larger separation distances allow the acquisition of larger signals with smaller signal variations, but, in order to maintain a good signal at these separation distances, light intensity must be increased (i.e. large separation distances cause a large decrease in signal amplitudes) [71]. Mendelson and Ochs demonstrated that to maintain a constant reflection during the increase of the separation distance, LEDs driving currents had to be increased up to 200 mA [71]. These large driving currents are not suggested since they can overheat the tissue or damage the LEDs. From the study performed by Mendelson and Ochs, a separation distance comprised between 4-6 mm should guarantee an acceptable signal quality, without exceeding 50 mA LEDs driving currents [71]. Therefore, the photodiode was positioned at the centre of the PCB, while the LEDs were placed at a centre-to-centre distance of 5 mm from the photodiode. The electrical connections between the pads were designed in order to configure the red and infrared LEDs in parallel with the anode of the red LED connected to the cathode of the infrared LED, as illustrated in Figure 6.1. As explained later in Chapter 7, this configuration permits the intermittent switching of the red/infrared LEDs when connected to the PPG processing unit. Through-holes pads were also added on the PCB to provide the connection for wires connecting the sensor and the processing system. Prior manufacturing, a visual assessment of the PCB and optical components' 3D model footprint was also performed in order to test the geometrical positions of the components (Figure 6.4b).

### 6.2.2 Printed Circuit Board manufacturing

After designing the PCB on the software platform, CAM files were generated in order to manufacture the PCB by CNC routing technology. CAM files are a set of software-generated manufacturing instructions, which consent to manufacture an object from a design file. The PCB was manufactured from a single-layer copper-laminated sheet by means of an advanced board plotter (Protomat S103, LPKF Laser & Electronics AG, Germany). The single-layer PCB was deemed sufficient for the manufacturing of a PPG sensor. Once the tracks, pads and through holes were created by the CNC

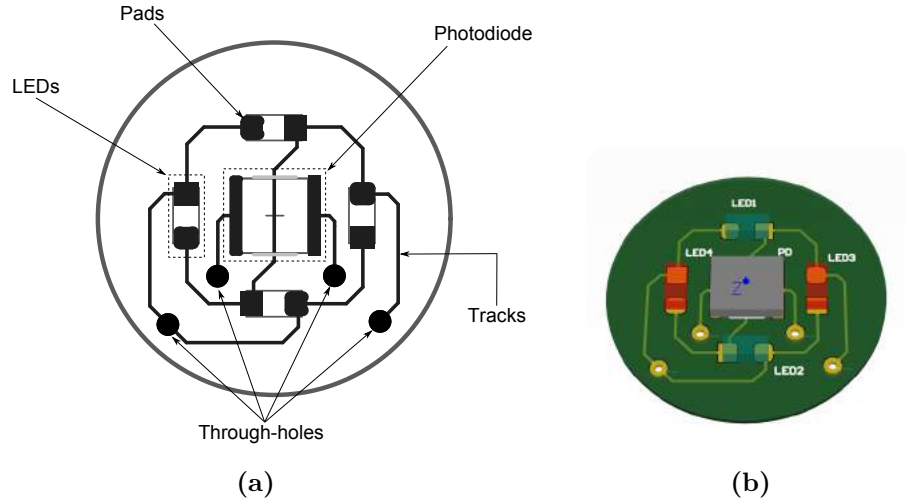


**Figure 6.4:** Reflectance PPG sensor (RPS1) PCB footprint (a) and PCB's 3D model (b). In the PCB footprint in (a), the pads are dedicated to the placement of the optical components, whereas the tracks and the through holes provide the connection between the components and the processing unit. The 3D model of the PCB in (b) was used to visually assess the components mounted on the PCB.

machine, the PCB was tin plated in order to protect the copper from oxidation. The tin plating process was carried out by immersing the manufactured PCBs in a tinning solution for at least 10 minutes.

The optical components were then soldered on the PCB. Small amounts of solder paste (SN62RA10BAS86-25G, Multicore, Henkel Techn. USA) were distributed on top of the pads. The LEDs and photodiode were then placed on top of the pads, taking care of the correct positioning of anodes/cathodes. Once the optical components were in place on the PCB, the board was inserted in the re-flow air oven (FT02, C.I.F, France) in order for the surface mount components to be soldered on the pads.

Once the optical components were soldered on the PCB and all electrical connections checked, a four-core screened cable was then used to provide connections from the sensor's PCB to the PPG processing system. More specifically, the wires provide the driving currents for the LEDs and transmit the detected signal from the photodiode to the processing circuit. On one end of the cable, each core was soldered on the PCB, while on the other end each core was soldered on the corresponding pin of a male D-Sub 9 connector, providing the link with the PPG processing unit (see Section 7.6).

Once the PCB, the optical components, and the wires were soldered, continuity and LEDs/photodiode functionality were verified before proceeding to the assembly of the mechanical structure.

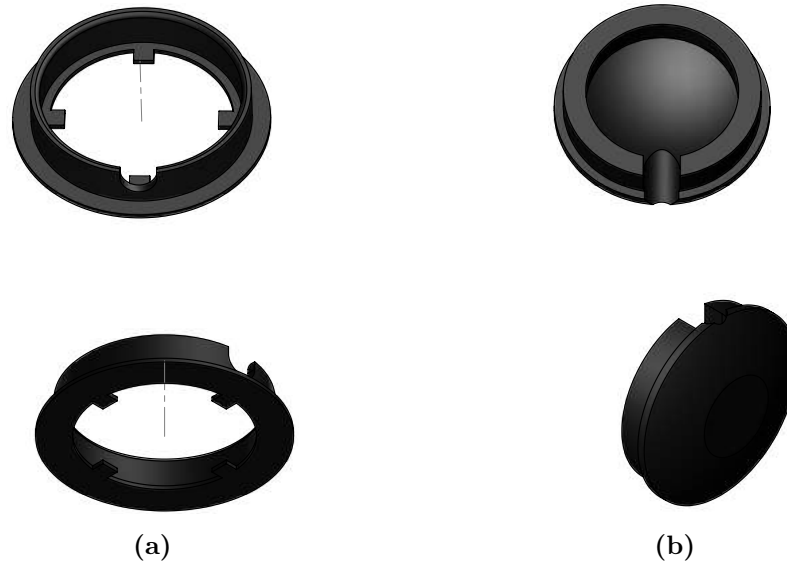


**Figure 6.5:** 3D model views of the RPS1 PPG sensor's case (a) and cover (b).

## 6.3 Mechanical structure

The soldering of the optical components on the PCB and provision of connection to the processing unit is not sufficient for the manufacture of a safe PPG sensor. Since the sensor needs to be applied on the skin, optical components and PCB required to be isolated and protected in order to avoid any shunting. In addition, without proper cover, ambient light may reach the photodiode, with the possibility of generating unwanted bias and interference [8]. This section describes the development of the sensor's mechanical structure, which was designed in order to cover the optical components, protect them from ambient light, and facilitate the attachment of the sensor on the skin.

### 6.3.1 Mechanical structure design

The mechanical structure of the RPS1 sensor was designed in a 3D CAD design software (Solidworks 2013, Dassault Systèmes SOLIDWORKS Corp., USA). The mechanical structure was composed of a case and a cover. The two parts were ring-shaped and they were designed separately in order to enclose the PCB. Figure 6.5 shows the views of the 3D models of the case and the cover of the RPS1 PPG sensor.

Once the case and cover were designed separately, the fit was assessed by generating a

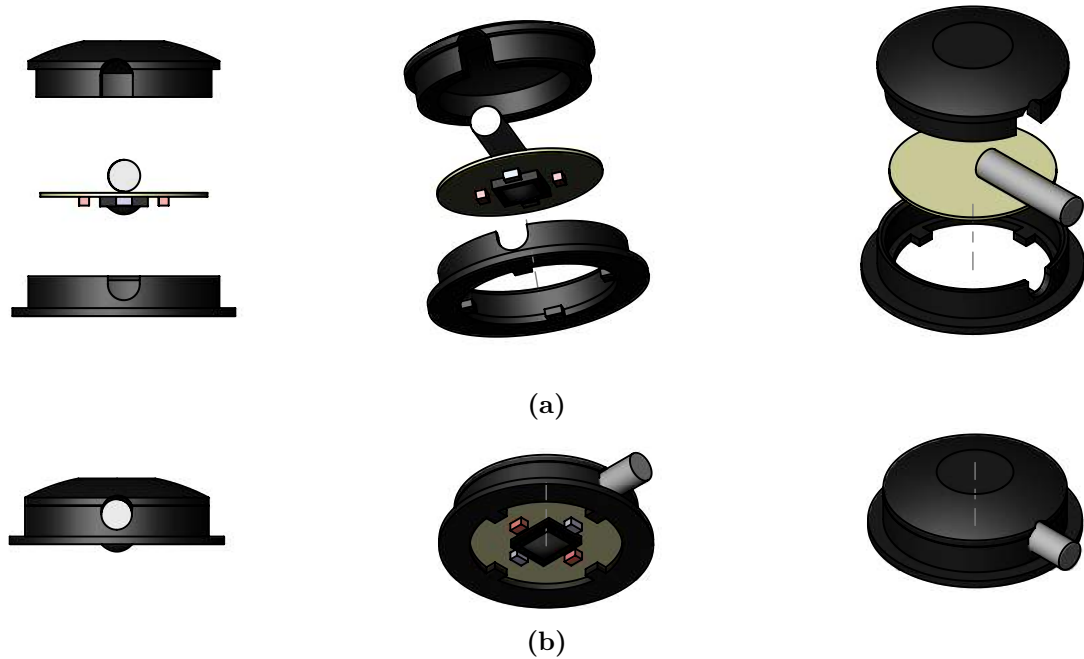


**Figure 6.6:** Exploded views (a) and assembly views (b) of the RPS1 PPG sensor's 3D model. The exploded view shows the 3D model composed of the sensor's case, sensor's cover, and the PCB with the optical components and the cable. The assembly view provides a model of the final assembled sensor.

3D model assembly. The model was composed of the sensor's case, sensor's cover, and a 3D model of the PCB comprising optical components and cable. The assembly allowed verifying the dimensions of all components (i.e. case, cover and PCB) by fitting the 3D models in the assembly without the necessity of pre-manufacture the components. Figure 6.6 shows the views of the 3D model assembly composed by case, cover and PCB.

As mentioned earlier the mechanical structure of the PPG sensor was designed in two parts (cover and case) in order to enclose the PCB. Figure 6.7 shows the drawing of the mechanical structure of the RPS1 PPG sensor. The drawing comprises of PCB, optical components, case, and cover. The case had an internal diameter of 22 mm in order to allow the insertion of the PCB ( $d = 20$  mm). The case's wall had a thickness of 1 mm, adding to an overall external diameter of 24 mm. At the bottom of the case, a ring with an external diameter of 28 mm had the function of keeping in place the PCB by the aid of four hooking plates. In addition, the bottom ring provides a wider flat surface for the attachment of the sensor on the skin.

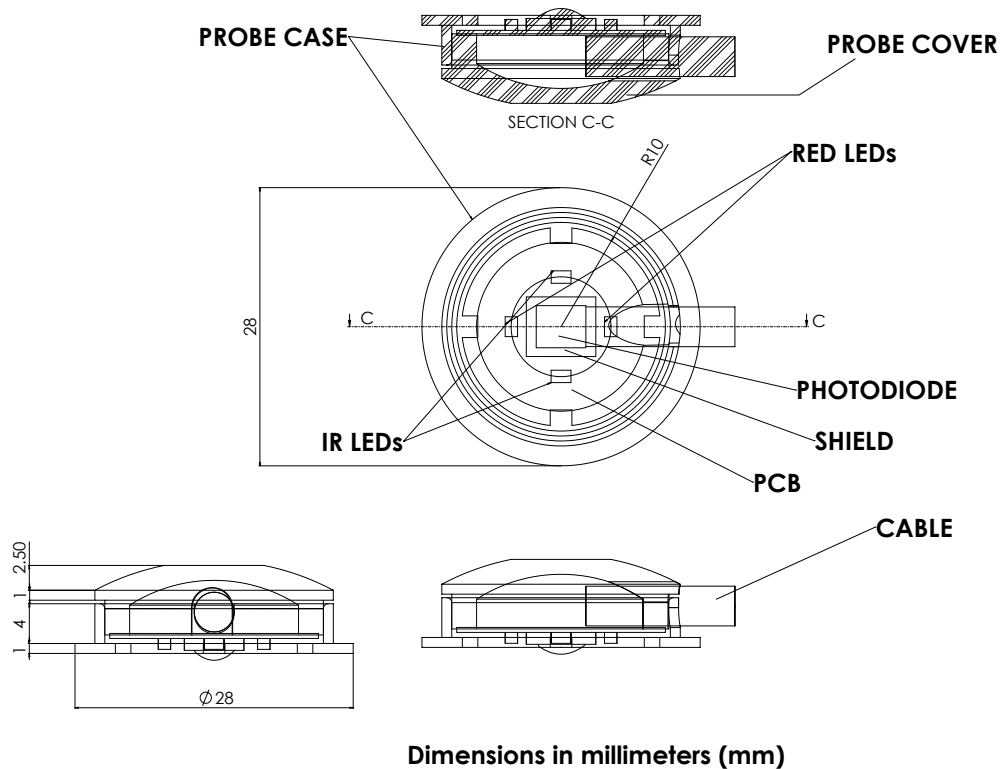


**Figure 6.7:** Drawing of the mechanical structure of the PPG sensor RPS1. The drawing comprises of case, cover, PCB and optical components.

### 6.3.2 Mechanical structure manufacturing

After designing the mechanical structure of the RPS1 sensor comprising case and cover, these were manufactured by 3D printing technology. 3D printers create objects by Fuse Filament Fabrication, in which solid filaments are fused and deposited on a heated surface. The machines deposit material layer-by-layer until the object is completed. In order to manufacture an object, the printer receives a set of instructions containing the geometrical information of the model. This method of fabrication has been attracting interest due to the possibility of in-house manufacturing of customised 3D models and objects [169]. The technique has also promising applications in bioengineering and medicine for the manufacture of custom prosthetic devices and, perhaps, even organs [169]. The 3D models of the sensor's case and cover previously designed in Solidworks were converted into a set of instructions (G-Code files) for the 3D printer. The case and cover were manufactured by a 3D printer (Replicator 2X, Makerbot Industries LLC, USA) in black Polylactic acid (PLA). While the biodegradability of this material guarantees a safe application on the skin, the black colour provides cover from ambient light.

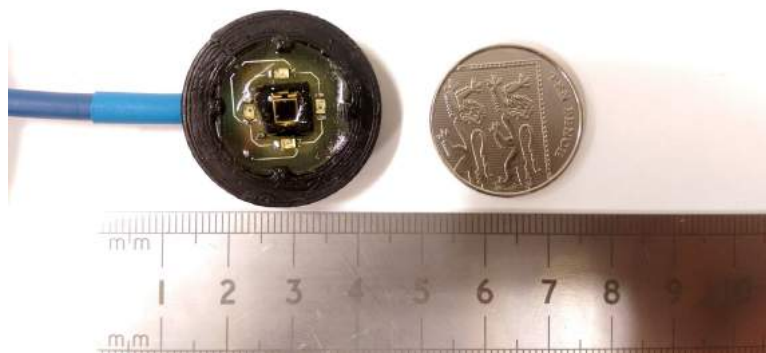


**Figure 6.8:** Final manufactured RPS1 PPG sensor.

Once the case and cover were manufactured, the PCB, comprising of previously soldered optical components and cable, was inserted within the case. When the PCB was in place, a small amount of glue was applied on the contours of the PCB and the case. Before the glue was set, the cover was inserted on top as showed in Figure 6.6b. The application of the glue was performed in order to seal eventual gaps between PCB and case's walls and to keep in place the cover on the case.

After the glue was set, the optical components were covered by applying a layer of clear medical epoxy (Dymax 141-M, Dymax Corp., USA). Prior to application of the epoxy, the photodiode was shielded by placing a black rubber around its contour. The shield was placed in order to avoid optical shunting from the LEDs to the photodiode (i.e. light reaching the photodiode without passing through the tissue) [8].

## 6.4 Evaluation of the Reflectance PPG sensor

### 6.4.1 Photoplethysmographic signals

The RPS1 PPG sensor was evaluated post-manufacturing by acquiring PPG signals from the forehead. The sensor was connected to the PPG processing unit (see Chapter 7) through the D-Sub 9 connector and it was attached on the forehead by means of a double-sided clear medical adhesive tape. The tape was cut in the central part to not cover the optical components. The sensor was attached on the forehead, above the eyebrow, as suggested in the literature [110]. The volunteer sat on a chair and

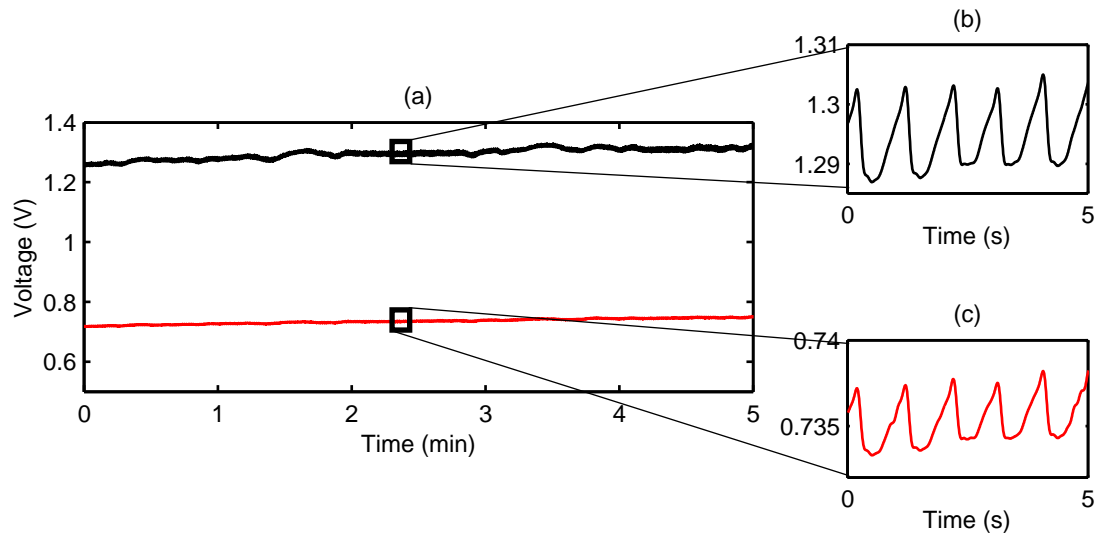


**Figure 6.9:** Red and infrared raw PPG traces acquired from the RPS1 sensor. (a) Five minutes measurement of red and infrared raw PPG (AC + DC). Red trace: red PPG; black trace: infrared PPG. The pulsatile components are riding on a DC offset (DC PPG). (b) Five-second zoom of the infrared pulsatile component. (c) Five-second zoom of the red pulsatile component. Signals were low-pass filtered at 7 Hz to remove high-frequency noise. The PPG traces in (b) and (c) are the raw pulsatile components detected by the photodiode, without being reversed as usually done in PPG analysis.

the measurements lasted for five minutes at rest and in normal breathing. The signals were acquired on LabVIEW (National Instruments, USA) at a sampling frequency of 1 kHz and they were later analysed on Matlab2013a (The MathWorks Inc., USA). The acquired raw PPG signals (AC + DC) were filtered from high-frequency noise by a low-pass filter with a cut-off frequency  $f_c = 7$  Hz.

Figure 6.9 shows PPG signals acquired from the RPS1 sensor. Good quality red and infrared raw PPG signals (AC+DC) were acquired from the sensor. The DC component can be noticed from the offsets of the signals. Low-frequency oscillations can also be observed on the DC component. The time scale zoom reveals a good quality AC PPG component riding over the DC offset. Thus, the designed and manufactured sensor successfully demonstrated the capability of measuring satisfactory PPG signals.

### 6.4.2 Temperature tests

In order to confirm that there will be no thermal injury to the tissue by the sensor when the LEDs are switched ON, temperature measurements were carried to verify that the sensor did not reach excessive temperatures.

Two sets of measurements were performed. In the first bench measurement, the tem-

perature was acquired from the sensor when this was not attached to the skin. In the second measurement, the temperature of the skin underneath the sensor was measured while simulating the normal measurement conditions. The purpose of two separate experiments was to investigate the increase in temperature first and, in second place, how this could affect the skin temperature.

The temperature was measured by a K-Type thermocouple (SA1-K, Omega Engineering Inc., USA) connected to a monolithic thermocouple amplifier (AD595AQ, Analog Devices Inc., USA). The AD595AQ is a thermocouple amplifier with ice point reference and pre-calibrated amplifier capable of producing a 10 mV/°C output directly from a thermocouple. Another amplifier was set-up as suggested by the manufacturer for the measure of ambient temperature. The two chips measuring the thermocouple's temperature ( $T_{TH}$ ) and ambient temperature ( $T_{AMB}$ ) were mounted on a breadboard and the connections were set as suggested by the manufacturer. The power supply of  $V_s = 5$  V was provided by a bench voltage power supply. The outputs of the thermocouple amplifiers were connected to a National Instruments data acquisition in order to be acquired on LabVIEW.

In the first measurement, the thermocouple was attached to the surface of the RPS1 sensor and covered with insulating tape in order to minimise any influence from fluctuations in room temperature. After five minutes of baseline measurements, the sensor LEDs were switched ON and they were driven at 60 mA for 30 minutes. Figure 6.10 shows the ambient and the thermocouple temperature traces during the first bench experiment. During baseline, the mean reference ambient temperature was 24.5 °C, while the temperature from the thermocouple attached to the sensor was 24.8 °C. After ten minutes with the LEDs ON, the thermocouple-measured temperature reached a steady state of 30.0 °C, while the ambient temperature remained constant throughout the entire measurement.

The second set of temperature measurements aimed at assessing the skin temperature during the utilisation of the RPS1 sensor on the skin. The RPS1 sensor was attached to the forehead by double-sided medical adhesive tape. The adhesive was previously cut in the centre, at the position of the optical components. The thermocouple was placed on the sensor's surface and it laid between the skin and the sensor. The thermocouple was positioned at the centre of the sensor's footprint. Again, the measurement started

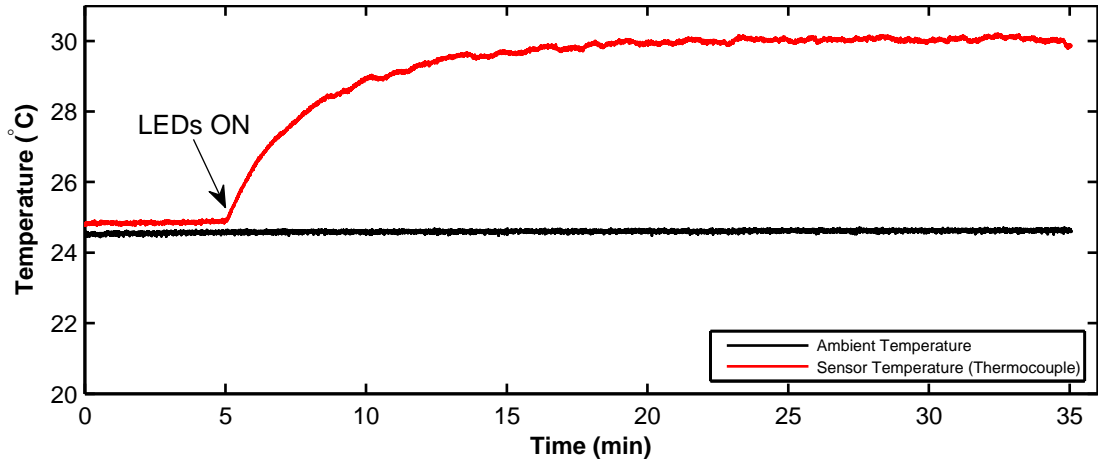


**Figure 6.10:** First temperature test on the RPS1 sensor's surface. The thermocouple was attached on the sensor's surface and kept in place by insulating tape. After five minutes of measurement with LEDs OFF, the light sources were switched ON and they were driven at 60 mA for thirty minutes.

with a five-minute baseline measurement followed by thirty minutes with the LEDs ON at 60 mA driving current. An independent skin temperature reading ( $T_{LDF}$ ) was provided by a laser Doppler flowmetry device (MoorVMS-LDF2, Moor Instruments, UK). The laser Doppler sensor was also attached on the forehead by a ring-shaped double-sided adhesive. Figure 6.11 shows the result of the second measurement. During baseline,  $T_{LDF}$  and  $T_{TH}$  were 30.9 °C and 32.7 °C respectively. When the LEDs were switched ON,  $T_{TH}$  gradually increased to 34.3 °C and reached a steady state after roughly ten minutes. The results from both temperature experiments indicated that the RPS1 sensor did not produce excessive or dangerous heating. The higher  $T_{TH}$  during baseline is most probably a temperature offset due to the pressure exerted on the thermocouple between skin and the sensor's surface. In addition, the LEDs were driven at the maximum current that the processing system could provide, which is still far higher the normal usage of 20-30 mA. Therefore, it can be concluded that the sensor did not pose any thermal risk to the skin.

## 6.5 RPS1-2 and RPS3 sensors development

The design and manufacturing methods presented in this chapter offer the flexibility of full customization of PPG sensors. Therefore, other PPG sensors were designed and manufactured with the same methods used for the RPS1 sensor. The design of an optical sensor may vary depending on its application, which may require a deeper light penetration into tissue or the miniaturisation for the attachment to a small measure-

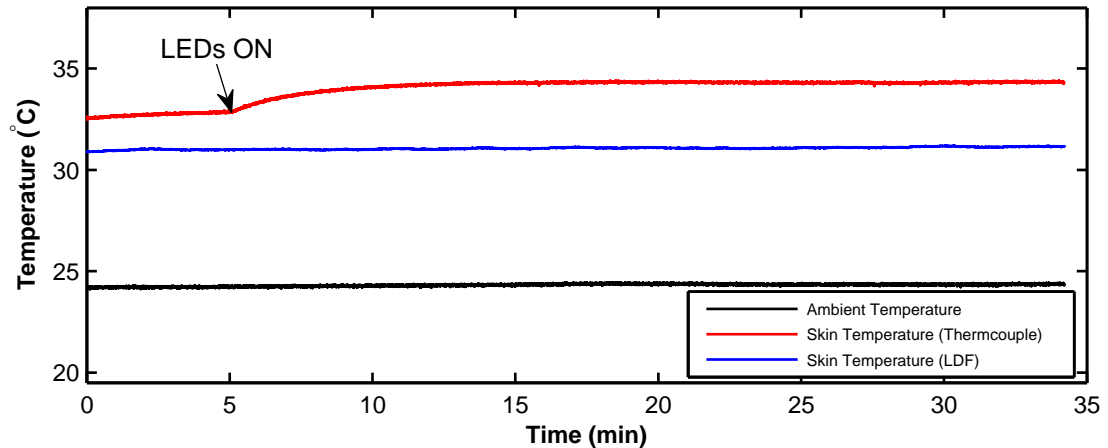


**Figure 6.11:** Second temperature test on the RPS1 sensor’s surface. The thermocouple was attached between the sensor’s surface and the skin. After five minutes of measurement with LEDs OFF, the light sources were switched ON and they were driven at 60 mA for thirty minutes.

ment area. This section describes the development of two additional sensors, RPS1-2 and RPS3. These sensors differed from the RPS1 in the configuration of their optical components (for a greater penetration depth) or in the overall dimensions of the sensors.

### 6.5.1 Larger emitter-detector separation distance

A second PPG sensor (RPS1-2) with a different separation distance was designed and manufactured. The RPS1-2 was designed identical to the RPS1 sensor, but with a different interoptodes distance. While the RPS1 had 5 mm separation distance between LEDs and photodiode, the RPS1-2 had 7 mm distance between emitters and detector. The increased interoptodes distance should provide a deeper penetration depth, without increasing the sensor size. The RPS1-2 sensor’s PCB had the same dimensions of the RPS1, but the PCB’s footprint was modified in order to allocate LEDs and photodiodes with 7 mm centre-to-centre separation distance. The PPG sensor comprised of the same LEDs (KP-2012SRC-PRV and KP-2012 SF4C) and same photodiode (TEMD5010X01) of the RPS1 sensor. Figure 6.12 shows the final manufactured RPS1-2 sensor.

### 6.5.2 Further miniaturisation

While NIRS sensors have a limited degree of customisation (due to the obligatory interoptode distance  $> 2.5$  cm), PPG sensors can be customised to almost any size.

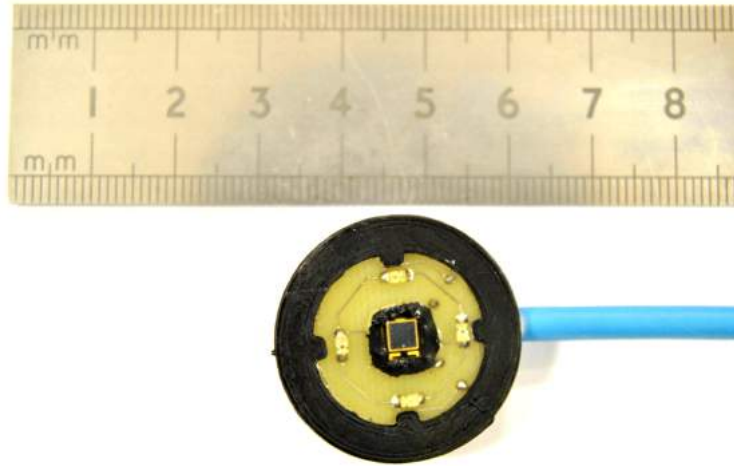


**Figure 6.12:** Final RPS1-2 manufactured sensor. The RPS1-2 sensor had the same external dimensions and optical components of the RPS1 sensor. The LEDs and photodiode were however placed at a centre-to-centre separation distance of 7 mm.

In this context, the RPS1 sensor may be too bulky for certain applications where the measuring area is very small. For this reason, the RPS1 sensor was further miniaturised into a smaller sensor, the RPS3.

Figure 6.13 shows the 3D model of the RPS3 sensor. The sensor comprises of one red LED, one infrared LED, and one photodiode. The LEDs selected for the RPS3 sensor were the same as the RPS1 (KP-2012SRC-PRV and KP-2012 SF4C), while the photodiode was changed to a VBPW34S (Vishay Intertechnology Inc. USA), preserving very similar characteristics to the TEMD5010X01. The PCB and mechanical structure of the RPS3 sensor were designed and manufactured in the same process used for the RPS1 sensor. The mechanical structure was again composed of a case and a cover manufactured in black PLA by 3D printing technology. However, the RPS3 sensor presented a smaller external diameter (15.5 mm) against the RPS1 (28 mm). In addition, the RPS3 had a smaller thickness (7 mm) compared to the RPS1 (8.50 mm). Figure 6.14 shows the picture of the final manufactured RPS1 and RPS3 PPG sensors.

## 6.6 Finger reflectance PPG sensor

In order to compare photoplethysmographic signals between different locations, a finger PPG sensor was developed as well.

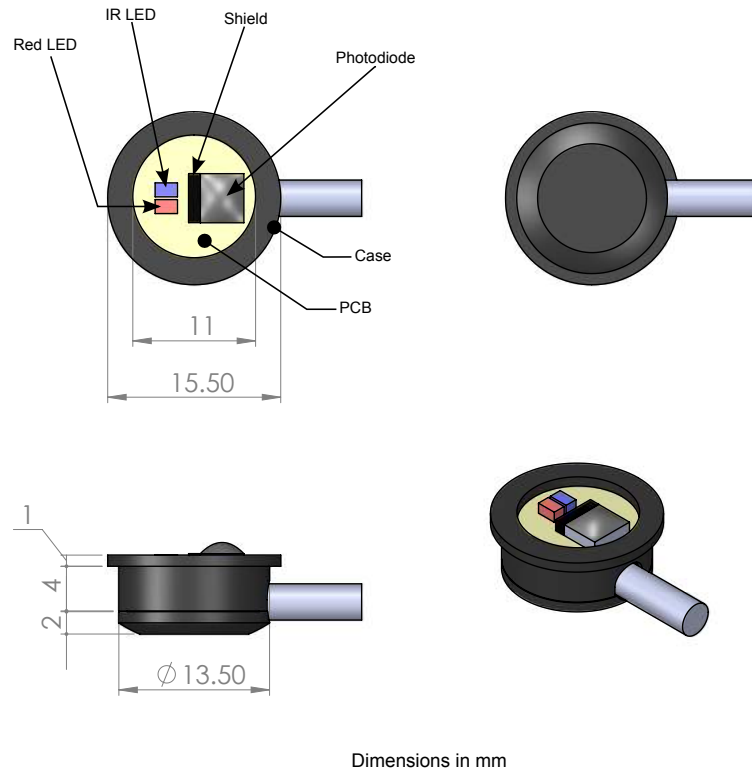


**Figure 6.13:** 3D model views and components of the RPS3 PPG sensor. The sensor comprised of one red LED, one infrared (IR) LED, and one photodiode soldered on an opposite PCB. A black case provided mechanical protection and isolation from ambient light interference. The black rubber shield between LEDs and photodiode avoided optical shunting from LEDs to photodiode.



**Figure 6.14:** Picture of the final manufactured RPS1 (left) and RPS3 (right) PPG sensors.

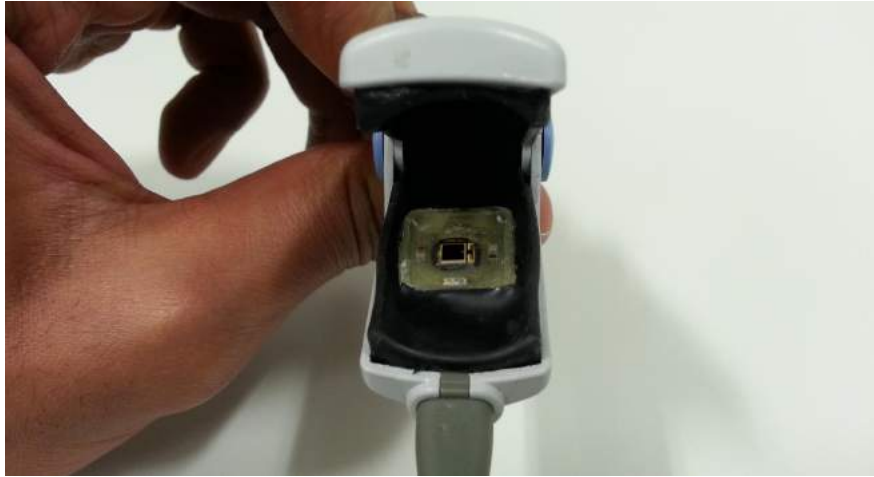


**Figure 6.15:** Manufactured finger reflectance PPG sensor.

The PCB of the finger PPG sensor was identical to the RPS1 sensor's PCB. Prior to the soldering of the optical components, the PCB was cut in a rectangular shape in order to be fit later into a shell of a pulse oximeter finger clip. The same optical components as the RPS1 sensor were soldered on the PCB. The PCB comprising of LEDs and photodiode was soldered to a four-core wire and inserted into the finger clip. After inserting the PCB and wire, the black rubber, which is used to accommodate the finger, was re-inserted in its original position. The black rubber was also cut in order to leave the optical components exposed. After assembling the PCB in the finger clip, the optical components were covered by a layer of clear medical epoxy (Dymax 141-M) and the clip's edges were finally sealed. The other end of the sensor's wire was soldered onto a D-Sub 9 connector for connection to the PPG processing system. Figure 6.15 shows the final manufactured finger PPG sensor. Figure 6.16 shows red and infrared PPG signals acquired from the finger PPG sensor, showing that good quality PPG signals were measured from the finger sensor.

## 6.7 Summary

This chapter described the design and development of reflectance PPG sensors. These were designed to acquire PPG signals from the forearm, forehead, and finger. The evaluation of the PPG sensors demonstrated that these were capable of acquiring good quality PPG signals. The temperature tests showed that the operating sensor did not reach elevated temperatures, thus not presenting any harm for the human skin. Other prototypes of larger interoptodes distance or smaller dimensions were designed and

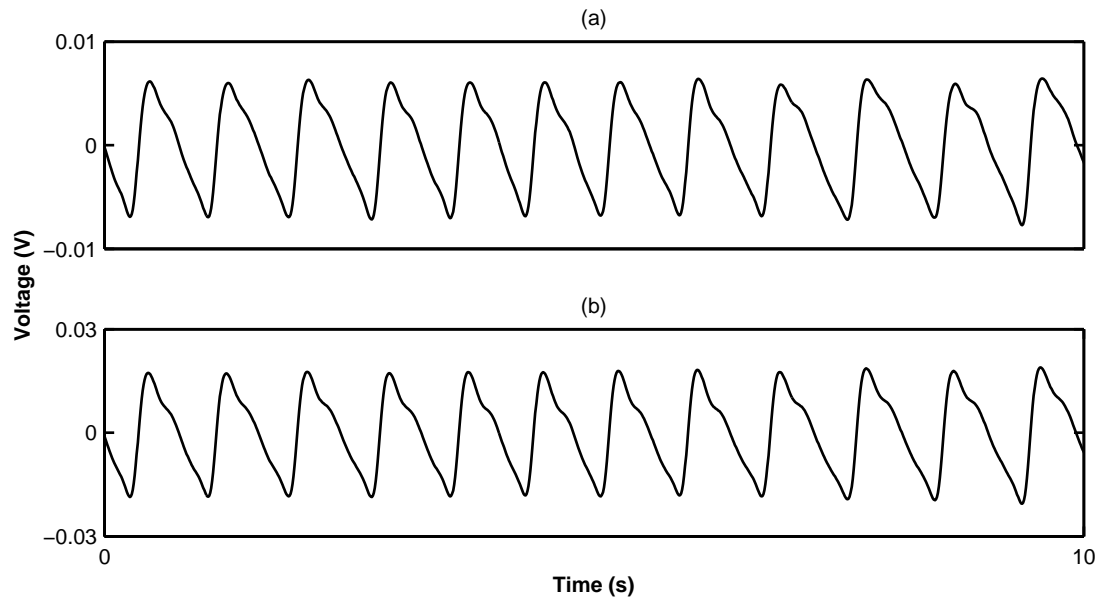


**Figure 6.16:** Red and infrared PPG signals acquired from the finger reflectance sensor. (a) red PPG. (b) Infrared PPG. Raw PPG signals were band-pass filtered (pass-band: 0.5-7 Hz) in order to remove high frequency noise and DC offsets.

manufactured as well. The next chapter will describe the structure, functionalities, and evaluation of a research PPG processing system that was used to drive the sensor's LEDs and process the signal detected by the photodiode.

# Chapter 7

## **Evaluation of a Research Photoplethysmography Processing System for the assessment of tissue perfusion and oxygenation**

The reflectance PPG sensors described in the previous chapter require a processing system in order to drive the LEDs and to process the currents detected by the photodiode. This chapter will describe the structure and functionalities a research photoplethysmographic system that was used for these purposes. The PPG processing system, along with the sensors, was used for the acquisition of raw PPG signals in the *in vivo* investigations that will be presented in the next chapters.

The processing system described in this chapter has been designed by the Research Group at City University of London. The system, also called ZenPPG, has been created with the intention of providing a common research tool for photoplethysmographic signals acquisitions. The system can be considered as an open source project and provides a common architecture that researchers can tailor for their specific purposes. As well as the open architecture, some of the main advantages of the processing system are the possibility of interchanging custom-made sensors and the full control of light intensities. Although the author of this thesis did not design the system himself, he carried out a series of tests and evaluations of the technology that led to improvements to the initial design, particularly on the core board. The main results of these tests are reported in this chapter and contributed to the acquisition of PPG signals in the

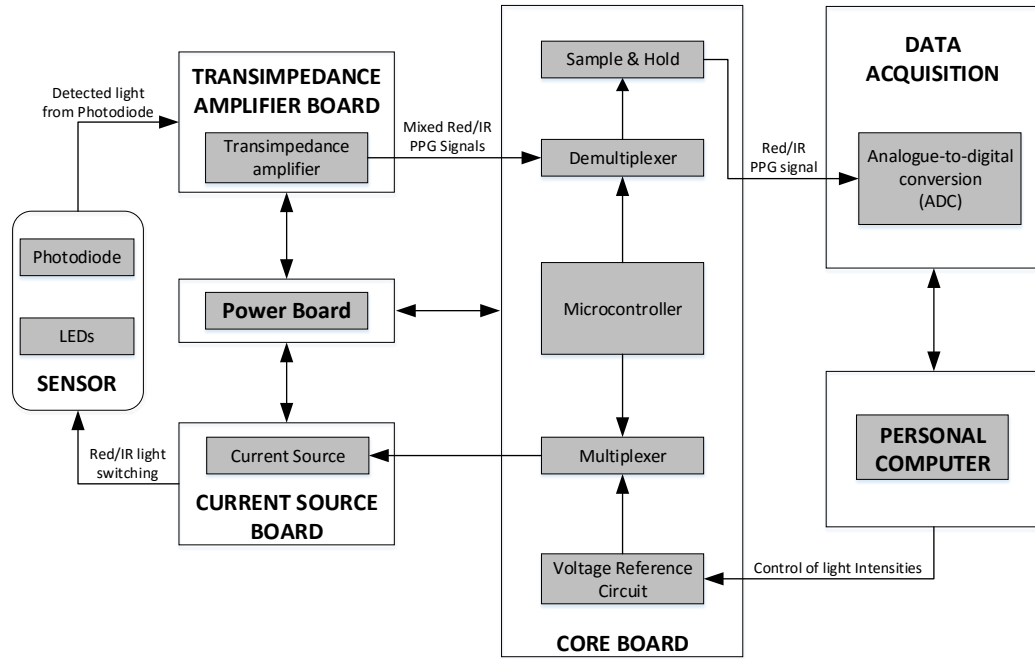


Figure 7.1: Block diagram of the ZenPPG architecture.

*in vivo* investigations. Since this PPG processing system played an essential role in the research objectives of this work, the inclusion of a chapter describing its structure, functionalities, and evaluation was deemed vital to this thesis.

## 7.1 Research photoplethysmography system: ZenPPG

ZenPPG is a dual-wavelength, dual-channel research PPG system developed by the Biomedical Research Group at City University. The main functionalities of ZenPPG are the acquisition of raw PPG signals (AC + DC), adjustment of light intensities and the ability of drive custom-made and commercial PPG sensors. The ZenPPG is composed by independent and interchangeable subsystems, each of them having different functions. Figure 7.1 shows the architecture of the ZenPPG. The instrument is composed of five different boards: power board, current source board, core board, transimpedance amplifier board and bus board.

The current source board supplies the driving currents for the LEDs, while the core board is responsible for intermittent light switching and separation of the signal in each respective wavelengths by multiplexer/demultiplexers. The transimpedance amplifier

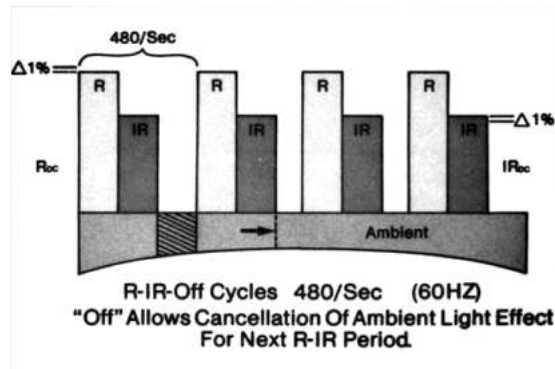


**Figure 7.2:** Generic light switching in pulse oximetry or NIRS. The red (R) and infrared (IR) light sources are switched sequentially ON/OFF in a 1/3 duty cycle in order to sample each wavelength and the ambient light separately. Figure reproduced from [105].

board transforms currents from the photodiodes into voltages and the power board is responsible for supplying power to the entire system. The bus board is responsible for allowing the connection between these boards and the transmission of the voltages and signals between boards. The ZenPPG is configured for the acquisition of PPG signals while the control and monitoring of light intensities are achieved through LabVIEW and National Instrument Data Acquisition Cards (DAQ). Each component of the ZenPPG structure illustrated in Figure 7.1 is described in the following sections. The system's components will be presented either by presenting each board or by specific functions.

## 7.2 LEDs currents time multiplexing

### 7.2.1 LEDs time multiplexing

Optical techniques such as Pulse Oximetry and Near Infrared Spectroscopy employ light at different wavelengths. In order to use independently these wavelengths, the light sources (i.e. LEDs) should be sequentially and intermittently switched ON and OFF. While this process is usually undertaken at high frequencies, the complexity and timing depend on the number of wavelengths and the specific application of the system. Figure 7.2 shows the generic dual-wavelength (red and infrared) light switching employed in pulse oximetry and/or NIRS [105]. The light sources are sequentially switched ON/OFF in order to sample each wavelength in time.

In ZenPPG, the LEDs switching is achieved by analogue multiplexing technology. Analogue multiplexers are composed of several input lines, a single output line and internal

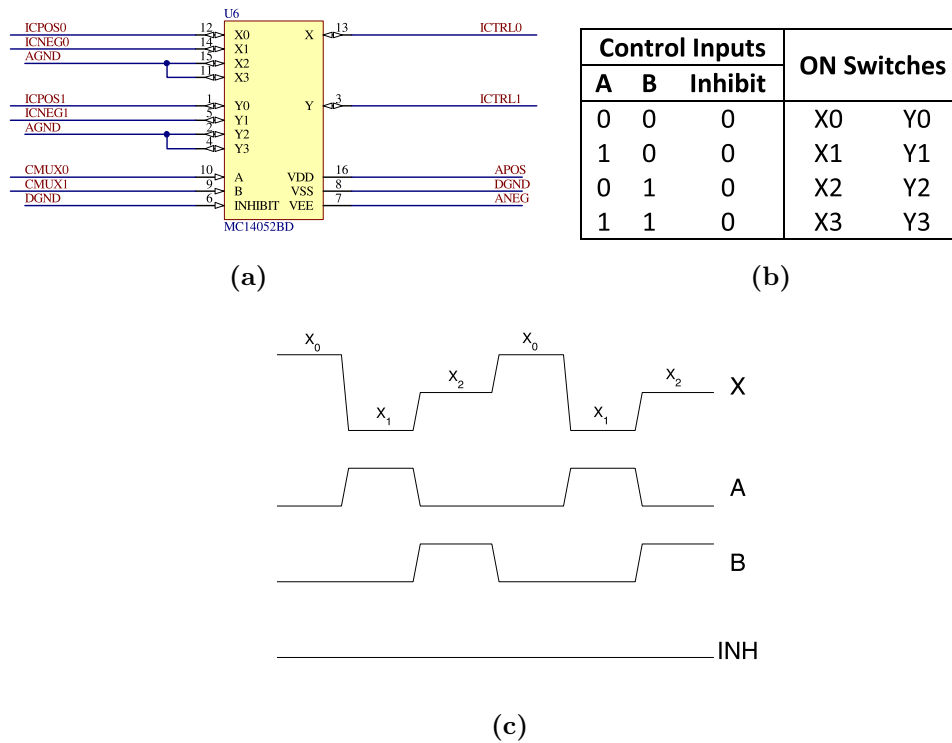


**Figure 7.3:** MC14052BD multiplexer connection schematic (a), truth table (b), and outputs vs. logical controls (c). The input voltage references ICPOS and ICNEG are transmitted to the outputs X (or Y) depending on the state of the logical controls A, B, and INHIBIT. According to the truth table in (b), the multiplexer's outputs will follow the signal X in (c), where the inputs X<sub>0</sub>, X<sub>1</sub>, and X<sub>2</sub> are sequentially transmitted to the output port.

switches. Logical ports control the state and timing of the switches, transmitting the input signals to the output port. Multiplexers are commonly used in applications such as telecommunications where different input signals are passed to a single output line. The multiplexer (MC14052BD, ON Semiconductor) employed in the ZenPPG is a dual 4-channel multiplexer/demultiplexer and is responsible for sequentially switching of the LEDs. The system has been designed for the implementation of a 1/3 duty cycle. This corresponds to a cycle divided into three periods: red wavelength ON and infrared OFF, red wavelength OFF and infrared ON, and both red and infrared wavelengths OFF.

The two channels of the multiplexer are used to synchronously drive the LEDs of the first and second channel of ZenPPG. The inputs of the MC14052BD in the ZenPPG are constant voltages, which are directly proportional to the driving current of the LEDs (see Section 7.3). These voltages are set by the system's user through a graphical user interface on LabVIEW for the first channel (see Chapter 8), or by trimmers for the second channel. The outputs of the multiplexer are controlled by the logical ports. These ports are directly connected to digital clocks driven by a micro-controller (see

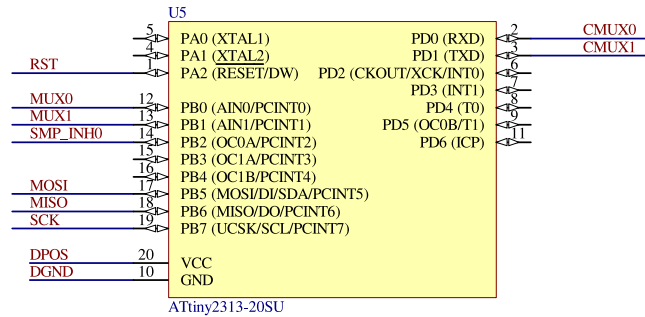


**Figure 7.4:** ATTiny2313-20SU I/O ports lines in ZenPPG. Ports PD0 and PD1 are used to generate multiplexing clocks CMUX0 and CMUX1, while ports PB0-2 are used for demultiplexing clocks MUX0, MUX1, and SMP\_INH. Ports PB5-7 and PA2 are adopted for programming the microcontroller.

subsection 7.2.2). Figure 7.3a illustrates the connections in MC14052BD employed in ZenPPG. The output of the multiplexer depends on the state of the logical ports A, B, and INHIBIT. The truth table in Figure 7.3b indicates how the switches between input and outputs in the MC14052BD are driven by the digital logical ports, while Figure 7.3c illustrates the output X of the multiplexer showed in Figure 7.3a.

## 7.2.2 Microcontroller

In order to provide the logical controls for multiplexing (and demultiplexing as seen later) the Atmel ATTiny2313-20SU (Atmel Corporation, CA, USA) microcontroller is used. The ATTiny2313 is a low-power programmable 8-bit microcontroller with an internally calibrated oscillator. The microcontroller has 18 programmable I/O lines and 2K Bytes internal programmable memory. The microcontroller is surface mounted on the ZenPPG's core board and it can be re-programmed by plugging the AVR STK500 development board (Atmel Corporation, CA, USA) to a 6-PIN connector mounted on the ZenPPG. This facilitates the customization of the clocks' sequence for different applications. The microcontroller's I/O lines were programmed through the AVR STK500 programming kit and Atmel Studio. As shown in Figure 7.4, two bits of PORT D were used to provide the multiplexing clocks CMUX0 and CMUX1, while three bits of PORT B were utilised for the demultiplexing clocks MUX0, MUX1, and SMP\_INH. Four ports were used to reset and reprogram the microcontroller. Appendix A shows the code that was implemented and programmed in the microcontroller for the multiplexing and demultiplexing sequence in ZenPPG.

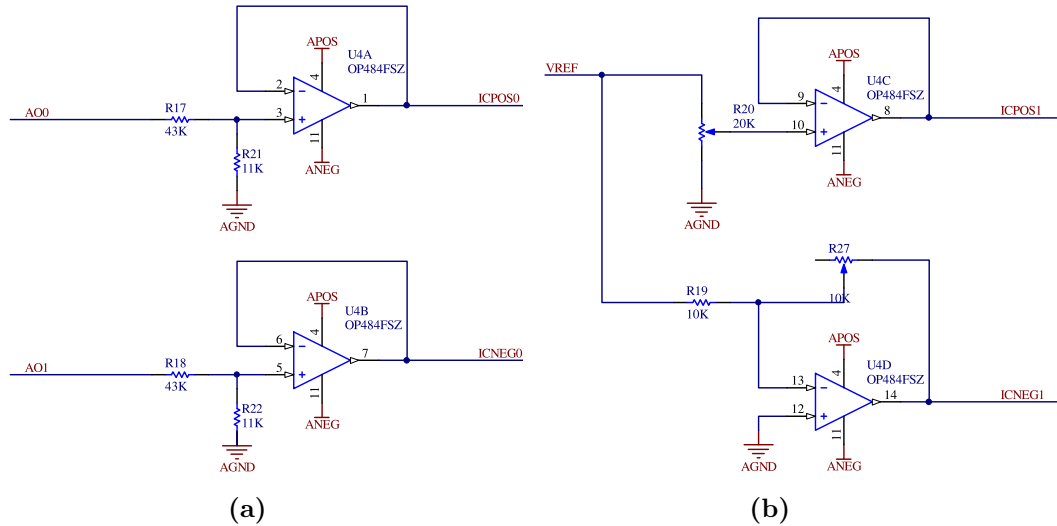


**Figure 7.5:** Voltage reference circuit for the first (a) and second (b) channel of ZenPPG.

### 7.2.3 Voltage Reference Circuits

As mentioned earlier, the inputs ICPOS0, ICNEG0, ICPOS1, and ICNEG1 of the multiplexer showed in Figure 7.3a are voltages selected directly by the user through trimmers or in LabVIEW. These voltages are controlled by the voltage reference circuits. Figure 7.5a shows the voltage reference circuit, for the first channel of ZenPPG. The analogue outputs AO0 and AO1 from the DAQ provide voltages ranges of 0/+5V and 0/-5V respectively, and are controlled through a graphical user interface in LabVIEW. Each of these signals is then connected to a voltage divider and a voltage follower. The voltage divider is composed by the two resistors at the op-amp input (i.e. R17-R21 and R18-R22) and it reduces the voltages AO0 and AO1 by a factor  $Q = 5$ . This reduction allows the conversion of 1 V input to a 200 mV output for AO0 and from -1 V input to a -200 mV for AO1, which are then used to drive the LEDs currents. The outputs of the voltage followers are then connected to the inputs of the multiplexer as showed in Figure 7.3a.

Figure 7.5b shows the voltage reference circuit for the second channel of ZenPPG. In the top circuit of Figure 7.5b, the constant voltage VREF is equal to 1.024 V and is generated by a low-noise voltage reference (LM4140-1.0, Texas Instruments). VREF is connected to a voltage divider composed by R19 and R20 and by a voltage follower. This creates a reduction in the positive voltage ICPOS1 by regulating the variable resistor R20. The bottom circuit is an inverting amplifier, which reduces VREF by adjusting the variable resistor R27. The resulting ICPOS1 and ICNEG1 are then used

as input to the second channel of the multiplexer. Similar to the voltage reference circuit of the first channel, the ICPOS1 and ICNEG1 can be regulated by trimming R20 and R27, to provide a voltage directly proportional to the LEDs driving currents.

#### 7.2.4 Evaluation of LEDs time multiplexing and voltage reference

The multiplexing and voltage reference circuits were evaluated by measuring the input and output voltages of the multiplexer. Figure 7.6 illustrates the voltages at the inputs and output of the multiplexer. The reference voltages AO0 and AO1 on LabVIEW were set at 1 V and -1 V, and the output of the voltage reference circuit ICPOS0 and ICNEG0 were measured on the oscilloscope. The measured voltages were 200 mV and -200 mV (for AO0 and AO1 at 1 V and -1 V respectively, Figure 7.6a). The voltages were then increased to 2 V and -2 V, corresponding to 400 mV and -400 mV respectively (Figure 7.6c). The output of the multiplexer was also measured, along with the logical controls A and B, at the two different voltage sets (Figure 7.6b and Figure 7.6d). The measurements were also repeated for the second channel, giving identical outputs (results not presented).

### 7.3 Current Source Board

In order for the LEDs to be switched ON, a driving current should be supplied to the LEDs. For this purpose, ZenPPG adopts a current source circuit for the conversion of voltages from the multiplexer's output into driving currents for the LEDs.

Figure 7.7 illustrates the current source in ZenPPG. The central part of the circuit is a Howland current source, while a non-inverting amplifier and a push-pull circuit (PNP-NPN pair) have been added in the overall circuit. Since the conventional Howland current source will transform voltages into currents in a unitary ratio (e.g. 1 V to 1 A), the non-inverting amplifier on the left side of Figure 7.7 has been added to reduce the input voltages by one-tenth (output of 100 mV with a maximal input of 1 V). The push-pull circuit switches ON either LED1 or LED2 depending whether the driving voltage is positive or negative and increases the circuit ability to work at high switching frequencies. The resistors R13 and R14 limit the current flowing through the

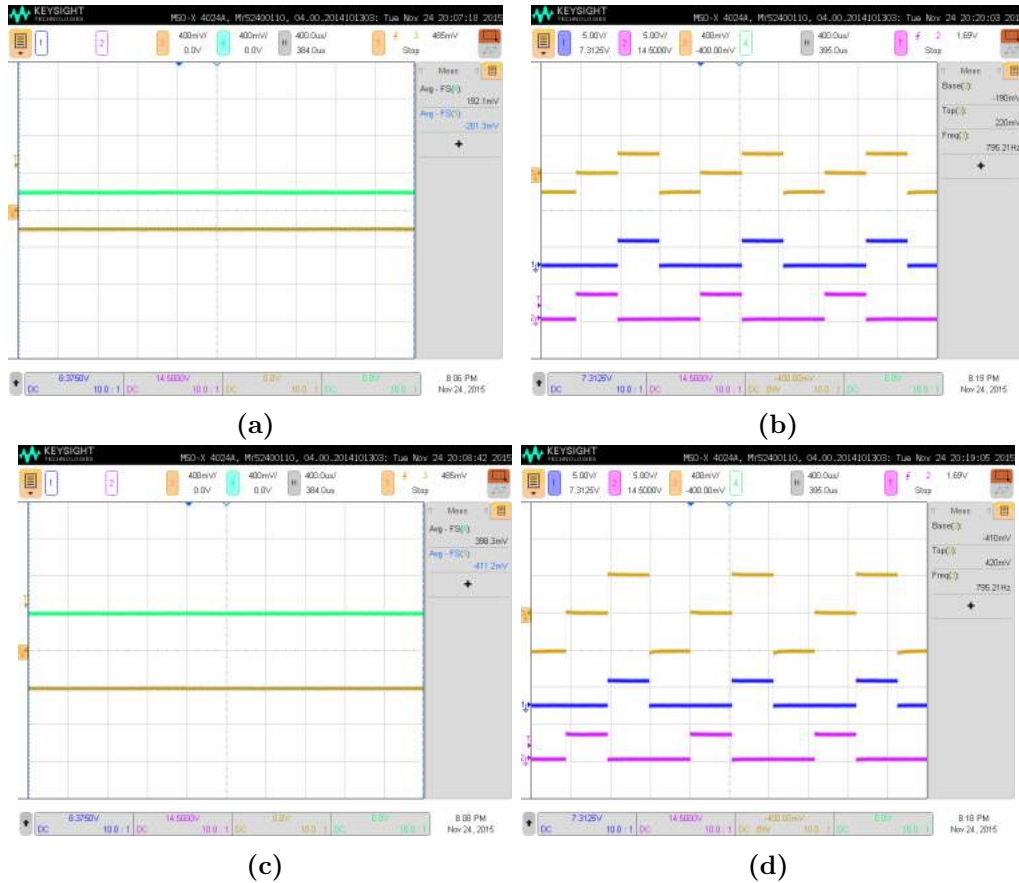


**Figure 7.6:** Reference voltages at 1 V (a) and 2 V (c), multiplexer output and clocks at 1 V (b), and multiplexer output and clocks at 2 V (d). The yellow traces in (b) and (d) are the multiplexer output, while the purple and blue are the digital controls

LEDs to 80 mA.

An instrumentation amplifier is employed to measure the voltage across the load resistor R21. By doing this, the output of the instrumentation amplifier can be used to monitor the driving currents from a LabVIEW interface. The instrumentation amplifier has a gain  $G = 10$ , in order to amplify even the small voltages before they are acquired by the DAQ.

Thus, the current source in Figure 7.7 independently switches two different LEDs (LED1 and LED2). When the output of the multiplexer is connected to the current source, light switching is achieved, while the sequence and frequency of the switching between the two LEDs (or wavelengths) are directly controlled by the logic controls A and B of the multiplexer.



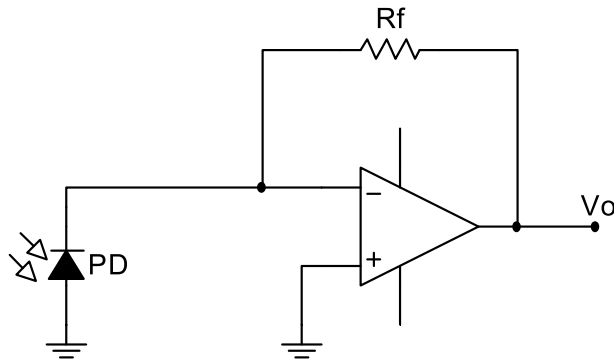


**Figure 7.8:** Basic transimpedance amplifier circuit. The virtual ground at the negative input creates no current flowing through the op-amp and the current flows only through the feedback resistor  $R_f$ . Thus, the voltage  $V_o$  is directly proportional to the current generated by the photodiode PD and  $R_f$ .

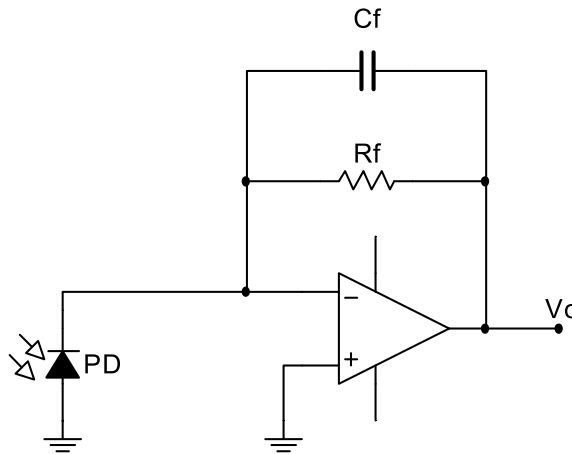


**Figure 7.9:** Transimpedance amplifier with compensation feedback capacitor. The capacitor  $C_f$  is inserted in parallel to  $R_f$  in order to counteract the unstable output of the circuit in Figure 7.8.

However, this ideal scenario is far from reality. The finite open-loop gain and the input capacitances of the op-amp can combine with the photodiode's capacitance and can result in an unstable circuit. The inductive behaviour of this circuit with the combination of the op-amp's noise gain and the open-loop gain create a resonating circuit [170, 171]. The addition of a capacitor  $C_f$  in parallel to  $R_f$  counteracts the inductive nature of the circuit and reduces the gain peaking of the resonating circuit [170, 171].

This compensating capacitor  $C_f$ , should be carefully matched with the input capacitances and the gain bandwidth of the op-amp and the photodiode's capacitance. Equation 7.1 illustrates the equation for the calculation of the optimal capacitor based on the above mentioned parameters [170, 171].

$$C_f = \sqrt{\frac{C_T}{2\pi R_f GBW}} \quad \text{Where } C_T = C_{PD} + C_{id} + C_{icm} \quad (7.1)$$

Where  $R_f$  is the feedback resistance, GBW is the gain bandwidth of the op-amp,  $C_{PD}$  is the photodiode's capacitance,  $C_{id}$  is the differential capacitance of the op-amp, and  $C_{icm}$  is the common mode input capacitance of the op-amp.

The op-amp used in the ZenPPG for transimpedance amplifier design is an OPA380. The main characteristics of the OPA380 are high speed, wide bandwidth and low input bias currents, making it appropriate for the transimpedance amplifier design. The calculated feedback capacitor of Equation 7.1 for the OPA380, with a feedback resistor equal to 120 k $\Omega$  and the photodiode employed in the sensors presented in Chapter 6, yields a solution of  $C_f = 1.04$  pF.

Even though Equation 7.1 indicates the optimal value of the capacitor  $C_f$ , the dimensioning of this component should match the specific applications of the circuit. This is due to the fact that the parasitic capacitances of the circuit can still overcome the selected  $C_f$  [170]. Therefore, an additional empirical tuning of the  $C_f$  may still be needed in certain applications. However, an increase of  $C_f$  from the calculated value will further limit the bandwidth of the circuit, but will also increase the stability of the circuit [170, 172].

#### 7.4.1 Evaluation of the Transimpedance Amplifier

Figure 7.10 shows the output of the transimpedance amplifier for the sensor connected on the forehead and  $R_f = 120$  k $\Omega$  and  $C_f = 15$  pF. During this measurement, the LEDs driving current was maintained at 20 mA. The light switching can be noticed from the three periods (Red LED ON, IR LED ON, and both LEDs OFF). The highest voltage can be observed when the IR LED was ON (i.e. lower absorption). This voltage depends on the light intensity and the feedback resistor  $R_f$  and, in order to avoid saturation, it should not exceed the voltage supply of the op-amp (i.e. 3.3 V). Thus, the value of  $R_f$  should be matched accordingly, depending on the specific location of the sensors (i.e. more or less light absorption) and the light intensities utilised. One approach can be to

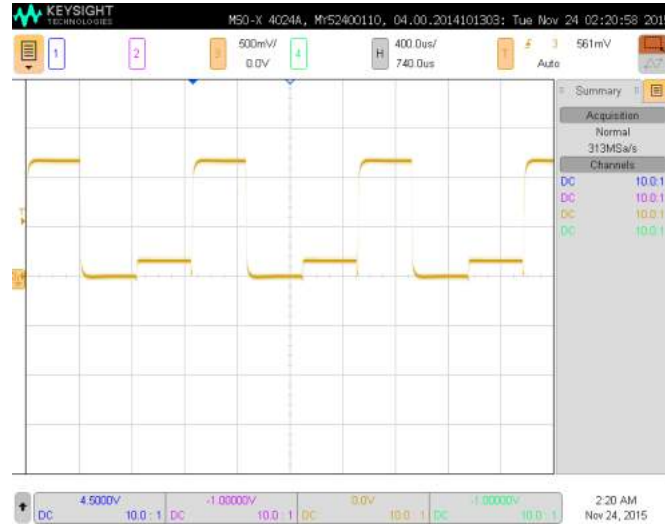


**Figure 7.10:** Transimpedance amplifier output in ZenPPG.

initially adopt a low-medium gain (e.g.  $R_f = 120 \text{ k}\Omega$ ) and increase the light intensities for each subject, until a satisfactory voltage is achieved.

However, as mentioned above, the value of  $C_f$  will also influence the stability of the circuit. Since the calculated value of  $C_f$  from Equation 7.1 was far too small ( $1.04 \text{ pF}$ ), an additional tuning of  $C_f$  was required. However, the value of  $C_f$  should not be too high, as this would also affect the transient response at the amplifier's output. As seen later, this could have unfavourable consequences on the demultiplexing of the signal (see Section 7.5). Figure 7.11 shows the output of the transimpedance amplifier for different capacitor values and constant feedback resistor  $R_f = 120 \text{ k}\Omega$ . Without capacitor compensation or for low capacitance values such as  $2.2 \text{ pF}$ , the circuit was unstable, with ringing over-imposing on the signal. For high capacitance values such as  $100 \text{ pF}$  and  $680 \text{ pF}$ , the transimpedance amplifier's output started to change shape due to an increase in the transient response. An optimal value of  $C_f = 15 \text{ pF}$  was empirically derived based on the stability of the signal at the output of the transimpedance amplifier. This approach overcompensated the circuit, but also increased the stability of the final transimpedance amplifier's output.

The selection of the feedback resistor  $R_f$  was performed for each measurement location in the studies presented in this thesis (e.g. forehead, forearm, finger, etc.), in order to maximise the signal amplification without saturating the op-amp. The capacitor  $C_f$  was also specifically selected depending on each application, sensor (photodiode), or resistor  $R_f$  (i.e. gain).

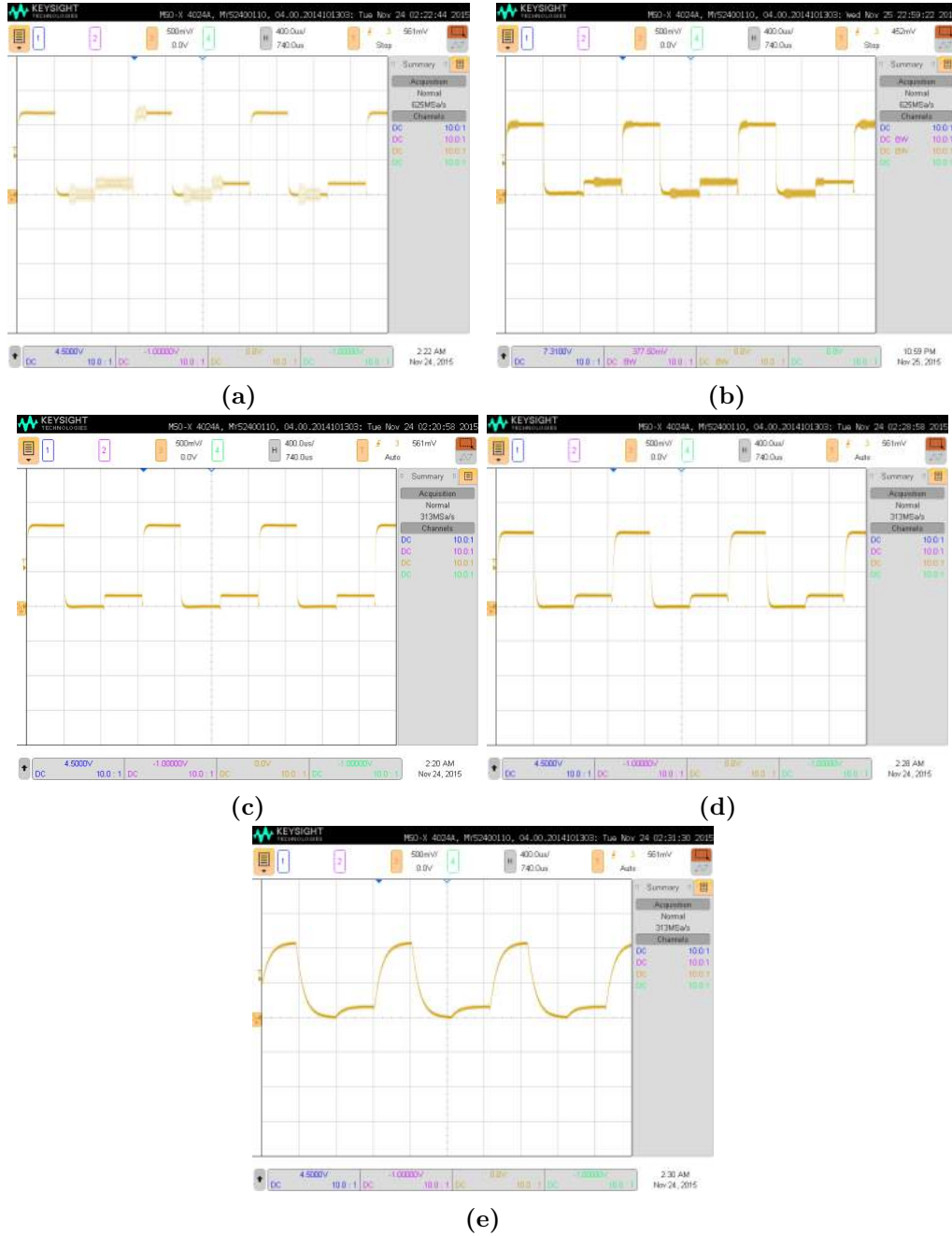


**Figure 7.11:** ZenPPG's transimpedance amplifier output without feedback capacitor (a), for feedback capacitor  $C_f = 2.2 \text{ pF}$  (b),  $C_f = 15 \text{ pF}$  (c),  $C_f = 100 \text{ pF}$  (d), and  $C_f = 680 \text{ pF}$  (e). The feedback resistor was kept at  $R_f = 120 \text{ k}\Omega$

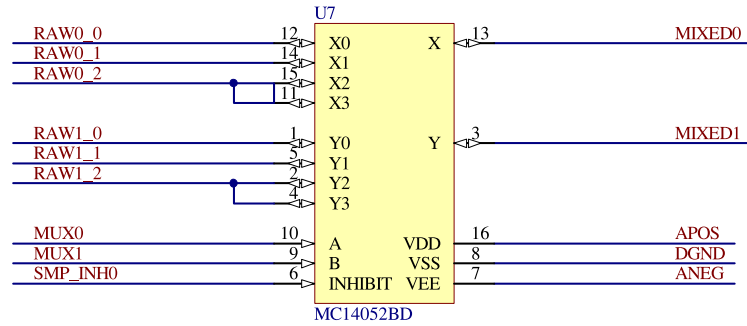


Figure 7.12: MC14052BD demultiplexer connections schematic in ZenPPG.

## 7.5 Demultiplexing and Sample & Hold

As mentioned in the previous sections, the signal generated by the photodiode is a continuous sequence of Red/Infrared light switching. The typical signal at the output of the transimpedance amplifier can be seen in Figure 7.10, where the switching sequence can be noticed by three different voltage levels corresponding to the three cycle periods. Since this signal is mixed, time separation of the signal in the respective wavelengths is required. In order to achieve this, the ZenPPG employs analogue demultiplexers.

Analogue demultiplexers are devices, which are commonly used in conjunction to multiplexers. In an opposite fashion compared to multiplexers, demultiplexers receive one input line and separate it into several output lines. Similar to multiplexers, demultiplexers are composed of internal switches, which are directly controlled by logical ports.

The ZenPPG employs a separate MC14052BD as demultiplexer. Figure 7.12 shows the schematics of the demultiplexer's connections. The outputs of the transimpedance amplifiers of both channels (MIXED0 and MIXED1) are connected to the inputs of the demultiplexer. The logical controls MUX0, MUX1 and SMP\_INH0 are provided by the microcontroller and control the sequence of the outputs for each channel (RAW0<sub>*n*</sub> and RAW1<sub>*n*</sub>, for  $n = 1..3$ ).

The process can be thought as the opposite of time multiplexing showed in Section 7.2, where the truth table in Figure 7.3b controls the demultiplexer outputs, depending on the state of the logical controls A, B, and INH. Figure 7.13 graphically illustrates the process of time demultiplexing achieved for the output of the transimpedance amplifier.

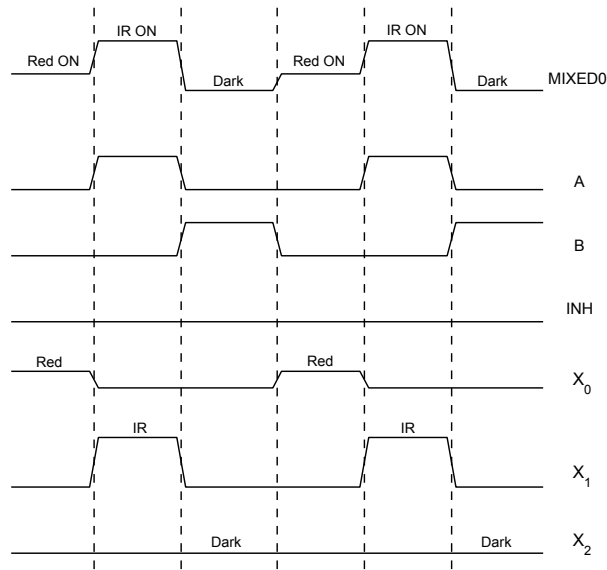


**Figure 7.13:** Illustration of the input, outputs, and logical controls of the demultiplexer during two consecutive cycles. MIXED0 is the output of the transimpedance amplifier and the input of the demultiplexer. A (MUX0), B (MUX1), and INH (SMP\_INH) are the logical controls. The input signal MIXED0 is time demultiplexed in  $X_0$ ,  $X_1$ , and  $X_2$ .

In this scenario, when the logical controls close the internal switches of the demultiplexer, the input is transmitted to corresponding output of the demultiplexer. If the logical controls of the multiplexer and demultiplexer are synchronous, the separation of the three different sequence of light switching is possible (i.e. red wavelength ON, Infrared wavelength ON and both wavelengths OFF).

However, demultiplexing an entire segment of the transimpedance amplifier's output could introduce some inaccuracies. At the margins of each segment, there are big voltage transitions, which should not be sampled. Moreover, the introduction of the feedback capacitor  $C_f$  in the transimpedance amplifier's output create a transient response during each transition (see Figure 7.11). In order to achieve an adequate quality in the PPG signal, these features of the intermittent transimpedance amplifier's output should be avoided.

The sampling in the entire segment is solved in the ZenPPG by only demultiplexing the central part of each segment. This is achieved by dividing each segment into four equal sub-segments (total of twelve sub-segments for each cycle Red ON, IR ON, Dark). The sampling is only performed in the two central sub-segments, while the other 'peripheral' sub-segments are avoided. Figure 7.14 shows the output/inputs of the demultiplexer when only the central part of each period is sampled. While the clocks A and B do not change compared to the traditional situation in Figure 7.13, the clock INHIBIT changes

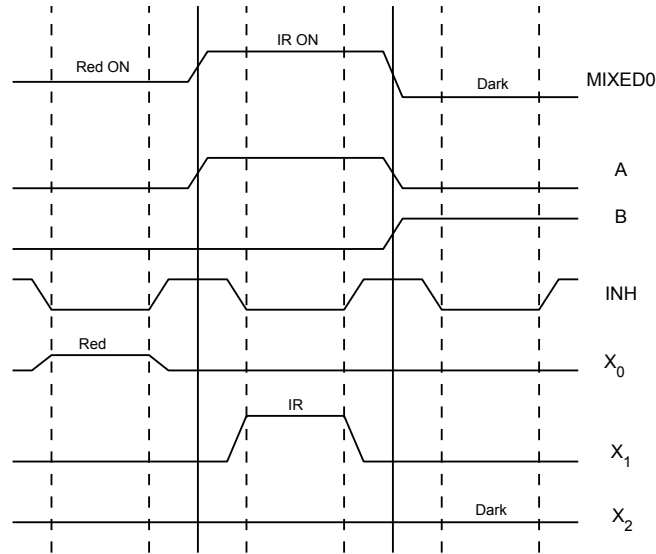


**Figure 7.14:** Illustration of the input, outputs, and logical controls of the demultiplexer during a single cycle. MIXED0 is the output of the transimpedance amplifier and the input of the demultiplexer. A (MUX0), B (MUX1), and INH (SMP\_INH) are the logical controls. The input signal MIXED0 is time demultiplexed in X<sub>0</sub>, X<sub>1</sub>, and X<sub>2</sub> only in the central part of the period (Red ON, IR ON, or Dark), when INH is in a low state (see truth table in Figure 7.3b).

to a low status (sampling) only in the central part of the period. The implementation of this division can be seen in the multiplexing/demultiplexing code in Appendix A, where the programming of the microcontroller was divided in twelve (4 by 3) different instructions.

The process explained above shows how the mixed raw PPG signal is time-demultiplexed (or simpler, split) into red and infrared signals. However, the output of the demultiplexer illustrated in Figure 7.14 are intermittent voltage pulses produced by the transimpedance amplifier output. Even though these pulses have high frequencies (i.e. in the order of few hundred Hertz switching frequency), they may not retain the voltage to the next cycle, with the consequent degradation of the PPG signal. Therefore, a sample and hold circuit is needed in order to retain the voltage until the next cycle.

The sample and hold circuit is a circuit composed of a switch, a capacitor, and an operational amplifier. The positive input of the op-amp is connected to the capacitor, while the negative input is feed-backed to the op-amp's output. The switch is connected to the capacitor and closes intermittently, passing a certain voltage. When the switch is closed, voltage is passed to the op-amp input and feed-backed to the op-amp's output. During this period, the capacitor charges. When the switch is released, the capacitor holds the charge and it keeps providing the voltage at the op-amp's input.

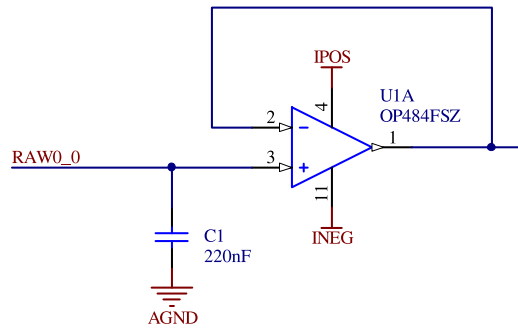


**Figure 7.15:** Sample and hold circuit in ZenPPG. The output of the demultiplexer is connected to the input of the op-amp and a capacitor C1 to hold the voltage. When the switch (i.e. demultiplexer) is closed, the voltage RAW0.0 is passed to the op-amp output while the capacitor C1 is charged. When the switch is opened the capacitor C1 continues to discharge to the op-amp input.

This configuration allows a slow discharge of the capacitor due to the low input bias currents of op-amp and a high output impedance (or low OFF currents) of the switch. In the ZenPPG, the sample and hold circuit is implemented by a capacitor and an op-amp connected to the output of the demultiplexer (switch). Figure 7.15 shows the sample and hold circuit adopted in the ZenPPG. The signal from the demultiplexer (switch) is connected to the positive input of an op-amp (OP484FSZ) and a capacitor C1. The negative input of the op-amp is feed-backed to the output. Each output of the demultiplexer is passed to separate circuits as in Figure 7.15, in order to sample and hold dual-wavelength PPG.

Once the signal is sampled and hold, the PPG signal needs to be filtered before being acquired by National Instruments Data Acquisition systems. Thus the output of the sample and hold circuit is connected to a low-pass RC filter. The filter has a cut-off frequency of 79.5 Hz in order to remove unwanted high-frequency noise from the signal and to restrict the signal bandwidth to avoid aliasing in the analogue-to-digital conversion. Remaining noise is filtered digitally after analogue-to-digital conversion. The filter is followed by a pre-acquisition voltage buffer. Figure 7.16 shows the sample and hold circuit, the low-pass filter and the voltage buffer.

### 7.5.1 Evaluation of time demultiplexing and Sample & Hold

Figure 7.17 shows the output of the transimpedance amplifier output of signal acquired from the forehead. The voltage reference was set at 1 V, transimpedance amplifier gain

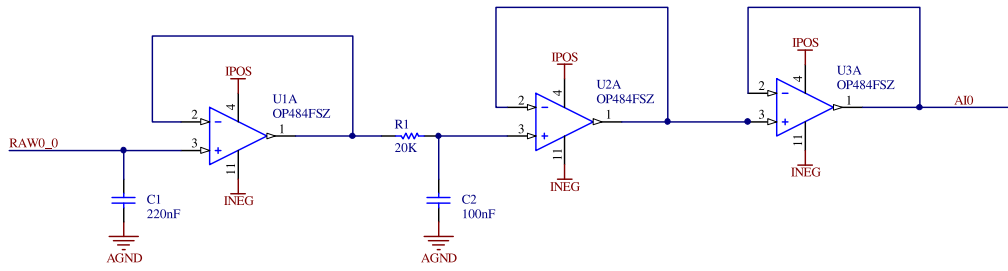


**Figure 7.16:** Sample and hold circuit, low-pass anti-aliasing filter and voltage follower (buffer).

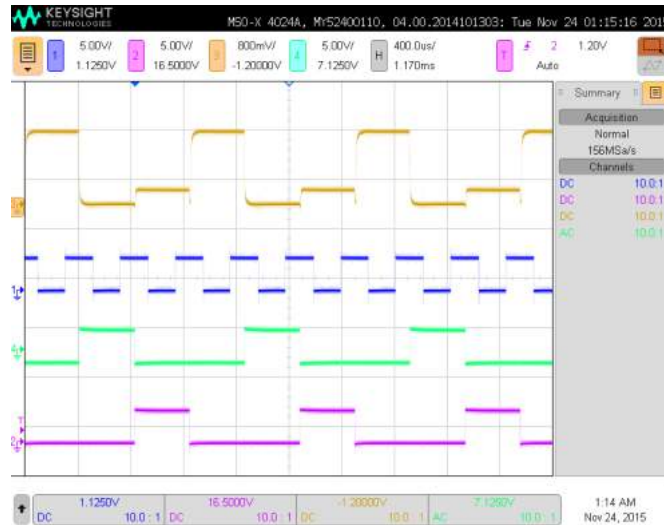


**Figure 7.17:** Transimpedance amplifier output and demultiplexer clocks. From top: transimpedance amplifier output; INH clock, A and B clocks. The INH clock (sampling) is in a low logical state only in the central part of each period (Red ON, IR ON, or dark)

$R_f = 120 \text{ k}\Omega$  and  $C_f = 15 \text{ pF}$ . As seen from the second upper trace in Figure 7.17, the INH clock, which is responsible for sampling the signal, is in a low state only during the second and third quarter of each period (Red ON, IR ON, or dark). The sample and hold circuit (comprised of filter and buffer) was evaluated by removing the transimpedance amplifier board and inputting a  $\sim 100 \text{ mV}_{pp}$  sine wave at 1 Hz and 20 Hz. The procedure was later repeated by inputting a simulated  $\sim 60 \text{ mV}_{pp}$  PPG signal at 1 Hz and 20 Hz (Figure 7.18).

## 7.6 Power board and external connections

The power board in the ZenPPG is responsible for supplying voltages to all working components in the system. The board provides two positive voltages (+ 5 V, + 3.3 V) and two negative voltages (- 5 V, -1.3 V), which are used depending on the specific

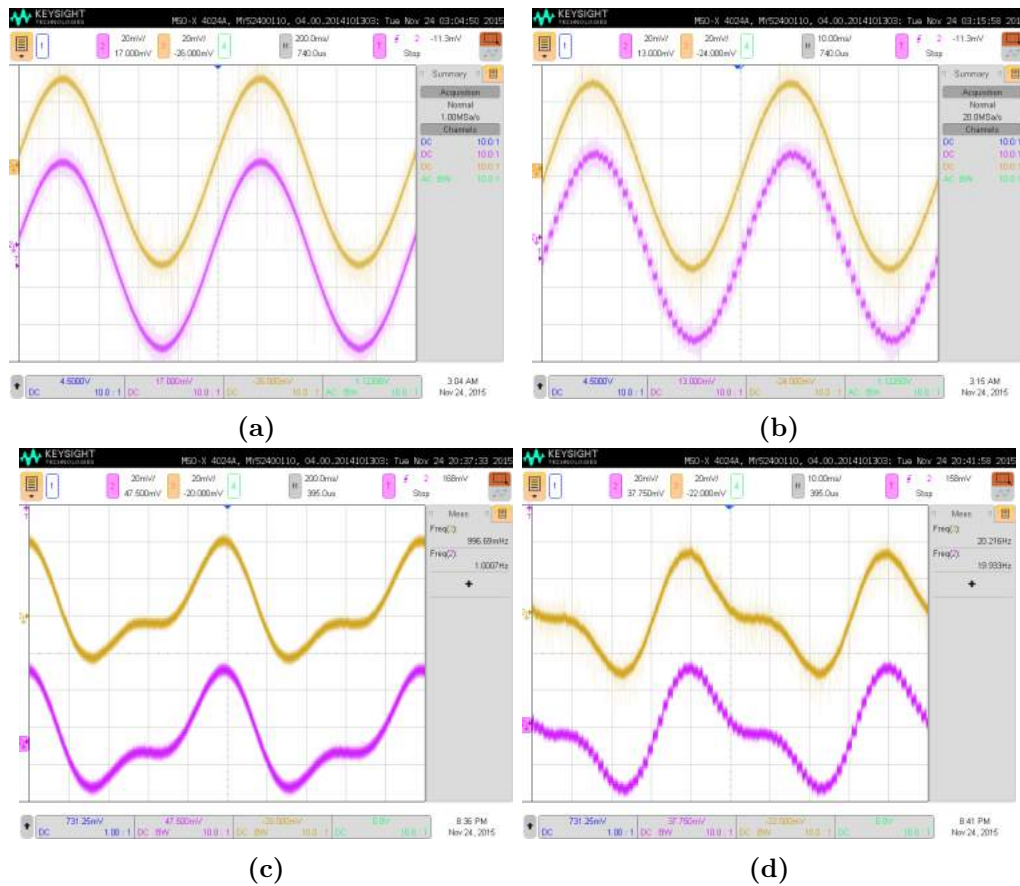


**Figure 7.18:** Evaluation of the sample and hold circuit with sine waves and simulated PPG signals. (a) Sine wave at 1 Hz and 100 mV<sub>pp</sub>. (b) Sine wave at 20 Hz and 100 mV<sub>pp</sub>. (c) PPG signal at 1 Hz and 60 mV<sub>pp</sub>. (d) PPG signal at 20 Hz and 60 mV<sub>pp</sub>. The sine wave and simulated PPG signals were connected to one of the inputs of the demultiplexer. The upper traces (yellow) are the input signals, while the bottom traces (purple) are the signals measured at the output of the circuit in Figure 7.16.

application. The system can be supplied either by connection through USB (portable battery packs or PC) or by connection to two 9 V PP3 batteries.

The ZenPPG allowed the connection of custom-made and commercial probes through two DB-sub 9-pin female connectors placed on the front panel. Two pins of this connector provided the driving currents for the LEDs (pins 2 and 3), two pins received the currents generated by the photodiode (pins 5 and 9), and one pin was connected to ground. Figure 7.19 shows the ZenPPG's front panel and the instrument with two PPG sensors connected. The research PPG system presented a 64-pin National Instruments connector for connection to Data Acquisition Card (DAQ). Through this connector, the PPG signals and functional parameters (e.g. driving currents, batteries status, etc.) can be digitised, acquired, and controlled through LabVIEW.

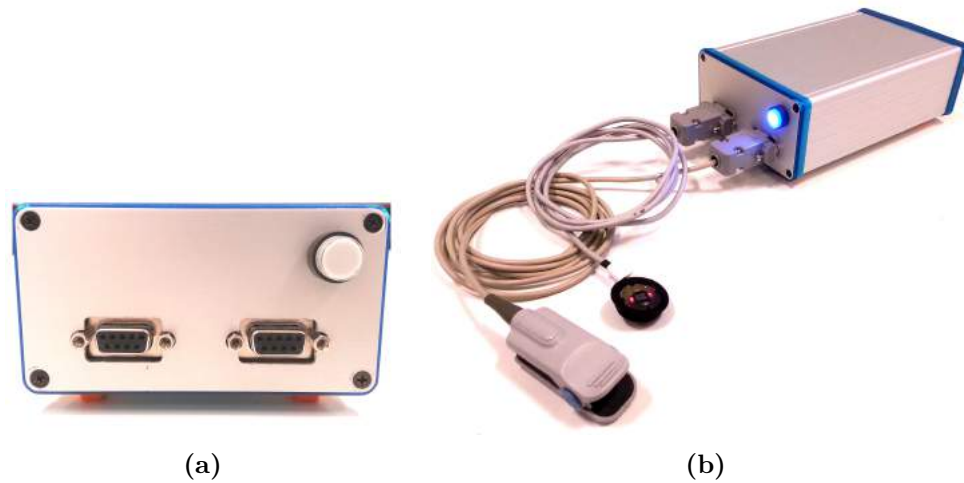


**Figure 7.19:** ZenPPG system's front panel (a) and ZenPPG with two PPG sensors connected (b). D-Sub 9-pin connectors for PPG probes can be noticed on the front panel (a).

## 7.7 Summary

In this chapter, a research PPG system has been presented. Even though each part of such complex system cannot be illustrated, the main components and functionalities for the purposes of this work have been described. The next chapter will describe the development of a virtual instrument (VI) in LabVIEW that was used for the acquisition of signals from custom-made (ZenPPG) and commercial devices, for the display of signals in real time, and for the saving of the acquired signals. Furthermore, the application of the modified Beer-Lambert law will be proposed and described.

## **Development of a Virtual Instrument for signal acquisition & the application of the modified Beer-Lambert law to PPG**

Chapter 6 and Chapter 7 described the development of reflectance PPG sensors and the evaluation of a research PPG processing system (ZenPPG). In order to acquire, display in real time, and save the signals for post-acquisition analysis, the instrumentation was connected to Data Acquisition devices for analogue-to-digital conversion (ADC) and a software was developed to acquire the digitised signals on a personal computer. This chapter briefly describes the connection set-up to dedicated Data Acquisition devices and the development of a software application designed in LabVIEW and used to acquire the physiological signals and interface with ZenPPG. For better clarity, only the configuration for the acquisition of signals from a single ZenPPG and one channel NIRS will be described in this chapter. However, the software application was adapted to each of the studies performed in this work, for the acquisition of additional signals.

The modified Beer-Lambert law, used in NIRS to infer haemoglobin concentration changes, was previously introduced in Chapter 5. This work aims at investigating the feasibility of applying this NIRS principle to PPG measurements. Therefore, the application of the modified Beer-Lambert law to PPG signals is proposed and described in the second part of this chapter.

## 8.1 Introduction to LabVIEW

LabVIEW (Laboratory Virtual Instrument Engineering Workbench) is a software tool by National Instruments used for designing tests, perform measurements and develop control systems [173]. LabVIEW is a program development application presenting a different flexibility and an improved productivity compared to other languages such as C. LabVIEW has been built with a user-friendly graphical interface. It is the first software application to use the G programming language, adopting graphical scripting techniques in a Virtual Environment [174].

In LabVIEW, the source code is developed graphically in a *Block Diagram* and it is ran in the *Front Panel* [173]. The Block Diagram contains the graphical code, while the Front Panel is used to display signals, indicators, and/or controls. These two constitute the code, also known as Virtual Instrument (VI) [173]. As other programming languages where the code can be broken into "sub-functions" or "sub-routines", the code can be divided in sub-VIs, or more generally called VIs [173]. Each VI usually has input(s) or output(s). These can be graphically connected to other VIs in order to pass variables (or to indicators and/or controls for display or automation) [173]. This can help the user to break complex programs in simpler tasks. Its hierarchical structure permits easy modification on the code and quicker developmental time [173, 174].

The graphical nature of LabVIEW makes it ideal for data acquisition, data analysis, instrument control, test and measurements, automation, and other tasks [173].

For these reasons, LabVIEW was chosen as the programming language for controlling ZenPPG light intensities and acquiring signals from ZenPPG and other physiological monitoring devices used in this work.

## 8.2 Analogue to Digital conversion set-up

Before being acquired and saved in a text file by a software application, the analogue signals require being converted in digital form. Data Acquisition Cards (DAQC) are pieces of equipment dedicated to converting analogue signals into a digital form, before

being passed to a personal computer [175]. The fundamentals of analogue-to-digital conversion are not discussed here and they can be found in most signal processing books such as [175]. This section briefly describes the connection of the physiological monitoring devices to dedicated data acquisition cards.

As mentioned before, the ZenPPG is equipped with a National Instruments 64-pin connector. The signals from the ZenPPG were acquired and digitised by connecting the device to a DAQC (NI-PcIe 6321 DAQ, National Instruments, USA) by a shielded 64-pins cable (SCH68-68-EPM, National Instruments). The NI-PcIe 6321 is a high-speed data acquisition card with 16-bit resolution and 16 input channels. The following sections in this chapter describe how the signals were acquired, manipulated, displayed, and saved in the software application.

The other medical devices such as NIRS or laser Doppler flowmetry, which were used in this work, were set-up to acquire their analogue outputs voltages. Custom-made cables were used to connect the analogue output ports of these devices to a shielded screw terminal block (SCB-68, National Instruments, USA). This block was then connected to a second NI-PcIe 6321 by another SCH68-68-EPM cable. The subsection 8.3.5 describes how these analogue voltages were then converted back to their original scale after being acquired.

### **8.3 Development of a Virtual Instrument for physiological signals acquisition and control of light intensities**

The first part of the VI described in this chapter was designed by the Research Centre of Biomedical Engineering at City University of London in conjunction with the ZenPPG. This section of the software application was designed to acquire signals from the PPG processing system through the dedicated DAQ connector mounted on the ZenPPG and to control the light intensities in the first channel of ZenPPG. This already existing part constituted the starting point from where the rest of the VI was extended further for the *in vivo* studies that were carried out in this work. The rest of this LabVIEW application was specifically developed for this thesis in order to acquire signals from other instruments such as NIRS or laser Doppler flowmetry, to apply calibration equa-



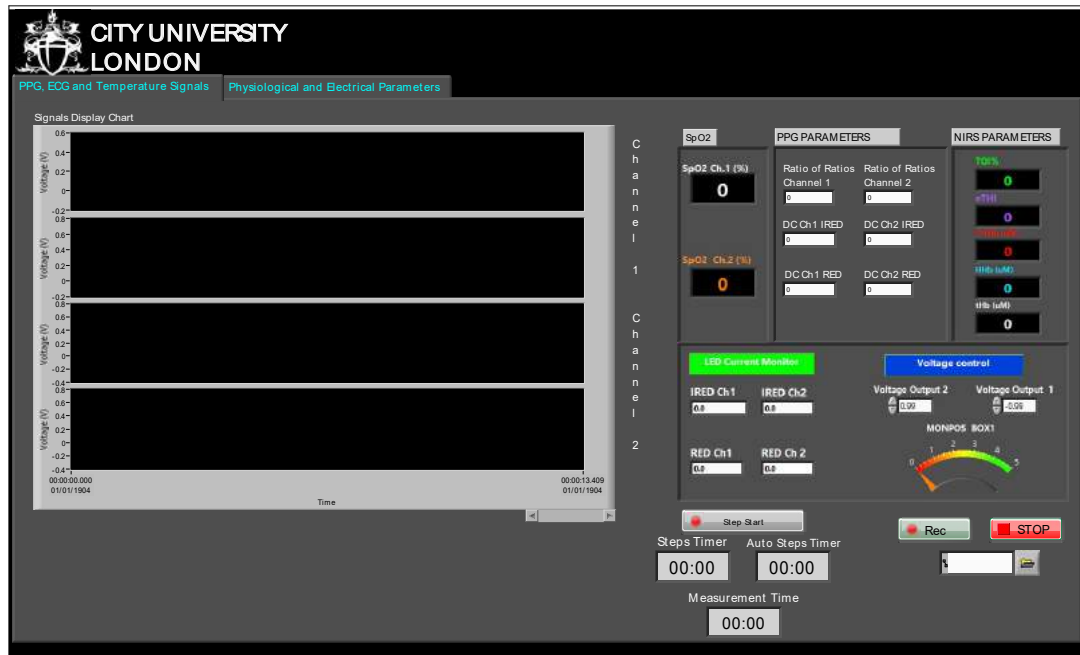


**Figure 8.2:** Front Panel (or user graphical interface) of the Virtual Instrument (VI) developed for acquisition of PPG and NIRS signals. The left side of the panel is dedicated to the display of the acquired signals, while indicators and controls are placed on the right side.

The ADC process was performed by National Instruments DAQC. While the DAQC transformed the analogue signals to digital, the process of continuously transferring the created bits to the computer's buffer is controlled through the VI.

The *DAQ Assistant VI* allowed reading data from a specific DAQC connected to the computer. The *DAQ Assistant VI* was placed in a while loop in order to perform the reading continuously in time until the user stopped the acquisition. Through the *DAQ Assistant VI*, the user could select the DAQC from where to read the signals, select the input channels, choose the sampling frequency, set the voltage inputs ranges, perform calibrations, and select other parameters/tasks related to the signal acquisition. The outputs of the *DAQ Assistant VI* were the digitized signals acquired by the DAQC. These output signals were a discrete sequence of numbers (internally represented in bits) composing the original analogue signals sampled in an equally time interval (i.e. sampling frequency). In order to separate the acquired voltages into single signals, a *Split Signals* function was used at the output of the *DAQ Assistant VI*. Figure 8.3 illustrates the *DAQ Assistant VI*, the *Split Signals* function and the acquired measurements separated into single signals. The first four signals acquired by the *DAQ Assistant VI* were the dual-wavelength and dual channel raw PPG signals (i.e. channel 1 Red PPG, channel 1 IR PPG, channel 2 Red PPG, and channel 2 IR PPG), the fifth and sixth were the LEDs driving currents, and the last was the voltage level of the battery.

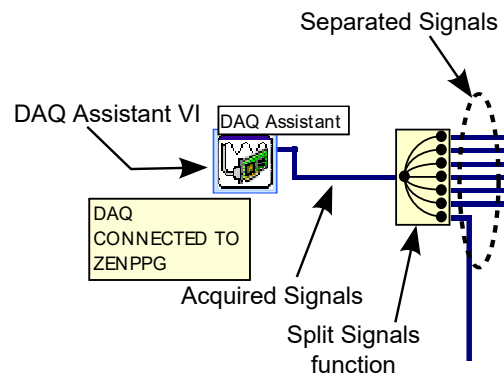


**Figure 8.3:** DAQ Assistant VI, split signals function and separated signals in the VI. The signals acquired by the DAQ Assistant VI are bundled in a single output. The split signals function separate these into single signals.

Once the signals were acquired together from the DAQC and split into each respective wavelength or signal, these were then prepared for being displayed on the front panel. The next section will describe how the signals were processed in order to be displayed in real time by means of graphical charts or indicators.

### 8.3.2 Display of acquired signals and indicators

One of the main reasons for adopting LabVIEW for the acquisition of physiological measurements is its graphical user interface and its capabilities of displaying the acquired signals in real time. The VI developed allowed the display of physiological signals simultaneously to their acquisition. Once the raw PPG signals (AC+DC) were acquired and split into their respective wavelengths and channels, the AC components of the signals were displayed on the screen in real time. The first four split signals showed in Figure 8.3 were bundled together by a *Merge signals* function. This facilitated the simultaneous and identical processing of the signals. After merging the signals, these were band-pass filtered by the *Filter Express VI* (pass-band: 0.5-7 Hz). The *Filter Express VI* received an input signal, filtered it and output the filtered signal. The filter parameters could be easily set through the settings window of the VI. Once the signals were filtered to obtain the AC PPG component, these were inverted and input into a graphical chart for display. The chart's icon was represented on the block diagram, while the graphical chart displaying the signals was on the front panel (left side of Figure 8.2). Figure 8.4 shows the connections in the VI for filtering and displaying.

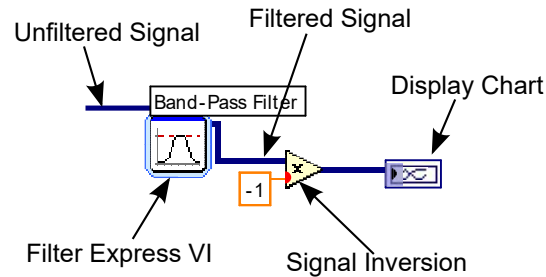


**Figure 8.4:** Filter Express VI and signal display chart. The PPG signals are band-pass filtered (pass-band: 0.5-7 Hz) and displayed on a chart in the VI's front panel.

### 8.3.3 Control and monitoring of ZenPPG's light intensities

As mentioned in Chapter 7, the PPG processing unit ZenPPG allows the control of the light intensities through voltage reference circuits (subsection 7.2.3). In addition, the LEDs driving current can be monitored by measuring, using an instrumentation amplifier, the voltage drop across a resistor (Section 7.3). This section describes the digital control of light intensities in the first channel of ZenPPG (the second channel's currents are set through trimmers) and the monitoring of the LEDs driving currents.

The voltage reference circuits in subsection 7.2.3 supplied a voltage directly proportional to the LEDs driving currents. In the first channel of ZenPPG, this was performed by supplying the voltage reference circuit with voltages generated by the analogue outputs of the DAQC. The range of the analogue output voltages supplied by the DAQC was  $\pm 5$  V and they can be controlled in LabVIEW by manual controls on the front panel. Figure 8.5a shows the part of the VI dedicated to supplying a voltage output through the DAQC. This was achieved by the use of the *DAQmx Create Virtual Channel VI* and the *DAQmx Write VI*. The latter one wrote a specified task (in this case a voltage, set manually by the user) and wrote it to the task created in the *DAQmx Create Virtual Channel VI* (supply voltage to the specified output channel of the DAQ card). The *DAQmx Create Virtual Channel VI* used the selected DAQC's output channel and the voltage range required to supply an analogue voltage. The *DAQmx Create Virtual Channel VI* was placed outside the loop for its independence from the running of the instrument, while the *DAQmx Write VI* was inside the while loop, stopping when the acquisition stopped. When the while loop stopped, the supply of the voltage output was stopped and the task was cleared by the *DAQmx Clear Task VI*.

Two instrumentation amplifiers in the ZenPPG's current source board measured a volt-

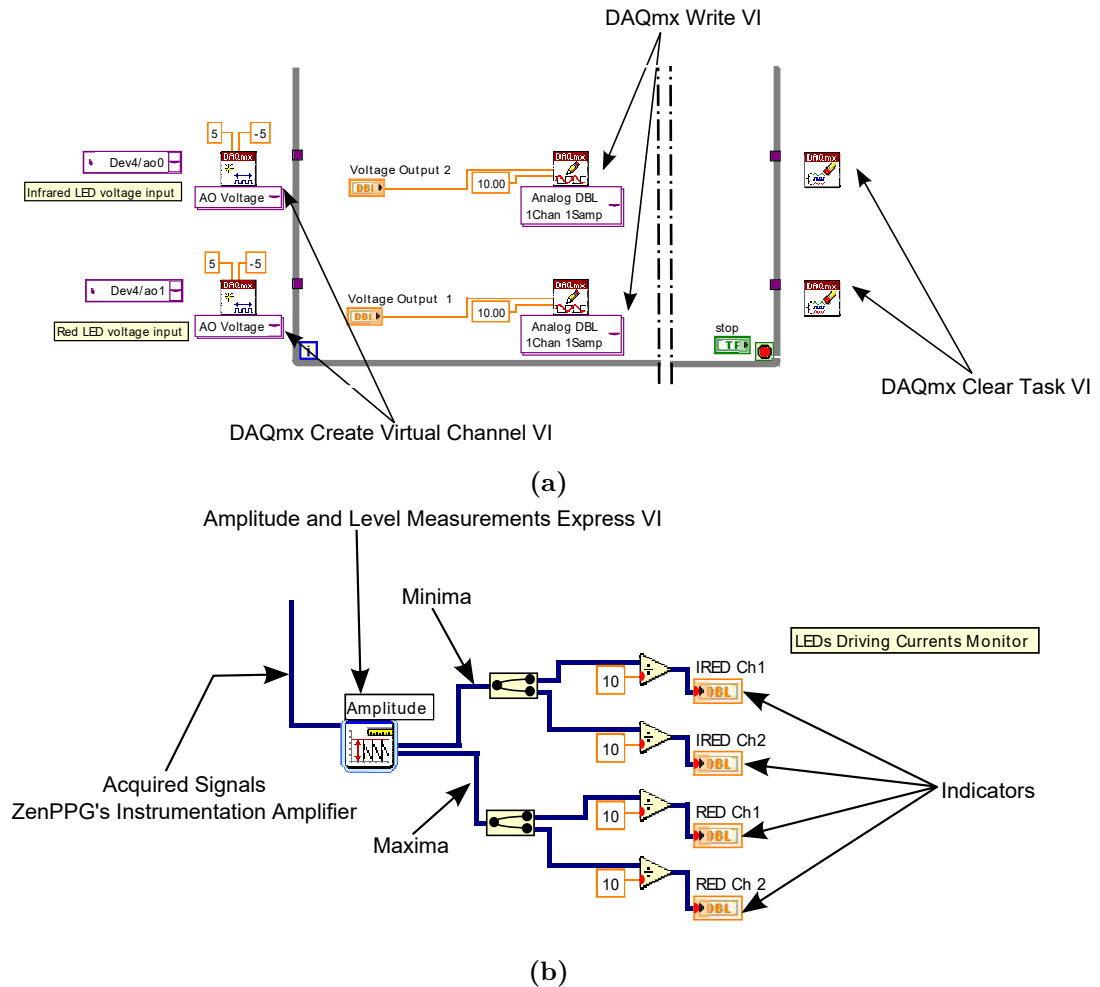


**Figure 8.5:** LEDs driving current control (a) and monitor (b) in the VI. (a) The LEDs currents are set by analogue voltages generated through the DAQC by the *DAQmx Create Virtual Channel VI* and the *DAQmx Write VI*. (b) The LEDs currents (red and infrared), in both ZenPPG's channels, are then monitored by acquiring the outputs of the ZenPPG instrumentation amplifiers, measuring the minimum and maximum, re-scaling the values, and displaying these by indicators on the front panel.

age directly proportional to the LEDs driving current. This voltages were measured for each ZenPPG's channels and were amplified by a gain  $G = 10$  before being acquired by the DAQC. These voltages were positive-negative intermittent signals due to the switching between red and infrared LEDs (see Figure 7.3c). The monitoring of the LEDs' driving currents was performed in the VI by acquiring the amplifiers' outputs and measuring the minimum and maximum of these oscillating signals by using the *Amplitude and Level Measurements Express VI* as illustrated in Figure 8.5b. The minimum and maximum of the signals were then reduced by the instrumentation amplifier gain  $G = 10$  before being displayed by indicators on the front panel.

The DC offset (or DC component) of the acquired PPG signals were also monitored on the VI. These are important parameters to monitor since they indicate whether the saturation rail of the transimpedance amplifier has been reached, with the consequent

corruption of the PPG signal. The DC offsets at both wavelengths were monitored by low-pass filtering the acquired signals at a cut-off frequency  $f_c = 0.05$  Hz and displaying the filtered signals on the front panel as numerical indicator.

### 8.3.4 Arterial oxygen saturation estimation from PPG signals

Arterial oxygen saturation ( $SpO_2$ ) was estimated in real time from PPG signals. Figure 8.6 shows the part of the VI designed to estimate the  $SpO_2$ . The acquired PPG signals were low-pass filtered at 7 Hz by a *Filter Express VI*. The filtered PPG signals were then input to a *Collector Express VI*. This function collected a certain amount of data and output the collected signal only when the target size was reached. The *Collector Express VI* was set to collect 3000 points, equivalent to three seconds of data. This length was deemed sufficient for windowing the signals with at least one cardiac pulsation, composed by one peak and one valley. The collected signal was then divided into each corresponding wavelength/channel by the *Split Signals*. In order for the ratio of ratios to be calculated from the PPG signals, the DC offsets and the peak-to-peak amplitude of the pulsatile PPG (AC component) were calculated by the *Amplitude and Level Measurements Express VI*. Once the ratio of ratios was calculated from the DC PPG and the AC PPG peak-to-peak amplitude at each wavelength, the  $SpO_2$  was calculated using the *Formula Express VI* and Equation 8.1.

$$SpO_2 = 110 - 25 \times R \quad (8.1)$$

### 8.3.5 Signal acquisition from commercial devices

The VI was also developed to acquire signals from other devices other than the ZenPPG. In this section, the part of the VI dedicated to acquiring signals from a commercial NIRS monitor (NIRO 200NX, Hamamatsu Photonics, Japan) is presented.

The analogue voltages from the device were digitised by a DAQC and acquired on LabVIEW by a dedicated *DAQ Assistant VI*. In Figure 8.7a the bundled signals at the output of the *DAQ Assistant VI* were separated in the four signals measured per

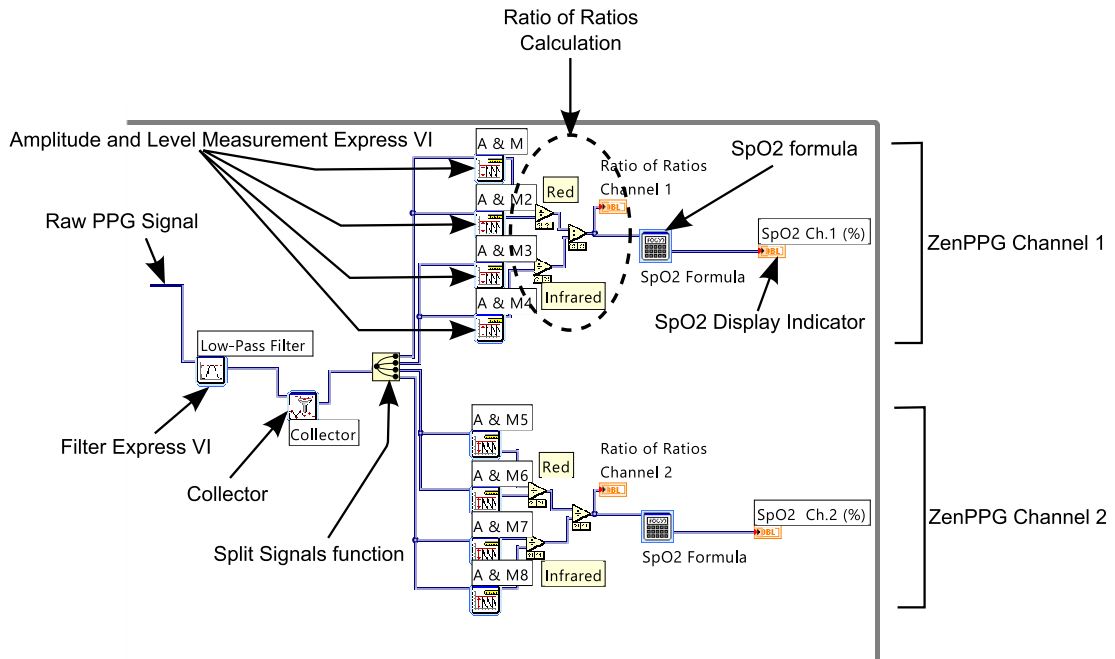


**Figure 8.6:** SpO<sub>2</sub> calculation in the VI. The DC PPG and the AC PPG peak-to-peak amplitude were calculated from dual-wavelength PPG signals by the Amplitude and Level Measurements Express VI. Once the ratio of ratios was calculated, the SpO<sub>2</sub> was calculated by applying Equation 8.1.

channel, TOI, nTHI, HbO<sub>2</sub> (O<sub>2</sub>Hb), and HHb. The analogue voltage outputs from medical devices are signals representing the measured parameter. However, due to safety reasons, these voltages are scaled to certain voltage ranges, which usually do not exceed the  $\pm 5$  V. Thus, a re-scaling process is required in order to transform the analogue voltages acquired back to the scale of the measured parameters (e.g. percentage for TOI). Therefore, calibration equations were generated as suggested by the manufacturers. The voltages across the analogue outputs' pins were measured by a multimeter. These were measured at two or three voltages in order to generate calibration lines. Figure 8.7b illustrates the calibration curve created for TOI's analogue outputs from the NIRO 200NX. The line and respective equation were obtained by the regression between two voltage points at 0 V and 1 V. For these two points, the measured voltages were respectively -0.003 and 0.994. The same process was repeated for all the parameters that were acquired from other commercial devices.

Once calibration equations were created for each parameter, the acquired analogue outputs signals were input to a *Formula Express VI* containing their specific calibration equation. After being rescaled, the signals were then displayed on the front panel by means of indicators or charts as showed in Figure 8.7a.

When necessary, the entire process described here (acquisition, rescaling and display)

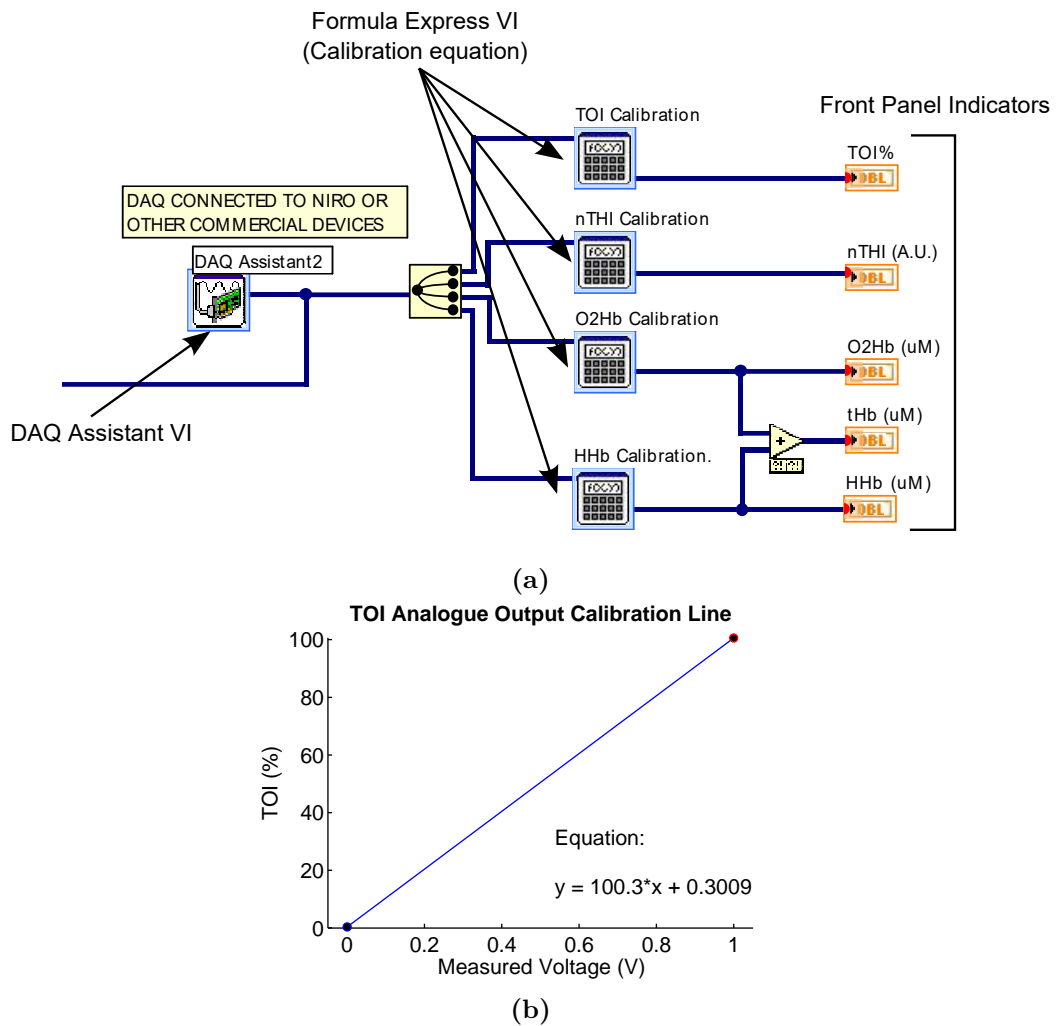


**Figure 8.7:** Acquisition, calibration and display of signals from commercial devices (a) and NIRS TOI analogue outputs calibration line and equation (b). In (a) the analogue outputs from the device are acquired by the dedicated DAQ Assistant before being split, re-scaled, and displayed on the front panel by indicators. All the analogue outputs were re-scaled by using an equation obtained from the calibration line as done in (b) for TOI.

was extended to the other NIRS channels or to other devices such as laser Doppler flowmetry monitors or pulse oximeters.

### 8.3.6 Measurements file saving and protocol timers

One of the main function of the developed VI was to save the acquired signals for post-acquisition analysis. The *Write To Measurement File Express VI* was used to save the acquired signals. The signals from all *DAQ Assistant VI* were first bundled together and then input to the *Write To Measurement File Express VI*. This received the signals as input and save them in a text file in which each column represented a signal. The saving of the measurements was taking place only when a button on the front panel

was pressed by the user and a file name was chosen.

In order to measure the experimental protocol times, different timers were developed on LabVIEW. The first timer, (*Timer 1*, was dedicated to indicate the overall measurement time on the front panel. *Timer 1* was starting only when the same button dedicated to initiating the saving of the measurement was pressed on the front panel. This allowed indicating the time elapsed since the measurement or protocol was started. The second timer, *Timer 2* was started when the same button on the front panel was pressed. However, *Timer 2* was automatically reset when a time target was reached. This allowed the automatic indication of protocol timing. The final timer, *Timer 3*, was restarted manually by the user through a button on the front panel of the VI. Figure 8.8 illustrates the parts of the VI dedicated to saving the measurements (Figure 8.8a) and timing (Figure 8.8b).

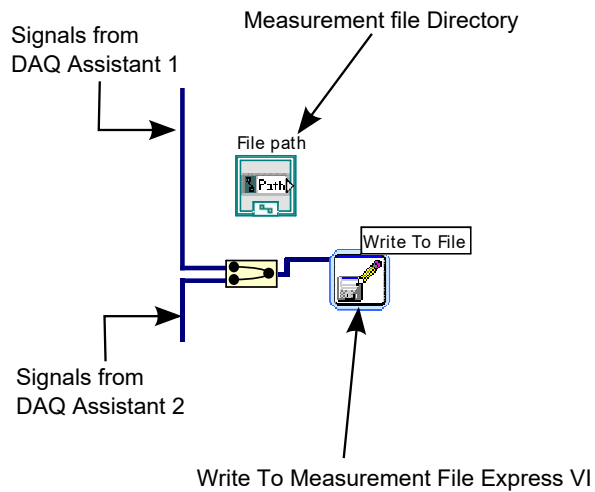
Figure 8.9 shows the front panel of a running VI. The acquired PPG signals are displayed on a chart on the left side of the panel. Other physiological parameters such as SpO<sub>2</sub> and TOI are displayed on the panel by means of indicators. The LEDs driving currents, DC PPG offsets, timers, and battery level are also displayed on the front panel by numerical or visual indicators.

## 8.4 Application of the modified Beer-Lambert law to Photoplethysmography

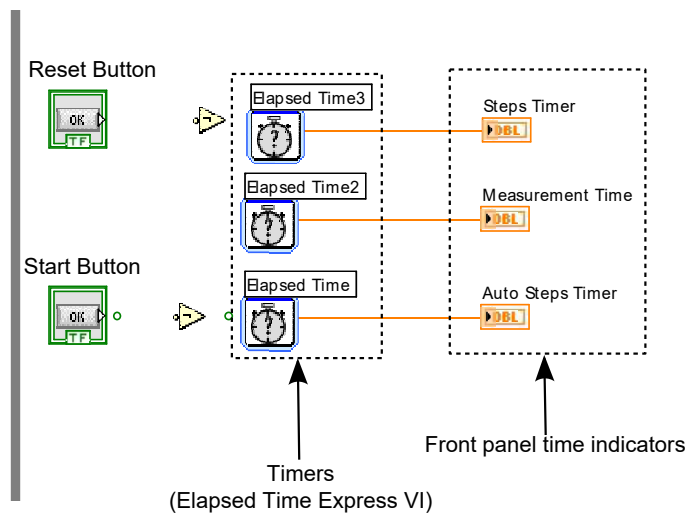
In Chapter 5, the modified Beer-Lambert law in Near Infrared Spectroscopy was introduced. The law associates the light attenuation  $A_\lambda$  at wavelength  $\lambda$  to concentrations  $c_n$  of the light absorbers present in a solution.

$$A_\lambda = (\varepsilon_{1\lambda} \cdot c_1 + \varepsilon_{2\lambda} \cdot c_2 + \dots \varepsilon_{n\lambda} \cdot c_n) \cdot d \cdot DPF + G. \quad (8.2)$$

The factor  $G$  relates to scattering and geometrical properties of the tissue, while the  $DPF$  is known as differential pathlength factor and it relates the increased optical path length (caused by scattering) to the distance  $d$  between light emitter and detector. If



(a)



(b)

**Figure 8.8:** Save measurements and timers in the VI. (a) The acquired signals are bundled together and saved in a text file by the *Write To Measurement File Express VI*. (b) The three timers with the start and reset buttons, and the time indicators for the front panel.

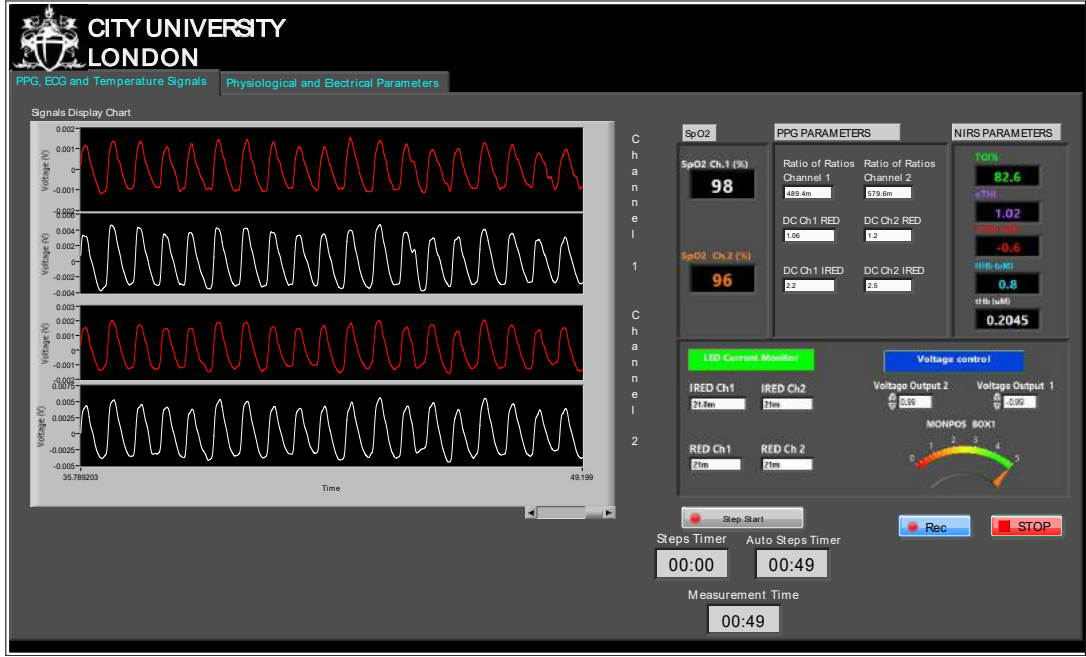


**Figure 8.9:** Front panel of the running VI. The PPG signals are displayed on a chart, while NIRS and other parameter are displayed as numerical or visual indicators.

the light is applied at two wavelengths  $\lambda_1$  and  $\lambda_2$ , and assuming that oxygenated HbO<sub>2</sub> and deoxygenated haemoglobin HHb are the only absorbers in blood, Equation 8.2 can be transformed into a solvable system of equations.

$$\begin{aligned} A_{\lambda_1} &= (\varepsilon_{HbO_2\lambda_1} \cdot [HbO_2] + \varepsilon_{HHb\lambda_1} \cdot [HHb]) \cdot d \cdot DPF + G \\ A_{\lambda_2} &= (\varepsilon_{HbO_2\lambda_2} \cdot [HbO_2] + \varepsilon_{HHb\lambda_2} \cdot [HHb]) \cdot d \cdot DPF + G. \end{aligned} \quad (8.3)$$

Photoplethysmography shares several characteristics with NIRS. Both techniques are optical and NIRS applies light at least two wavelengths for the determination of concentrations of HbO<sub>2</sub> and HHb. Light switching in photoplethysmography is common and it is usually performed between two wavelengths for the estimation of SpO<sub>2</sub>. Thus, the PPG signals used in pulse oximetry could be potentially adapted to the application of NIRS processing, obtaining additional information to the conventional SpO<sub>2</sub>.

For the application to dual-wavelength PPG signals, the wavelengths  $\lambda_1$  and  $\lambda_2$  in Equation 8.3 can be respectively modified to the common red (R) and infrared (IR) used in pulse oximetry. The light intensities for the calculation of light attenuations at these two wavelengths can be expressed from the DC components of the PPG signals, denoting the overall incident light. However, absolute light attenuations cannot be de-

terminated from DC PPG, but changes in attenuations can be derived from the variations in DC relative to baseline. Therefore, the relative changes in light attenuations at red and infrared can be expressed as:

$$\Delta A_R = \frac{DC_R(0)}{DC_R(t)} \quad (8.4)$$

$$\Delta A_{IR} = \frac{DC_{IR}(0)}{DC_{IR}(t)} \quad (8.5)$$

Where  $DC_R(0)$  and  $DC_{IR}(0)$  are respectively the red and infrared DC PPGs at the start of the measurement (baseline), whereas  $DC_R(t)$  and  $DC_{IR}(t)$  are respectively the red and infrared DC PPG throughout the measurement. With a differential approach to the modified Beer-Lambert law (see subsection 5.2.3), the relative changes in attenuations can be related to relative changes in haemoglobin concentrations.

$$\begin{aligned} \Delta A_R &= (\varepsilon_{HbO_2R} \cdot \Delta[HbO_2] + \varepsilon_{HHbR} \cdot \Delta[HHb]) \cdot d \cdot DPF + \Delta G \\ \Delta A_{IR} &= (\varepsilon_{HbO_2IR} \cdot \Delta[HbO_2] + \varepsilon_{HHbIR} \cdot \Delta[HHb]) \cdot d \cdot DPF + \Delta G. \end{aligned} \quad (8.6)$$

Assuming constant scattering during the entire measurement, the factor  $\Delta G$  can be eliminated ( $\Delta G = 0$ ), and solving the system of equations in Equation 8.6 yields the solution for  $\Delta HbO_2$  and  $\Delta HHb$ .

$$\Delta[HbO_2] = \frac{\Delta A_R \cdot \varepsilon_{HHbIR} - \Delta A_{IR} \cdot \varepsilon_{HHbR}}{(\varepsilon_{HbO_2R} \cdot \varepsilon_{HHbIR} - \varepsilon_{HbO_2IR} \cdot \varepsilon_{HHbR}) \cdot d \cdot DPF} \quad (8.7)$$

$$\Delta[HHb] = \frac{\Delta A_{IR} \cdot \varepsilon_{HbO_2R} - \Delta A_R \cdot \varepsilon_{HbO_2IR}}{(\varepsilon_{HbO_2R} \cdot \varepsilon_{HHbIR} - \varepsilon_{HbO_2IR} \cdot \varepsilon_{HHbR}) \cdot d \cdot DPF} \quad (8.8)$$

The actual path length  $d \cdot DPF$  cannot be used since DPF values for short interoptodes distances are not available in the literature [120,121]. Therefore, the haemoglobin concentration changes should be expressed as relative changes with respect to the optical path length ([concentration  $\times$  optical pathlength]). Assuming that  $HbO_2$  and  $HHb$  are the only haemoglobin species present in blood during the measurement, total haemoglobin can be calculated as the sum of  $\Delta HbO_2$  and  $\Delta HHb$ .

**Table 8.1:** Extinction coefficients or millimolar absorptivity, in  $\text{L} \cdot \text{mmol}^{-1} \cdot \text{cm}^{-1}$ , of oxygenated ( $\text{HbO}_2$ ) and deoxygenated haemoglobin ( $\text{HHb}$ ) at 660 nm (red) and 880 nm (infrared). Values obtained from [17].

Wavelength $\lambda$ (nm)	Extinction coefficient $\varepsilon$ ( $\text{L} \cdot \text{mmol}^{-1} \cdot \text{cm}^{-1}$ )	
	$\text{HbO}_2$	$\text{HHb}$
660 (R)	0.080	0.814
880 (IR)	0.284	0.200

$$\Delta[tHb] = \Delta[HbO_2] + \Delta[HHb] \quad (8.9)$$

Finally, the extinction coefficients  $\varepsilon$  for solving Equation 8.7 and Equation 8.8 can be extracted from standard absorption spectra measurements such as [17]. Table 8.1 shows the extinction coefficients obtained from Zijlstra et al. for oxygenated and deoxygenated haemoglobin, at the red and infrared wavelengths employed in the reflectance sensors described in Chapter 6 (660 nm and 880 nm).

The method described above allows to estimate relative changes in oxygenated, deoxygenated, and total haemoglobin from dual-wavelength PPG signals. This method is at the core of this research work and it has been applied for the determination of perfusion changes from PPG signals in the *in vivo* studies described in the next chapters.

## 8.5 Summary

After presenting the PPG sensors and processing system in Chapter 6 and Chapter 7, this chapter described the software application used to acquire PPG signals. The application was developed in LabVIEW for acquisition, display, and archiving of all the acquired signals. The application was also extended for the simultaneous acquisition of signals from other devices such as NIRS. In the second part of the chapter, the application of the modified Beer-Lambert law to PPG signals was described and discussed. The method was investigated in a series of *in-vivo* studies performed on healthy volunteers. The next chapters will describe the methods and results of those investigations.

## **Investigation of photoplethysmography, Near Infrared Spectroscopy, laser Doppler flowmetry and pulse oximetry for assessing perfusion and oxygenation changes during vascular occlusions**

In the previous chapter, the application of the modified Beer-Lambert law to dual-wavelength PPG signals has been proposed and the mathematical process to infer relative changes in haemoglobin concentration has been described. The next chapters will present a series of *in vivo* studies that were performed to investigate the feasibility of using PPG signals to obtain haemoglobin concentration changes as in NIRS. In the three studies, healthy volunteers underwent vascular occlusions on the arm, head-down bed tilting, and whole-body cold exposure. Haemoglobin concentrations that were estimated from PPG signals acquired from the forearm, forehead, finger, and ear canal were compared with state-of-the-art NIRS measurements.

The principles of different optical techniques such as NIRS, PPG, pulse oximetry, and laser Doppler flowmetry have been introduced in Chapter 3, Chapter 4, and Chapter 5. These noninvasive techniques are used daily for the clinical assessment of blood volume, blood oxygenation, and blood flow. In this chapter, a vascular occlusion study on healthy volunteers is presented. The PPG signals acquired from a custom-made system are used to infer haemoglobin concentrations, as done in NIRS. In the first part of this

chapter, comparative analysis between haemoglobin concentrations estimated by PPG and NIRS is presented. In the second part of the chapter, the simultaneous responses of several parameters obtained by different non-invasive optical techniques such as NIRS, PPG, pulse oximetry, and laser Doppler flowmetry are presented, analysed and compared.

## 9.1 Introduction

In Chapter 4, the Photoplethysmography technique was presented. The technique has found a main application for the non-invasive estimation of arterial oxygen saturation ( $\text{SpO}_2$ ) by pulse oximetry [1, 3, 4, 9, 106, 176]. However, the success and potential of pulse oximetry have almost obscured the potentials of the PPG signal in providing physiological information other than  $\text{SpO}_2$  [9]. The pulsatile component of the signal has also found another fundamental usage by providing the heart rate [1, 9, 68, 177]. In addition, the visual display of the pulsatile part of the PPG signal has an indisputable importance in clinical settings such as anaesthesia and emergency and can have huge impacts in the daily clinical care. In fact, contrary to other haemodynamic signals, the PPG curve in a standard pulse oximeter can be visualised within just a few seconds, by applying a single sensor on the fingertip, earlobe, or forehead. In this context, the steady DC component of the PPG signal is almost neglected. The component is used in the calculation of the ratio of ratios and it contributes to the calculation of the perfusion index [3, 4, 80, 82, 106, 178]. In these situations, the DC component is just a factor in the formula, and it is almost irrelevant compared to the more notorious pulsatile component. So far, the most important applications of the DC PPG are the estimation of respiratory rates and the calculation of venous oxygen saturation [1, 115, 116].

While the AC PPG mainly contains information on the pulsating arterial blood, the DC component carries information on different structures within the interrogated tissue [1–3]. The signal is composed of almost-static arterial blood, venous blood, skin, fat, bones, and all the structure interrogated within the light path [3]. Therefore, the DC PPG contains plenty of physiological information that has been timidly investigated in the literature [2, 41, 79]. The assumption is that the DC PPG component already acquired by PPG systems, and being only used for calculating  $\text{SpO}_2$  and perfusion index,

can be used to estimate other important haemodynamic and oxygenation information. Following the NIRS example, where the pulsatile component is neglected and only the DC part is used [12], the DC PPG components could be exploited. In particular, if the DC PPG is measured at two distinct wavelengths (like always done in pulse oximeters), the relative concentrations of oxygenated ( $\text{HbO}_2$ ) and deoxygenated (reduced) haemoglobin (HHb) can be derived, as performed in NIRS.

The first aim of this study was to investigate the feasibility of applying NIRS analysis (modified Beer-Lambert law) to PPG signals in order to infer relative changes in the concentrations of oxygenated, deoxygenated, and total haemoglobin. These were compared with standard NIRS-measured parameters simultaneously acquired during the study.

The second aim of this study is to investigate the simultaneous behaviour of NIRS, photoplethysmography, pulse oximetry, and laser Doppler flowmetry during proximal vascular occlusions. These techniques have been investigated singularly, or in pair, in their ability to indicate haemodynamic changes during vascular occlusions [38, 41, 118, 157, 179–181]. However, the results from these studies are scattered due to different methods, applications, anatomical areas, or population investigated. To the author's knowledge, there has not been an attempt to investigate all these techniques simultaneously. Therefore, NIRS, laser Doppler flowmetry, PPG, and pulse oximetry sensors were applied on the forearm and digits of healthy volunteers and two sets of vascular occlusions were induced by inflating a pressure cuff on the upper arm. The response of Tissue Oxygenation Index and normalised Tissue Haemoglobin Index from NIRS, Flux from laser Doppler flowmetry,  $\text{SpO}_2$  from pulse oximetry, perfusion index and optical densities from finger PPG were simultaneously recorded, analysed and compared.

## 9.2 Measurements set-up, protocols and data analysis

### 9.2.1 Measurement system

The research PPG processing unit (ZenPPG) presented in Chapter 7 was used to acquire raw PPG signals (AC+DC).

A commercial NIRS monitor (NIRO 200NX, Hamamatsu Photonics, Japan) was used to acquire NIRS signals. The device uses LEDs to shine light at three different wavelengths (735, 810 and 850 nm) [182]. The backscattered light is then detected by two silicon photodiodes placed close to each other. The NIRO 200NX applies the modified Beer-Lambert law to the light attenuations measured by a single photodiode for the estimation of relative concentration changes in oxygenated haemoglobin ( $\Delta\text{HbO}_2$ ), deoxygenated (reduced) haemoglobin ( $\Delta\text{HHb}$ ), and total haemoglobin ( $\Delta\text{tHb}$ ) [182]. Furthermore, Spatially Resolved Spectroscopy is adopted for the estimate of the Tissue Oxygenation Index (TOI), expressed as the ratio of concentrations of  $\text{HbO}_2$  over  $\text{tHb}$  [124,182]. The monitor measures the Normalised Tissue Haemoglobin Index (nTHI) as the normalised changes of concentrations of  $\text{tHb}$  from the start of the measurement. The nTHI has a baseline value of 1 and its changes reflect the variations in haemoglobin (blood volume) in the measured tissue. Appendix B illustrates the NIRO 200NX's specifications in details.

A laser Doppler flowmetry device (moorVMS-LDF2, Moor Instruments Ltd, UK) was used to measure blood flow in the skin. The device employs laser light with peak emission at 785 nm and fibre optics to transmit the light [183]. The VP1T sensor, with a fibres separation distance of 0.5 mm, was used to measure the blood flow in this experiment [183]. The Doppler shift from RBC is measured from the detected light and the blood flow is expressed as Flux, a unit-less index [183].

A commercial pulse oximeter (Radical 7, Masimo Corp., USA) was adopted as a reference for arterial oxygen saturation ( $\text{SpO}_2$ ) measurements.

Signals were acquired in LabVIEW through two 16-bit NI-PcIe 6321 Data Acquisition Cards (National Instruments, USA). The VI described in Chapter 8 was adapted for the additional acquisition of signals from the laser Doppler flowmeter and the pulse

oximeter. Analogue outputs scaling equations were obtained from all the devices as described in subsection 8.3.5. All signals were acquired simultaneously at a sampling frequency of 400 Hz and they were saved in a text file for post-acquisition analysis.

### 9.2.2 Subjects and investigation set-up

Nineteen (19) healthy subjects with mean age  $\pm$  SD of  $31.05 \pm 7.07$  (12 males and 7 females) were recruited for the investigation. Ethical approval was granted by the Senate Research Ethics Committee at City University London and written consent was sought from the volunteers before commencing of the investigation. Subjects with a history of cardiovascular disorders were excluded from the study.

The subjects were seated in a comfortable chair in the Biomedical laboratory at City University London. After measuring the subject's arterial blood pressure by an automatic blood pressure monitor (HEM-907, Omron Healthcare, USA), the subject's left arm was rested on a pillow in order to avoid excessive vascular compression on the forearm. The room was kept at a constant temperature of  $23 (\pm 1) ^\circ\text{C}$  throughout the entire measurements.

The NIRS sensor was placed on the left forearm, above the brachioradialis and it was kept in place by double-sided clear medical adhesive tape. The tape was cut at the emitter and detectors locations in order to avoid any optical obstruction by the tape. An emitter-detector distance of 4 cm was used in order to maximise the light penetration. The LDF VP1T sensor was placed on the forearm's skin, proximal to the NIRS sensor. The LDF sensor was kept in place by ring-shaped adhesive pads provided by the manufacturer. The RPS1 sensor (Chapter 6) was positioned on the volar side of the same left forearm, distal from the NIRS sensor. The PPG reflectance sensor was attached to the skin by means of a double-sided clear medical adhesive tape. Again, the tape was cut in the centre, at the optical components position, in order to avoid optical obstruction. The sensor was connected to the first channel of the ZenPPG. PPG signals were also acquired from the fingers. The finger PPG sensor (Section 6.6) was attached to the second digit of the left hand. In addition, the commercial pulse oximeter sensor was connected to the third digit of the same hand, in order to measure arterial oxygen saturation ( $\text{SpO}_2$ ).



**Figure 9.1:** Measurement system set-up (a) and placement of PPG, NIRS, and LDF sensors on the forearm (b).

A blood pressure cuff was wrapped around the upper left arm. In order to induce vascular occlusions on the forearm, the cuff was connected to a manual sphygmomanometer (Big Ben Round, Riester GmbH, Germany). Figure 9.1a and Figure 9.1b show the set-up of the investigation in the laboratory and the positioning of PPG, NIRS, and laser Doppler sensors on the forearm.

### 9.2.3 Investigation protocols

The investigation consisted of different degrees of vascular occlusions on the forearm. Two sets of measurement protocols were used:

- Protocol 1: baseline measurements were acquired for five minutes followed by two minutes of venous occlusion at 60 mmHg. The cuff pressure was then released for two minutes before being re-inflated for additional two minutes at 20 mmHg exceeding the volunteer's systolic pressure. The cuff was finally released until all the signals returned to their baseline values.
- Protocol 2: five minutes baseline measurements were followed by seven intermittent occlusions at 20 mmHg, 40 mmHg, 60 mmHg, 80 mmHg, 100 mmHg, the volunteer's systolic pressure, and total occlusion (20 mmHg over the volunteer's systolic pressure). Each occlusion lasted for one minute and it was followed by one minute of recovery period when the pressure was released. After the last occlusion (total occlusion), measurements continued until the signals returned to baseline values.

The inflations and deflations of the cuff were performed manually by means of a bulb and a valve connected to the sphygmomanometer. The maximum cuff inflation time was 5 seconds (for total occlusion), whereas complete deflation time did not exceed 3 seconds. Participants rested for a minimum of 10-15 minutes between the two different protocols in order to allow a full haemodynamic recovery. ECG was monitored throughout the experimental protocols.

#### 9.2.4 Data analysis & statistics

Post-acquisition analysis was performed in Matlab2013a. Before processing, all the acquired signals were down-sampled to 100 Hz. TOI, nTHI, haemoglobin concentrations from NIRS, and Flux signals were cleaned from any high-frequency noise by a zero-phase low-pass filter ( $f_c = 0.05$  Hz). In order to reduce inter-subject variability and assess only the degree of change, the Flux signals were normalised with respect to 10 seconds baseline reading (nFlux). The finger AC PPG component was obtained from raw PPG signals by applying a zero-phase band-pass filter (pass-band: 0.5-5 Hz), while the forearm AC PPG was extracted by another band-pass filter with passband 0.5-4 Hz. The DC PPGs were obtained by low-pass filtering the signal at  $f_c = 0.1$  Hz. SpO<sub>2</sub> was estimated from both the finger and forearm PPG signals by applying Equation 9.1 in a three-seconds rolling window. Perfusion index was calculated from infrared PPG signals as showed in Equation 9.2, and it was normalised to 10 seconds baseline readings to compensate for inter-subject variability (nPI).

$$SpO_2 = 110 - (25 \cdot R); \text{ Where: } R = \frac{AC_R/DC_R}{AC_{IR}/DC_{IR}} \quad (9.1)$$

$$PI = \frac{AC_{IR}}{DC_{IR}} \times 100 \quad (9.2)$$

Changes in oxygenated ( $\Delta\text{HbO}_2$ ), reduced ( $\Delta\text{HHb}$ ) and total haemoglobin ( $\Delta\text{tHb}$ ) were estimated by applying the modified Beer-Lambert law to DC PPG signals acquired from the forearm. From these, the index  $\text{Hb}_{ratio}$ , expressing changes in oxygenations, was calculated from the ratio  $\text{Hb}_{ratio} = \Delta\text{HbO}_2 / \Delta\text{tHb}$ . The index indicates the relative

changes in oxygenation from a starting baseline and it was expressed as percentage changes.

The dynamic changes of the signals during the occlusions were expressed by the slopes of the changes. The slopes were computed as the slope of the regression line on the data during each occlusion, and they were expressed as unit measure/minute, depending on the variable (e.g. %/min for TOI). In order to test the difference in magnitude of the measured variables between baseline and occlusions, the signals were averaged over a period of 30 seconds during baseline and the last 30 seconds of each occlusion.

Trending agreement between techniques or variables was assessed by measuring the Pearson correlation coefficients  $r$  and the 95 % confidence intervals (CI). In addition, the trending was evaluated by four-quadrant plot analysis [184]. The concordance rate  $C$  was calculated as the ratio of the number of points in the first and third quadrant and the total number of points in all quadrants. An exclusion zone of 10 % was used for the calculations [184]. A concordance rate  $C \geq 90$  % was considered satisfactory for indicating trending agreement.

Statistically significant changes from baseline were tested by repeated measures using a Wilcoxon signed-rank test. A p-value less than 0.05 was considered satisfactory for significance.

### 9.3 Results

Figure 9.2 illustrates the acquired signals from a volunteer during protocol 1. The acquired signals indicated changes in perfusion and oxygenation during the vascular occlusions. These responses are analysed in detail in the next sections. Figure 9.3 shows an example of ten seconds readings of AC PPG signals acquired from the forearm and fingers. Good quality AC PPG signals were acquired from the custom-made sensors (ZenPPG) and were comparable with the PPG signals acquired from the standard pulse oximeter.

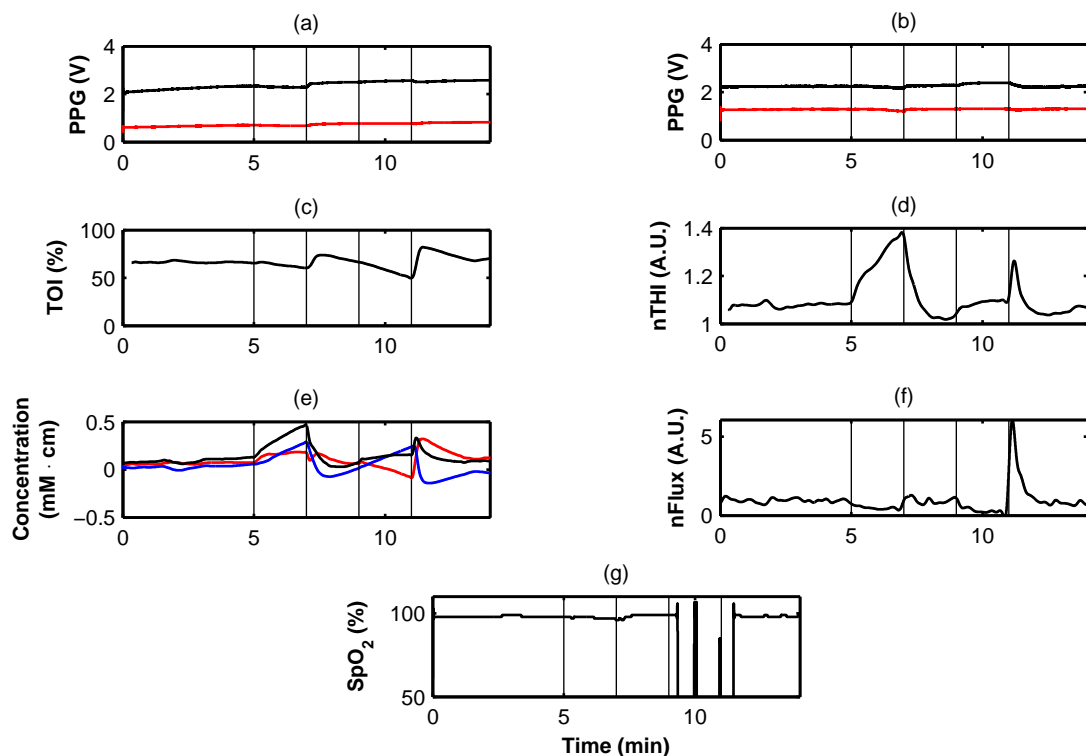


**Figure 9.2:** Example of PPG, NIRS, laser Doppler, and pulse oximetry signals acquired from a volunteer. (a) Red and infrared raw PPG (AC + DC) acquired from the forearm. (b) Red and infrared raw PPG (AC + DC) acquired from the finger. (c) TOI from NIRS. (d) nTHI from NIRS. (e) Relative haemoglobin concentrations from NIRS. Red trace:  $\Delta\text{HbO}_2$ ; blue trace:  $\Delta\text{HHb}$ ; black trace:  $\Delta\text{tHb}$ . (f) normalised Flux from laser Doppler flowmetry. (g)  $\text{SpO}_2$  from the commercial pulse oximeter. Vertical lines indicate the duration of the occlusions. Five minutes of baseline measurements were followed by two minutes of venous occlusion, two minutes of recovery, two minutes of total occlusion, and final recovery to baseline.

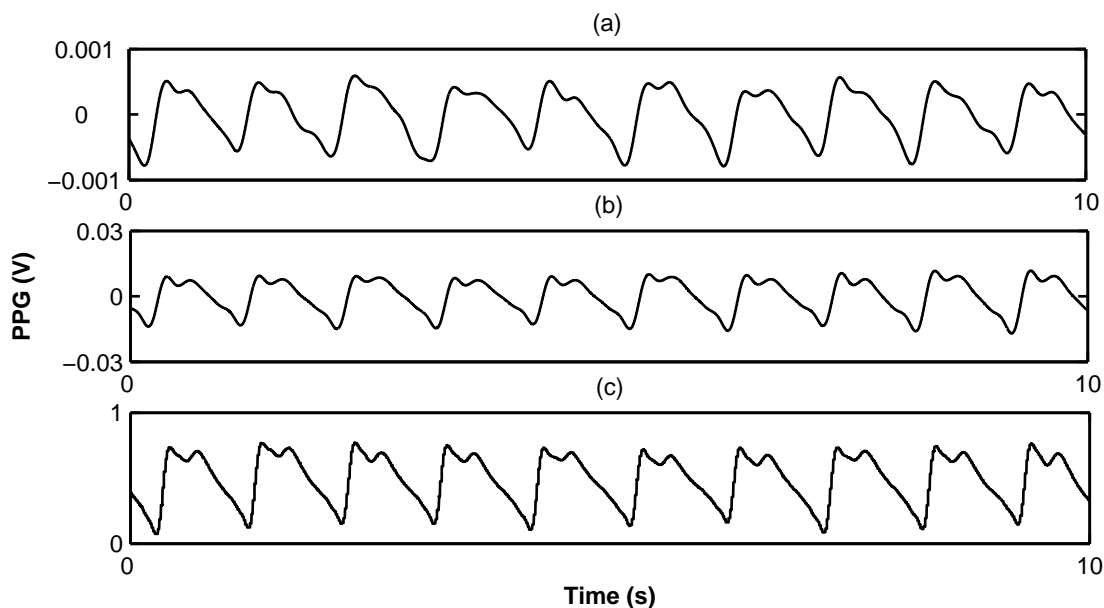


**Figure 9.3:** Infrared AC PPG signal acquired from forearm (a), fingers by custom-made PPG (b), and from commercial pulse oximeter (c).

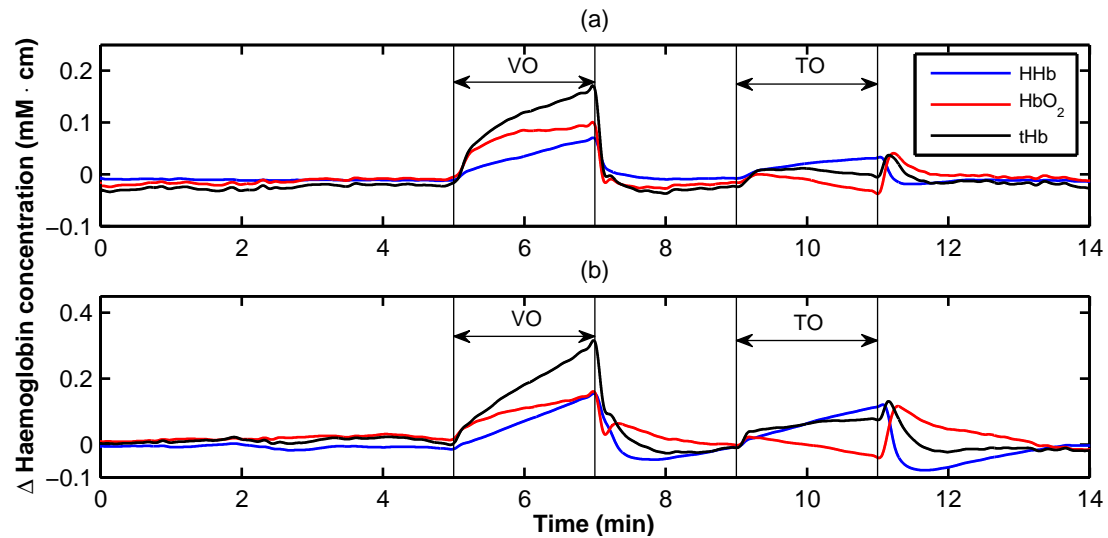


**Figure 9.4:** Example of relative haemoglobin concentrations changes estimated by PPG (a) and NIRS (b). Vertical lines indicate the duration of the occlusions. Five minutes of baseline measurements were followed by two minutes of venous occlusion (VO), two minutes of recovery, two minutes of total occlusion (TO), and final recovery to baseline. HHb: deoxygenated haemoglobin; HbO<sub>2</sub>: oxygenated haemoglobin; tHb: total haemoglobin.

### 9.3.1 Haemoglobin concentration changes from PPG signals

Changes in relative concentrations of oxygenated, reduced, and total haemoglobin were estimated from DC PPG signals as done in conventional NIRS. Figure 9.4 illustrates an example of  $\Delta\text{HbO}_2$ ,  $\Delta\text{HHb}$ , and  $\Delta\text{tHb}$  estimated from PPG, along with the same parameters estimated by NIRS. As can be seen from Figure 9.4, the relative haemoglobin concentrations estimated by PPG changed consistently during the occlusions and these responses are described in detail in this section.

Figure 9.5 shows the mean changes among all subjects of  $\Delta\text{HbO}_2$ ,  $\Delta\text{HHb}$ , and  $\Delta\text{tHb}$  estimated from PPG and NIRS during the venous occlusion in the first protocol. The occlusion at 60 mmHg occluded the veins, with a consequent congestion of venous blood in the forearm. The accumulation of venous blood can be seen in Figure 9.5 by the increase of reduced haemoglobin. This increase progressed until the occlusion was released after two minutes. The occlusion of the venous branch of the circulation in the forearm also caused an increase in concentration of the oxygenated haemoglobin, due to the blockage of the arterial-to-venous blood flow. The total haemoglobin tHb, which is the sum of oxygenated and reduced haemoglobin and represents the total blood volume, increased as well during venous occlusion. This corresponded to the incremental venous blood engorgement in the forearm. At the release of the occlusion, all parameters returned to baseline values.

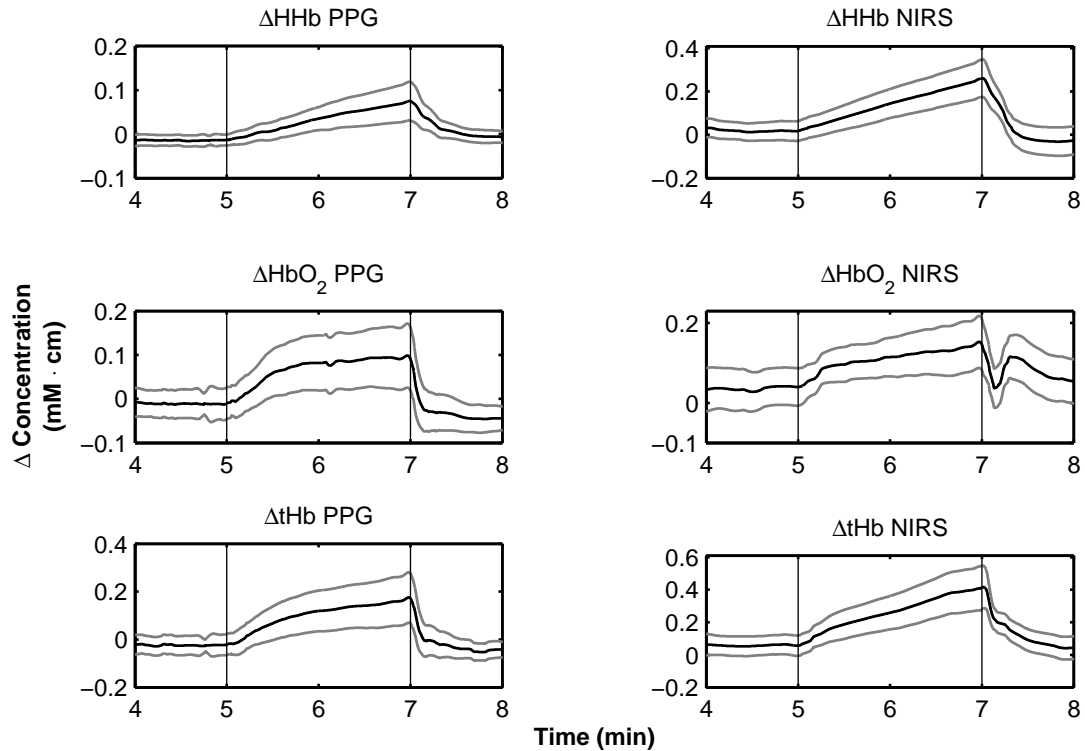


**Figure 9.5:** Mean ( $\pm$ SD) changes in relative haemoglobin concentrations estimated from PPG and NIRS during venous occlusion in the first protocol. Black traces are the means; grey traces are  $\pm$  SD.  $\Delta\text{HbO}_2$ : oxygenated haemoglobin;  $\Delta\text{HHb}$ : deoxygenated haemoglobin;  $\Delta\text{tHb}$ : total haemoglobin. Vertical lines represent the inflation and deflation of the cuff. The occlusion pressure was 60 mmHg and it lasted for two minutes. PPG and NIRS measurements have been plotted on different y-axis scales to facilitate the visual assessment of the trends.

Figure 9.6 shows the mean changes among all subjects of  $\Delta\text{HbO}_2$ ,  $\Delta\text{HHb}$ , and  $\Delta\text{tHb}$  estimated from PPG and NIRS during the total occlusion in the first protocol. During total (over-systolic) occlusion, the reduced haemoglobin increased again due to the impediment of venous blood return. The occlusion of the arterial circulation caused a drop in oxygenated haemoglobin concentration. After slowly increasing at the beginning of the occlusion, the total haemoglobin  $\Delta\text{tHb}$  reached a steady state. This was due to null arterial-to-venous flow caused by occlusion of both arterial and venous circulation in the forearm. The initial increase in  $\Delta\text{tHb}$  at the commencement of the total occlusion was caused by a residual venous engorgement due to the non-instantaneous (i.e. 3-5 seconds) inflation of the cuff. At the release of the occlusion, the rapid increase of  $\Delta\text{HbO}_2$  and  $\Delta\text{tHb}$  indicated the post-occlusion reactive hyperaemia. After this, the signals returned to baseline readings.

Table 9.1 summarises the mean values of  $\Delta\text{HbO}_2$ ,  $\Delta\text{HHb}$ , and  $\Delta\text{tHb}$  estimated by both PPG and NIRS during the first protocol. The relative haemoglobin concentrations had significant changes from baseline ( $p < 0.05$ ) in both venous and total occlusion.

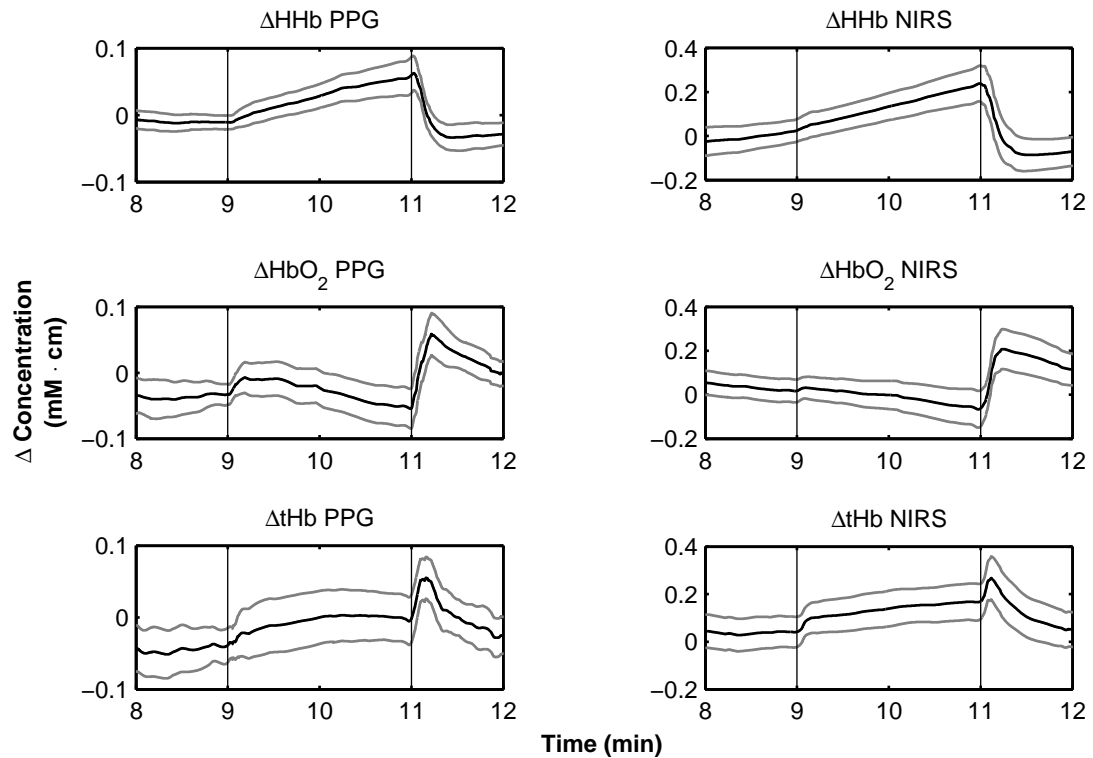


**Figure 9.6:** Mean ( $\pm$ SD) changes in relative haemoglobin concentrations estimated from PPG and NIRS during total occlusion in the first protocol. Black traces are the means; grey traces are  $\pm$  SD.  $\Delta$ HbO<sub>2</sub>: oxygenated haemoglobin;  $\Delta$ HHb: deoxygenated haemoglobin;  $\Delta$ tHb: total haemoglobin. Vertical lines represent the inflation and deflation of the cuff. The occlusion pressure was 20 mmHg over the subjects' systolic pressure and it lasted for two minutes. PPG and NIRS measurements have been plotted on different y-axis scales to facilitate the visual assessment of the trends.

**Table 9.1:** [Mean changes ( $\pm$ SD), in mM·cm, of relative haemoglobin concentrations changes estimated by PPG and NIRS during baseline, venous occlusion, and total occlusion. The values are the average of 30 s baseline, and the last 30 s of each occlusion.

	Baseline (mM·cm)	Venous Occlusion (mM·cm)	Total Occlusion (mM·cm)
$\Delta$ HbO <sub>2</sub> (PPG)	-0.015 $\pm$ 0.022	0.092 $\pm$ 0.076*	-0.048 $\pm$ 0.029*
$\Delta$ HHb (PPG)	0.010 $\pm$ 0.040	0.063 $\pm$ 0.040*	0.051 $\pm$ 0.024*
$\Delta$ tHb (PPG)	0.023 $\pm$ 0.029	0.153 $\pm$ 0.102*	0.000 $\pm$ 0.034*
$\Delta$ HbO <sub>2</sub> (NIRS)	-0.021 $\pm$ 0.047	0.135 $\pm$ 0.064*	-0.050 $\pm$ 0.079*
$\Delta$ HHb (NIRS)	0.026 $\pm$ 0.045	0.227 $\pm$ 0.082*	0.210 $\pm$ 0.076*
$\Delta$ tHb (NIRS)	0.063 $\pm$ 0.069	0.385 $\pm$ 0.132*	0.164 $\pm$ 0.077*

\* Significant change from baseline ( $p < 0.05$ )

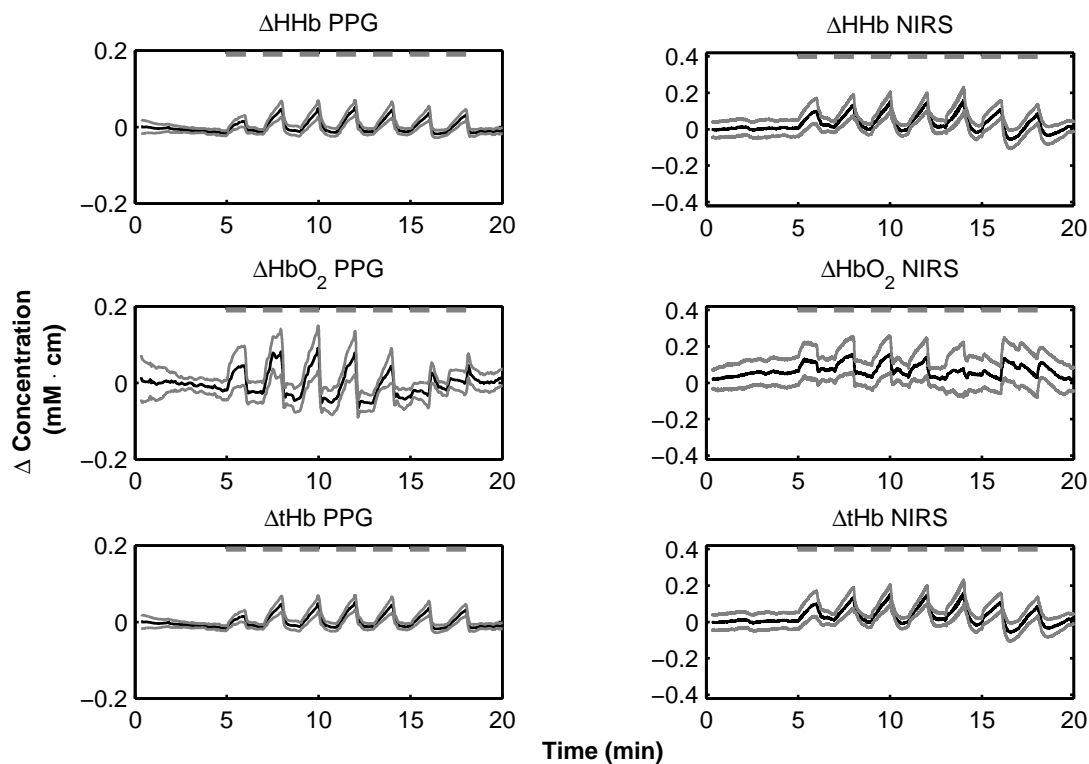


**Figure 9.7:** Mean ( $\pm$ SD) changes in relative haemoglobin concentrations during the second protocol. Black traces are the means; grey traces are  $\pm$  SD.  $\Delta\text{HbO}_2$ : oxygenated haemoglobin;  $\Delta\text{HHb}$ : deoxygenated haemoglobin;  $\Delta\text{tHb}$ : total haemoglobin. Grey horizontal bars on top represent the duration of the occlusions. The order of the occlusions was 20 mmHg, 40 mmHg, 60 mmHg, 80 mmHg, 100 mmHg, subject's systolic pressure, and over-systolic pressure. Each occlusion lasted for one minute and it was followed by one-minute recovery.

The second protocol aimed at investigating the responses to different degrees of vascular occlusions. Figure 9.7 shows the mean changes of  $\Delta\text{HbO}_2$ ,  $\Delta\text{HHb}$ , and  $\Delta\text{tHb}$  during the different occlusions of the second protocol. The relative haemoglobin concentrations estimated from PPG were able to respond to all the different occlusions induced. Even small venous occlusions of 20 mmHg and 40 mmHg were indicated by the parameters and the haemoglobin concentrations followed the responses of the same parameters measured by NIRS. Table 9.2 summarises the mean values of  $\Delta\text{HbO}_2$ ,  $\Delta\text{HHb}$ , and  $\Delta\text{tHb}$  estimated by the two methods during the steps of the second protocol. The table also shows the results of the significance tests, showing that there were significant changes from baseline ( $p < 0.05$ ) in almost all occlusions.

The haemoglobin concentrations estimated from PPG presented some quantitative differences from the haemoglobin concentrations measured by NIRS. This is most probably due to the different penetration depths and the different wavelengths adopted. To investigate this, the Bland & Altman plots were used to analyse these differences. However, since there cannot be limits of agreement set *a priori*, the ratio of the two measures

**Table 9.2:** Mean changes ( $\pm$ SD) in  $\Delta$ HbO<sub>2</sub>,  $\Delta$ HHb, and  $\Delta$ tHb estimated by both PPG and NIRS during the second protocol. The values are in mM · cm and were averaged over 30 s of baseline and the last 30 s of each occlusion. There were significant changes from baseline in all the occlusions, except when indicated.

	Baseline	Occlusion Steps (mmHg)						Systolic	Total
		20	40	60	80	100	100		
$\Delta$ HbO <sub>2</sub> (PPG)	0.000 $\pm$ 0.024	0.040 $\pm$ 0.051	0.065 $\pm$ 0.060	0.061 $\pm$ 0.056	0.060 $\pm$ 0.057	0.024 $\pm$ 0.048	-0.026 $\pm$ 0.026	0.007 $\pm$ 0.032*	
$\Delta$ HHb (PPG)	-0.005 $\pm$ 0.008	0.013 $\pm$ 0.014	0.034 $\pm$ 0.018	0.030 $\pm$ 0.018	0.037 $\pm$ 0.016	0.030 $\pm$ 0.017	0.022 $\pm$ 0.014	0.021 $\pm$ 0.013	
$\Delta$ tHb (PPG)	-0.006 $\pm$ 0.030	0.059 $\pm$ 0.061	0.099 $\pm$ 0.074	0.091 $\pm$ 0.066	0.091 $\pm$ 0.063	0.046 $\pm$ 0.057	-0.001 $\pm$ 0.029*	0.024 $\pm$ 0.036	
$\Delta$ HbO <sub>2</sub> (NIRS)	0.049 $\pm$ 0.075	0.115 $\pm$ 0.098	0.143 $\pm$ 0.097	0.137 $\pm$ 0.100	0.109 $\pm$ 0.103	0.062 $\pm$ 0.137	0.030 $\pm$ 0.081*	0.052 $\pm$ 0.111*	
$\Delta$ HHb (NIRS)	0.005 $\pm$ 0.043	0.088 $\pm$ 0.065	0.102 $\pm$ 0.054	0.109 $\pm$ 0.049	0.108 $\pm$ 0.042	0.114 $\pm$ 0.064	0.083 $\pm$ 0.051	0.054 $\pm$ 0.050	
$\Delta$ tHb (NIRS)	0.044 $\pm$ 0.104	0.186 $\pm$ 0.148	0.253 $\pm$ 0.143	0.255 $\pm$ 0.138	0.228 $\pm$ 0.143	0.190 $\pm$ 0.194	0.126 $\pm$ 0.107	0.120 $\pm$ 0.124	

\* Not significant change from baseline ( $p > 0.05$ )

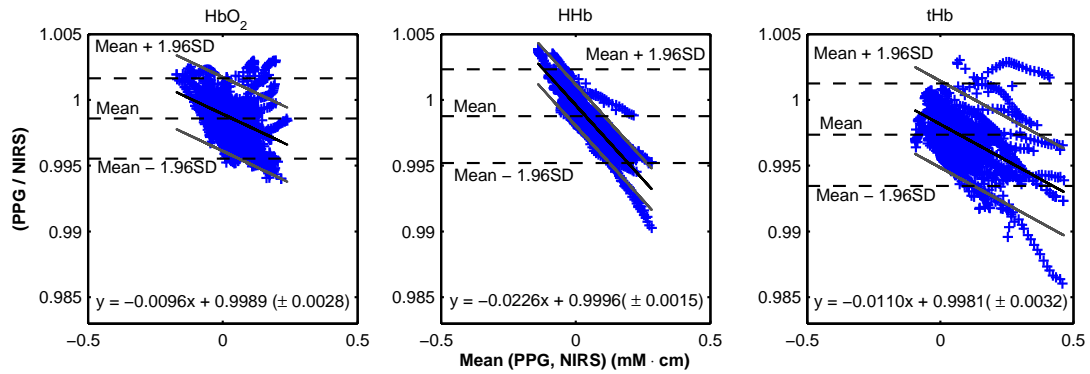


**Figure 9.8:** Bland & Altman plots and analysis of the haemoglobin concentrations estimated from PPG against the reference NIRS method during the first protocol. X-axes are the mean between the two methods, while the y-axes are the ratio of the measures. Blue crosses are the data. Horizontal solid lines are the standard mean bias and the dashed lines are the standard limits of agreement (mean  $\pm$  1.96SD). The black solid line is the regression line on the data, representing the mean bias. The grey lines are the  $\pm$  95 % confidence intervals. The equation of the fitted regression line is reproduced at the bottom of the graphs. The original signals were resampled every 5 seconds.

was used instead of the absolute difference [185, 186]. This method still provides comparative information on the two measures.

Figure 9.8 shows the Bland & Altman plots of the haemoglobin concentration estimated from PPG against the reference NIRS method during the first protocol. The dashed lines in the figure show the limits of agreements between the two methods, calculated with the standard Bland & Altman analysis [185]. The mean bias difference  $\pm$  1.96SD (i.e. 95 % C.I.) for  $\Delta\text{HbO}_2$ ,  $\Delta\text{HHb}$ , and  $\Delta\text{tHb}$  were  $0.9986 \pm 0.0031$ ,  $0.9987 \pm 0.0035$ , and  $0.9973 \pm 0.0039$  respectively. These represent the mean bias ratio and suggest an overall underestimation of PPG against NIRS. However, the mean bias between the two methods varied over the ranges of measurements (average). In particular, the mean bias ratio between the measures seemed to decrease when the measurements increased. Thus, a regression line was fitted to the data as suggested by Bland and Altman [186]. The line and the 95 % C.I. are plotted on the data, along with the equation line.

The same Bland & Altman analysis was performed on the haemoglobin concentrations estimated during the second protocol. Figure 9.9 illustrates the Bland & Altman plots for the second protocol. The standard limits of agreement for  $\Delta\text{HbO}_2$ ,  $\Delta\text{HHb}$ , and  $\Delta\text{tHb}$  were respectively  $0.9985 \pm 0.0035$ ,  $0.9992 \pm 0.0022$ , and  $0.9978 \pm 0.0047$ . These values were very similar to those calculated for the first protocol. In addition, the slopes of the fitted regression lines for the second protocol were very similar to the first protocol. This indicated the presence of a regular bias between the two techniques and

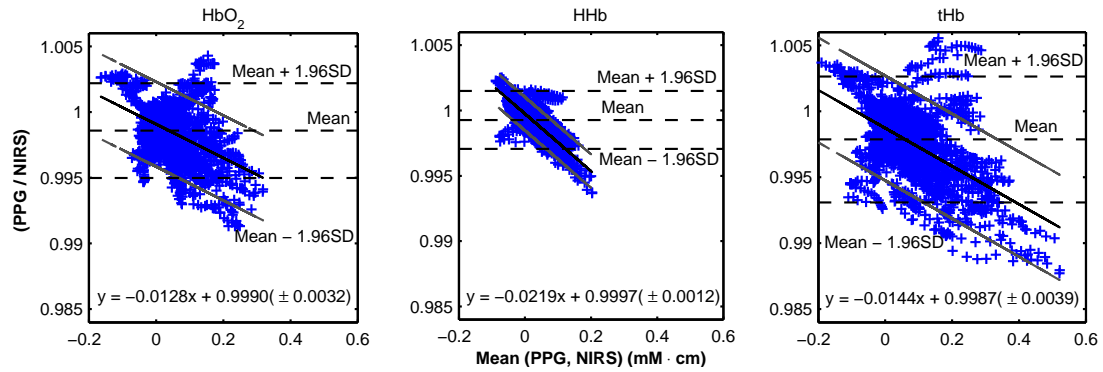


**Figure 9.9:** Bland & Altman plots and analysis of the haemoglobin concentrations estimated from PPG against the reference NIRS method during the second protocol. X-axes are the mean between the two methods, while the y-axes are the ratio of the measures. Blue crosses are the data. Dashed lines are the standard mean and limits of agreement (mean  $\pm$  1.96SD). The black line is the regression line on the data, representing the mean bias. The grey lines are the  $\pm$  95 % confidence intervals. The equation of the fitted regression line is reproduced at the bottom of the graphs. The original signals were resampled every 5 seconds.

a good repeatability of the measurements.

### 9.3.2 Assessment of correlation and trending between PPG and NIRS

Figure 9.5, Figure 9.6, and Figure 9.7 visually showed that the relative haemoglobin concentrations estimated from PPG followed the trends of the same parameters measured by the reference NIRS monitor. The correlation between the variables measured by the two techniques was assessed by the Pearson correlation coefficient  $r$ , while the trending agreement between the measures was assessed by the concordance rate calculated from the analysis of four-quadrant plots between variables.

In the first protocol, the correlation coefficients calculated between the haemoglobin concentrations during venous occlusion were 0.74 (95 % CI: 0.46, 0.90), 0.95 (95 % CI: 0.87, 0.98), and 0.96 (95 % CI: 0.89, 0.98) for  $\Delta\text{HbO}_2$ ,  $\Delta\text{HHb}$ , and  $\Delta\text{tHb}$  respectively. The same coefficients calculated during total occlusion were 0.84 (95 % CI: 0.62, 0.93), 0.96 (95 % CI: 0.89, 0.98), and 0.80 (95 % CI: 0.54, 0.92) for  $\Delta\text{HbO}_2$ ,  $\Delta\text{HHb}$ , and  $\Delta\text{tHb}$  respectively. These values indicated high correlation between the haemoglobin concentrations estimated from PPG and NIRS.

The same correlation coefficients were calculated for  $\Delta\text{HbO}_2$ ,  $\Delta\text{HHb}$ , and  $\Delta\text{tHb}$  during the second protocol. Table 9.3 summarises the correlation coefficients calculated during the occlusions in the second protocol. Again, the haemoglobin concentrations estimated from PPG showed high correlation with NIRS during all occlusions. However, the

**Table 9.3:** Correlation coefficients between PPG and NIRS haemoglobin concentrations during the second protocol. 95 % confidence intervals are presented within parenthesis.

Occlusions	Correlation coefficient $r$		
	HbO <sub>2</sub>	HHb	tHb
20 mmHg	0.89 (0.68, 0.94)	0.89 (0.72, 0.95)	0.93 (0.81, 0.97)
40 mmHg	0.92 (0.76, 0.96)	0.94 (0.88, 0.98)	0.97 (0.92, 0.98)
60 mmHg	0.90 (0.78, 0.96)	0.96 (0.89, 0.98)	0.96 (0.91, 0.98)
80 mmHg	0.93 (0.81, 0.97)	0.97 (0.91, 0.98)	0.97 (0.92, 0.98)
100 mmHg	0.85 (0.65, 0.94)	0.97 (0.91, 0.98)	0.96 (0.91, 0.98)
Systolic	0.59 (0.10, 0.79)	0.92 (0.76, 0.96)	0.80 (0.63, 0.93)
Total	0.35 (-0.08, 0.71)	0.93 (0.85, 0.97)	0.88 (0.72, 0.95)

oxygenated haemoglobin  $\Delta\text{HbO}_2$  demonstrated a lower correlation during systolic and over-systolic occlusions.

The trending agreement between haemoglobin concentrations estimated from PPG and NIRS was assessed by four-quadrant plots as well. Figure 9.10 shows the four-quadrant plots for  $\Delta\text{HbO}_2$ ,  $\Delta\text{HHb}$ , and  $\Delta\text{tHb}$  during venous and total occlusions in the first protocol. Deoxygenated and total haemoglobin presented high concordance rate  $C$  during both venous and total occlusion. Although the high correlation, oxygenated haemoglobin did not show high trending agreement during both occlusions.

The four-quadrant analysis was carried on the haemoglobin concentrations during the second protocol as well. Figure 9.11, Figure 9.12, and Figure 9.13 illustrate the four quadrant plots of  $\Delta\text{HHb}$ ,  $\Delta\text{HbO}_2$ , and  $\Delta\text{tHb}$  throughout the occlusions in the second protocol. The concordance rates calculated indicated a high trending agreement of  $\Delta\text{HHb}$  and  $\Delta\text{tHb}$ . Again, the oxygenated haemoglobin showed a poor trending agreement during systolic and total occlusions.

### 9.3.3 Slopes from haemoglobin concentration changes

The slopes of the dynamic changes in haemoglobin concentrations from PPG and NIRS were assessed as well. In particular, the positive slope of  $\Delta\text{HHb}$  during venous occlusion and the decay of  $\Delta\text{Hb}_{Diff}$  ( $\Delta\text{Hb}_{Diff} = \Delta\text{HbO}_2 - \Delta\text{HHb}$ ) during total (over-systolic) occlusion were estimated from the signals. These features of  $\Delta\text{HHb}$  and  $\Delta\text{Hb}_{Diff}$  during venous and total occlusion have been previously recognised to provide indication of the tissue oxygen consumption [147, 148, 156].

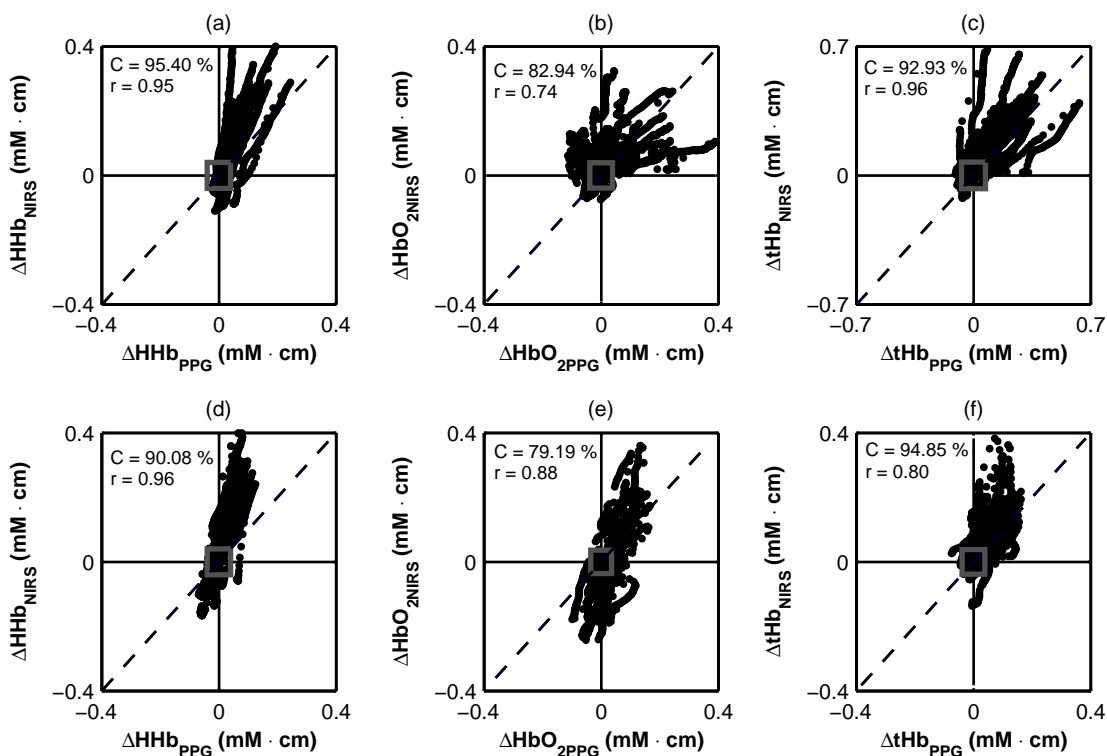


**Figure 9.10:** Four quadrant plots between  $\Delta\text{HbO}_2$ ,  $\Delta\text{HHb}$ , and  $\Delta\text{tHb}$  estimated from PPG and NIRS during venous and total occlusion in the first protocol. The concordance rate  $C$  and correlation coefficients  $r$  between the measures are presented as well. The concordance rate was calculated as the ratio of the number of points in the first and third quadrant and the total number of points in all quadrants. An exclusion zone of 10 % was used for the calculation of  $C$ . Dashed lines are the line of equality. Grey boxes indicate the 10 % exclusion zone. (a), (b), and (c) are respectively  $\Delta\text{HHb}$ ,  $\Delta\text{HbO}_2$ , and  $\Delta\text{tHb}$  during venous occlusion. (d), (e), and (f) are respectively  $\Delta\text{HHb}$ ,  $\Delta\text{HbO}_2$ , and  $\Delta\text{tHb}$  during total occlusion. Original signals were resampled every 5 seconds.

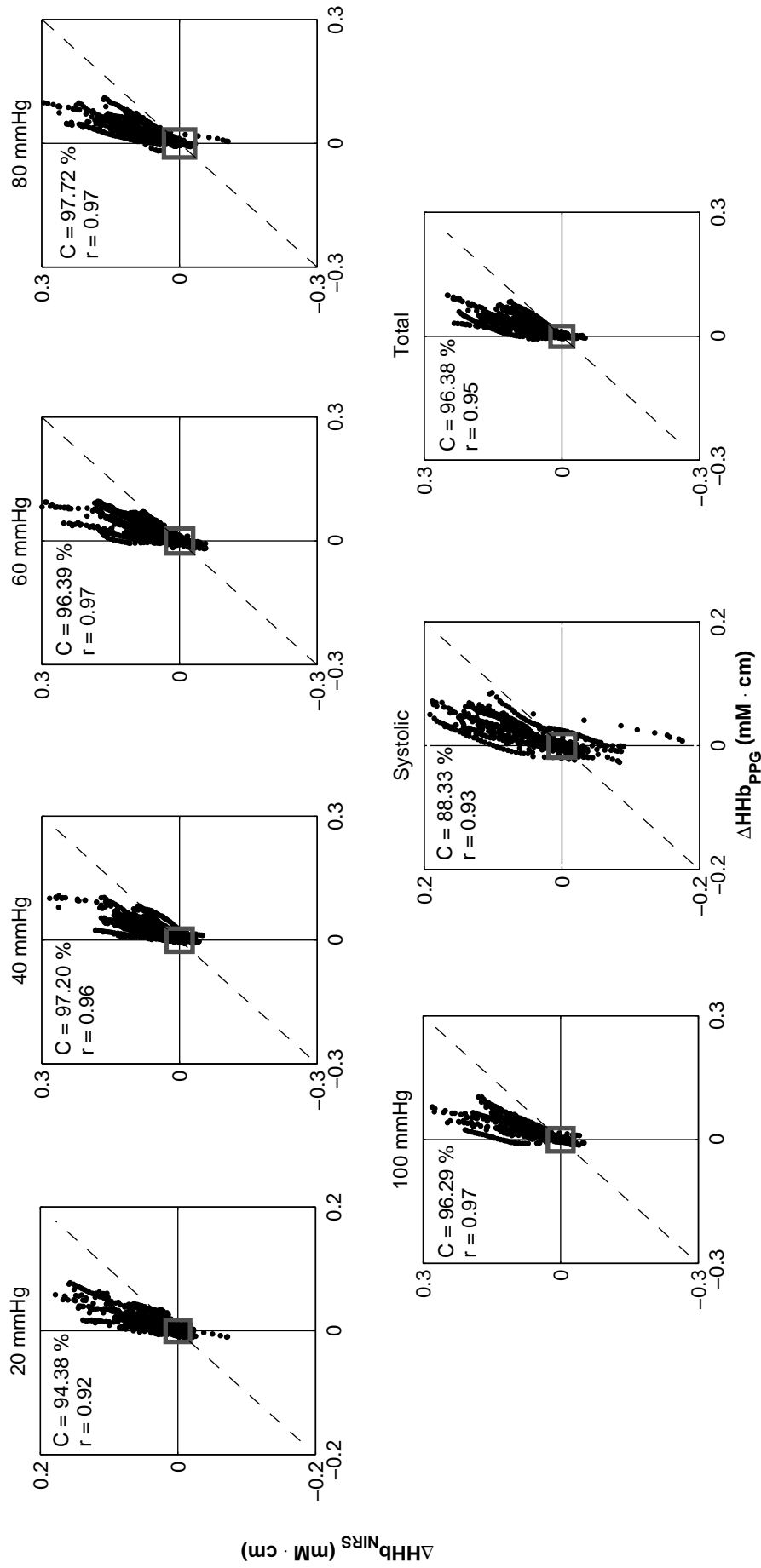


**Figure 9.11:** Four quadrant plots between deoxygenated haemoglobin ( $\Delta\text{HHb}$ ) estimated from PPG and NIRS during the second protocol. The concordance rate  $C$  and correlation coefficients  $r$  between the measures are presented as well. The concordance rate was calculated as the ratio of the number of points in the first and third quadrant and the total number of points in all quadrants. An exclusion zone of 10 % was used for the calculation of  $C$ . The dashed line is the line of equality. Grey boxes indicate the 10 % exclusion zone. X-axes are the  $\Delta\text{HHb}$  from PPG; y-axes are  $\Delta\text{HHb}$  from NIRS.

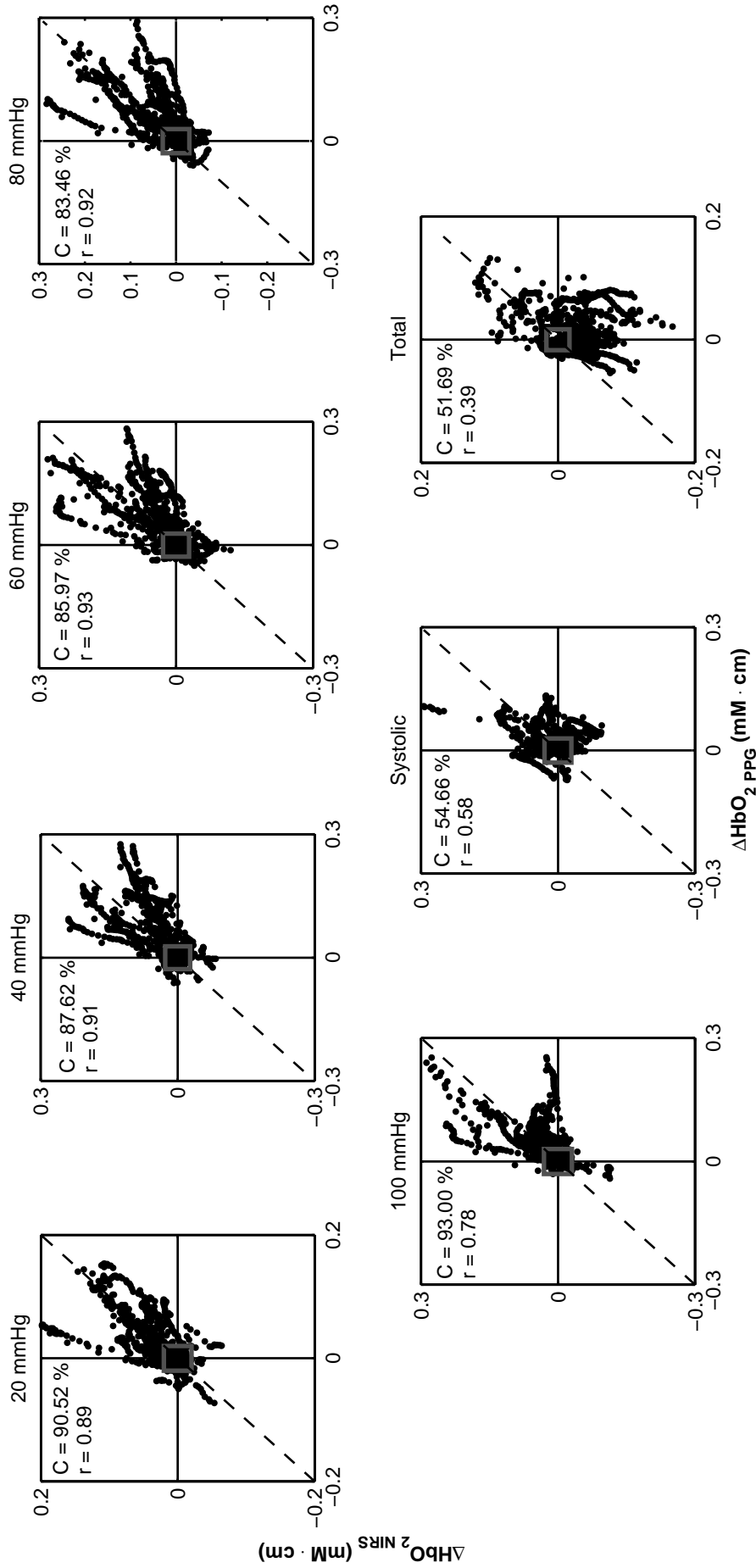


**Figure 9.12:** Four quadrant plots between oxygenated haemoglobin ( $\Delta\text{HbO}_2$ ) estimated from PPG and NIRS during the second protocol. The concordance rate  $C$  and correlation coefficients  $r$  between the measures are presented as well. The concordance rate was calculated as the ratio of the number of points in the first and third quadrant and the total number of points in all quadrants. An exclusion zone of 10 % was used for the calculation of  $C$ . The dashed line is the line of equality. Grey boxes indicate the 10 % exclusion zone. X-axes are the  $\Delta\text{HbO}_2$  from PPG; y-axes are  $\Delta\text{HbO}_2$  from NIRS.

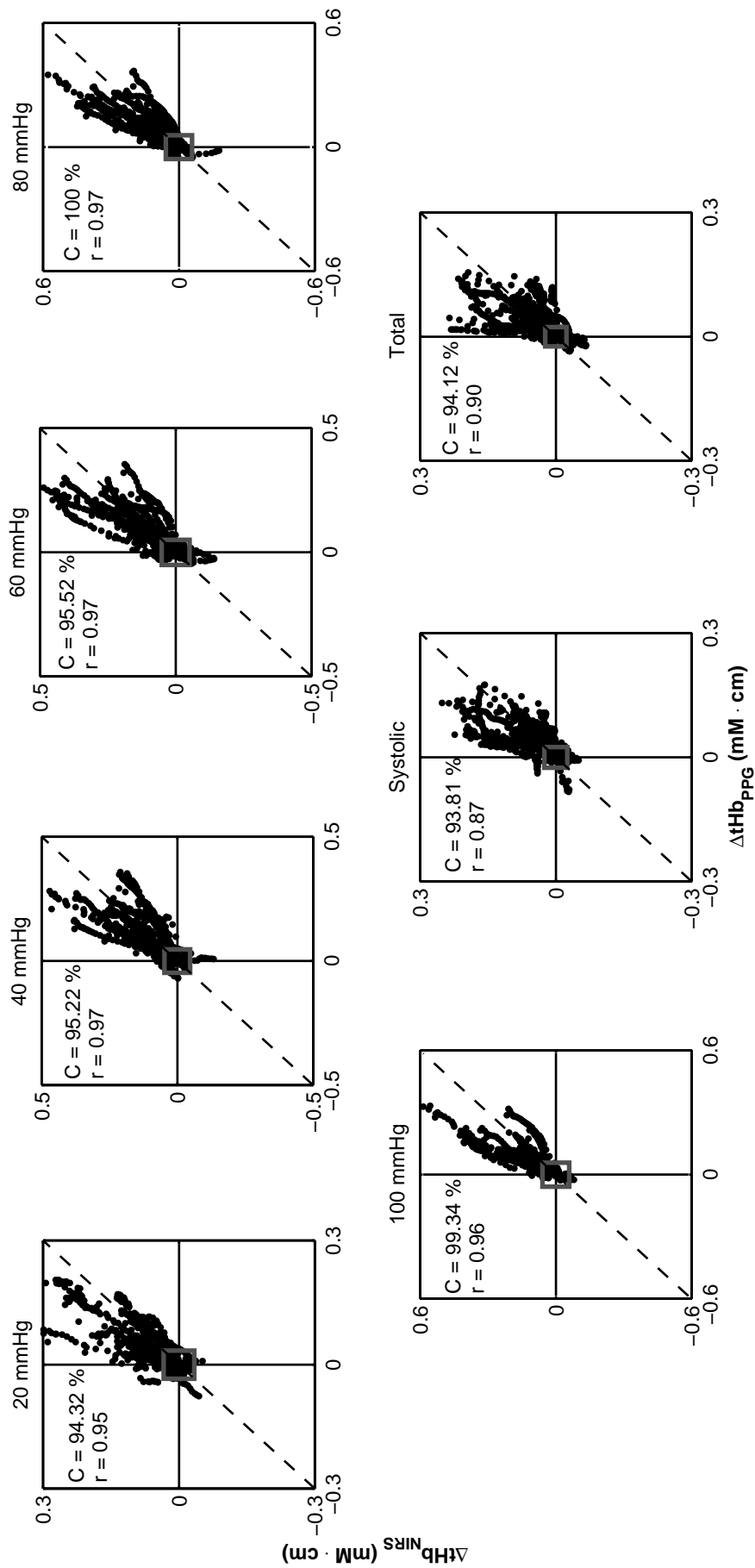


**Figure 9.13:** Four quadrant plots between total haemoglobin ( $\Delta tHb$ ) estimated from PPG and NIRS during the second protocol. The concordance rate  $C$  and correlation coefficients  $r$  between the measures are presented as well. The concordance rate was calculated as the ratio of the number of points in the first and third quadrant and the total number of points in all quadrants. An exclusion zone of 10 % was used for the calculation of  $C$ . The dashed line is the line of equality. Grey boxes indicate the 10 % exclusion zone. X-axes are the  $\Delta tHb$  from PPG; y-axes are  $\Delta tHb$  from NIRS.

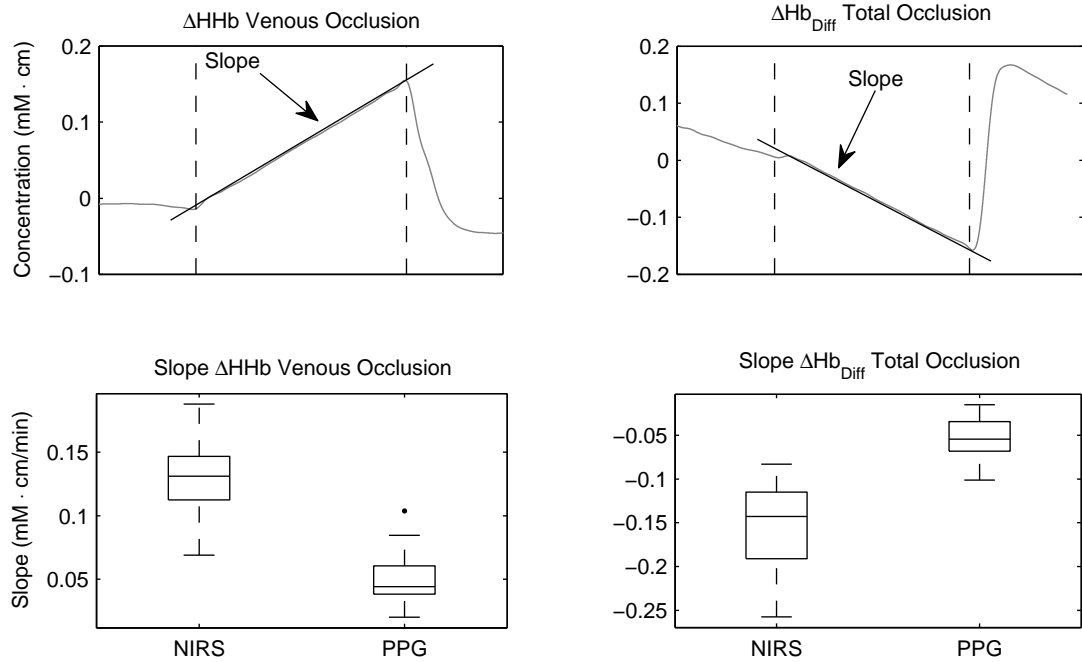


**Figure 9.14:** Top: example of the slope of the regression lines on  $\Delta\text{HHb}$  and  $\Delta\text{Hb}_{\text{Diff}}$  during venous and total occlusions. Grey traces are the signals; black traces are the regression lines on the data. Vertical dashed lines indicate the duration of the occlusions. Bottom: box and whisker plots of the slopes from  $\Delta\text{HHb}$  and  $\Delta\text{Hb}_{\text{Diff}}$ , estimated by both PPG and NIRS, during venous and total occlusion.

Figure 9.14 shows the box and whisker plot of the slopes calculated from  $\Delta\text{HHb}$  and  $\Delta\text{Hb}_{\text{Diff}}$  during venous and total occlusion. During venous occlusion, the slopes calculated from  $\Delta\text{HHb}$  were significantly lower for PPG than NIRS ( $p < 0.01$ ), with mean values of 0.044 mM·cm/min and 0.131 mM·cm/min for PPG and NIRS respectively. During total occlusion, the mean slopes for  $\Delta\text{Hb}_{\text{Diff}}$  were respectively -0.054 mM·cm and -0.142 mM·cm/min for PPG and NIRS, with an overall significantly lower slope for NIRS ( $p < 0.01$ ).

Since the PPG signal does not penetrate as deep as the NIRS, the comparison between slopes could provide an indication of oxygen consumption at different penetrations. In particular, oxygen consumption of the skin (PPG) and muscle (NIRS) can be compared. From the results during both venous and total occlusions, the skin had a significantly lower oxygen consumption than the muscle. This is in concordance with published oxygen consumption rates of different organs [16].

**Table 9.4:** Mean ( $\pm$  SD) changes in  $\Delta\text{Hb}_{\text{Ratio}}$  during the second protocol and correlation coefficients  $r$  between  $\Delta\text{Hb}_{\text{Ratio}}$  and TOI during the occlusions of the second protocol. The means were calculated in 30 s baseline reading and in the last 30 s of each occlusion. The 95 % confidence intervals of  $r$  are presented within parenthesis.

Occlusions	Mean $\pm$ SD (%)	$r$
Baseline	$0.19 \pm 0.29$	-
20 mmHg	$-0.33 \pm 0.44$	0.63 (0.29, 0.83)
40 mmHg	$-1.02 \pm 0.56$	0.71 (0.42, 0.87)
60 mmHg	$-0.96 \pm 0.56$	0.75 (0.49, 0.89)
80 mmHg	$-1.10 \pm 0.48$	0.80 (0.58, 0.91)
100 mmHg	$-0.99 \pm 0.53$	0.81 (0.59, 0.91)
Systolic	$-0.73 \pm 0.47$	0.85 (0.67, 0.93)
Total	$-0.71 \pm 0.46$	0.88 (0.77, 0.94)

### 9.3.4 Haemoglobin oxygenation changes from PPG signals

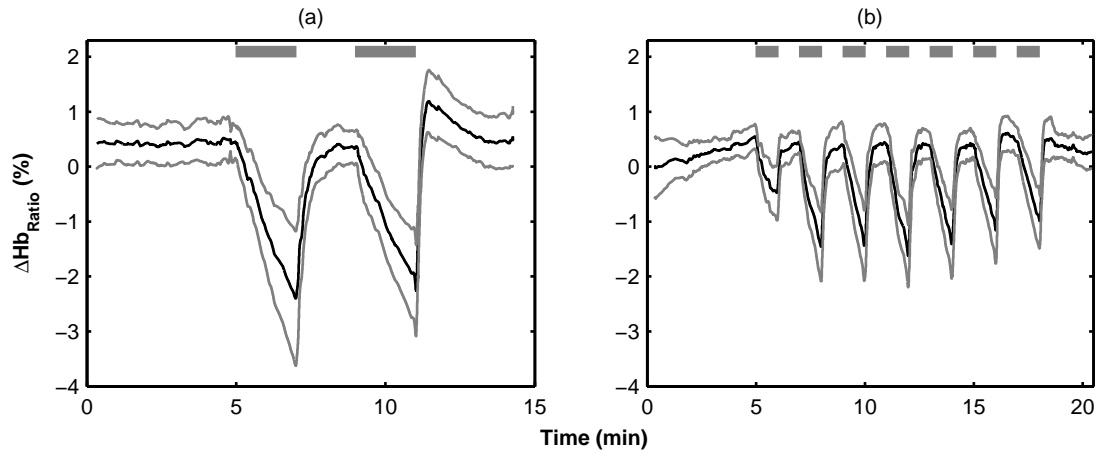
The relative concentrations of  $\Delta\text{HbO}_2$ ,  $\Delta\text{HHb}$ , and  $\Delta\text{tHb}$  estimated from PPG were also used to infer changes in haemoglobin oxygenation during the occlusions in the first and second protocol. An oxygenation index,  $\Delta\text{Hb}_{\text{Ratio}}$ , was calculated as the ratio of  $\Delta\text{HbO}_2$  and  $\Delta\text{tHb}$ , similarly to TOI. The changes were then expressed as relative changes from the baseline, in percentage units.

Figure 9.15 shows the mean changes in  $\Delta\text{Hb}_{\text{Ratio}}$  during the first and second protocol. During venous occlusion in the first protocol, the  $\Delta\text{Hb}_{\text{Ratio}}$  dropped from a baseline of  $0.39 \pm 0.35$  % to  $-2.04 \pm 1.18$  % ( $p < 0.01$ ), while during total occlusion decreased to  $-1.68 \pm 0.81$  % ( $p < 0.01$ ). In addition, the correlation calculated between  $\Delta\text{Hb}_{\text{Ratio}}$  and TOI was  $r = 0.73$  (95 % CI: 0.41, 0.87).

In the second protocol, the  $\Delta\text{Hb}_{\text{Ratio}}$  changed consistently during the occlusions. Table 9.4 shows the mean values of  $\Delta\text{Hb}_{\text{Ratio}}$  during the second protocol. The drops in  $\Delta\text{Hb}_{\text{Ratio}}$  were statistically significant from baseline in all occlusions ( $p < 0.01$ ). Table 9.4 also shows the correlation coefficients  $r$  between  $\Delta\text{Hb}_{\text{Ratio}}$  and TOI during the occlusions of the second protocol.

### 9.3.5 Estimation of arterial oxygen saturation from PPG signals

Arterial oxygen saturation ( $\text{SpO}_2$ ) was estimated from PPG signals acquired from the custom-made finger sensor and the forearm. The  $\text{SpO}_2$  was calculated by applying Equation 9.1 on the acquired red and infrared PPG signals. The response of the



**Figure 9.15:** Mean changes in  $\Delta Hb_{Ratio}$  during the first protocol (a) and the second protocol (b). Black traces are means grey traces are the  $\pm$  SD intervals. Grey horizontal bars indicate the duration of the occlusion.

calculated  $SpO_2$  to vascular occlusions will be analysed later in this chapter, along with other NIRS, laser Doppler, and PPG signals.

The estimated  $SpO_2$  were then compared with  $SpO_2$  values estimated from the finger by a state-of-the-art pulse oximeter. Figure 9.16 shows the Bland and Altman plots between  $SpO_2$  values from a standard finger pulse oximeter and from custom-made finger and forearm PPG sensors.

The custom-made finger slightly under-estimated the  $SpO_2$  when compared with the commercial (standard) pulse oximeter. The limits of agreement between the custom-made finger  $SpO_2$  and the commercial pulse oximeter were  $-0.34 \pm 1.96 \times 1.96$ . The limits of agreement between custom-made forearm  $SpO_2$  and the standard pulse oximeter were  $-9.15 \pm 1.96 \times 8.58$ , whereas the limit of agreement between custom-made finger and forearm  $SpO_2$  were  $-8.81 \pm 1.96 \times 9.15$ . These lower limits of agreement between the forearm and both fingers  $SpO_2$  indicated a consistent underestimation of the  $SpO_2$  calculated from the forearm.

### 9.3.6 Comparison of TOI, Flux, Perfusion Index and $SpO_2$ during protocol 1

The changes in Tissue Oxygenation Index (TOI), normalised Tissue Haemoglobin Index (nTHI), normalised Flux (nFlux), PPG normalised Perfusion Index (nPI) and arterial oxygen saturation ( $SpO_2$ ) were compared during the protocols. These indexes

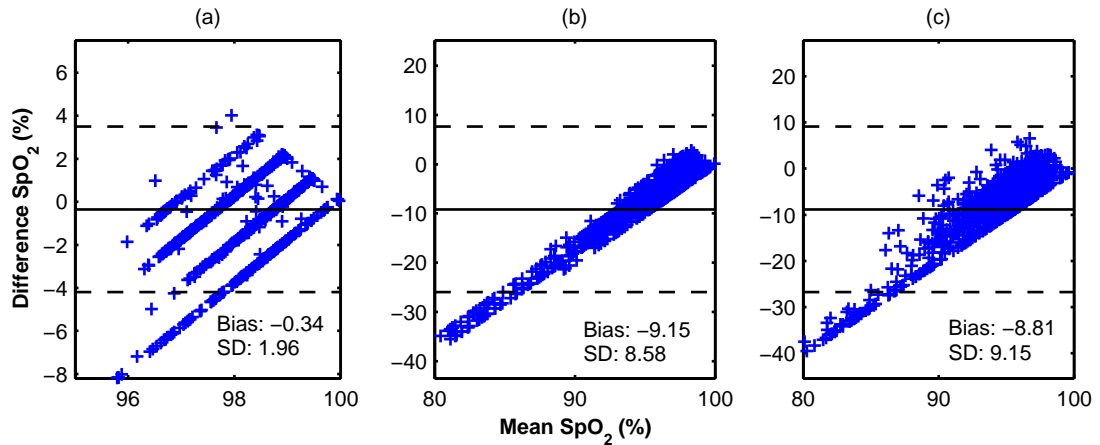


**Figure 9.16:** [Bland and Altman comparison plots between the  $\text{SpO}_2$  estimated from custom-made finger PPG, custom-made forearm PPG, and standard finger pulse oximeter. (a) Bland and Altman plot between custom made finger  $\text{SpO}_2$  and standard finger pulse oximeter. (b) Bland and Altman plot between custom made forearm  $\text{SpO}_2$  and standard finger pulse oximeter. (c) Bland and Altman plot between custom made forearm  $\text{SpO}_2$  and custom-made finger  $\text{SpO}_2$ . X-axes are the mean between the two compared methods, while the y-axes are the differences between the methods. The mean bias and standard deviation (SD) are presented as well. Solid lines are the mean bias of the differences. Dotted lines are the limits of agreement, mean bias  $\pm 1.96 \times \text{SD}$ . The original signals were resampled every 5 seconds.

are widely used as a measure of perfusion and oxygenation, but they have been rarely compared in the same settings. Figure 9.17 shows the mean changes in TOI, nTHI, nPI,  $\text{SpO}_2$ , and nFlux during the first protocol. The nPI, as well as the  $\text{SpO}_2$ , was derived from both forearm ( $\text{nPI}_{\text{Forearm}}$ ) and finger ( $\text{nPI}_{\text{Finger}}$ ) PPG signals.

During venous occlusion, TOI gradually decreased from  $68.10 \pm 4.51$  % baseline to  $63.37 \pm 5.33$  % ( $p < 0.001$ ). The blockage of arterial inflow caused a more severe TOI drop to  $56.39 \pm 7.52$  % ( $p < 0.001$ ). Venous blood pooling caused an increase in nTHI from  $1.02 \pm 0.05$  A.U. to  $1.22 \pm 0.12$  A.U. ( $p < 0.001$ ), while the nTHI slightly increased to  $1.09 \pm 0.09$  A.U. ( $p = 0.005$ ) during total occlusion. Theoretically, there should not be any change in nTHI (i.e. blood volume) during total occlusion since there should be no net venous-arterial flow. However, this increase is due to the not-instantaneous inflation of the cuff to over-systolic pressures.

The  $\text{nPI}_{\text{Finger}}$  and  $\text{nPI}_{\text{Forearm}}$  respectively dropped to  $0.69 \pm 0.25$  A.U. ( $p = 0.03$ ) and  $0.43 \pm 0.14$  A.U. ( $p < 0.001$ ) during venous occlusion from respective baseline of  $0.83 \pm 0.21$  A.U. and  $0.78 \pm 0.12$  A.U.. During total occlusion, the perfusion indexes almost reached zero values of  $0.06 \pm 0.06$  A.U. ( $p < 0.001$ ) and  $0.22 \pm 0.11$  A.U. ( $p < 0.001$ ) for finger and forearm respectively.

Baseline  $\text{SpO}_2$  estimated from the custom-made finger PPG sensor, commercial pulse

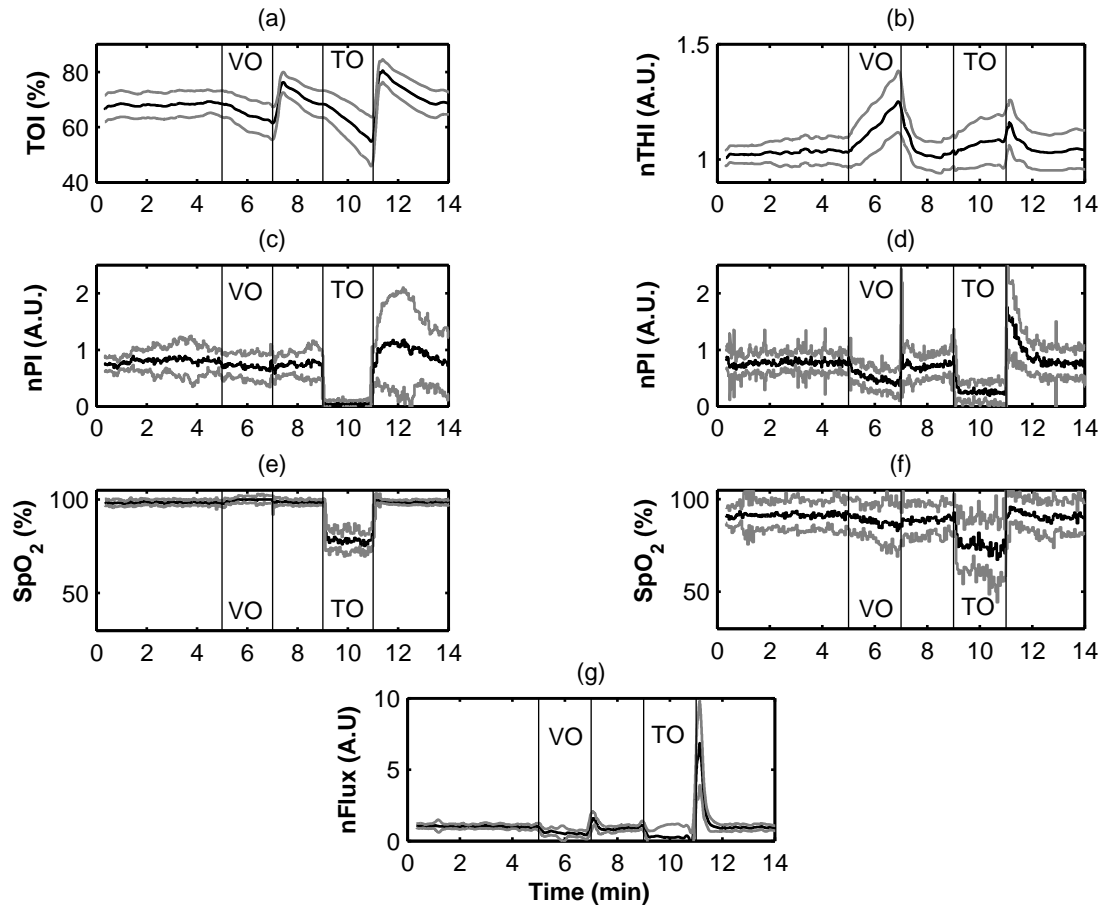


**Figure 9.17:** Mean ( $\pm$  SD) changes in TOI, nTHI, nPI, SpO<sub>2</sub>, and nFlux during the first protocol. (a) TOI; (b) nTHI; (c) Finger nPI; (d) Forearm nPI; (e) SpO<sub>2</sub> from finger PPG; (f) SpO<sub>2</sub> from forearm; (g) nFlux. Black traces are the means and grey traces are the  $\pm$  SD intervals. Vertical lines indicate the onset and conclusion of the occlusions. VO: venous occlusion; TO: total (over-systolic) occlusion. Five minutes of baseline were followed by two minutes of venous occlusion, two minutes of recovery and two minutes of total occlusion before waiting for the signals to return to baseline.

oximeter, and forearm were respectively  $98.82 \pm 1.49$  %,  $98.91 \pm 1.06$  %, and  $92.0 \pm 3.1$  %. During venous occlusion the commercial SpO<sub>2</sub> dropped to  $97.85 \pm 1.68$  % ( $p < 0.001$ ), while the SpO<sub>2</sub> estimated from the custom-made finger PPG sensor had a non-significant increase ( $p = 0.06$ ). The SpO<sub>2</sub> on the forearm dropped as well during venous occlusion ( $88.9 \pm 3.6$  %,  $p = 0.006$ ). The disappearance of arterial pulsations (AC PPG) in total (over-systolic) occlusion caused the inability to provide reliable SpO<sub>2</sub> readings for both commercial and custom-made devices.

Red blood cells (RBC) flow (Flux) was measured by a laser Doppler device and the measures were normalised with respect to the baseline. The normalised value, nFlux, during baseline was  $1.00 \pm 0.14$  A.U. and it significantly reduced during induction of venous occlusion ( $0.44 \pm 0.27$  A.U.,  $p < 0.001$ ). In total occlusion, the nFlux decreased further to  $0.21 \pm 0.71$  A.U. ( $p = 0.001$ ). At over-systolic occlusion pressure, the RBC flow is completely suppressed. However, there is still a residual nFlux signal,

which is widely defined as *biological zero* and it is attributed to molecular Brownian motion [28, 187].

### 9.3.7 Comparison of TOI, Flux, Perfusion Index and SpO<sub>2</sub> during protocol 2

The second protocol aimed at investigating the response of the different techniques to a sequence of occlusions. These occlusions either induced a degree of venous engorgement or arterial blockage. Figure 9.18 shows the mean changes during the second protocol, while Table 9.5 illustrates the numerical results more in details. NIRS TOI and nTHI, and laser Doppler nFlux demonstrated significant changes ( $p < 0.05$ ) from baseline in all the occlusions. The nTHI increased in all occlusions, until reaching maximum values (i.e. maximum blood volume due to venous pooling) during venous occlusions ranging from 40 to 100 mmHg occlusion pressures. In this same range of venous occlusions, the nFlux decreased to half baseline values. The remaining part of the nFlux signal is due to RBC mobility caused by the unaffected arterial inflow. The normalised Perfusion Index nPI estimated from finger PPG signals changed significantly from baseline only for occlusions exceeding 40 mmHg, while the same nPI from forearm PPGs significantly changed earlier, from 40 mmHg occlusion pressure onwards.

As expected, the SpO<sub>2</sub> estimated from the finger by both custom-made and commercial device significantly changed ( $p < 0.05$ ) at occlusion pressures exceeding 80-100 mmHg. At these pressures, the arterial vessels started to occlude, affecting the arterial inflow in the tissue. However, the SpO<sub>2</sub> estimated from the forearm started to decrease significantly at 60 mmHg occlusion pressure, and showed consistent changes onwards. At systolic and over-systolic occlusion pressures, due to the absence of arterial blood pulsations, all the SpO<sub>2</sub> from both fingers and forearm failed in providing reliable SpO<sub>2</sub> values.

**Table 9.5:** Mean changes ( $\pm$ SD) in TOI, nTHI, nFlux, nPI (finger and forearm), and SpO<sub>2</sub> (fingers and forearm) during the second protocol. The values were averaged in the last 30 s of each occlusion. SpO<sub>2</sub> failed during systolic and total (over-systolic) occlusions.

	Occlusion Steps (mmHg)							Systolic	Total
	Baseline	20	40	60	80	100			
TOI (%)	70.05 $\pm$ 4.58	67.43 $\pm$ 5.80	67.80 $\pm$ 4.72	67.57 $\pm$ 5.04	66.73 $\pm$ 5.46	65.86 $\pm$ 4.42	67.09 $\pm$ 4.35	67.34 $\pm$ 5.43	
nTHI (A.U.)	1.00 $\pm$ 0.06	1.05 $\pm$ 0.13	1.11 $\pm$ 0.17	1.10 $\pm$ 0.18	1.10 $\pm$ 0.19	1.11 $\pm$ 0.23	1.06 $\pm$ 0.14	1.04 $\pm$ 0.15	
nFlux (A.U.)	0.95 $\pm$ 0.22	0.70 $\pm$ 0.30	0.49 $\pm$ 0.33	0.49 $\pm$ 0.32	0.48 $\pm$ 0.24	0.48 $\pm$ 0.21	0.24 $\pm$ 0.23	0.25 $\pm$ 0.23	
nPI <sub>Finger</sub> (A.U.)	0.81 $\pm$ 0.24	0.84 $\pm$ 0.50*	0.78 $\pm$ 0.36*	0.76 $\pm$ 0.26	0.57 $\pm$ 0.25	0.19 $\pm$ 0.16	0.03 $\pm$ 0.09	0.03 $\pm$ 0.12	
nPI <sub>Forearm</sub> (A.U.)	0.82 $\pm$ 0.27	0.77 $\pm$ 0.33*	0.56 $\pm$ 0.30	0.49 $\pm$ 0.22	0.44 $\pm$ 0.20	0.28 $\pm$ 0.17	0.18 $\pm$ 0.19	0.14 $\pm$ 0.22	
SpO <sub>2</sub> (%) <sup>a</sup>	97.82 $\pm$ 1.05	97.81 $\pm$ 1.02*	97.80 $\pm$ 1.19*	97.78 $\pm$ 1.31*	97.77 $\pm$ 1.45	96.88 $\pm$ 1.14	-	-	
SpO <sub>2</sub> (%) <sup>b</sup>	97.29 $\pm$ 2.76	97.19 $\pm$ 2.86*	98.42 $\pm$ 2.43*	98.97 $\pm$ 2.80*	98.81 $\pm$ 4.31*	98.72 $\pm$ 9.61	-	-	
SpO <sub>2</sub> (%) <sup>c</sup>	93.25 $\pm$ 7.39	92.34 $\pm$ 6.89*	88.47 $\pm$ 10.48*	87.54 $\pm$ 9.37	86.82 $\pm$ 9.22	81.57 $\pm$ 9.89	-	-	

<sup>a</sup> Finger commercial SpO<sub>2</sub>

<sup>b</sup> Finger custom-made SpO<sub>2</sub> (ZenPPG)

<sup>c</sup> Forearm custom-made SpO<sub>2</sub> (ZenPPG)

\* Not significant change from baseline ( $p > 0.05$ )

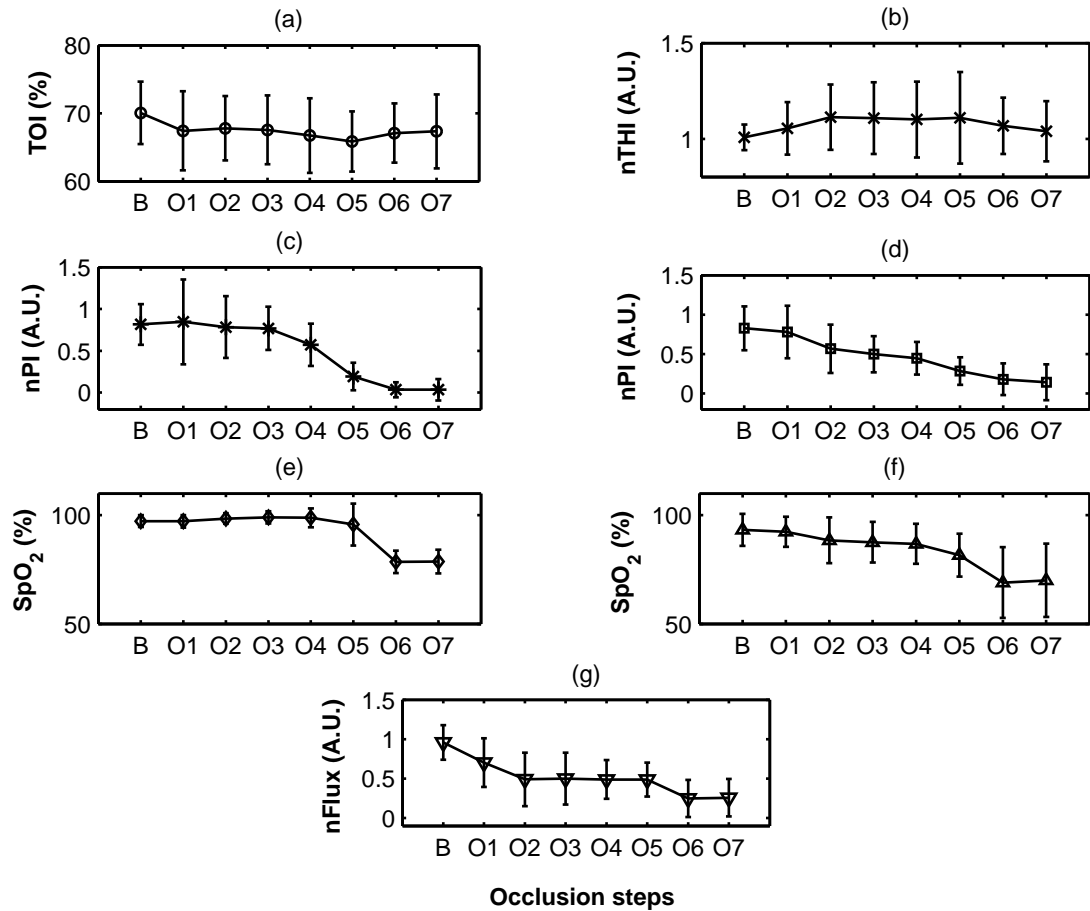


**Figure 9.18:** Mean changes in TOI, nTHI, nPI, SpO<sub>2</sub>, and nFlux during the second protocol. (a) TOI; (b) nTHI; (c) Finger nPI; (d) Forearm nPI; (e) SpO<sub>2</sub> from finger PPG; (f) SpO<sub>2</sub> from forearm; (g) nFlux. Errorbars indicate the  $\pm$ SD interval. B: baseline; O1: 20 mmHg; O2: 40 mmHg; O3: 60 mmHg; O4: 80 mmHg; O5: 100 mmHg; O6: systolic pressure; O7: total (over-systolic) pressure.

### 9.3.8 Changes in finger PPG Optical Densities during vascular occlusion challenges

The optical densities were calculated from finger DC PPG signals in order to investigate changes in blood volume at the digits. The DC component of the PPG, compared to the pulsatile component, should be more adequate to detect changes in venous blood volume due to venous congestion.

The optical densities were calculated from the red DC PPG signals acquired by the custom-made finger PPG sensor. The rationale behind using the red wavelength (600 nm) was that reduced haemoglobin (venous blood) has an absorptivity eight to ten times higher than oxygenated haemoglobin (arterial blood) [17]. Therefore, the DC PPG at 660 nm should mainly provide changes in venous blood volumes. Figure 9.19 shows the changes in optical densities measured at the finger during the first protocol.

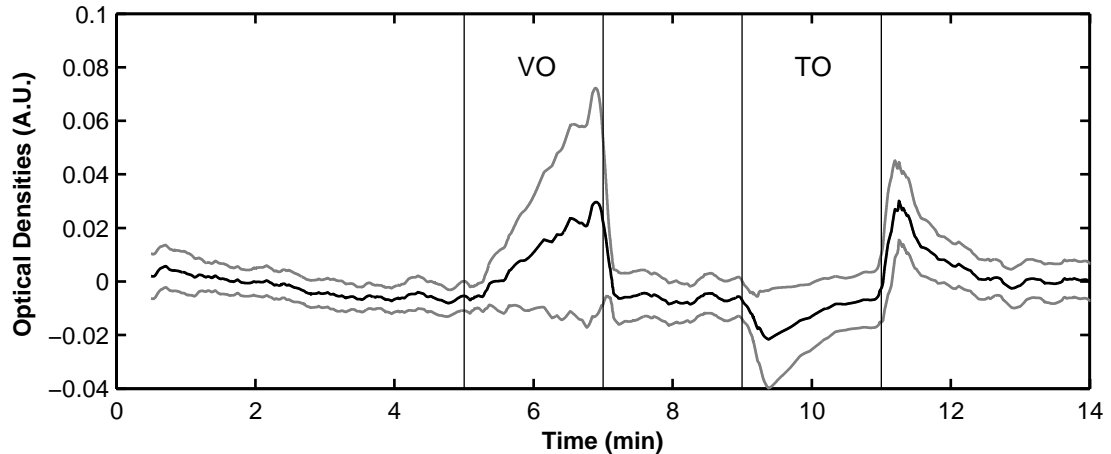


**Figure 9.19:** Mean changes ( $\pm$ SD) in optical densities during the first protocol. The optical densities were calculated from the red DC PPG signal (660 nm) acquired from the finger. Black trace is the mean; grey traces are the  $\pm$ SD intervals. Vertical lines indicate the onset and conclusion of the occlusion. VO: venous occlusion; TO: total (over-systolic) occlusion. Five minutes of baseline measurement were followed by two minutes of venous occlusion, two minutes of recovery, and two minutes of total occlusion. Signals returned to baseline before stopping the acquisition.

During the venous occlusion, the optical densities gradually increased, indicating the accumulation of venous blood (i.e. reduced haemoglobin). The increase in optical densities during venous occlusion was consistent in the population investigated ( $p = 0.005$ ). During the total occlusion, the optical densities decreased ( $p < 0.001$ ).

In the second protocol, the optical densities showed changes in blood volume due to vascular occlusions. Figure 9.20 illustrates the box and whisker plot of the changes in optical densities during the second protocol. Significant changes from baseline were observed only for venous occlusions exceeding 40 mmHg. Maximal changes were at 80 mmHg, when maximal venous occlusion was obtained, resulting in the greatest accumulation of venous blood. Optical densities dropped in both systolic and over-systolic pressures.

### 9.3.9 Dynamic changes in TOI, nTHI and Optical Densities during vascular occlusions challenges

The dynamic changes of non-stationary signals were analysed. The slopes of the decrease/increase of TOI, nTHI and Optical Densities were calculated, as done in subsection 9.3.3, in all the occlusions of both the first and second protocol. Figure 9.21 shows the box and whiskers plot of the slopes of TOI, nTHI, and Optical Densities. In the first protocol, the mean ( $\pm$ SD) TOI desaturations during venous and total oc-

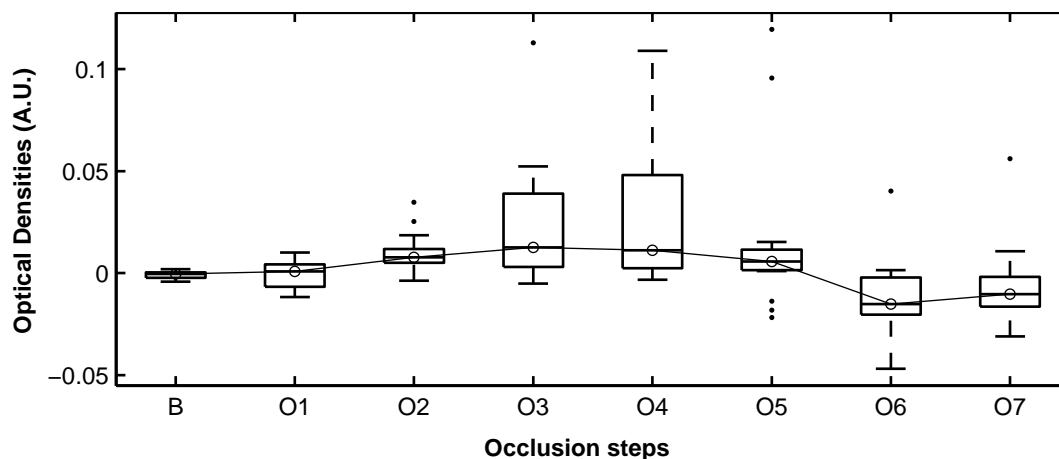


**Figure 9.20:** Box and whisker plot of the changes in optical densities during the second protocol. B: baseline; O1: 20 mmHg; O2: 40 mmHg; O3: 60 mmHg; O4: 80 mmHg; O5: 100 mmHg; O6: systolic pressure; O7: total (over-systolic) pressure.

clusion were respectively  $-3.67 \pm 1.64$  %/min and  $-6.52 \pm 2.51$  %/min. The slopes during venous occlusions were significantly lower than total occlusion ( $p < 0.001$ ). The nTHI slope during venous occlusion, which expresses the rate of venous blood pooling, was  $0.10 \pm 0.03$  A.U./min, while, during total occlusion, it was significantly lower ( $-0.02 \pm 0.03$  A.U./min,  $p < 0.001$ ). The calculated slopes of the Optical Densities were significantly higher during venous occlusion than total occlusion ( $p < 0.001$ ), with respective mean values of  $0.01 \pm 0.02$  A.U./min and  $0.00 \pm 0.00$  A.U./min.

During the second protocol, TOI's slopes in the occlusions range 20-80 mmHg (i.e. venous occlusions) were not different between each other ( $p < 0.05$ ). Significant changes in TOI's slope were only observed between the venous occlusions (20-80 mmHg) and the occlusions  $> 100$  mmHg ( $p < 0.003$ ). This suggests that more severe desaturations were taking place when the arteries began to occlude. Similarly, the nTHI slopes during 40-100 mmHg were very similar between each other ( $p < 0.05$ ), and a significant variation of slope in nTHI occurred during systolic and over-systolic occlusion pressures. The nTHI's slopes at 20 mmHg were similar to the slopes at 100 mmHg ( $p < 0.05$ ), whereas they were different from the slopes at occlusions ranging between 40-80 mmHg ( $p < 0.001$ ). The higher nTHI's slopes during occlusions in the 40-80 mmHg occlusion range indicated the maximal venous blood engorgement in these occlusions. The marginal slopes during systolic and total occlusions should be attributed to the manual inflation of the cuff, thus unable to occlude instantaneously both veins and arteries. Similar to nTHI, the optical densities' slopes between 60-100 mmHg occlusions were not different between each other ( $p > 0.05$ ). In this range, however, only the slopes at

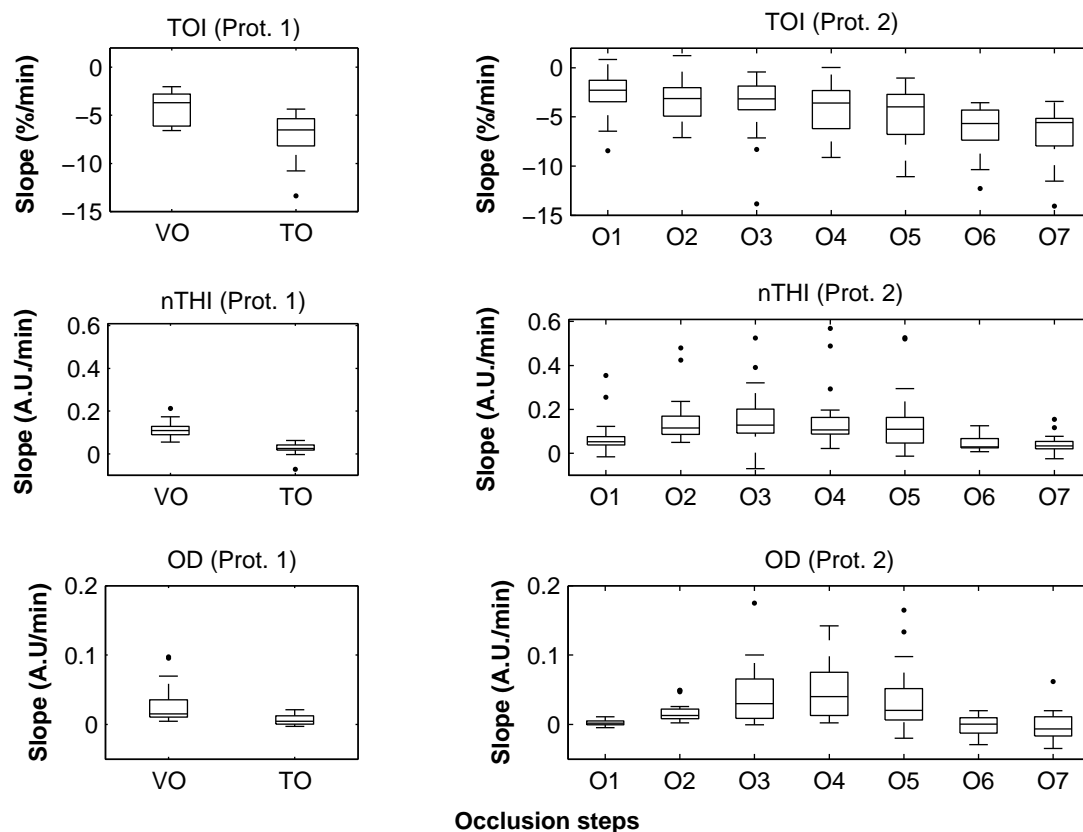


**Figure 9.21:** Slope changes for TOI, nTHI and optical densities (OD) during the first and second protocol. Prot. 1: first protocol. Prot. 2: second protocol. VO: venous occlusion; TO: total (over-systolic) occlusion. O1: 20 mmHg; O2: 40 mmHg; O3: 60 mmHg; O4: 80 mmHg; O5: 100 mmHg; O6: systolic pressure; O7: total (over-systolic) pressure.

80 mmHg differed from 40 mmHg, suggesting a maximal venous engorgement during the occlusion at 80 mmHg. There was no significant difference between the slopes at 20 mmHg, systolic pressure, and over-systolic pressure ( $p < 0.001$ ).

## 9.4 Summary

In this chapter, different non-invasive optical techniques have been investigated during vascular occlusion challenges. The first aim of the study was to investigate the feasibility of using photoplethysmography to estimate relative changes in oxygenated (HbO<sub>2</sub>), deoxygenated (HHb), and total haemoglobin (tHb), as done in NIRS. The results obtained from the PPG were then compared with state-of-the-art NIRS measurements. Correlation and trending agreement between PPG and NIRS showed good correlation and trending agreement. The Bland & Altman agreement analysis revealed an underestimation of haemoglobin concentration by PPG, with respect to NIRS. In

addition, the analysis of the slope of HHb and Hb<sub>Diff</sub> by both PPG and NIRS indicated a lower oxygen consumption in the anatomical area measured by the PPG sensor (skin), compared to NIRS (muscle). Oxygenation changes were also estimated from haemoglobin concentrations estimated from PPG and they showed good correlation with oxygenation changes measured by NIRS (TOI).

A comparative analysis between NIRS, laser Doppler, photoplethysmography, and pulse oximetry during vascular occlusions was also performed, in order to investigate the simultaneous responses of these optical methods. Changes in TOI (NIRS), Flux (LDF), PI (PPG), and optical densities (PPG) indicated the onset of occlusions of both venous and arterial nature, while changes in SpO<sub>2</sub> took place mostly during occlusions involving the arterial vasculature.

This chapter presented the results from a study in which PPG signals were used to express changes in blood perfusion and oxygenation induced by vascular occlusions in the forearm. However, in order not to limit the validation to the forearm only, it was decided to extend the investigation to other measurement locations and to induce different physiological stimuli. Therefore, the next chapter will present results from a second *in vivo* investigation, where PPG and NIRS signals were acquired from the forehead of healthy volunteers during a head-down bed tilting protocol.

# Chapter 10

## **Photoplethysmography and Near Infrared Spectroscopy perfusion and oxygenation changes at the forehead during a bed tilting protocol**

The previous chapter illustrated the results from a vascular occlusion study in which the haemoglobin concentrations, estimated from PPG signals, showed good levels of trending agreement and correlation with NIRS measurements. In this chapter, a similar comparison will be performed during a head-down tilting study. PPG and NIRS sensors were applied on the forehead of healthy volunteers and the haemodynamic responses of PPG and NIRS during the orthostatic stress were compared. In the previous study, measuring PPG from the forearm allowed to investigate the effects of proximal vascular occlusions. However, the forearm is not a common location for PPG measurements and this prompted the investigation of a more conventional location such as the forehead. Since a change in position of the subject (i.e. tilting) should cause a physiological change, which can be reflected in the PPG acquired at the forehead, a tilting protocol was performed in order to investigate the ability of the PPG to indicate perfusion and/or oxygenation changes at the forehead. This new physiological challenge, where changes are induced by gravitation rather than mechanical restrictions, will offer a unique point of view in investigating the research hypothesis. Furthermore, the presence of large veins on the forehead allowed to analyse the effects that such vessels may have on the haemoglobin concentrations estimated by PPG, as well as on the SpO<sub>2</sub>.

## 10.1 Introduction

The forehead is one of the most common locations for PPG and SpO<sub>2</sub> measurements. The forehead's region is well perfused by arteries branching from the internal carotid, thus, providing good quality PPG signals [110, 111, 188]. PPG measurements on the forehead have been reported to be less affected by vasoconstriction and quicker in indicating deoxygenations than fingers [109–111, 188–190]. In addition, the forehead is less susceptible to movements and, for intra-operative monitoring, it is a more accessible location than fingers [188]. However, the PPG signals acquired from the forehead contain a stronger venous component compared to the fingers [111, 191]. This venous component can be worsened by the positioning of the patients such as the Trendelenburg position [111, 117, 188]. The venous presence in the PPG measured at the forehead could be identified in the form of cardio-synchronous venous pulsations, which deteriorate the quality of the signal [111]. In the presence of venous pulsations, pulse oximetry readings acquired from the forehead could be lower than the digits because of the mixture of venous and arterial blood in the measurement area [4, 117, 188]. In order to overcome these limitations, the application of a low pressure on the sensor was suggested for pushing venous blood from beneath the sensor [111, 117, 188]. This low pressure aims at removing venous presence (pulsations) from the PPG signals, without affecting the arterial component of the signal, thus providing more reliable SpO<sub>2</sub> readings [111, 188]. Manufacturers usually provide a headband along with their forehead sensors, but these headbands, however, do not guarantee the full solution to the problem. Since there is no standard measure of the actual pressure applied, the headband may suppress arterial pulses (in particular in hypotensive patients) by exerting an excessive pressure and it can cause skin damages in the measuring site [111]. In addition, the headband can slip-off from the patient during the measurement and the applied pressure may not be sufficient to suppress the venous component in the signal [189]. To date, there is no measure of the presence of venous blood underneath the sensor. Venous pulsations can only be visually recognised in the PPG signals, or the venous presence can be presumed from the position of the patient (e.g. Trendelenburg).

Another factor that may influence PPG/SpO<sub>2</sub> readings on the forehead is the presence of large vasculature on the forehead. The forehead is populated with large arteries and veins, which lay between the skin and scalp. Therefore, the placement of the

sensor on the forehead plays an important role in performing the correct measurement. Mannheimer et al. investigated, by tissue optical modelling and *in vivo* measurements, the effect of large arteries on the SpO<sub>2</sub> measured by three reflectance pulse oximetry sensors [110]. In their studies, one sensor was placed on the temple (over a large pulsating artery), another sensor was positioned just above the left eyebrow and one last sensor was placed just above the right eyebrow. The sensors positioned above the eyebrows were not laying above a large vessel. The SpO<sub>2</sub> readings from the three sensors were compared in order to determine whether the positioning of the sensors over large vasculatures affected the SpO<sub>2</sub> measurements. The large artery beneath the sensor (temple) significantly altered the optical path travelled by the light in the tissue, causing a significant bias with the reference measurements. The authors then suggested avoiding placing PPG/pulse oximetry sensors on top of large pulsating arteries [110].

The first aim of this study was to investigate whether PPG signals acquired from the forehead could be used to estimate relative changes in oxygenated, deoxygenated (reduced), and total haemoglobin as performed in NIRS. The estimated parameters were then compared with state-of-the-art NIRS measurements as done previously in Chapter 9. The possibility of estimating haemoglobin concentrations, in particular, deoxygenated haemoglobin, from the same PPG/SpO<sub>2</sub> sensor could provide an indication of the increased (or decreased) presence of venous blood underneath the sensor (i.e. venous blood pooling). In addition, the effect that large vasculature in the forehead (e.g. a vein) could have on the estimation of haemoglobin concentrations was also investigated by comparing two identical PPG sensors placed on different locations on the forehead. In this setting, the bias in SpO<sub>2</sub> readings caused by the presence of a large vein underneath the sensor was also investigated. The experimental methods and the comparative results of the measurements will be presented in the following sections of this chapter.

## 10.2 Measurements set-up, protocols and data analysis

### 10.2.1 Measurement system

The research PPG processing unit presented in Chapter 7 was used to acquire raw PPG signals (AC+DC). Two identical RPS1 sensors were used to acquire PPG signals from the forehead. As described later, one sensor was positioned on top of a large vessel, while the other PPG sensor was placed distant from any vessel on the forehead.

A commercial NIRS monitor (NIRO 200NX, Hamamatsu Photonics, Japan) was used to acquire NIRS signals, whereas a non-invasive blood pressure monitor (CNAP Monitor 500, CNSystems Medizintechnik AG, Austria) was used to monitor non-invasively the arterial blood pressure (ABP). The device is based on photoplethysmography and it measures beat-to-beat ABP signal, providing a continuous indication of systolic and diastolic pressure. The signal is measured at the fingers by a double-fingers sensor, whereas the blood pressure is calibrated with a pressure cuff placed on the upper arm. An electric bed was used for head-down tilting the volunteers.

PPG and NIRS signals were acquired on LabVIEW through two 16-bit NI-PcIe 6321 Data Acquisition Cards (National Instruments, USA). The VI described in Chapter 8 was adapted for the acquisition of PPG signals from the ZenPPG and the NIRS monitor. Analogue outputs scaling equations were applied for the NIRS signals (subsection 8.3.5). PPG and NIRS signals were acquired simultaneously at a sampling frequency of 1000 Hz and saved in a text file for post-acquisition analysis. The ABP was acquired separately through the dedicated signal amplifier (USBamp, g.tec Medical Engineering GmbH, Austria) at a sampling rate of 600 Hz.

### 10.2.2 Subjects and investigation set-up

Sixteen (16) healthy subjects with mean age  $\pm$  SD of  $28 \pm 6.7$  (13 males and 3 females) were recruited for the investigation. Ethical approval was gained from the Senate Research Ethics Committee at City University London and written consent was sought from the volunteers before commencing of the investigation. Subjects with a history of cardiovascular disorders were excluded from the study.

Two PPG sensors and one NIRS sensor were applied on the volunteers' forehead. One PPG sensor was designated to be placed on top of a large vessel, while the second PPG sensor and the NIRS sensor were positioned away from large vasculatures on the forehead. Locating large vessels on the forehead *a priori* may be challenging. Therefore, the position of the large vessels was checked and marked before the commencement of the study. In order to visualise the vein, a head-down tilt was performed before placing the sensors. The supratrochlear vein, which lays roughly on the centre part of the forehead, is one of the largest veins present in the forehead and it can be easily identified by tilting the head. The subjects were secured to the bed by fastening a belt around their legs, thus avoiding slipping during tilting. After securing the subjects, the bed was slightly tilted for few seconds in order to facilitate the exposure of vasculatures on the forehead. The large supratrochlear vein was marked for the positioning of the first PPG sensor. An area free from large vasculatures, above the eyebrow, was used for the positioning of the second PPG. The NIRS sensor's position was on the opposite eyebrow with respect to the second PPG sensor and slightly superior in order to avoid midline sinuses. After marking the sensor's positions, the bed was restored in a supine position and the subjects were untied. The subjects rested for five minutes before the placement of the sensors commenced.

The ABP sensor was placed on the digits of the left hand, as suggested by the manufacturer. The ABP monitor also required the placement of a pressure cuff on the upper left arm for calibration purposes. The two PPG sensors and the NIRS sensor were placed in the previously marked positions on top of and distant from the large vessels. Figure 10.1a illustrates the positioning of PPG and NIRS sensors on the forehead. The NIRS sensor had an interoptodes separation distance of 4 cm. All sensors were attached to the forehead's skin by means of a clear double-sided medical adhesive tape. The tapes were cut at the optical components positions in order to avoid optical obstruction.

### 10.2.3 Investigation protocol

The investigation protocol consisted of three stages: supine, head-down, and supine. The subjects were lying on the bed in supine position and they were secured to the bed. The room temperature was kept constant at  $23 \pm 1$  °C. After all the sensors were

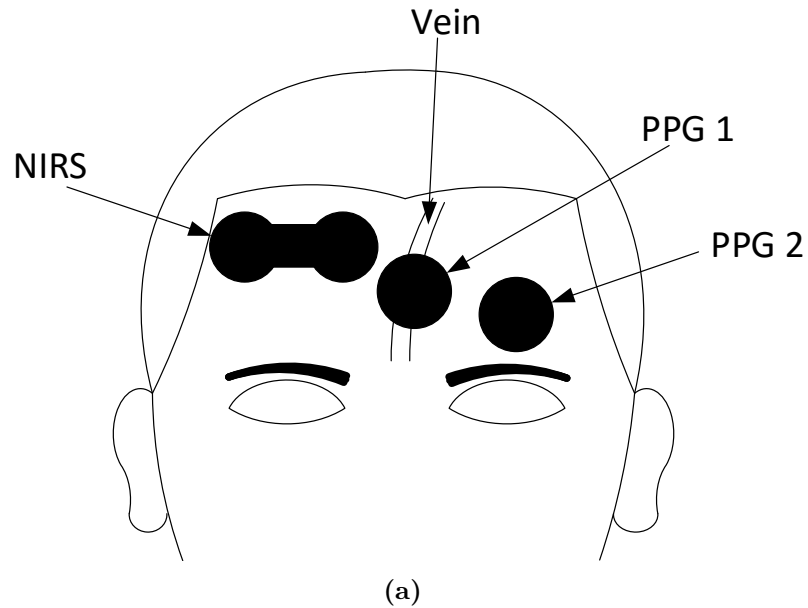


**Figure 10.1:** Positioning of the PPG and NIRS sensors on the forehead (a) and investigation set-up (b). The first PPG sensor (PPG-1) was placed on top of the supratrochlear vein, while the second PPG sensor (PPG-2) was placed over the eyebrow, distant from any large vasculature. The NIRS sensor was placed lateral and opposite to the PPG-2 sensor, distant from any large vasculature. The bed was tilted -30 deg as showed in (b) for five minutes.

positioned as showed in Figure 10.1a and the volunteers were relaxed, the initial calibration of the ABP monitor was initiated. Once this initial calibration was concluded, the monitor's auto-calibration was switched OFF and the protocol was started.

Five minutes of baseline were recorded in the supine position. After baseline, the bed was inclined at -30 deg. The head-down position was maintained for five minutes, at the end of which the bed was restored in the initial supine position for other five minutes. Each transition (supine-to-tilt and tilt-to-supine) did not last more than ten seconds. Figure 10.1b shows the head-down position at which the volunteers were tilted.

### 10.2.4 Data analysis & statistics

Post-acquisition analysis was performed in Matlab2013a. Before processing, all the acquired signals were down-sampled to 100 Hz. TOI, nTHI and haemoglobin concentrations from NIRS were filtered from high-frequency noise and components by a zero-phase low-pass filter ( $f_c = 0.05$  Hz). The finger AC PPG component was obtained from raw PPG signals by applying a zero-phase band-pass filter (pass-band: 0.5-7 Hz). The DC PPGs were obtained by low-pass filtering the signal at  $f_c = 0.1$  Hz. SpO<sub>2</sub> was estimated from PPG signals by applying Equation 10.1 in a three-seconds rolling window. Similarly, the mean arterial pressure (MAP) was calculated in a three-seconds rolling window on the acquired ABP signals by computing the diastolic (DP) and systolic (SP) pressures as in Equation 10.2 [14].

$$SpO_2 = 110 - (25 \cdot R); \text{ Where: } R = \frac{AC_R/DC_R}{AC_{IR}/DC_{IR}} \quad (10.1)$$

$$MAP = \frac{2}{3}DP + \frac{1}{3}SP \quad (10.2)$$

Changes in oxygenated (HbO<sub>2</sub>), reduced (HHb) and total haemoglobin (tHb) were estimated by applying the modified Beer-Lambert law to DC PPG signals acquired from the forehead as described in Section 8.4. From these, the index  $\Delta Hb_{ratio}$ , expressing changes in oxygenations, was calculated from the ratio  $\Delta Hb_{ratio} = \Delta HbO_2 / \Delta tHb$ . The index indicates the relative changes in oxygenation from a starting baseline and it was expressed as percentage changes.

Correlation between techniques or variables was assessed by measuring the Pearson correlation coefficient  $r$  and the 95 % confidence intervals (CI). The trending agreement was evaluated by four-quadrant plot analysis [184]. The concordance rate  $C$  was calculated as the ratio of the number of points in the first and third quadrant and the total number of points in all quadrants. An exclusion zone of 10 % was used for the calculations [184]. A concordance rate  $C \geq 90$  % was considered satisfactory for indicating trending agreement.

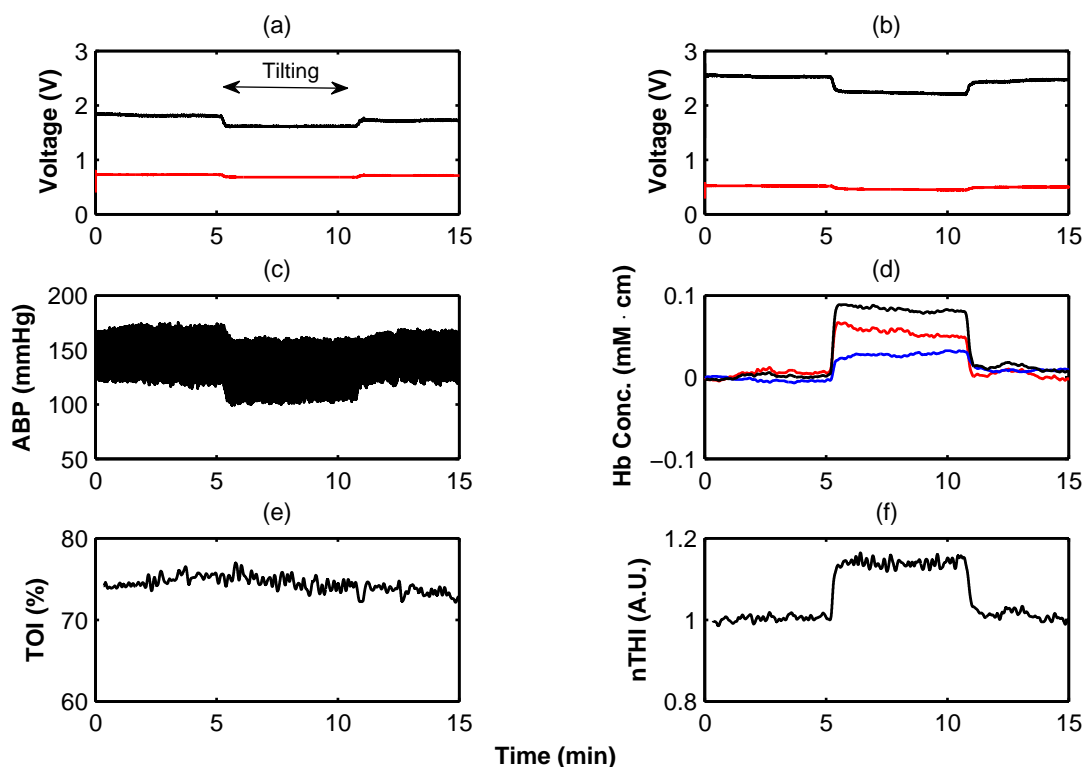


**Figure 10.2:** Example of PPG, arterial blood pressure and NIRS signals acquired from one volunteer. (a) Red and infrared raw PPG signals (AC+DC) acquired from the first PPG sensor (on top of the vein). (b) Red and infrared raw PPG signals (AC+DC) acquired from the second PPG sensor (distant from large vessels). (c) Arterial blood pressure (ABP). (d) Relative haemoglobin concentrations from NIRS. Red trace:  $\Delta\text{HbO}_2$ ; blue trace:  $\Delta\text{HHb}$ ; black trace:  $\Delta\text{tHb}$ . (e) TOI from NIRS. (f) nTHI from NIRS. The tilting was performed in the central part of the protocol, after five minutes of baseline readings. The head-down tilting was followed by five minutes of recovery in the supine position.

The changes during each stage of the protocol (i.e. baseline, tilting, and recovery) were averaged over the central three minutes of each step. Statistically significant changes from baseline were tested by repeated measures Wilcoxon signed-rank tests. A p-value less than 0.05 was considered satisfactory for significance.

### 10.3 Results

Figure 10.2 illustrates the acquired signals from a volunteer during the investigation protocol. The acquired signals indicated the haemodynamic changes due to head-down tilting. These responses of each signal are analysed in detail in the next sections.

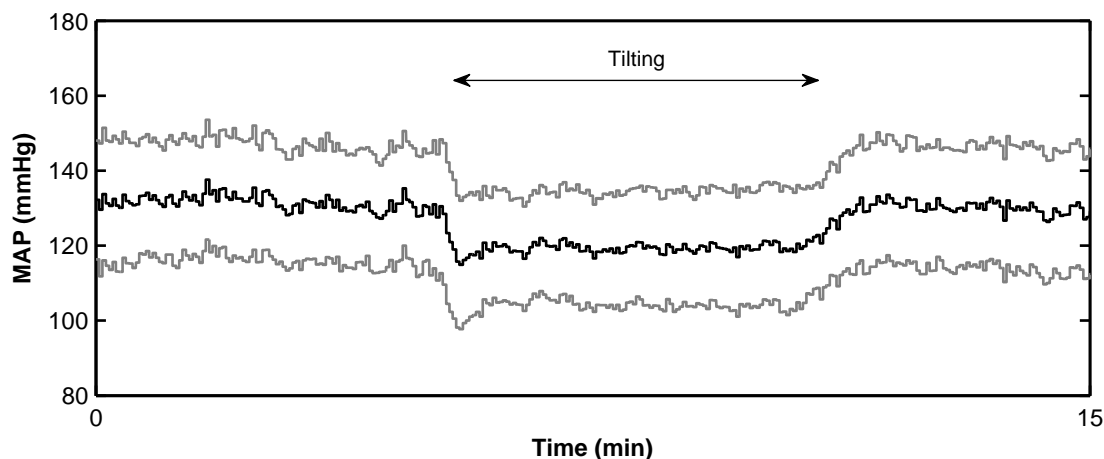


**Figure 10.3:** Mean changes ( $\pm$ SD) in mean arterial pressure (MAP) across all subjects investigated during the tilting protocol. Black trace is the mean, while the grey traces are the  $\pm$ SD intervals.

### 10.3.1 Haemoglobin concentration changes estimated from PPG

The all-body head-down tilting created a quick shift of blood to the upper part of the body, causing temporary hypovolaemia in the lower body. This caused a consequent drop in the systemic arterial blood pressure measured at the digits. The mean arterial pressure (MAP) dropped during tilting and it recovered when the volunteers returned to supine position. Figure 10.3 depicts the mean changes in MAP caused by the head-down tilting. The mean drop during tilting was  $-16.24 \pm 5.90$  mmHg and it was statistically significant in the population investigated ( $p < 0.01$ ). In addition, there was no difference between baseline and post-tilting recovery MAP readings ( $p > 0.05$ ), indicating a full recovery of the blood pressure when the supine position was restored.

Relative concentration changes in oxygenated, reduced, and total haemoglobin were estimated from PPG signals by applying the modified Beer-Lambert to DC PPG signals. Figure 10.4 shows the mean changes ( $\pm$ SD) of  $\Delta$ HbO<sub>2</sub>,  $\Delta$ HHb, and  $\Delta$ tHb estimated from the PPG2 sensor and NIRS on the forehead during bed tilting. The changes in haemoglobin concentration indicated the haemodynamic changes occurred due to bed tilting. The -30deg head-down tilt produced a simultaneous impediment of the venous return from the upper part of the body (head) and an increase in arterial inflow due to the hydrostatic position. This gravitational change was reflected in an increase in the concentration of oxygenated haemoglobin ( $\Delta$ HbO<sub>2</sub>). The venous blood pooling on the upper part of the body (head) produced an increase in the concentration of reduced haemoglobin ( $\Delta$ HHb). Both increases in oxygenated and reduced haemoglobin contributed to the rise of total haemoglobin  $\Delta$ tHb measured at the fore-

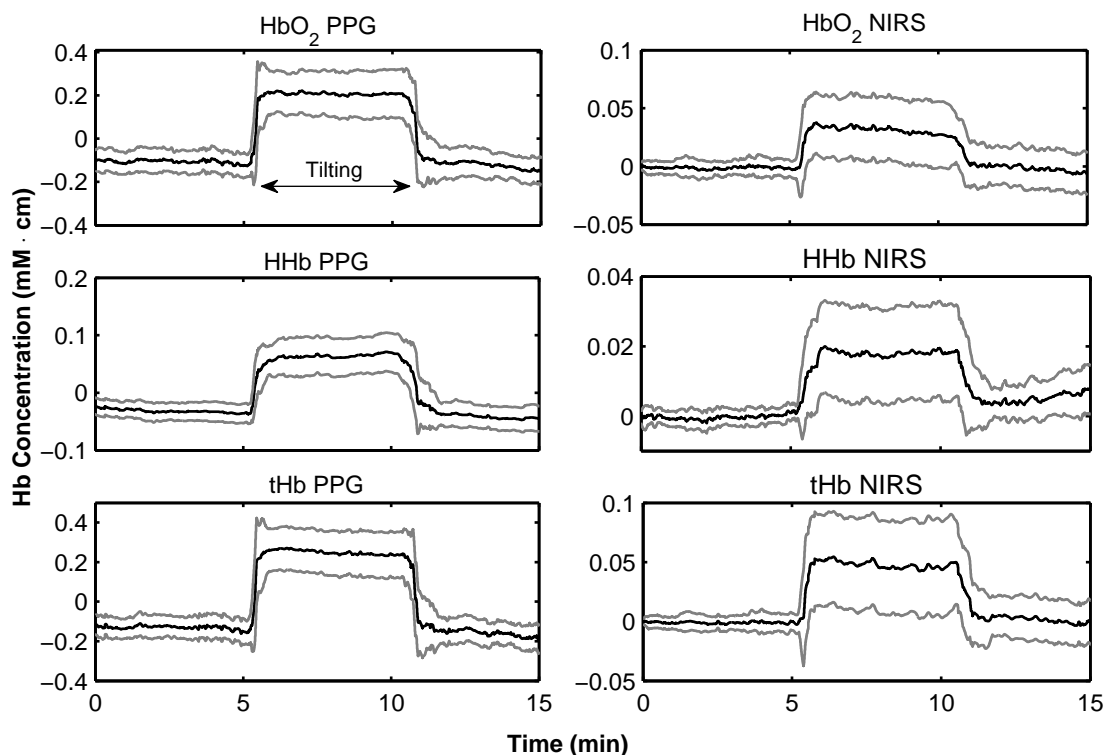


**Figure 10.4:** Mean changes ( $\pm$ SD) in  $\Delta$ HbO<sub>2</sub>,  $\Delta$ HHb, and  $\Delta$ tHb from the forehead estimated by PPG and NIRS during bed tilting. The haemoglobin concentrations were estimated from the PPG sensor positioned distant from large vasculature on the forehead (PPG-2). The tilting was performed in the central part of the protocol, after five minutes of baseline readings. The head-down tilting was followed by five minutes of recovery in the supine position. Black traces are the means, while grey traces represent the  $\pm$ SD intervals. PPG and NIRS measurements have been plotted on different y-axis scales in order to facilitate the visual assessment of the trends.

head (i.e.  $\Delta$ tHb =  $\Delta$ HbO<sub>2</sub> +  $\Delta$ HHb). Therefore, the increase in  $\Delta$ tHb could be attributed to both an increase of arterial inflow and to a reduced return of venous blood.

Table 10.1 presents the mean changes ( $\pm$ SD) in  $\Delta$ HbO<sub>2</sub>,  $\Delta$ HHb, and  $\Delta$ tHb, estimated by both PPG and NIRS, during baseline, tilting, and recovery. Tilting caused significant changes from baseline ( $p < 0.05$ ) in all parameters estimated by both PPG and NIRS.

As can be noticed from the y-axis scale of Figure 10.4 and Table 10.1, there was a quantitative difference between the haemoglobin concentrations estimated from PPG and NIRS. Therefore, the bias between the two techniques was assessed by the same Bland & Altman analysis performed in Chapter 9. The analysis involved the calculation of limits of agreements with respect to the ratio between the two techniques, instead of the traditional difference [185,186]. Figure 10.5 illustrates the Bland & Altman plots of the  $\Delta$ HbO<sub>2</sub>,  $\Delta$ HHb, and  $\Delta$ tHb estimated by PPG and NIRS during the bed tilting protocol. The standard limits of agreement for  $\Delta$ HbO<sub>2</sub>,  $\Delta$ HHb, and  $\Delta$ tHb were

**Table 10.1:** Mean changes ( $\pm$ SD), in mM·cm, of relative haemoglobin concentrations changes estimated by PPG and NIRS during baseline, tilting, and recovery. The PPG-derived haemoglobin concentrations refer to the second PPG sensor, which was placed distant from the large vasculature. The values are averaged over the central three minutes of baseline, tilting, and recovery.

	Baseline (mM·cm)	Tilting (mM·cm)	Recovery (mM·cm)
$\Delta$ HbO <sub>2</sub> (PPG)	-0.104 $\pm$ 0.056	0.202 $\pm$ 0.109*	-0.110 $\pm$ 0.069
$\Delta$ HHb (PPG)	0.033 $\pm$ 0.143	0.068 $\pm$ 0.031*	-0.039 $\pm$ 0.019
$\Delta$ tHb (PPG)	0.130 $\pm$ 0.057	0.262 $\pm$ 0.115*	-0.150 $\pm$ 0.065
$\Delta$ HbO <sub>2</sub> (NIRS)	-0.001 $\pm$ 0.006	0.032 $\pm$ 0.028*	0.001 $\pm$ 0.017
$\Delta$ HHb (NIRS)	0.000 $\pm$ 0.002	0.018 $\pm$ 0.014*	0.004 $\pm$ 0.005*
$\Delta$ tHb (NIRS)	-0.001 $\pm$ 0.005	0.050 $\pm$ 0.041*	0.004 $\pm$ 0.018

\* Significant change from baseline ( $p < 0.05$ )

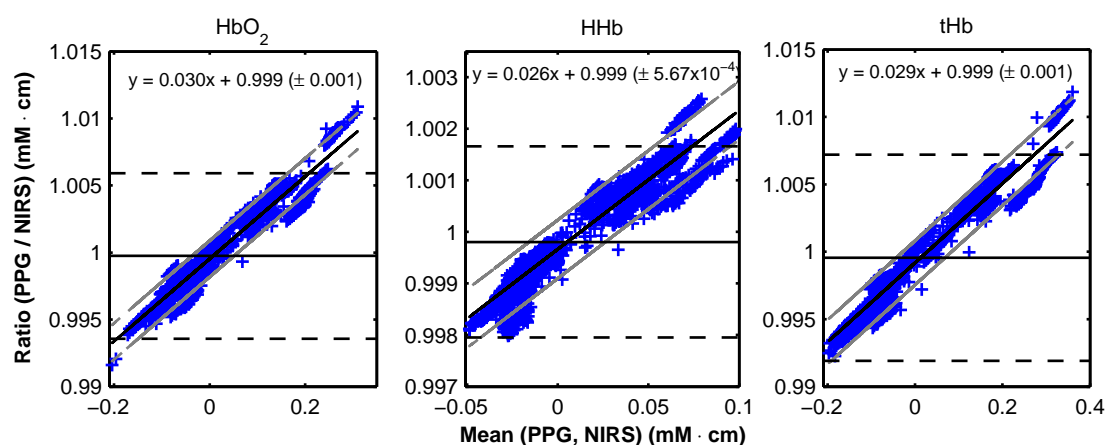


**Figure 10.5:** Bland & Altman plots and analysis of the haemoglobin concentrations estimated from the second PPG sensor (PPG-2) against the reference NIRS method during the bed tilting protocol. X-axes are the mean between the two methods, while the y-axes are the ratio of the measures. Blue crosses are the data. Horizontal solid lines are the standard mean bias and the dashed lines are the limits of agreement (mean  $\pm$  1.96SD). The second solid line in black is the regression line on the data, representing the mean bias. The grey lines are the  $\pm$  95 % confidence intervals. The equation of the fitted regression line is reproduced at the top of the graphs.

respectively  $0.999 \pm 1.96 \times 0.0032$ ,  $0.999 \pm 1.96 \times (9.45 \cdot 10^{-4})$ , and  $0.999 \pm 1.96 \times 0.0039$ . These represent the consistent mean bias ratio between the measures and it indicated a small underestimation of PPG compared to NIRS. However, the Bland & Altman analysis revealed a non-constant linear relationship between the average (x-axis) and the ratio (y-axis) of the measures. Regression analysis shows that the mean bias between the measures increased when the magnitude (average) of the measurements increases, with an overestimation of PPG compared to NIRS. The best-fit regression lines on the data, representing the mean bias, are showed in Figure 10.5, along with the  $\pm$  95 % CI and the regression line's equation.

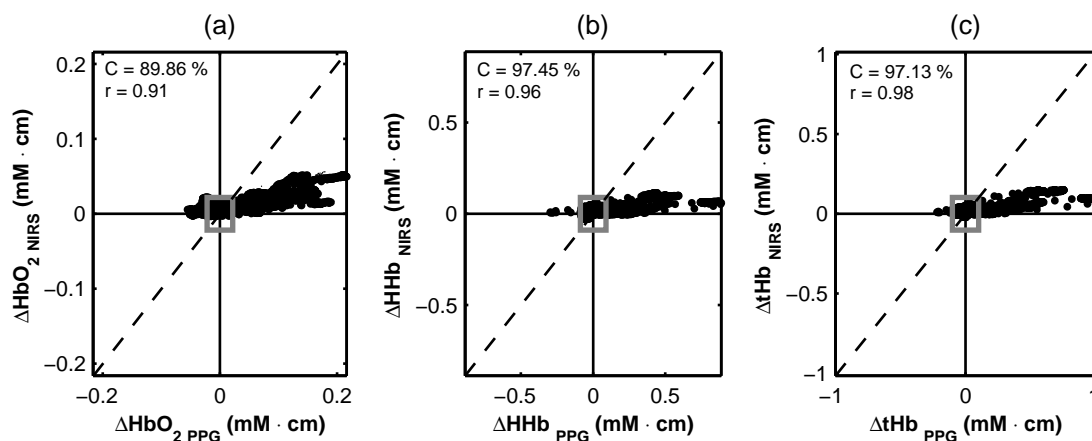


**Figure 10.6:** Four quadrant plots between  $\Delta\text{HbO}_2$ ,  $\Delta\text{HHb}$ , and  $\Delta\text{tHb}$  estimated from the second PPG sensor (PPG-2) and NIRS during the bed tilting protocol. The concordance rate  $C$  and correlation coefficients  $r$  between the measures are presented as well. The concordance rate was calculated as the ratio of the number of points in the first and third quadrant and the total number of points in all four quadrants. An exclusion zone of 10 % was used for the calculation of  $C$ . Dashed lines are the lines of equality. Grey boxes indicate the 10 % exclusion zone. (a) changes in  $\Delta\text{HbO}_2$ . (b) Changes in  $\Delta\text{HHb}$ . (c) Changes in  $\Delta\text{tHb}$ .

### 10.3.2 Assessment of correlation and trending between PPG and NIRS

As shown in Figure 10.4, the haemoglobin concentrations estimated from PPG followed the trends of the same NIRS-derived parameters. The correlation between PPG and NIRS parameters was assessed by calculating the Pearson correlation coefficient  $r$ . The two techniques had good correlation, with coefficients of  $r = 0.91$  (95 % CI: 0.83, 0.97),  $r = 0.88$  (95 % CI: 0.72, 0.96), and  $r = 0.97$  (95 % CI: 0.92, 0.99) for  $\Delta\text{HbO}_2$ ,  $\Delta\text{HHb}$ , and  $\Delta\text{tHb}$  respectively.

Trending agreement was evaluated by four-quadrant plots analysis between  $\Delta\text{HbO}_2$ ,  $\Delta\text{HHb}$ , and  $\Delta\text{tHb}$  measured by PPG and NIRS. Figure 10.6 depicts the four-quadrant plots of  $\Delta\text{HbO}_2$ ,  $\Delta\text{HHb}$ , and  $\Delta\text{tHb}$  estimated from PPG and NIRS during the bed tilting protocol. The haemoglobin concentrations from PPG presented a satisfactory trending agreement with NIRS measurements. The concordance rates were 89.86 %, 97.45 %, and 97.13 % respectively for  $\Delta\text{HbO}_2$ ,  $\Delta\text{HHb}$ , and  $\Delta\text{tHb}$ .

### 10.3.3 Haemoglobin oxygenation from PPG signals

The haemoglobin concentrations changes  $\Delta\text{HbO}_2$ ,  $\Delta\text{HHb}$ , and  $\Delta\text{tHb}$  indicated changes in perfusion in the measurement area. The parameters were also used to estimate changes in haemoglobin oxygenation. The index  $\Delta\text{Hb}_{Ratio}$  was calculated from the

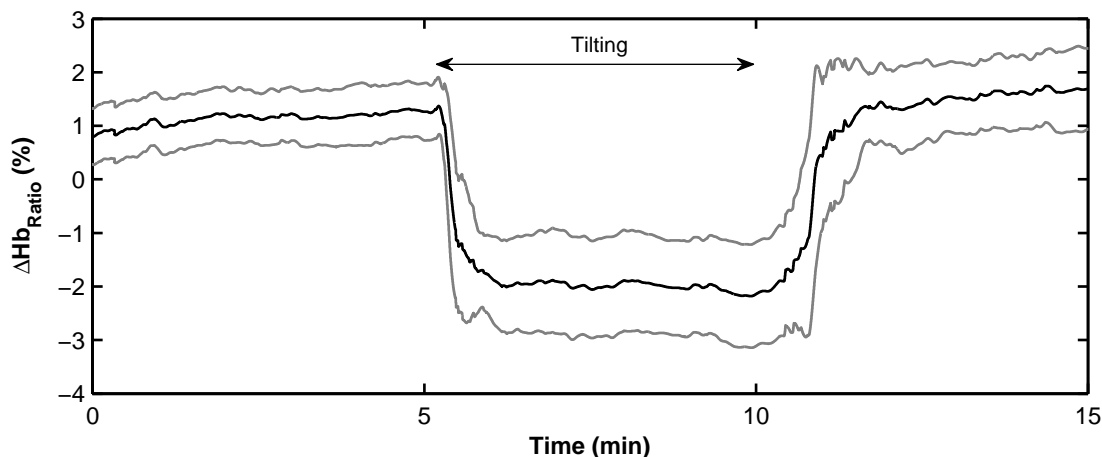


**Figure 10.7:** Mean changes ( $\pm$ SD) of  $\Delta\text{Hb}_{\text{Ratio}}$  during the bed tilting protocol. Black trace is the mean, grey traces are the  $\pm$ SD intervals.

ratio of  $\Delta\text{HbO}_2$  over  $\Delta\text{tHb}$  and it was expressed as percentage change from the baseline. Figure 10.7 shows the mean changes in  $\Delta\text{Hb}_{\text{Ratio}}$  from the PPG sensor placed distant from the large vasculature. Significant changes from baseline were observed in  $\Delta\text{Hb}_{\text{Ratio}}$  during tilting ( $p < 0.01$ ) and recovery ( $p < 0.01$ ).

Differently from subsection 9.3.4, the changes in  $\Delta\text{Hb}_{\text{Ratio}}$  were not correlated with the TOI changes.  $\Delta\text{Hb}_{\text{Ratio}}$  and TOI had a mean correlation coefficient  $r = -0.33$  (95 % CI: -0.70, 0.17), showing a poor and negative correlation. The TOI, differently from  $\text{Hb}_{\text{Ratio}}$ , did not exhibit any significant change from baseline ( $p > 0.05$ ). This different behaviour is most probably originating from the different penetration depths of TOI (NIRS) and  $\Delta\text{Hb}_{\text{Ratio}}$  (PPG). In this specific case, TOI is believed to reflect the oxygenation of the cerebral cortex, while PPG interrogates the forehead's skin only. The different responses of TOI and  $\Delta\text{Hb}_{\text{Ratio}}$  may suggest that tilting triggered an auto-regulatory mechanism in the brain, which was absent in the forehead's skin.

Contrarily to TOI, the nTHI exhibited significant increases ( $p < 0.01$ ) during tilting. Provided that TOI is the ratio between  $\text{HbO}_2$  and tHb (i.e.  $\text{tHb} = \text{HbO}_2 + \text{HHb}$ ) and that nTHI and TOI originate from the interrogation of the same tissue volume, the increase in nTHI (blood volume, tHb) and the stationary TOI, suggest that the brain auto-regulated its consumption (HHb) after an abrupt increase in  $\text{HbO}_2$ . Figure 10.8 illustrates the changes in  $\Delta\text{Hb}_{\text{Ratio}}$ , TOI and nTHI in all the subjects investigated, while Table 10.2 summarises the mean changes in  $\text{Hb}_{\text{Ratio}}$ , TOI, and nTHI.

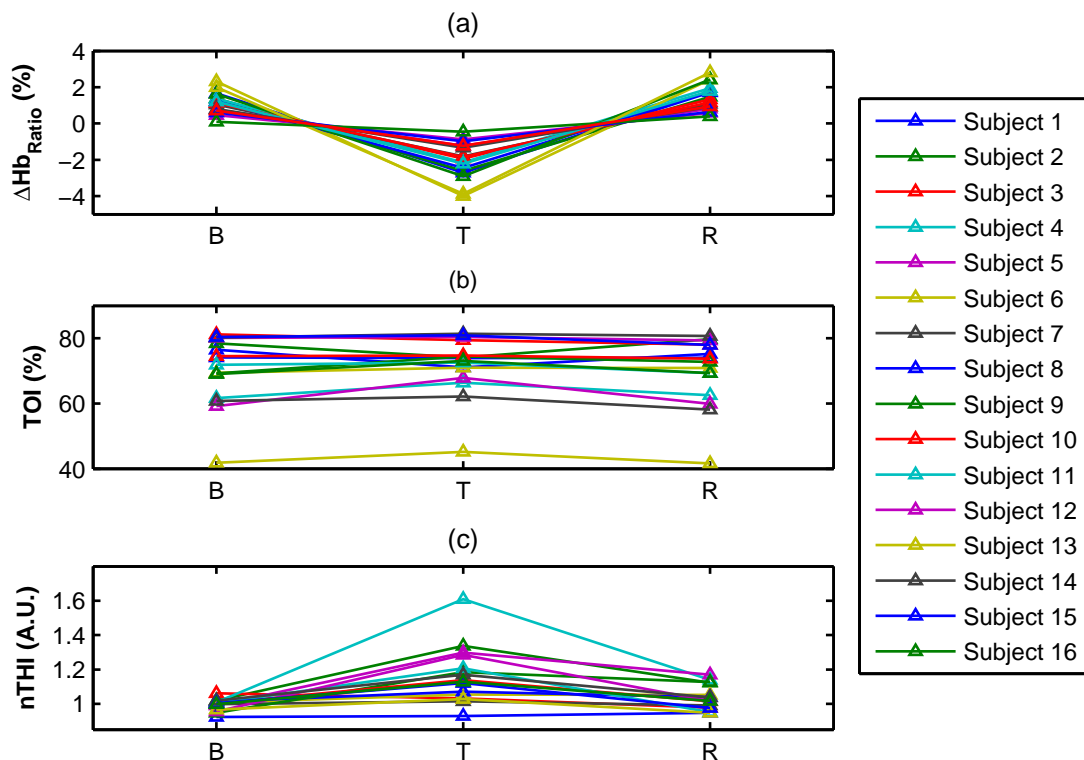


**Figure 10.8:** Changes in  $\Delta Hb_{Ratio}$ , TOI, and nTHI in all volunteers during the bed tilting protocol. (a) Changes in  $\Delta Hb_{Ratio}$ . (b) Changes in TOI. (c) Changes in nTHI. The signals were averaged over the central three minutes of each stage (baseline, tilting, and recovery). The consistent drops in  $\Delta Hb_{Ratio}$  and stationary TOI may suggest that the brain, differently from the skin, responded to tilting with some degree of auto-regulation. The increases in nTHI, which represent total blood volume changes ( $\Delta tHb$ ), indicate that the brain may regulate the HHb concentrations. B: baseline. T: tilting. R: recovery.

**Table 10.2:** Mean changes ( $\pm$ SD), of  $\Delta Hb_{Ratio}$ , TOI and nTHI during the bed tilting protocol. The signals were averaged over the central three minutes of each stage (baseline, tilting, and recovery).

	Baseline	Tilting	Recovery
$\Delta Hb_{Ratio}$ (%)	$1.14 \pm 0.56$	$-1.94 \pm 0.99^*$	$1.33 \pm 0.70^*$
TOI (%)	$74.16 \pm 10.53$	$73.94 \pm 8.82$	$73.75 \pm 10.20$
nTHI (A. U.)	$1.00 \pm 0.03$	$1.12 \pm 0.16^*$	$1.01 \pm 0.07$

\* Significant change from baseline ( $p < 0.05$ )

### 10.3.4 Influence of large vasculature on haemoglobin concentrations estimation by PPG

In the previous sections, the comparison between changes in haemoglobin concentrations measured by PPG and NIRS during bed tilting was presented. The PPG demonstrated to indicate the same haemodynamic changes measured by NIRS when a -30deg bed tilting procedure was performed. However, quantitative differences between the two techniques were present. Bland & Altman analysis indicated an overestimation of relative haemoglobin concentrations estimated by PPG when compared to NIRS. Correlation and trending analysis showed a high correlation and a good level of trending

concordance between the techniques.

This section will focus on analysing the effect of the large vasculature in the estimation of haemoglobin concentrations. It is expected that large vasculature will affect the estimation of haemoglobin concentrations. This is due to the greater light absorption of large vasculatures. In particular, the PPG should be more affected by the superficial large vasculatures present on the forehead due to its shallower penetration. In addition, the venous nature of the investigated vasculature is expected to affect mainly the estimation of deoxygenated haemoglobin.

Figure 10.9 shows the mean changes ( $\pm$ SD) of  $\Delta\text{HbO}_2$ ,  $\Delta\text{HHb}$ , and  $\Delta\text{tHb}$  estimated from both PPG sensors. The PPG sensor placed on top of the large vein (PPG-1) indicated the same changes in the parameters as the PPG sensor positioned distant from large vasculatures (PPG-2). The sensor on the large vessel followed the same trends as the other PPG sensor. There was a good correlation between the two PPG measures, with Pearson correlation coefficients  $r = 0.98$  (95 % CI: 0.94, 0.99),  $r = 0.96$  (95 % CI: 0.89, 0.98), and  $r = 0.98$  (95 % CI: 0.96, 0.99), for  $\Delta\text{HbO}_2$ ,  $\Delta\text{HHb}$  and  $\Delta\text{tHb}$  respectively.

Differences between the two PPG measures were assessed by testing for statistical significance between the means averaged over the central three minutes of each stage (i.e. baseline, tilting, and recovery). Figure 10.10 shows the box and whiskers plots of the means of haemoglobin concentrations calculated from both PPG sensors. When compared to the sensor placed distant from large vessels, the deoxygenated haemoglobin HHb estimated from the PPG sensor on the large vein demonstrated a significant difference during baseline ( $p = 0.03$ ), tilting ( $p = 0.03$ ), and recovery ( $p = 0.01$ ). Oxygenated haemoglobin ( $\text{HbO}_2$ ) and total haemoglobin (tHb) did not show any significant difference ( $p > 0.05$ ).

Bland & Altman analysis was also performed on the deoxygenated haemoglobin concentration changes ( $\Delta\text{HHb}$ ) estimated by both PPG sensors. Figure 10.11 depicts the Bland & Altman plots between the  $\Delta\text{HHb}$  estimated by both PPG sensors during the three stages of the bed tilting protocol (i.e. baseline, tilting, and recovery). The limits of agreement were  $1.0002 \pm 1.96 \times (4.21 \cdot 10^{-1})$ ,  $0.9995 \pm 1.96 \times (8.20 \cdot 10^{-1})$ , and  $1.0003 \pm 1.96 \times (4.63 \cdot 10^{-1})$ . These limits of agreement indicated that the PPG sensor

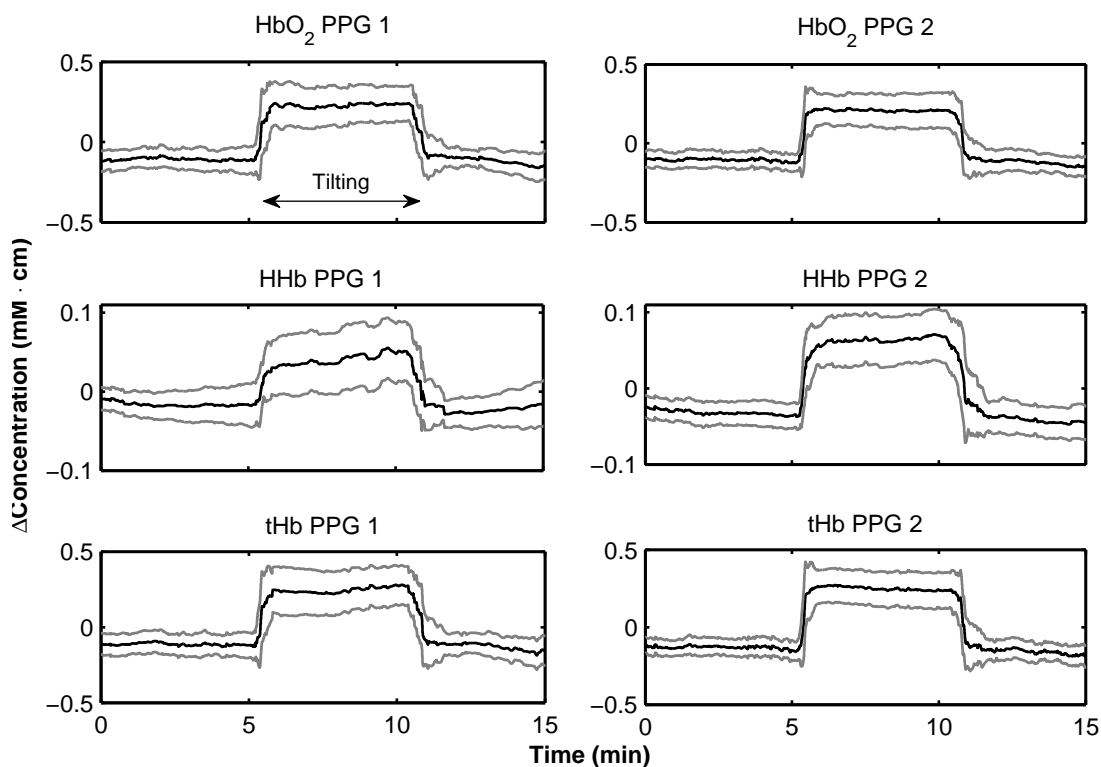


**Figure 10.9:** Mean changes ( $\pm$ SD) in HbO<sub>2</sub>, HHb, and tHb from the forehead estimated by the two PPG sensors. The haemoglobin concentrations were estimated from the PPG sensor positioned on the large vessel (PPG-1) and from the PPG sensor placed distant from large vasculature on the forehead (PPG-2). The tilting was performed in the central part of the protocol, after five minutes of baseline readings. The head-down tilting was followed by five minutes of recovery in the supine position. Black traces are the means, while grey traces represent the  $\pm$ SD intervals.

on top of the large vein slightly overestimated  $\Delta$ HHb during baseline and recovery, while in tilting the presence of the vein underneath the sensor causes an underestimation of  $\Delta$ HHb. In addition, the positioning of the sensor on top of the vein caused an increase of the limits of agreements between the two PPG sensors during tilting.

Mean absolute errors (MAE) were calculated between the haemoglobin concentrations estimated from the two PPG sensors. The MAE values were calculated in the three minutes central section of each stage (i.e. baseline, tilting, and recovery) and are summarised in Table 10.3. MAE analysis revealed a greater error during tilting than baseline or recovery and a larger error in deoxygenated haemoglobin compared to oxygenated and total haemoglobin. The MAE values indicated that the sensor positioned on the large vein overestimated the deoxygenated haemoglobin during baseline and recovery, while it underestimated the parameter during tilting. Even though the error for HHb during tilting may seem very small, it may signify an underestimation of roughly 25 % of the full range measured in this study by the PPG sensor placed in the correct position (i.e. away from large vasculature).

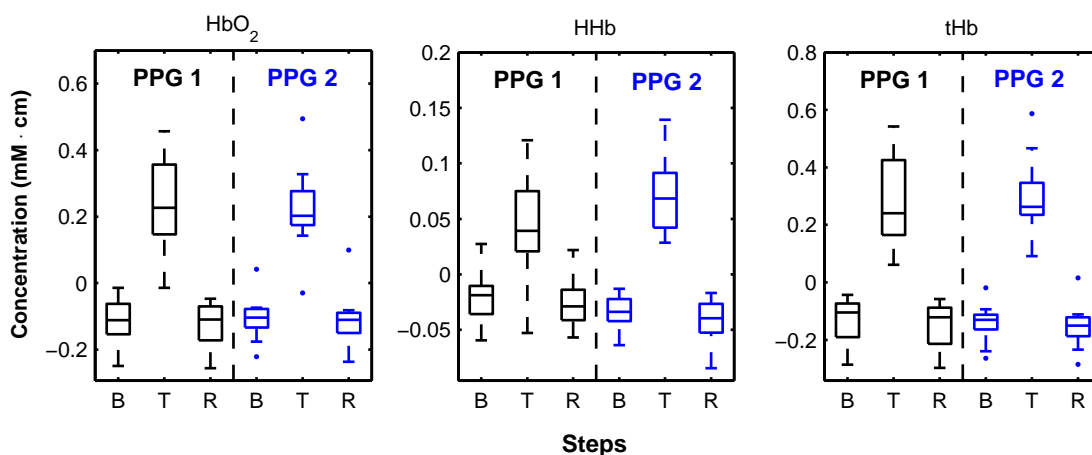


**Figure 10.10:** Box and whiskers plots of the mean changes in  $\text{HbO}_2$ ,  $\text{HHb}$ , and  $\text{tHb}$  estimated from both PPG sensors during baseline, tilting, and recovery. Black boxes on the left side of each sub-plot are the changes from the PPG sensor positioned on top of the large vessel (PPG-1). Blue boxes on the right side of each sub-plot are the changes from the PPG sensor placed distant from large vasculatures (PPG-2). B: baseline. T: tilting. R: recovery). The values were averaged over the central three-minute section of each stage (baseline, tilting, and recovery).

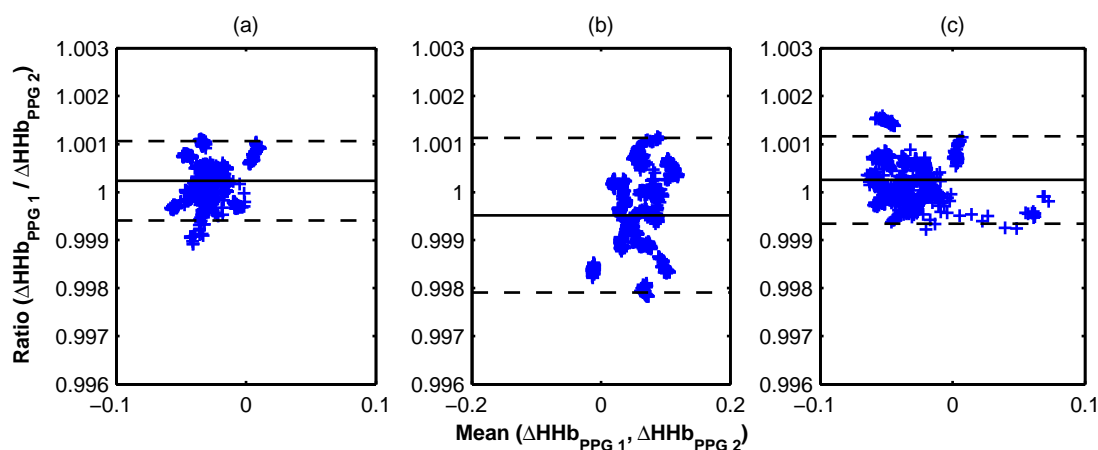


**Figure 10.11:** Bland & Altman plots of the deoxygenated haemoglobin ( $\Delta\text{HHb}$ ) estimated from the PPG sensor on the large vein (PPG-1) and the PPG sensor distant from large vasculatures on the forehead (PPG-2) during the three stages of the bed tilting protocol. (a) Baseline. (b) tilting. (c) Recovery. X-axes are the mean between the two measures, while the y-axes are the differences between the measures. Blue crosses are the data. Horizontal solid lines are the standard mean bias ratios and the dashed lines are the limits of agreement (mean  $\pm$  1.96SD).

**Table 10.3:** Mean absolute errors (MAE) between haemoglobin concentrations estimated from the two PPG sensors during the bed tilting protocol. The MAE values were calculated over three-minutes long section at each stage of the protocol (baseline, tilting, and recovery).

	Baseline (mM·cm)	Tilting (mM·cm)	Recovery (mM·cm)
$\Delta\text{HbO}_2$	-0.007	0.014	-0.011
$\Delta\text{HHb}$	0.013	-0.026	0.013
$\Delta\text{tHb}$	0.005	-0.011	0.002

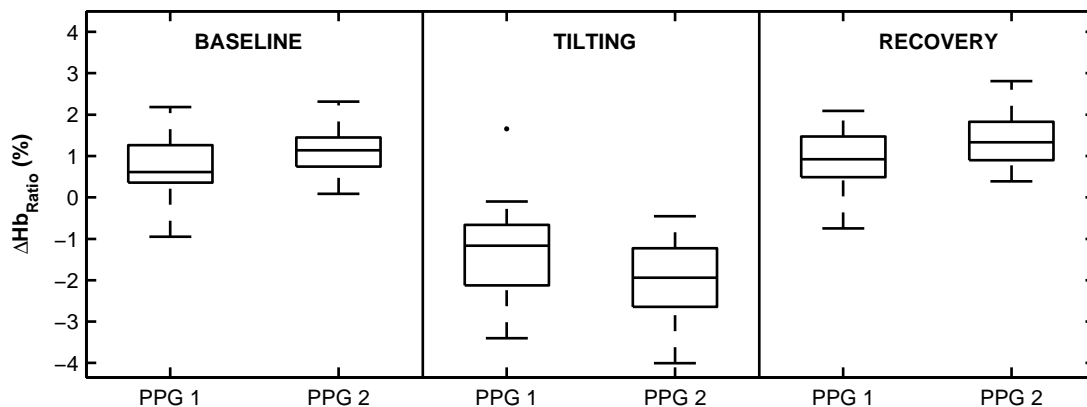


**Figure 10.12:** Box and whiskers plots of the mean changes in  $\Delta\text{Hb}_{Ratio}$  estimated from the PPG sensor on the large vein and the PPG sensor distant from large vasculatures on the forehead during the three stages of the bed tilting protocol. PPG-1: sensor placed on top of the large vein. PPG-2: sensor positioned distant from large vasculatures on the forehead.

### 10.3.5 Influence of large vasculature on haemoglobin oxygenation estimation by PPG

The  $\Delta\text{Hb}_{Ratio}$  was also estimated from the PPG sensor placed on top of the large vein. Figure 10.12 illustrates the box and whiskers plot of the mean values of  $\Delta\text{Hb}_{Ratio}$  estimated from both PPG sensors. The changes measured by the sensor positioned over the vein correlated well ( $r = 0.96$ , 95 % CI: 0.88, 0.98) with the measurements from the sensor placed just above the eyebrow. However, there was a statistically significant difference between the two  $\Delta\text{Hb}_{Ratio}$  during tilting ( $p = 0.04$ ) and recovery ( $p = 0.02$ ), while there was no difference during baseline ( $p > 0.05$ ). The mean absolute errors MAEs between  $\text{Hb}_{Ratio}$  measured by the two sensors during baseline, tilting and recovery were respectively -0.406 %, 0.746 %, and -0.432 %.

Bland & Altman analysis between  $\Delta\text{Hb}_{Ratio}$  estimated from the two PPG sensors revealed mean bias ratios of  $0.992 \pm 1.96 \times 0.014$ ,  $1.015 \pm 1.96 \times 0.026$ , and  $0.991 \pm 1.96 \times 0.015$  respectively for baseline, tilting, and recovery. The Bland & Altman plots for the different stages of the protocol are presented in Figure 10.13. The limits of agreement, along with the MAE values, indicated that the presence of the large vein beneath the PPG sensor caused a consistent overestimation of  $\Delta\text{Hb}_{Ratio}$  during tilting, whereas in recovery and baseline  $\Delta\text{Hb}_{Ratio}$  was underestimated.

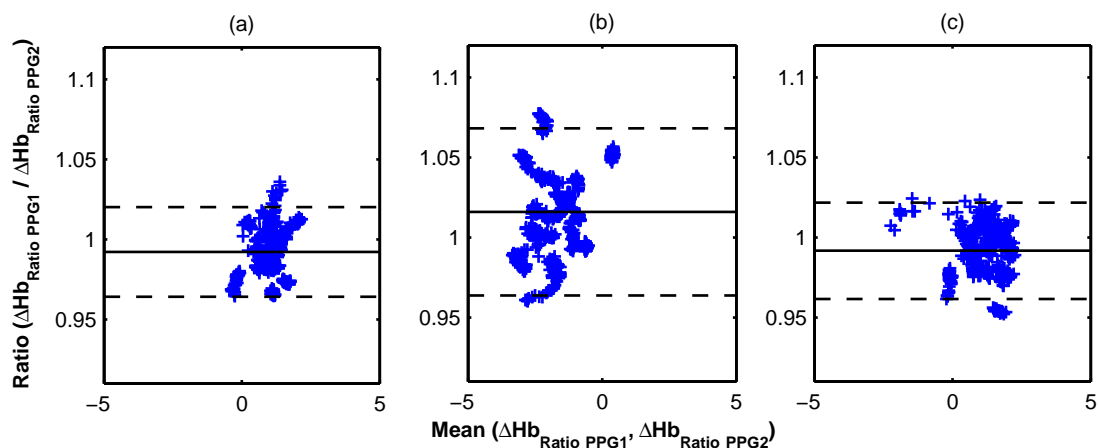


**Figure 10.13:** Bland & Altman plots of  $\Delta Hb_{Ratio}$  estimated from the PPG sensor on the large vein (PPG-1) and the PPG sensor distant from large vasculatures on the forehead (PPG-2) during the three stages of the bed tilting protocol. (a) Baseline. (b) Tilting. (c) Recovery. X-axes are the mean between the two measures, while the y-axes are the ratio of the measures. Blue crosses are the data. Horizontal solid lines are the standard mean bias ratios and the dashed lines are the limits of agreement (mean  $\pm$  1.96SD).

### 10.3.6 Influence of large vein on $SpO_2$ estimation by PPG

Arterial oxygen saturation ( $SpO_2$ ) was estimated from PPG signals acquired by both PPG sensors, either placed on top of or distant from the large vein. When the two sensors were compared, there was no statistical difference ( $p > 0.05$ ) in the mean  $SpO_2$  values throughout baseline. However, Bland & Altman analysis (Figure 10.14) revealed a mean bias of 0.96 % between the two  $SpO_2$  and limits of agreement of  $0.96 \pm 1.96 \times 4.17$  %. Although the mean bias is not excessive, the limits of agreement are wide. This may indicate that the  $SpO_2$  measured on top of the vein has a substantial variability compared to an identical sensor placed distant from vasculatures. In addition, when the root mean square error (RMSE) between the  $SpO_2$  at the two locations was calculated like Mannheim et al. did in [110], it revealed a greater error, with  $RMSE = 4.38$  %.

Figure 10.15 shows the mean changes of the estimated  $SpO_2$  from both sensors throughout the entire protocol. During baseline, both  $SpO_2$  dropped significantly from baseline ( $p < 0.01$ ). This drop was mainly due to two factors. Firstly, during tilting, the AC PPG signal deteriorated due to venous engorgement. Figure 10.16 shows an example of AC PPG traces acquired at baseline, tilting and recovery. The negative tilting, and consequent venous engorgement, caused a significant deterioration of the signal due to the appearance of venous pulsations in the PPG signals [111]. Secondly, the shifting of venous blood underneath the sensor caused the mixture of venous and arterial blood,

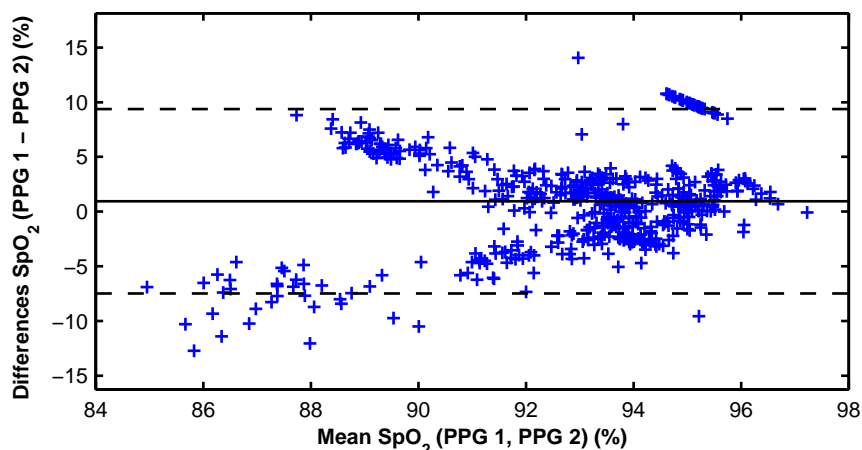


**Figure 10.14:** Bland & Altman plots of  $\text{SpO}_2$  estimated from the PPG sensor on the large vein (PPG-1) and the PPG sensor distant from large vasculatures on the forehead (PPG-2) during baseline. X-axes are the means between the two measures, while the y-axes are the differences between the measures. Blue crosses are the data. The horizontal solid line is the mean bias ratio and the dashed lines are the limits of agreement ( $\text{mean} \pm 1.96\text{SD}$ ). Limits of agreement were  $0.96 \pm 1.96 \times 4.17$  (%). The original signals were resampled every 5 seconds.

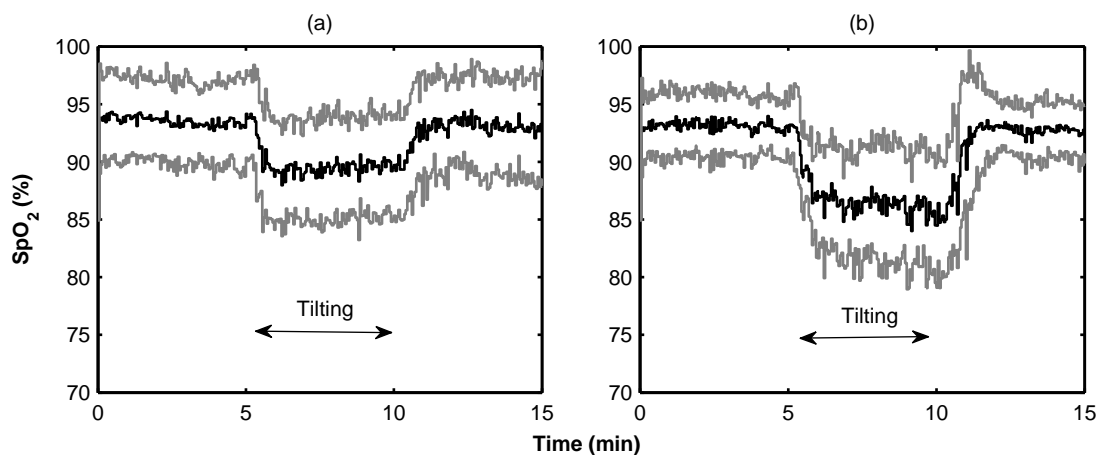


**Figure 10.15:** Mean changes ( $\pm\text{SD}$ ) in  $\text{SpO}_2$  estimated from the PPG sensor placed on top of the large vein PPG-1 (a) and the PPG sensor positioned distant from large vasculatures PPG-2 (b) during the bed tilting protocol. Black traces are the means, while grey traces represent the  $\pm\text{SD}$  intervals.

with a consequent overestimation of the ratio of ratios and  $\text{SpO}_2$ . The drop in  $\text{SpO}_2$  during the protocol should not be interpreted as a decrease in the oxygen content of arterial blood, but instead be related to a limitation of the technique in providing reliable  $\text{SpO}_2$  readings in the presence of venous blood and/or venous pulsations.

## 10.4 Summary

After investigating in Chapter 9 the response of haemoglobin concentrations estimated by PPG during vascular occlusions on the forearm, this chapter aimed at analysing the haemoglobin concentrations from PPG signals acquired from the forehead. PPG

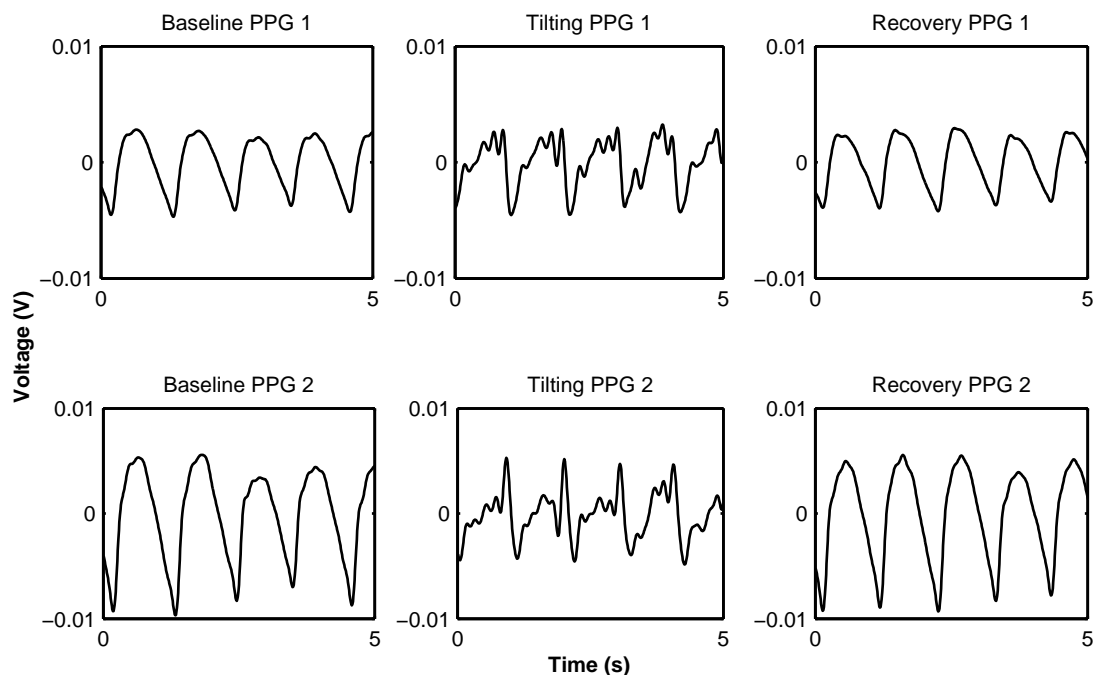


**Figure 10.16:** Five second traces of infrared AC PPG signals acquired from the PPG sensor on top of the large vein (PPG-1) and distant from large vasculature (PPG-2) during the three stages of the bed tilting protocol (i.e. baseline, tilting, and recovery). During tilting the shape of the PPG signal changes due to the presence of venous pulsations.

and NIRS sensors were applied on the forehead and a negative bed tilting protocol was performed in order to induce a haemodynamic change. One PPG sensor was placed on top of a large vein, whereas another identical PPG sensor and one NIRS sensor were positioned distant from any large vasculature.

Relative changes in oxygenated, deoxygenated, and total haemoglobin estimated from the PPG sensor distant from large vasculature were compared with the same parameters measured by NIRS. Haemoglobin concentration changes correlated well with NIRS measurements. In addition, four-quadrant plots analysis revealed good trending agreement between haemoglobin concentrations estimated by PPG and NIRS. However, there were quantitative differences between the measures most probably due to the different penetration depth. Bland & Altman analysis revealed a bias between the measures, which was dependent on the magnitude of the change. Changes in haemoglobin oxygenation ( $\Delta\text{Hb}_{Ratio}$ ) were also calculated from the haemoglobin concentrations. The  $\Delta\text{Hb}_{Ratio}$  significantly changed during bed tilting. However, the measure of  $\text{Hb}_{Ratio}$  did not correlate with the oxygenation changes estimated from NIRS (TOI). The absence of any significant change in TOI, concomitant to the increase in nTHI, was probably due to an autoregulatory response of the brain to tilting.

The effect of the placement of the PPG sensor on top of a large vein was investigated. The changes in haemoglobin concentrations, haemoglobin oxygenation, and  $\text{SpO}_2$  estimated from the two PPG sensors were compared during the three stages of the protocol (i.e. baseline, tilting, and recovery). There was a good correlation between the changes measured by both PPG sensors. Amongst the haemoglobin concentration changes measured at the two locations, only deoxygenated haemoglobin ( $\Delta\text{HHb}$ ) showed a significant difference in all stages of the protocol. In particular, the  $\Delta\text{HHb}$  measured on top of the vein seemed to be underestimated when compared to the location free from the large vasculature. The haemoglobin oxygenation changes ( $\Delta\text{Hb}_{\text{Ratio}}$ ) measured at the two locations also showed a bias during tilting.

The analysis of differences in  $\text{SpO}_2$ , when this was measured on top of a large vein, revealed a large mean error with the  $\text{SpO}_2$  measured distant from any vein. Bland & Altman plots also showed wide limits of agreement between the  $\text{SpO}_2$  measured at the two locations, indicating a large variability caused by the presence of the vein underneath the sensor.

After investigating the response of PPG at the forearm during vascular occlusions and at the forehead during tilting, a new physiological challenge and other measurement locations were also explored. The next chapter will present results from an investigation in which PPG signals measured at the finger and ear canal were used to infer relative haemoglobin concentration changes during a whole-body exposure to a cold temperature.

# Chapter 11

## **Investigation of Photoplethysmography and Near Infrared Spectroscopy during an induced thermal stress**

The studies presented in the previous chapters showed the response of PPG signals acquired from two different anatomical locations (forearm and forehead) and during two different physiological challenges (vascular occlusions and tilting). In those investigations, the PPG signals acquired from a single sensor were analysed (Chapter 9) or two identical sensors placed close to each other were compared (Chapter 10). The study presented in this chapter differs from the previous studies in both the physiological challenge induced and in the measurement locations from which the PPG signals were acquired. After mechanically occluding the vasculature (occlusions) or causing blood pooling by changing the subject's position (tilting), the study in this chapter aims at causing a vasoconstrictive response by exposing the subjects to a cold temperature. This can be considered a more natural stimulus, to which most people are exposed in winter. This study also aims to compare the perfusion at two different locations by analysing the haemoglobin concentration changes estimated from the PPGs acquired from the finger and the ear canal.

## 11.1 Introduction

In Chapter 9 and Chapter 10, the feasibility of estimating relative concentration changes of oxygenated ( $\Delta\text{HbO}_2$ ), deoxygenated ( $\Delta\text{HHb}$ ), and total haemoglobin ( $\Delta\text{tHb}$ ) from PPG signals was investigated. In Chapter 9, the changes in  $\Delta\text{HbO}_2$ ,  $\Delta\text{HHb}$ , and  $\Delta\text{tHb}$  estimated from PPG indicated the changes in perfusion when venous outflow or arterial inflow were blocked by different levels of vascular occlusions on the arm. In Chapter 10, the changes in haemoglobin concentrations revealed an increased presence of venous blood in the forehead when the subjects were tilted head-down. In both studies,  $\Delta\text{HbO}_2$ ,  $\Delta\text{HHb}$ , and  $\Delta\text{tHb}$  estimated from PPG signals were well correlated and showed good trending agreement with state-of-the-art NIRS measurements.

The changes in perfusion performed in Chapter 9 and Chapter 10 (i.e. vascular occlusions and bed tilting) were achieved by directly occluding vasculature or forcing venous engorgement on the head by gravitation. This chapter investigates the response of relative haemoglobin concentrations estimated from PPG during a more natural change in perfusion such as an exposure to a cold temperature. Healthy subjects were placed in a room kept at 10 °C and the haemodynamic responses were recorded.

In the previous studies, the haemoglobin concentrations were estimated from reflectance PPG signals acquired from the forearm or the forehead. In this study, other measurement locations such as the finger and the ear canal were also investigated. In addition, the haemoglobin concentrations from the two locations were compared in order to reveal any differences in perfusion between the two locations. The ear canal, being supplied by branches of the carotid artery, should be more resilient to vasoconstriction when compared to the fingers. This property of the ear canal was previously described by Budidha and Kyriacou, who reported more stable  $\text{SpO}_2$  measurements and higher signal amplitude in the ear canal compared to the fingers in the presence of vasoconstriction [93, 94].

In the study presented in this chapter, haemoglobin concentrations were acquired by a state-of-the-art NIRS sensors applied on the forearm and forehead and they were used as a reference for the PPG measurements. The Tissue Oxygenation Index (TOI) and normalised Tissue Haemoglobin Index (nTHI) were also acquired by NIRS. TOI and nTHI, measured by spatially resolved spectroscopy, reflect changes in oxygenation

and blood volume in deep tissues. TOI and nTHI were also analysed and compared in order to reveal any variation in oxygenation or blood volume in the brain and muscle during exposure to cold temperatures. The following sections in this chapter describe the study's methods and results.

## **11.2 Measurements set-up, protocols and data analysis**

### **11.2.1 Measurement system**

The research PPG processing unit presented in Chapter 7 was used to acquire raw PPG signals (AC+DC). As described later, one finger PPG sensor was used to acquire PPG signals from the finger, whereas a second sensor was used to measure PPG signals from a more central location such as the ear canal.

A commercial NIRS monitor (NIRO 200NX, Hamamatsu Photonics, Japan) was used to acquire NIRS signals, whereas a laser Doppler flowmetry device (moorVMS-LDF2, Moor Instruments Ltd, UK) was used to measure blood flow in the skin.

PPG and NIRS signals were acquired on LabVIEW through two 16-bit NI-PcIe 6321 Data Acquisition Cards (National Instruments, USA). The VI described in Chapter 8 was adapted for the acquisition of PPG signals from the ZenPPG, the NIRS monitor and the laser Doppler monitor. Analogue outputs scaling equations were applied for the NIRS, Flux, and temperature signals (subsection 8.3.5). All the signals were acquired simultaneously at a sampling frequency of 1000 Hz and saved in a text file for post-acquisition analysis.

### **11.2.2 Subjects and investigation set-up**

Thirteen (13) healthy subjects with mean age ( $\pm$  SD) of  $28 \pm 3.6$  (6 males and 7 females) were recruited for the investigation. Ethical approval was gained from the Senate Research Ethics Committee at City University London and written consent was sought from the volunteers before commencing of the investigation. Subjects with a history of cardiovascular disorders were excluded from the study.

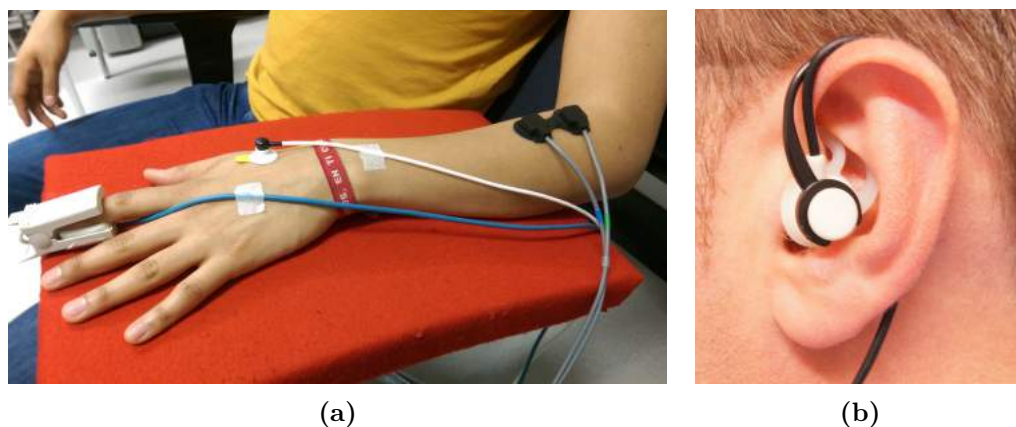


**Figure 11.1:** Figures showing the placement of PPG, NIRS, and LDF sensors on the forearm (a) and the PPG ear canal sensor (b).

Subjects were asked to sit in a comfortable chair, with their arms placed on the armrests. Finger PPG signals were acquired from the second digit of the left hand by a reflectance PPG sensor. A reflectance ear canal PPG sensor was used to acquire PPG signals from the subjects' left ear canal [93,94,192]. The sensor comprised the same optical components (LEDs and photodiode) as the PPG finger sensor applied on the left hand. The ear canal and finger PPG sensors were developed by Budidha as part of another research project [93,94,192] and they were conjointly used for this investigation.

The Laser Doppler flowmetry (LDF) VP1T sensor was positioned on the dorsal side of the left hand. The LDF sensor was kept in place by ring-shaped adhesive pads provided by the manufacturer. In addition to measuring skin blood flow (Flux), the sensor measured continuously the subject's skin temperature.

An NIRS sensor with a separation distance of 4 cm was placed on the left forearm, above the brachioradialis. A second NIRS sensor, with a separation distance of 4 cm, was placed on the subject's forehead in order to measure cerebral NIRS signals. The sensor was positioned high above the left eyebrow and external in order to avoid midline sinuses. The sensors were attached to the skin by means of clear double-sided medical adhesive tapes. The tapes were previously cut at the emitter and detector positions in order to avoid any optical obstruction. All the instrumentation comprising of the PPG system, NIRS monitor, LDF monitor, and personal computer were positioned on a wheelbase trolley.

Figure 11.1 shows the placement of the sensors on the left forearm and hand, and the position of the ear canal sensor.

### 11.2.3 Investigation protocol

Throughout the study, the subjects were exposed to different ambient temperatures. The investigation protocol consisted of three stages: baseline, cold exposure, and recovery. In the baseline, the volunteers sat for two minutes on the chair, in a room at a constant ambient temperature of  $23 \pm 1$  °C. After these two minutes baseline readings, the subjects were moved into a second temperature controlled room, at a temperature of  $10 \pm 1$  °C. The subjects were exposed at this temperature for ten minutes, before being moved back to the initial room at 23 °C (recovery stage). The subjects were left to recover at 23 °C for an additional ten minutes.

The volunteers were moved between each room by carefully pushing the trolley containing the instrumentation and the wheelchair on which they were sitting on. In order to avoid recording any movement artefacts caused by the transfer, the measurements were paused during the transfer. In addition, the NIRS measurements (haemoglobin concentrations and nTHI) were zero-set at the end of each transfer to obtain only relative changes in each stage (i.e. baseline, cold, recovery).

The volunteers were wearing only light clothes such as t-shirts or shirts and they were asked to remove their shoes. Prior to commencing the investigation, the volunteers were left for at least 15 minutes to acclimatise at 23 °C.

### 11.2.4 Data analysis & statistics

Post-acquisition analysis was performed in Matlab2013a. Before processing, all the acquired signals were down-sampled to 100 Hz. TOI, nTHI and haemoglobin concentrations from NIRS were filtered from high-frequency noise and components by a zero-phase low-pass filter ( $f_c = 0.05$  Hz). The finger AC PPG component was obtained from raw PPG signals by applying a zero-phase band-pass filter (pass-band: 0.5-7 Hz). The DC PPGs were obtained by low-pass filtering the signal at  $f_c = 0.1$  Hz.

The perfusion index (PI) was calculated in a three seconds rolling window from infrared PPG signals by computing the AC PPG amplitude and normalise it to the DC value (see Equation 9.2). The PI and the laser Doppler Flux were normalised to ten seconds

baseline readings in order to compensate for inter-subject variability.

Changes in oxygenated ( $\Delta\text{HbO}_2$ ), reduced ( $\Delta\text{HHb}$ ) and total haemoglobin ( $\Delta\text{tHb}$ ) were estimated by applying the modified Beer-Lambert law to DC PPG signals acquired from the finger and ear canal, as showed in Section 8.4.

Correlation between techniques or variables was assessed by measuring the Pearson correlation coefficient  $r$  with the 95 % confidence intervals (CI). The trending agreement was evaluated by four-quadrant plot analysis [184]. The concordance rate  $C$  was calculated as the ratio of the number of points in the first and third quadrant and the total number of points in all quadrants. An exclusion zone of 10 % was used for the calculations [184]. A concordance rate  $C \geq 90$  % was considered satisfactory for indicating trending agreement.

The changes during each stage of the protocol (i.e. baseline, cold, and recovery) were averaged over the central minute of baseline, the last minute of cold exposure, and the last minute of recovery. Statistically significant changes from baseline were tested by repeated measures Wilcoxon signed-rank tests. A p-value less than 0.05 was considered satisfactory for significance.

## 11.3 Results

Figure 11.2 shows all the acquired signals from one of the subjects investigated. During the protocol, all the signals indicate the haemodynamic changes caused by the exposure to cold. The following sections will analyse these changes in more detail.

### 11.3.1 Haemoglobin concentration changes estimated from PPG

Haemoglobin concentrations were estimated from dual-wavelength finger PPG signals by applying the modified Beer-Lambert law to DC PPG signals. Figure 11.3 shows examples of changes in oxygenated ( $\Delta\text{HbO}_2$ ), deoxygenated ( $\Delta\text{HHb}$ ), and total haemoglobin ( $\Delta\text{tHb}$ ) estimated from the finger throughout the protocol. The cold exposure caused an almost immediate vasoconstriction of the microcirculation. This was

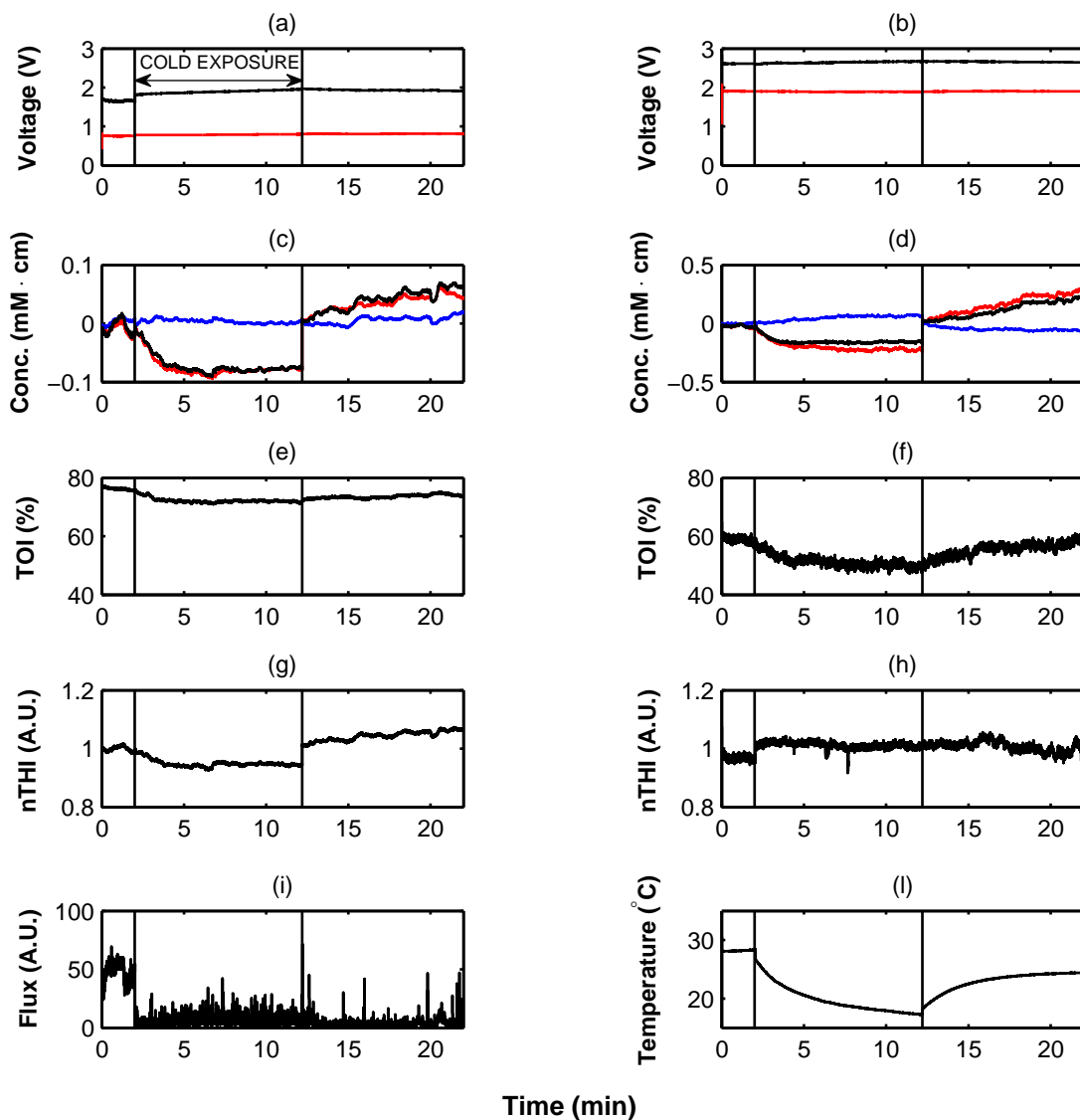


**Figure 11.2:** Example of PPG, NIRS, laser Doppler flowmetry and skin temperature signals acquired from one subject during the investigation protocol. (a) Raw PPG signals (AC+DC) acquired from the finger. (b) Raw PPG signals acquired from the ear canal. (c) NIRS relative haemoglobin concentrations measured at the forearm. (d) NIRS relative haemoglobin concentrations measured at the forehead. (e) NIRS TOI measured at the forearm. (f) NIRS TOI measured at the forehead. (g) NIRS nTHI measured at the forearm. (h) NIRS nTHI measured at the forehead. (i) Laser Doppler Flux. (l) Skin temperature. Vertical lines indicate the duration of the exposure to cold.

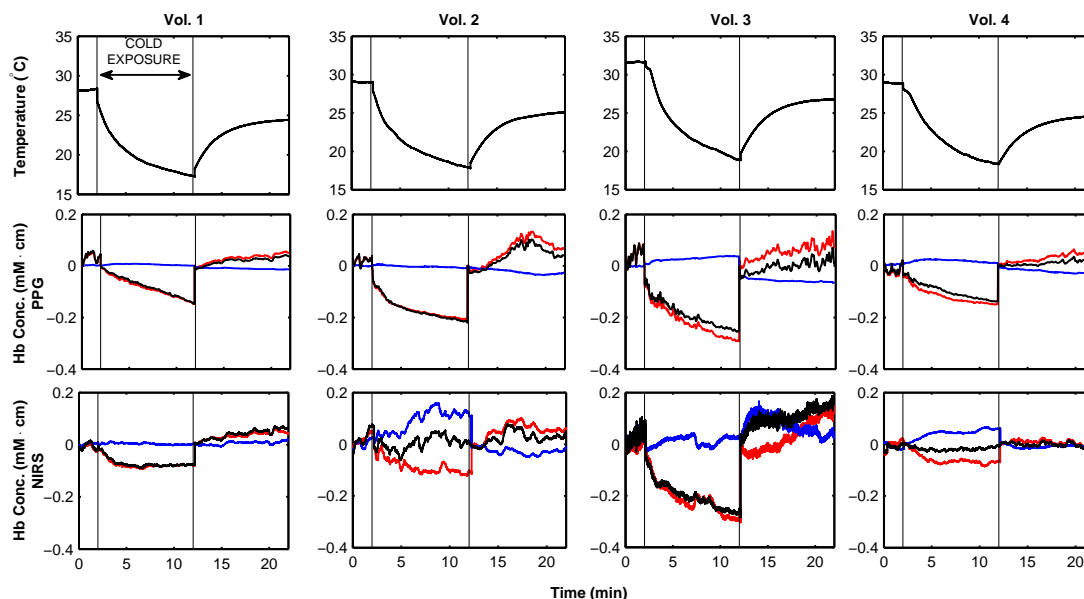
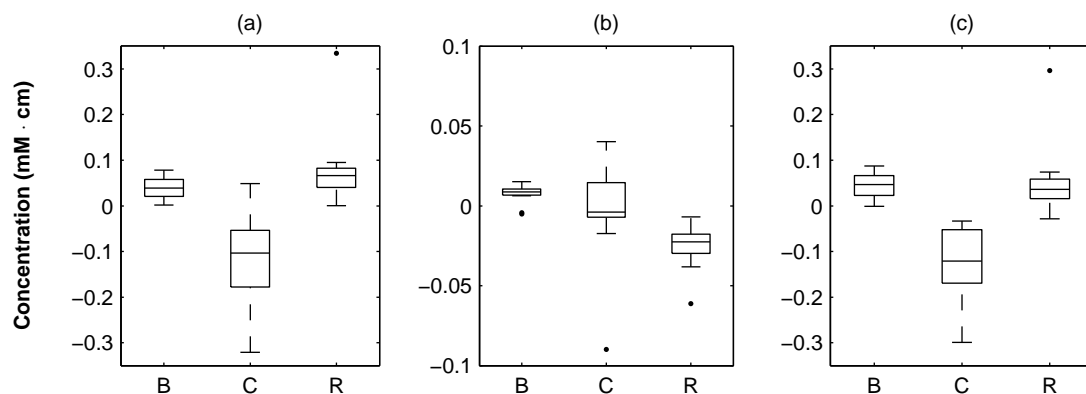


**Figure 11.3:** Example of  $\Delta\text{HbO}_2$ ,  $\Delta\text{HHb}$ , and  $\Delta\text{tHb}$  estimated from finger (PPG) and forearm (NIRS) of four subjects during cold exposure. Each column represent one volunteer. Top row: skin temperatures. Middle row: haemoglobin concentrations estimated from the PPG measured at the fingers. Bottom row: haemoglobin concentrations estimated by NIRS at the forearm. Red traces:  $\Delta\text{HbO}_2$ . Blue traces:  $\Delta\text{HHb}$ . Black trace:  $\Delta\text{tHb}$ . Vertical lines represent the duration of the cold exposure.

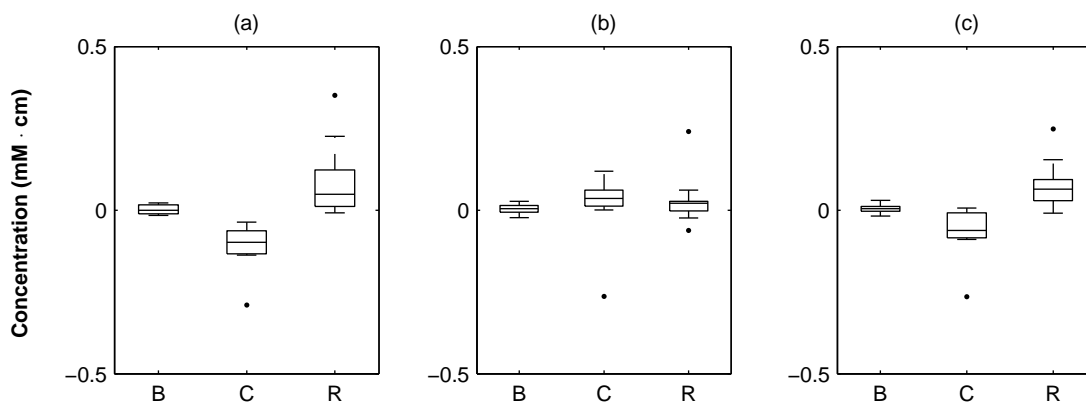
represented by the drop in  $\Delta\text{HbO}_2$  as soon as the volunteers were introduced in the cold room. Contrarily to  $\Delta\text{HbO}_2$ , the  $\Delta\text{HHb}$ , representing venous blood, did not appear to change significantly during exposure to cold. The  $\Delta\text{tHb}$ , being the sum of  $\Delta\text{HbO}_2$  and  $\Delta\text{HHb}$ , followed the drop in  $\text{HbO}_2$ . The  $\Delta\text{HbO}_2$ ,  $\Delta\text{HHb}$ , and  $\Delta\text{tHb}$  estimated from the PPG signals acquired from the finger followed the changes of the same parameters estimated from the forearm by NIRS.

Figure 11.4 shows the box and whiskers plots of the means of the haemoglobin concentration changes estimated from the finger PPG in the three different stages of the protocol (i.e. baseline, cold, and recovery) for all volunteers. Exposure to cold caused a statistically significant drop of  $\Delta\text{HbO}_2$  from baseline ( $p < 0.01$ ), whereas  $\Delta\text{HHb}$  did not change from baseline ( $p > 0.05$ ). Similar to  $\Delta\text{HbO}_2$ , a significant change in  $\Delta\text{tHb}$  occurred during exposure to cold temperature ( $p < 0.01$ ).

Figure 11.5 illustrates the box and whisker plots of  $\Delta\text{HbO}_2$ ,  $\Delta\text{HHb}$ , and  $\Delta\text{tHb}$  measured at the forearm by NIRS. Again,  $\Delta\text{HbO}_2$  and  $\Delta\text{tHb}$  significantly decreased during cold ( $p < 0.01$ ), while  $\Delta\text{HHb}$  increased. However, the increase in  $\Delta\text{HHb}$  was not statistically significant ( $p = 0.06$ ). While the decrease in  $\Delta\text{HbO}_2$  and  $\Delta\text{tHb}$  could be attributed to vasoconstriction, the increase in  $\Delta\text{HHb}$ , although not significant, was most probably caused by an increase in muscle oxygen consumption due to shivering in some subjects.



**Figure 11.4:** Box and whiskers plot of the means of  $\Delta\text{HbO}_2$ ,  $\Delta\text{HHb}$ , and  $\Delta\text{tHb}$  measured at the finger by PPG during cold exposure. (a)  $\Delta\text{HbO}_2$ . (b)  $\Delta\text{HHb}$ . (c)  $\Delta\text{tHb}$ . B: baseline; C: cold exposure; R: recovery. Values were averaged in the central one minute of baseline, last one minute of cold, and last one minute of recovery.



**Figure 11.5:** Box and whiskers plot of the means of  $\Delta\text{HbO}_2$ ,  $\Delta\text{HHb}$ , and  $\Delta\text{tHb}$  measured from the forearm by NIRS during cold exposure. (a)  $\Delta\text{HbO}_2$ . (b)  $\Delta\text{HHb}$ . (c)  $\Delta\text{tHb}$ . B: baseline; C: cold exposure; R: recovery. Values were averaged in the central one minute of baseline, last one minute of cold, and last one minute of recovery.

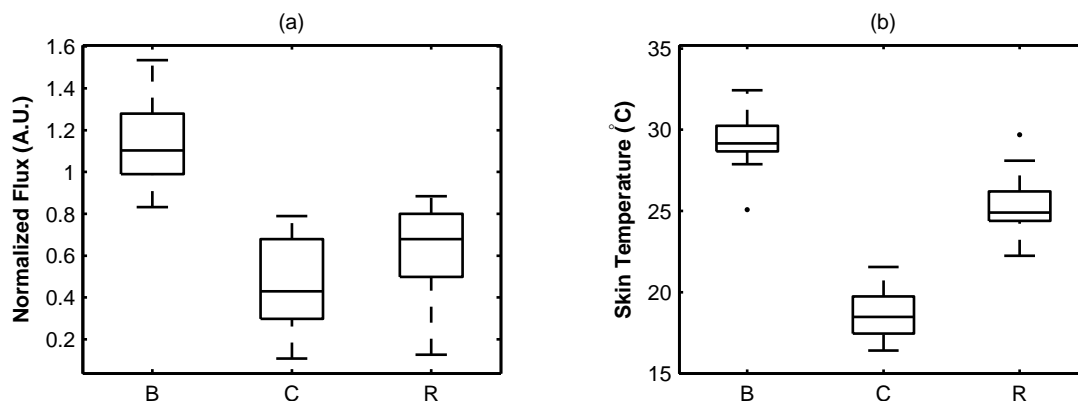


**Figure 11.6:** Box and whiskers plot of the means of normalised Flux and skin temperature during cold exposure. (a) Flux. (b) Skin temperature (c). B: baseline; C: cold exposure; R: recovery. Values were averaged in the central one minute of baseline, last one minute of cold, and last one minute of recovery. Flux was normalised with respect to ten seconds of baseline readings.

The decreases in  $\Delta\text{HbO}_2$  and  $\Delta\text{tHb}$  could be attributed to skin vasoconstriction, which was taking place as soon as the subjects were introduced in the cold room. The severe vasoconstriction was confirmed by laser Doppler flowmetry and skin temperature readings. Figure 11.6 shows the box and whiskers of the mean changes in Flux and skin temperature throughout the protocol. During the cold exposure, the Flux significantly dropped from  $1.12 \pm 0.18$  A.U. in baseline to  $0.44 \pm 0.22$  A.U. ( $p < 0.01$ ). Similarly, the skin temperature decreased to  $18.62 \pm 1.40$  °C from a baseline of  $29.40 \pm 1.94$  °C.

### 11.3.2 Assessment of correlation and trending between PPG and NIRS

As can be seen from Figure 11.3, the haemoglobin concentrations estimated from the finger by PPG and from the forearm by NIRS indicated similar haemodynamic variations caused by exposure to cold. The variables of interests followed the same trends except for deoxygenated haemoglobin (HHb). Correlation analysis between PPG and NIRS showed a correlation between  $\Delta\text{HbO}_2$  during cold exposure ( $r = 0.75$ , 95 % CI: 0.35, 0.92) and recovery ( $r = 0.68$ , 95 % CI: 0.19, 0.89).  $\Delta\text{HHb}$  had revealed a poor correlation between PPG and NIRS during both cold exposure ( $r = -0.14$ , 95 % CI: -0.64, 0.44) and recovery ( $r = -0.08$ , 95 % CI: -0.66, 0.41). Changes in total haemoglobin  $\Delta\text{tHb}$  had correlation coefficients of  $r = 0.61$  (95 % CI: 0.12, 0.87) and  $r = 0.66$  (95 % CI: 0.17, 0.88) respectively for cold exposure and recovery.

Analysis of trending agreement was also performed by four-quadrant plots analysis.

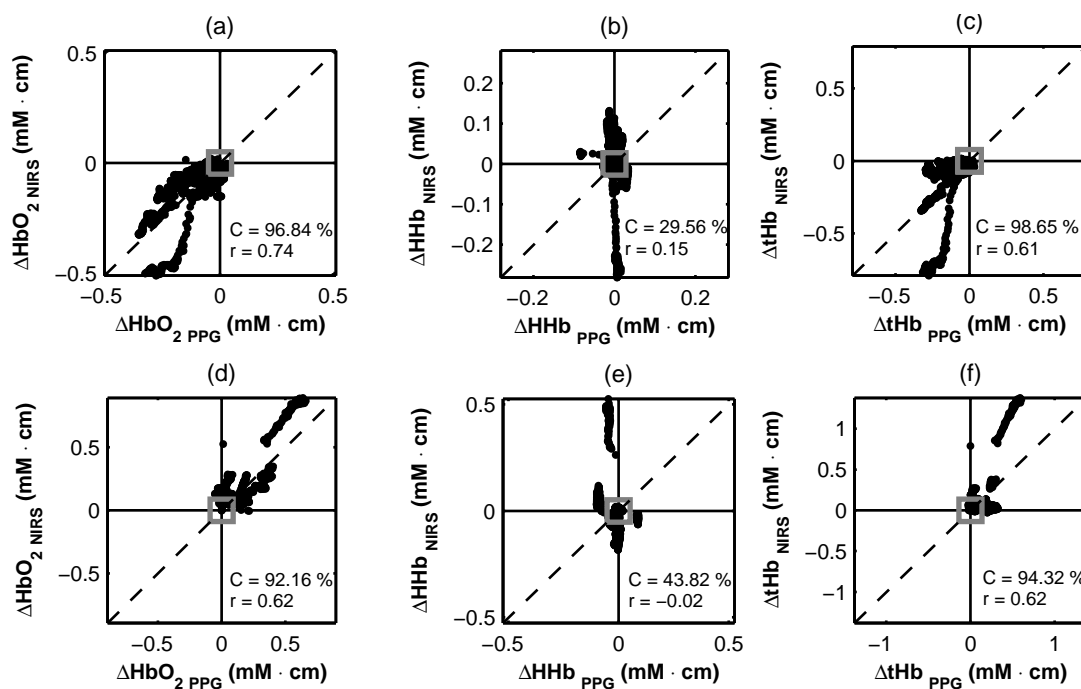


**Figure 11.7:** Four-quadrant plots between  $\Delta\text{HbO}_2$ ,  $\Delta\text{HHb}$ , and  $\Delta\text{tHb}$  estimated from PPG (finger) and NIRS (forearm) during cold exposure and recovery. The concordance rate  $C$  and correlation coefficients  $r$  between the measures are presented as well. The concordance rate was calculated as the ratio of the number of points in the first and third quadrant and the total number of points in all quadrants. An exclusion zone of 10 % was used for the calculation of  $C$ . Dashed lines are the line of equality. Grey boxes indicate the 10 % exclusion zone. (a), (b), and (c) are respectively the four-quadrant plots of  $\Delta\text{HHb}$ ,  $\Delta\text{HbO}_2$ , and  $\Delta\text{tHb}$  during cold exposure. (d), (e), and (f) are respectively the four-quadrant plots of  $\Delta\text{HHb}$ ,  $\Delta\text{HbO}_2$ , and  $\Delta\text{tHb}$  during recovery. Original signals were resampled every 5 seconds.

Figure 11.7 illustrates the four quadrant plots between  $\Delta\text{HbO}_2$ ,  $\Delta\text{HHb}$ , and  $\Delta\text{tHb}$  estimated from PPG and NIRS during cold exposure and recovery.  $\Delta\text{HbO}_2$  and  $\Delta\text{tHb}$  exhibited good trending concordance during both cold exposure and recovery. However,  $\Delta\text{HHb}$  showed a poor agreement during both stages of the protocol.

### 11.3.3 Comparison between haemoglobin concentrations from finger and ear canal

As mentioned earlier, PPG signals were also acquired from a more central location like the ear canal. The ear canal, being supplied by branches of the carotid artery, is less affected by vasoconstriction when compared to a peripheral location such as the fingers, and it has been proved to provide more resilient  $\text{SpO}_2$  readings than the fingers [93]. The relative haemoglobin concentrations estimated from PPG signals, acquired from two different locations, should provide a comparative measure of the differences in perfusion during exposure to cold temperatures. Therefore, the haemoglobin concentrations estimated from the finger and ear canal were compared in order to test whether

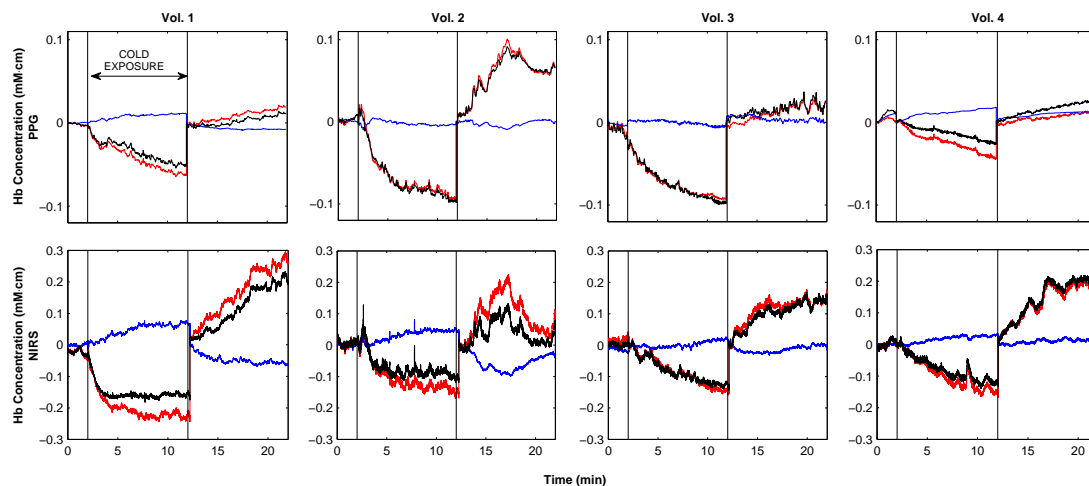


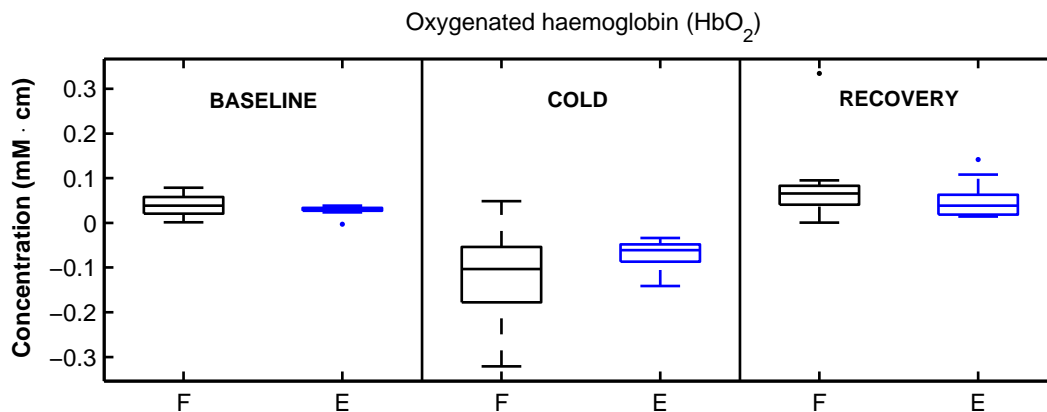
**Figure 11.8:** Example of  $\Delta\text{HbO}_2$ ,  $\Delta\text{HHb}$ , and  $\Delta\text{tHb}$  estimated from ear canal (PPG) and forehead (NIRS) of four subjects during cold exposure. Each column represent one volunteer. Top row: haemoglobin concentrations estimated from the PPG measured at the ear canal. Bottom row: haemoglobin concentrations estimated by NIRS at the forehead. Red traces:  $\Delta\text{HbO}_2$ . Blue traces:  $\Delta\text{HHb}$ . Black trace:  $\Delta\text{tHb}$ . Vertical lines represent the duration of the cold exposure.

the ear canal's perfusion is less influenced than the fingers during exposure to cold temperatures. The ear canal PPG sensor comprised of identical optical components as the finger sensor, therefore facilitating the comparison between the two locations. The perfusion index (PI) was used to confirm any difference in perfusion at the two locations.

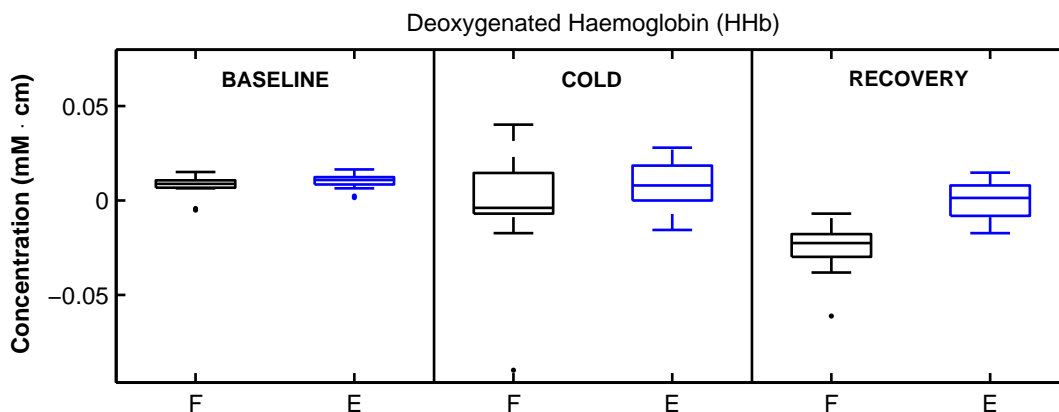
Figure 11.8 illustrates examples of haemoglobin concentrations estimated from ear canal PPG signals and simultaneous NIRS measurements from the forehead from four volunteers.  $\Delta\text{HbO}_2$ ,  $\Delta\text{HHb}$ , and  $\Delta\text{tHb}$  estimated from the ear canal indicated the same haemodynamic responses measured by NIRS. During exposure to cold, oxygenated haemoglobin  $\Delta\text{HbO}_2$  and total haemoglobin  $\Delta\text{tHb}$  decreased indicating the onset of vasoconstriction. Deoxygenated haemoglobin  $\Delta\text{HHb}$  increased in a lower magnitude or it did not change during the cold exposure.

Figure 11.9, Figure 11.10, Figure 11.11 show the comparative box and whiskers plots of the mean changes in  $\Delta\text{HbO}_2$ ,  $\Delta\text{HHb}$ , and  $\Delta\text{tHb}$  from both finger and ear canal. The  $\Delta\text{HbO}_2$  estimated from the finger dropped to  $-0.103 \pm 0.105$  mM·cm from baseline, while the drop in the ear canal was significantly lower ( $-0.060 \pm 0.030$  mM·cm,  $p = 0.02$ ).

There was no statistical difference ( $p > 0.05$ ) between changes in deoxygenated haemoglobin  $\Delta\text{HHb}$  from finger and ear canal ( $-0.004 \pm 0.030$  mM·cm and  $0.007 \pm 0.012$  mM·cm respectively) during exposure to cold.



**Figure 11.9:** Box and whisker plot of the changes in oxygenated haemoglobin ( $\Delta\text{HbO}_2$ ) estimated from finger and ear canal during exposure to cold. F: finger; E: ear canal. Values were averaged over the central minute of baseline, last one minute of cold, and last one minute of recovery.



**Figure 11.10:** Box and whisker plot of the changes in deoxygenated haemoglobin ( $\Delta\text{HHb}$ ) estimated from finger and ear canal during exposure to cold. F: finger; E: ear canal. Values were averaged over the central minute of baseline, last one minute of cold, and last one minute of recovery.

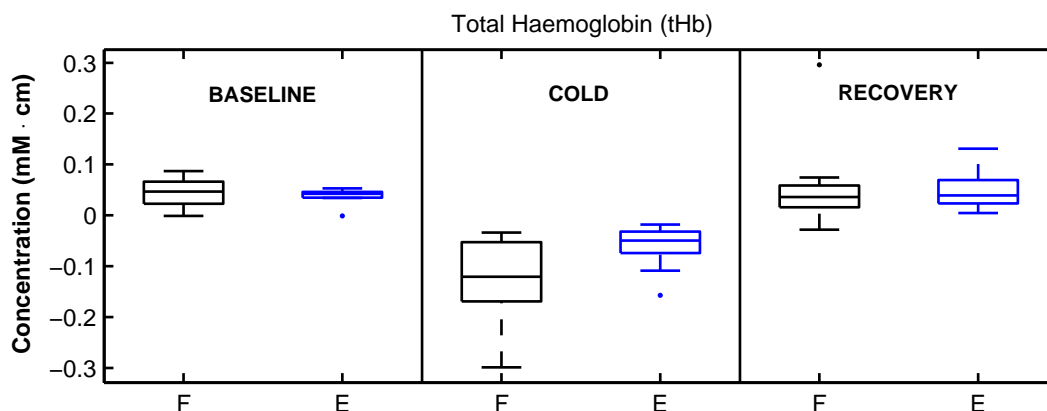


**Figure 11.11:** Box and whisker plot of the changes in total haemoglobin ( $\Delta tHb$ ) estimated from finger and ear canal during exposure to cold. F: finger; E: ear canal. Values were averaged over the central minute of baseline, last one minute of cold, and last one minute of recovery.

Similar to  $\Delta HbO_2$ , the changes in total haemoglobin  $\Delta tHb$  from the finger and ear canal were different ( $p < 0.01$ ), with mean drops of  $-0.120 \pm 0.087$  mM·cm and  $-0.049 \pm 0.039$  mM·cm for finger and ear canal respectively.

The differences in perfusion ( $\Delta HbO_2$  and  $\Delta tHb$ ) between the two locations were also verified by measuring the perfusion index. The normalised PI measured at the finger dropped from  $1.00 \pm 0.28$  A.U. in baseline to  $0.34 \pm 0.22$  A.U. ( $p < 0.01$ ) during cold exposure. The PI at the ear canal dropped from  $1.04 \pm 0.14$  A.U. baseline readings to  $0.65 \pm 0.28$  A.U. ( $p < 0.01$ ) during cold exposure. During exposure to cold, the perfusion index measured at the finger was lower ( $p < 0.01$ ) than the perfusion index measured at the ear canal, suggesting that the perfusion at the ear canal was less compromised during exposure to cold. Figure 11.12 illustrates the comparative box and whiskers plot of the mean changes in PI at both locations.

#### 11.3.4 Comparison of muscle and brain TOI and nTHI during exposure to cold

The haemoglobin concentrations estimated from NIRS indicated the changes in perfusion due to exposure to cold. However, these were composed by the mixed contribution of superficial (skin) and deep structures (muscle/brain). When the light is emitted to the tissue, the light is detected by a single photodiode for inferring the haemoglobin concentrations, thus making difficult to distinguish the origins of the signal.

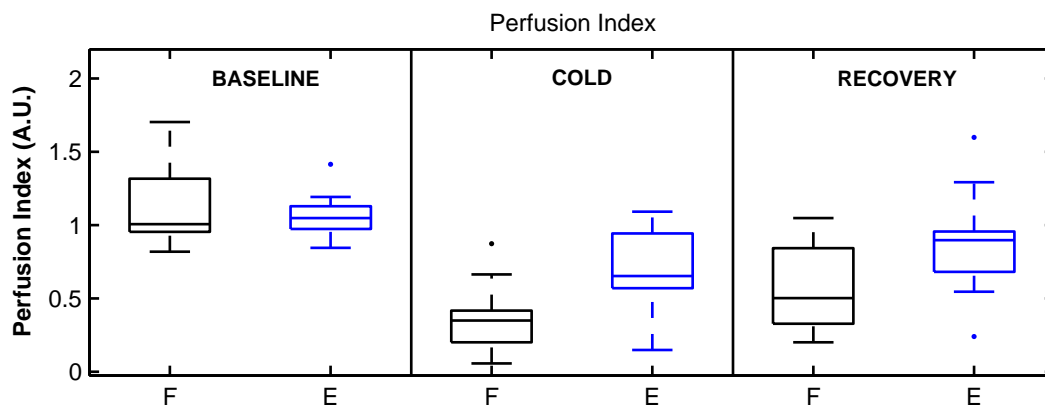


**Figure 11.12:** Box and whisker plot of the changes in perfusion index estimated from finger and ear canal during exposure to cold. F: finger; E: ear canal. Values were averaged over the central minute of baseline, last one minute of cold, and last one minute of recovery. The perfusion index was normalised with respect to ten seconds of baseline readings.

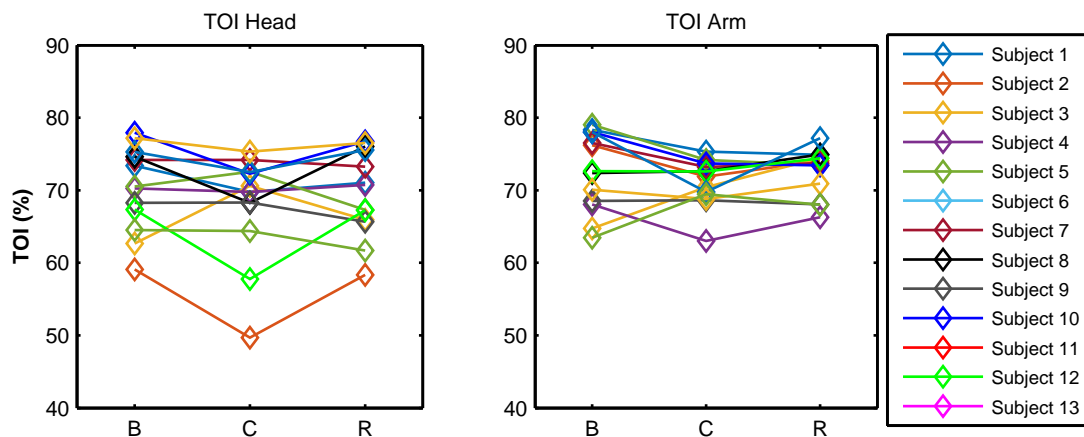
**Table 11.1:** Mean changes ( $\pm$ SD), of TOI, measured at the forehead and forearm, during the cold exposure protocol. The signals were averaged over the central minute of baseline, last minute of exposure to cold and the last minute of recovery.

	Baseline	Cold	Recovery
TOI <sub>Head</sub> (%)	70.31 $\pm$ 5.80	68.10 $\pm$ 7.17	69.59 $\pm$ 5.93
TOI <sub>Forearm</sub> (%)	72.76 $\pm$ 5.39	71.04 $\pm$ 3.23	72.59 $\pm$ 3.26

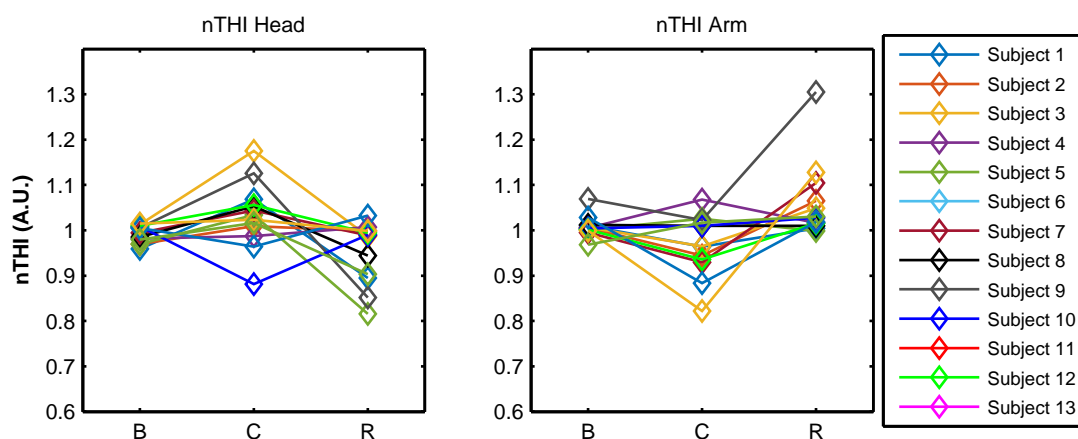
When the subject was exposed to cold for a relatively short period (i.e. 10 min), the haemoglobin concentrations underwent significant changes from baseline (Figure 11.3). Since these changes represent a mixed contribution of different tissue's structures, analysis of nTHI and TOI signals would give an insight on the origin of the changes. Differently from the haemoglobin concentrations, nTHI and TOI are computed by using the Spatially Resolved Spectroscopy, providing an assessment of oxygenation and blood volume of only deep structures, with little contribution of shallower regions such as the skin [125]. Therefore, the analysis of nTHI and TOI measured at the forehead (brain) and forearm (brachioradialis) would reveal if exposure to cold caused any significant change in oxygenation or blood volume in these organs.

Figure 11.13 shows the mean changes in TOI measured at the forehead and forearm during the protocol. The mean TOI across the subjects had a drop in both brain and muscle when the volunteers were exposed to a cold temperature. However, these deoxygenations did not result statistically significant at both locations in the population investigated ( $p > 0.05$ ). Table 11.1 summarises the means ( $\pm$ SD) of TOI during all stages of the protocol (i.e. baseline, cold, recovery).

The nTHI expresses the normalised changes in total haemoglobin, which reflects changes



**Figure 11.13:** Mean changes in TOI in all volunteers during the protocol. Values were averaged over the central minute of baseline, last one minute of cold, and last one minute of recovery. B: baseline; C: cold; R: recovery.



**Figure 11.14:** Mean changes in nTHI in all volunteers during the protocol. Values were averaged over the central minute of baseline, last one minute of cold, and last one minute of recovery. B: baseline; C: cold; R: recovery.

in the overall blood volume in the measured area (i.e. brain or muscle). The exposure to cold caused no significant decrease in nTHI measured at the forearm ( $p > 0.05$ ). On the contrary, nTHI originating from the brain had a significant increase from baseline ( $p = 0.04$ ). This increase in nTHI may suggest the shifting of blood from vasoconstricting peripheries (finger) to a central organ such as the brain. Even though the decrease in nTHI at the forearm was not statistically significant, the blood volume increased during recovery ( $p = 0.01$ ), suggesting a hyperaemic response when normal room temperature ( $23\text{ }^{\circ}\text{C}$ ) was restored. Figure 11.14 illustrates the response of nTHI measured at both locations, while Table 11.2 summarises the mean ( $\pm$ SD) values of nTHI during the different stages of the protocol.

**Table 11.2:** Mean changes ( $\pm$ SD), of nTHI measured at the forehead and forearm during the cold exposure protocol. The signals were averaged over the central minute of baseline, last minute of exposure to cold and the last minute of recovery.

	Baseline	Cold	Recovery
nTHI <sub>Head</sub> (A.U.)	0.99 $\pm$ 0.02	1.03 $\pm$ 0.07*	0.95 $\pm$ 0.07
nTHI <sub>Forearm</sub> (A.U.)	1.00 $\pm$ 0.02	0.96 $\pm$ 0.07	1.05 $\pm$ 0.08*

\* Significant change from baseline ( $p < 0.05$ )

## 11.4 Summary

This chapter investigated the feasibility of measuring haemoglobin concentrations from PPG signals during a whole-body cold exposure protocol. PPG sensors were applied on the finger and ear canal, whereas NIRS sensors were positioned on the forearm and forehead. The volunteers were moved from a room which was set at a temperature of 23 °C to a second room where the temperature was set at 10 °C.

The haemoglobin concentrations estimated from finger PPGs indicated haemodynamic changes related to the exposure to a cold temperature. Oxygenated ( $\Delta$ HbO<sub>2</sub>) and total haemoglobin ( $\Delta$ tHb) decreased, indicating vasoconstriction, while the deoxygenated haemoglobin ( $\Delta$ HHb) did not change.  $\Delta$ HbO<sub>2</sub> and  $\Delta$ tHb estimated from PPG signals acquired from the finger were in good correlation and trending agreement with the NIRS measurements from the forearm. However,  $\Delta$ HHb was not correlated. This difference between finger PPG and forearm NIRS should be attributed to the shivering occurring in the muscle during exposure to cold, causing an increase in  $\Delta$ HHb measured by NIRS.

Haemoglobin concentrations were also estimated from PPG signals measured at the ear canal and they were compared with finger PPG measurements. The two locations were compared in order to determine whether the haemoglobin concentration changes revealed a more reliable perfusion at the ear canal compared to the fingers. There was a significant difference between  $\Delta$ HbO<sub>2</sub> measured at the two locations. A difference was also found between  $\Delta$ tHb. These differences in perfusion indicated by  $\Delta$ HbO<sub>2</sub> and  $\Delta$ tHb were in agreement with the PPG perfusion index measured from the two locations.

The response of TOI and nTHI measured by NIRS were also analysed in order to investigate whether the exposure to cold caused any substantial change in oxygenation or blood volume in muscle and brain. Although there was a mean decrease in TOI

measured at both muscle and brain, the deoxygenations were not statistically significant in the population investigated. Cold exposure caused a significant increase in blood volume (nTHI) in the brain, but it did not cause any significant change in the muscle.

# Chapter 12

## Discussion

This thesis proposes the utilisation of Photoplethysmography as an alternative noninvasive and continuous technique in monitoring tissue perfusion, by estimating relative haemoglobin concentrations changes, as currently done in Near Infrared Spectroscopy (NIRS). The hypothesis is that the continuous DC component of the PPG signal at two different wavelengths could be employed to extract information on the changes in haemoglobin content in blood. In order to investigate this, *in vivo* studies on healthy volunteers were carried out, in which PPG signals were acquired from various locations at different haemodynamic interventions.

In order to acquire PPG signals from the forearm and forehead, a reflectance PPG sensor was designed and developed. The optical components were two red (660 nm) and two infrared (880 nm) light emitting diodes and a single photodiode. The sensor comprised a PCB on which the optical components were soldered, and a mechanical structure that was designed to cover from ambient light and facilitate the attachment on the skin. In addition, a similar finger PPG sensor, with the same optical components, was developed for the simultaneous acquisition of PPG signals from the finger. Additional sensors, with larger interoptodes distances (i.e. the distance between LEDs and photodiode) or smaller dimensions, were developed with similar design and manufacturing procedures. A research photoplethysmography processing system (ZenPPG) was employed to drive the sensors and to acquire the currents produced from the photodiode. The ZenPPG was able to drive dual-wavelength PPG sensors and to process

---

the PPG signal before the acquisition. The system allowed the acquisition of raw (AC + DC) PPG signals, the flexibility of sensors customization, and the possibility to control light intensities. The evaluation of the PPG sensors and processing system demonstrated that satisfactory raw PPG signals could be acquired. Furthermore, temperature tests showed that the sensor did not produce any harmful overheating when applied on the skin under maximal working conditions. A software application, developed in LabVIEW, was used to acquire the signals from the ZenPPG and provided the interface for controlling LEDs' light intensities and archive of all acquired physiological data. The second part of the software application was developed specifically for the acquisition of signals from state of the art devices such as NIRS, laser Doppler flowmetry, and pulse oximetry. These were used, along with the PPG system, for the measurement of haemodynamic parameters during the *in vivo* studies performed in this thesis.

The first investigation on healthy volunteers presented in Chapter 9 described vascular occlusions on the forearm. The custom-made reflectance PPG sensor and a commercial NIRS sensor were attached to the left forearm and the responses of PPG and NIRS were simultaneously acquired. The protocols consisted of different levels of intermittent vascular occlusions induced by inflation of a cuff pressure positioned around the upper left arm. This approach was used since it allowed a simple method to induce blood perfusion changes in the forearm. Furthermore, this method is commonly used as a first *in vivo* evaluation of NIRS instruments, and the changes in haemoglobin concentrations induced by this procedure are covered in the literature [13, 140, 141, 143, 155]. Relative concentrations changes in oxygenated ( $\Delta\text{HbO}_2$ ), deoxygenated ( $\Delta\text{HHb}$ ), and total haemoglobin ( $\Delta\text{tHb}$ ) were estimated for the first time from PPG signals by applying the modified Beer-Lambert law (MBLL) to PPG signals (see Chapter 8).  $\Delta\text{HbO}_2$ ,  $\Delta\text{HHb}$ , and  $\Delta\text{tHb}$  estimated from PPG changed accordingly during the different venous or total occlusions (i.e. combined venous and arterial occlusions). In particular, venous occlusions caused the increase of all the three parameters, while additional occlusions of the arterial vasculature caused the simultaneous drop of  $\Delta\text{HbO}_2$ , increase in  $\Delta\text{HHb}$ , and a minor increase in  $\Delta\text{tHb}$ . Therefore, the relative haemoglobin concentrations estimated from PPG showed the ability to differentiate between venous or arterial occlusions. Furthermore,  $\Delta\text{HbO}_2$ ,  $\Delta\text{HHb}$ , and  $\Delta\text{tHb}$  from PPG were responsive enough to indicate partial occlusions of the venous circulation induced by low-pressure occlusions (e.g. 20-40 mmHg). As explained above, the pattern of the changes in haemoglobin concentrations indicates the typology of haemodynamic change that is occurring (e.g.

---

venous or total occlusion). For this reason, correlation analysis was performed between the changes in  $\Delta\text{HbO}_2$ ,  $\Delta\text{HHb}$ , and  $\Delta\text{tHb}$  estimated from PPG and the reference NIRS monitor. There was a high correlation between the haemoglobin concentrations estimated by both techniques during almost all different occlusions. The lower correlation for  $\Delta\text{HbO}_2$  during the systolic and total occlusions in the second protocol could be associated with a short recovery time between occlusions. This is also supported by the good correlation during the total occlusion in the first protocol, in which a longer recovery between occlusions was allowed. The four-quadrant plot analysis is usually used to assess the agreement in the direction of change between different measurements of cardiac output [184]. The technique does not consider the magnitude of the change but it only assesses the agreement in the direction of change by calculating the concordance index expressed in percentage [184]. Therefore, the four-quadrant plot analysis provided an additional tool to assess the direction of change, or trending, of the haemoglobin concentrations from PPG against NIRS measures. There was good concordance between the two techniques, indicating the trending capabilities of the haemoglobin concentrations estimated from PPG. Although  $\Delta\text{HbO}_2$ ,  $\Delta\text{HHb}$ , and  $\Delta\text{tHb}$  from PPG showed comparable trending against NIRS, there were quantitative differences between the techniques. During both occlusion protocols, there was a consistent underestimation of PPG over NIRS assessed by Bland & Altman plots analysis. This was probably expected and possible reasons are discussed later in this chapter. The relative haemoglobin concentrations estimated from PPG were also used to express oxygenation changes by calculating the ratio of  $\Delta\text{HbO}_2$  over the total haemoglobin content as expressed by TOI in NIRS. Correlation analysis against TOI showed that  $\Delta\text{Hb}_{Ratio}$  was able to indicate the oxygenation changes due to blood flow occlusions in the forearm.

The addition of a laser Doppler flowmetry (LDF) sensor on the forearm, and custom-made and commercial PPG/pulse oximetry finger sensors, offered for the first time the possibility of investigating the simultaneous responses of NIRS, LDF, photoplethysmography, and pulse oximetry during vascular occlusions. Several studies in the literature have investigated these modalities, either alone or in pair, for detecting changes in perfusion and/or oxygenation, or for differentiating between healthy and diseased subjects [35, 38, 39, 41, 75–77, 79, 118, 141, 143, 157, 165, 179–181]. However, to the author’s knowledge, NIRS, LDF, photoplethysmography, and pulse oximetry have never been investigated altogether during vascular occlusions, thus providing with this study a

---

unique setting for investigating all these techniques simultaneously. Different indexes were obtained from the different modalities and their changes were simultaneously recorded and analysed. NIRS (TOI and nTHI) and LDF (Flux) demonstrated to be able to indicate changes in perfusion and oxygenation during all different occlusions. However, differentiation between venous or arterial occlusions by LDF may be challenging since the Flux decreased similarly during both types of occlusions, with values close to the *biological zero* of LDF measurements. A very analogous behaviour was previously observed and reported by Galla et al. [41]. In the literature, it has also been reported that the decay time of Flux during arterial occlusion is significantly shorter than venous occlusion, with an abrupt fall subsequent to arterial occlusion and a gradual decrease during venous occlusion [41, 179]. However, such difference was not observed in the signals acquired in this thesis. Also, LDF measurements have a wide inter- and intra-subject variability, thus normalising the Flux with respect to the baseline, as done in this work, seems to provide an indication of the actual change in perfusion, with a decrease to half baseline readings being associated with full venous or total occlusion. The TOI from NIRS significantly decreased in all the occlusions, whereas the nTHI, expressing blood volume changes, increased in all the venous occlusions, or increased to a lower degree during systolic and total occlusions. Observing the trends in both TOI and nTHI could provide information for the differentiation of venous or arterial/total occlusions. The perfusion index (PI) was calculated from infrared PPG signals acquired from both forearm and finger. Although there have been some previous efforts to determine a threshold in PI for indicating the adequacy of perfusion [80, 83], any inter-subject variability in the measurements was avoided by normalising the PI to baseline. The PI changed during all occlusions and it reached almost nil values during arterial/total occlusions. However, there were not significant changes for partial venous occlusions, thus doubting the sensitivity of the PI on detecting this kind of occlusions. It should also be noted that the PI is strictly dependent on the amplitude of the pulsatile component. This component of the PPG can change during gradual occlusions [77], but variations in this component may also depend on different factors other than vascular occlusions [1, 9]. The arterial oxygen saturation  $SpO_2$  was estimated from forearm and finger PPG signals, as well as acquired from a reference pulse oximeter attached to another finger. Significant changes in  $SpO_2$ s were only noticed at occlusion pressures exceeding 60 mmHg. Similar results have been observed in previous studies in which these changes in  $SpO_2$  were still in the normoxic

---

range of pulse oximetry [77, 118], making difficult to assess venous occlusions by pulse oximetry. Only the  $\text{SpO}_2$  estimated from the forearm had major changes during venous occlusions. This was most probably due to the origin of the PPG signal acquired from the forearm. The signal was likely to originate from the skin capillaries, where the arterial blood and venous blood are mixed. This was also confirmed by lower baseline  $\text{SpO}_2$ s at the forearm compared to fingers. As expected, all the  $\text{SpO}_2$ s failed when the arterial flow began to be compromised by occlusions close to the volunteers' systolic pressure. The response of the light attenuations or optical densities (OD) obtained from finger DC PPGs may provide an additional indication of venous occlusion when the PI and  $\text{SpO}_2$  may not be sufficient. In particular, using the red wavelength PPG (660 nm) increases the sensitivity to light attenuations due to increases in venous blood volumes (i.e. venous engorgement). Obtaining direct indication of venous engorgement from the DC PPG was also observed in previous studies that reported changes in the DC PPG during venous occlusions [78, 79]. The OD estimated from the DC PPG changed during venous occlusions, and the additional analysis of the slopes of changes demonstrated that the magnitude of change in OD was directly proportional to the degree of venous engorgement, with a maximal engorgement in the range 60-100 mmHg.

Overall, correlation and trending analysis between PPG and NIRS showed that PPG had comparable trending capabilities to NIRS for indicating changes in blood perfusion and oxygenation during vascular occlusions. These promising results could offer the use of relative haemoglobin concentrations estimated from PPG for detecting and differentiating vascular perturbations. For instance, in some clinical applications such as the monitoring of flaps in plastic surgery, the early detection of vascular complications is essential and could have a significant impact on the patient's clinical outcomes [27, 44]. The comparison between NIRS, LDF, PPG, and pulse oximetry suggests that NIRS and LDF, differently from conventional PPG and pulse oximetry analysis, may be the most appropriate measures to indicate changes in blood perfusion and oxygenation during vascular occlusions. In this context, estimating  $\Delta\text{HbO}_2$ ,  $\Delta\text{HHb}$ , and  $\Delta\text{tHb}$  from PPG signals could provide complementary indicators of the changes in perfusion that would probably be undetected by PI or  $\text{SpO}_2$  alone.

The bed tilting study allowed the investigation of  $\Delta\text{HbO}_2$ ,  $\Delta\text{HHb}$ , and  $\Delta\text{tHb}$  from forehead PPG measurements. Differently from the mechanical occlusions performed in the previous study, tilting the bed caused the movement or congestion of blood by gravity.

---

Previous studies such as Kurihara et al. have shown how haemoglobin concentrations and TOI measured by NIRS can reveal changes induced by variations in posture or, more generally, by gravity [136,138]. Therefore, the current study wanted to evaluate if these gravity-induced changes could also be detected by the haemoglobin concentrations estimated from PPG signals measured at the forehead. The  $\Delta\text{HbO}_2$ ,  $\Delta\text{HHb}$ , and  $\Delta\text{tHb}$  estimated from PPG changed accordingly to the haemodynamic changes caused by bed tilting.  $\Delta\text{HbO}_2$  increased due to the gravitational difference between supine and negative tilting.  $\Delta\text{HHb}$  increased as well for the induction of venous blood engorgement on the upper part of the body, while  $\Delta\text{tHb}$  increased proportionally to the sum of  $\Delta\text{HbO}_2$  and  $\Delta\text{HHb}$ . The parameters were again compared with reference NIRS measurements at the forehead. PPG and NIRS correlated highly during the protocol, whereas trending analysis by four quadrant plots also indicated good agreement in the direction of change between the parameters estimated from the two techniques. Again, there were quantitative differences in the magnitude of changes between PPG and NIRS as assessed by Bland & Altman analysis. Oxygenation changes were assessed from PPG by estimating  $\Delta\text{Hb}_{\text{Ratio}}$  and comparing it with TOI. The poor correlation between these two measures suggested a possible autoregulation of the brain in the presence of tilting. TOI and nTHI are believed to represent respectively deep tissue oxygenation and blood volumes, with little contribution of extra-cerebral tissues such as skin. Interestingly, nTHI increased, indicating an increase in blood volume during tilting. This may suggest that the brain autoregulates its oxygenation (TOI) despite the blood volume change, but more work is still needed to elucidate this further.

The anatomy of the forehead offered the possibility to investigate the effect of large vessels on the PPG measurements. An identical reflectance PPG sensor was placed on top of a large vein on the forehead and  $\Delta\text{HbO}_2$ ,  $\Delta\text{HHb}$ , and  $\Delta\text{tHb}$  were estimated from the PPG signals. The responses recorded from the two PPG sensors were compared in order to assess any difference caused by the presence of a large vein beneath the sensor. There were no differences in the direction of change between the two locations, thus apparently not affecting the trending in the presence of a large vessel. However, there was a significant quantitative difference in  $\Delta\text{HHb}$  between the two locations, while there was no significant difference for  $\Delta\text{HbO}_2$  and  $\Delta\text{tHb}$ . As expected, this affected the  $\Delta\text{Hb}_{\text{Ratio}}$  as well, with a significant difference between the two sensors. It appeared that the vein, containing a larger concentration of deoxygenated blood, influenced the estimation of  $\Delta\text{HHb}$ . Furthermore, optical modalities such as NIRS

---

and PPG suffer from heterogeneity within the sample volume, and large vessels tend to absorb light abnormally compared to their surroundings [13], and a large vessel underneath the sensor could affect the optical path [110]. However, it is difficult to conclude which of these possible effects (i.e. an elevated presence of HHb underneath the sensor or the optical heterogeneity) contributed most on the measurements in this work. The influence of the large vein on the SpO<sub>2</sub> estimation was also assessed, as similarly performed by Mannheimer et al. for pulsating arteries underneath the sensor [110]. As expected, the presence of a large vein beneath the sensor caused a significant overestimation and a greater variability in the population investigated. During tilting, the SpO<sub>2</sub> measured by both sensors dropped below the baseline. It is believed that this drop in SpO<sub>2</sub> is due to the degradation of the PPG signal with the appearance of cardio-synchronous venous pulsations (i.e. arterial and venous blood pulsate synchronously, making impossible to separate them) [111,188,189]. Also, the shifting of venous blood underneath the sensor (venous engorgement), causes the mixture of arterial and venous blood, with a consequent drop in SpO<sub>2</sub> [188].

Forehead PPG measurements are known for the influence of the venous circulation on the forehead. While in normal conditions this does not cause any issue, the situation can be worsened by the position of the patient (e.g. Trendelenburg position) [188,189]. Although elastic headbands have been introduced to overcome this problem, there have been limited attempts to assess the pressure exerted [188], whereas there are no measures of the venous presence underneath the sensor. Furthermore, these bands may not fully solve the problem or may slip of the patient [189]. Monitoring the relative haemoglobin concentrations from PPG may provide a tool to assess the presence of venous blood in the volume sampled by the sensor. The main advantage of this method is that dual-wavelength PPG signals are already measured by the sensor for the determination of SpO<sub>2</sub>, thus not requiring any additional sensor or instrumentation.

In the cold study, blood perfusion changes due to cold exposure were investigated. In addition, the study allowed to explore the changes in  $\Delta\text{HbO}_2$ ,  $\Delta\text{HHb}$ , and  $\Delta\text{tHb}$  from other PPG measurements locations such as the finger and the ear canal. The exposure to a cold temperature environment caused the instantaneous change in blood perfusion and the onset of vasoconstriction was observed by the quick drop in  $\Delta\text{HbO}_2$  and  $\Delta\text{tHb}$ . The vasoconstriction of blood supply to the peripheries was reflected by the simultaneous drop in the skin temperature and blood flow measured by laser Doppler flowmetry.

---

Since changes in  $\Delta\text{HHb}$  mostly correspond to changes in venous blood perfusion, there were no significant changes in  $\Delta\text{HHb}$ . Comparison with forearm NIRS measurements revealed a correlation for  $\Delta\text{HbO}_2$  and  $\Delta\text{tHb}$  from finger PPG and NIRS measurements. Analysis of trending by four-quadrant plots showed a concordant direction of change between  $\Delta\text{HbO}_2$  and  $\Delta\text{tHb}$  measured by the two techniques. However,  $\Delta\text{HHb}$  from the fingers had a poor correlation and trending with forearm NIRS. This difference could be attributed to the different measurement location (finger vs. forearm) and the penetration depth of NIRS. At the forearm, the NIRS light pathway transverse skin, adipose tissues, and muscle. While the drops in  $\Delta\text{HbO}_2$  and  $\Delta\text{tHb}$  originate from the vasoconstriction of the skin, the increase in  $\Delta\text{HHb}$  in NIRS measurements could be associated with shivering. It is common that during hypothermia, skeletal muscles start to contract in order to increase the metabolic rate. This increase in metabolic rate also coincides with the increase in oxygen consumption as depicted by the increase in  $\Delta\text{HHb}$  measured by NIRS. The relative haemoglobin concentrations from PPG were also used to assess blood perfusion differences between a peripheral (finger) and a more central location (ear canal). The finger and the ear canal PPG sensors had identical optical components, thus differences between the two locations could be hypothetically assessed. Raw PPG signals acquired from the ear were used to infer  $\Delta\text{HbO}_2$ ,  $\Delta\text{HHb}$ , and  $\Delta\text{tHb}$ . The ear canal demonstrated to be more resilient to vasoconstriction compared to the finger. The results were also confirmed by comparison of the perfusion index measured at the two locations and showed that the relative haemoglobin concentrations from PPG might be used to compare perfusion measurements between two locations, similarly to the perfusion index.

The cold study also allowed to assess differences in oxygenation and blood volumes at the muscle and brain measured by NIRS. Comparison of TOI and nTHI, representing deep tissue oxygenation and blood volumes, revealed that oxygenation in deep muscle and brain did not change during exposure to cold temperatures. However, nTHI at the brain showed a significant increase during cold, which may represent blood volumes shifts from peripheries to a central organ like the brain. Although these results may be promising for the assessment of blood flow regulations in the human body by NIRS, more rigorous studies are still required to investigate this further.

Photoplethysmography and Near Infrared Spectroscopy have very different penetration depths. Light penetrates in tissue in a banana-shaped trajectory and the depth of the

---

path is directly dependent on the wavelength (i.e. scattering is wavelength-dependent) and the interoptodes distance [24]. The interoptodes distance in PPG usually does not exceed 7 mm, whereas in NIRS a minimum separation of 2.5 cm is required [23]. Therefore, the techniques have significantly different penetration depths, with an assumed penetration of only a few millimetres for PPG, while NIRS has been reported to penetrate up to two centimetres into tissue [13,23]. This different penetration depth can be considered the primary cause of quantitative differences between  $\Delta\text{HbO}_2$ ,  $\Delta\text{HHb}$ , and  $\Delta\text{tHb}$  estimated by PPG and NIRS. The comparison of the slopes of change in  $\Delta\text{HHb}$  during venous occlusion and  $\Delta\text{Hb}_{Diff}$  during total occlusion, from both PPG and NIRS, also supported the hypothesis that the techniques interrogate different depths. In the occlusion and bed tilting studies, the different penetration depth did not cause any effect on the correlation or trending agreement between parameters, since the perturbations induced similar changes as measured by both PPG and NIRS. However, in the cold study, this difference became more evident and, as explained beforehand, had primary effects on the changes in  $\Delta\text{HHb}$ . Additional reasons for the quantitative differences could also be the different wavelengths adopted in the two techniques and the different algorithms. It should also be emphasised that PPG cannot be used to replace NIRS for the assessment of perfusion and oxygenation in deep tissues such as muscle and brain. If applied transcutaneously, PPG can only measure blood perfusion and oxygenation in the skin, whereas NIRS would be able to reach deep tissues. However, monitoring the skin has still several advantages, since global disturbances in the blood circulation are first seen in the skin while central organs such as brain or kidneys tend to maintain an adequate blood perfusion and oxygenation [34,193]. In addition, monitoring skin blood perfusion and oxygenation changes by PPG can be used in certain clinical applications such as flap monitoring, where the small measurement areas of these tissues may not provide an adequately large surface for NIRS sensors. Finally, if deep tissue perfusion and oxygenation is not required, PPG has the main advantage of being relatively inexpensive, compared to NIRS devices.

So far, the application of the modified Beer-Lambert law to PPG allowed the measurement of relative changes in haemoglobin concentrations from a stable baseline. From these, only relative changes in oxygenation ( $\Delta\text{Hb}_{Ratio}$ ) can be estimated. This novel work was a pilot investigation of the feasibility of applying NIRS processing to PPG, therefore the MBLL was used as a first approach. Absolute haemoglobin concentrations can only be determined by other methods such as Time Resolved Spectroscopy (TRS)

---

or Phase Modulated Spectroscopy (PMS), which cannot be applied to conventional PPG/pulse oximetry measurements due to specific requirements in the instrumentation adopted in TRS and PMS (e.g. laser light, streak camera, high frequency light modulation, etc.) [11,24,119]. However, by using two photodiodes, the application of Spatially Resolved Spectroscopy may be investigated in the future as well. Furthermore, NIRS algorithms assume that oxygenated and deoxygenated haemoglobin are the only light absorbers present in blood, excluding any contribution of other haemoglobin derivatives. This assumption holds in the great majority of cases, but other haemoglobin derivatives may be present in critical patients (e.g. subjects who were exposed to and inhaled high concentrations of carbon monoxide). This, however, can be excluded in the healthy volunteers that were investigated in this thesis. Since the DPF for the specific separation distance employed in the PPG sensors employed, the changes in haemoglobin concentrations have been expressed throughout the thesis as relative to the light path length ( $\text{mM} \times \text{cm}$ ). If future studies would determine the DPF values for short distances, the changes in haemoglobin concentrations could be expressed directly in concentration units ( $\text{mM}$ ).

Although the studies that were carried out allowed to investigate the proposed aims of this research, some limitations existed and should be acknowledged. The vascular occlusions performed were not instantaneous since they were induced by manual inflation of the cuff. This had an effect in the total occlusions, in which a residual increase in blood volume was observed at the onset of the occlusion. Unfortunately, it is not possible to occlude only the arterial vasculature and this could only be achieved by occluding the venous circulation as well. The occlusion of the arterial vasculature required occluding the venous circulation first during the occlusion, causing an initial venous blood engorgement. In the second protocol, the recovery period between intermittent occlusions was probably short. Although the recovery period was identical to the occlusion time, the short recovery had an impact on the total occlusions, where the arterial vasculature needed more time to recover fully from the previous occlusion. However, extending the occlusion and recovery time would have prolonged excessively the duration of the protocol. In the same study, the finger clip on the custom-made sensor was exerting a significant pressure on the finger vascular bed. This pressure did not cause any shortcoming during venous occlusion, but it caused an abnormal response in the optical densities calculated from finger PPGs during total occlusions. The absence of arterial inflow in the total occlusions caused the clip to press the blood

---

from beneath the measurement area. As a result, the optical densities decreased instead of increasing as expected. The use of a pressure-free clip could have solved the problem and should be used in future similar studies. In the bed tilting study, it would have been interesting to investigate the effect of a forehead headband. However, due to the numerous presence of sensors on the forehead in the current settings, the use of a headband was rather difficult. Following this preliminary investigation, a forehead headband could be used to investigate the presence of venous blood during tilting. Nevertheless, monitoring the applied pressure would be the ideal approach and more work is still required to develop an instrument capable of doing so.

## Conclusion

This chapter concludes this thesis by summarising the main results and linking these to the initial aims and objective. Whereas some suggestions for the improvement of the methodologies used have been given in the previous chapter, final suggestions on the direction of future work are also given at the end of this chapter.

This thesis aimed to investigate the feasibility of using the DC component of the PPG signal to infer relative changes in oxygenated ( $\Delta\text{HbO}_2$ ), deoxygenated ( $\Delta\text{HHb}$ ), and total haemoglobin ( $\Delta\text{tHb}$ ), and use these parameters to assess changes in blood perfusion. In order to do so, reflectance PPG sensors were designed and manufactured for the acquisition of PPG signals from different locations and *in vivo* investigations in healthy volunteers were carried out. The developed reflectance PPG sensors were successfully coupled to a PPG processing system and they demonstrated to be able to acquire dual-wavelength PPG signals. By inducing different changes in perfusion and by acquiring signals from different measurement locations, the *in vivo* studies in the healthy volunteers allowed to investigate the aim in different settings. The limitations of the single studies have been previously acknowledged in the Discussion chapter, and it is suggested to consider these for any future similar study.

The modified Beer-Lambert was successfully applied to PPG signals. As mentioned previously, the absolute haemoglobin concentrations could not be extracted at this point with the conventional PPG/pulse oximetry instrumentation and the current method allowed to provide an indication of the changes in perfusion. Similarly to NIRS, the

---

trends in the haemoglobin concentrations are most important, since any variation in the signals could reveal a change in perfusion. Also, it is hoped that future studies would contribute in determining the DPF for short separation distances of PPG measurements, whereas the application of more sophisticated algorithms may be investigated as well.

The comparison between the haemoglobin concentration changes estimated by PPG and NIRS revealed very promising results. During different types of changes in perfusion and in different measurement locations,  $\Delta\text{HbO}_2$ ,  $\Delta\text{HHb}$ , and  $\Delta\text{tHb}$  from PPG demonstrated to be able to indicate the changes in perfusion similarly as NIRS. As well as revealing strong similarities between the PPG and NIRS, the comparison also showed some differences between the techniques. These dissimilarities appeared more evident during the cold study, where the different volumes of tissues sampled by the two techniques played a major role in the physiological responses recorded. Similar investigations in the future may help in further exploring these differences.

The *in vivo* studies that were carried out in this thesis also allowed the investigation of some secondary aims. One of these secondary aims was the comparison of some optical techniques during different levels of vascular occlusions. By comparing NIRS, LDF, PPG, and pulse oximetry, an insight into the simultaneous responses of the techniques during vascular occlusion was provided. From the comparison, it appeared that NIRS and LDF were the most responsive to the full range of vascular occlusions induced. Future similar comparisons may focus on the diagnostic usefulness of all these techniques in differentiating between healthy and diseased subjects. Another research aim that this thesis wanted to address was the investigation on the influence that large vasculature on the forehead may have on PPG measurements. More specifically, the influence that a large vein on the forehead may have on PPG measurements was analysed. The results revealed that a large vein underneath the sensor can cause a significant difference in the deoxygenated haemoglobin concentration and a large variability in the measured  $\text{SpO}_2$ . The haemoglobin concentration changes estimated from PPG also showed to be useful in assessing any difference in perfusion between two measurement locations, such as finger and ear canal, during exposure to cold. These results open to new possible applications, in particular, the haemoglobin concentrations from PPG could be used, similarly to the perfusion index, to reveal any difference in perfusion between two body locations.

---

Future work could focus on the developments of new sensors and improvement of the current algorithms. The addition of a third wavelength at the isobestic point (either in the green or near-infrared region) would provide a direct measure of total haemoglobin concentrations (blood volume), independently from the oxygenation status. Different wavelength pairing could be investigated as well. As mentioned earlier, the addition of multiple photodiodes could provide the ability to apply Spatially Resolved Spectroscopy. This approach could also lead to the development of multi-distance sensors incorporating PPG and NIRS measurements into one sensor, with proximal photodiodes acquiring PPG signals and distal photodiodes for the assessment of blood perfusion and oxygenation in deep tissue. Subtraction algorithms could then be applied to isolate the contribution from shallower regions. Extensive *in vivo* or *in vitro* studies could focus on the validation of the method against a gold standard measure of haemoglobin concentrations such as co-oximetry. However, the *in vivo* evaluation will require the withdrawal of blood samples, which could only be performed in clinical settings.

Concluding, the novel results presented in this thesis demonstrate that the full capabilities of the PPG signal are still not fully exploited and the range of applications of this technique may be successfully extended beyond its current limits.

# Appendix A

## Multiplexing/demultiplexing code implementation

The following illustrates the code used to program the microcontroller's clocks. The code programs the timing sequence of the multiplexing/demultiplexing cycle by assigning logical states to the microcontroller ports. These, in turn, transmit the sequence to the control inputs of the multiplexer/demultiplexer. This cycle was divided into three periods: first wavelength ON, second wavelength ON and dark period (both LEDs OFF). These periods were then divided into four segments in which the demultiplexing (sampling) occurred in the two central segments.

```
/*
 * ZENPPG_CLOCKS.c
 * Author: Tomas Ysehak Abay
 */

// The code multiplexes the driving currents for the LEDs in ZenPPG.
// The Demultiplex part samples the middle part of the multiplex period.
// The three periods of the cycle (RED ON, IR ON and DARK) are each divided
in four parts
// --> Total of 12 segments.

#include <avr/io.h>
```

---

```

# define F_CPU 1000000
#include <util/delay.h>

int main(void)
{
  DDRD = _BV(DDD1) | _BV(DDD0); // Ports (register D) as outputs
  DDRB = _BV(DDB2) | _BV(DDB1) | _BV(DDB0); // Ports (register B) as outputs

  // or this version is also possible:
  // DDRD = 0x03; // Assign ports (register D) as outputs
  // DDRB = 0x07; // Assign ports (register B) as outputs

  while(1)
  {
    int dt1;
    dt1 = 104; // Duration of the period. dt1=(1/fs)/12, where fs= 800 Hz.

    // First Period (first Wavelength ON)
    // 1st segment
    PORTD = 0b00000000; // X0(Y0) [ICPOS0 or ICPOS1]
    PORTB = 0b00000100;
    _delay_us(dt1);
    // 2nd segment
    PORTD = 0b00000000; // X0(Y0) [ICPOS0 or ICPOS1]
    PORTB = 0b00000000; // Demultiplexer: Sampling X0
    _delay_us(dt1);
    // 3rd segment
    PORTD = 0b00000000; // X0(Y0) [ICPOS0 or ICPOS1]
    PORTB = 0b00000000; // Demultiplexer: Sampling X0
    _delay_us(dt1);
    // 4th segment
    PORTD = 0b00000000; // X0(Y0) [ICPOS0 or ICPOS1]
    PORTB = 0b00000100;
    _delay_us(dt1);
  }
}

```

---

```

// Second Period (second Wavelength ON)
// 5th segment
PORTD = 0b00000001; // X1(Y1) [ICNEGO or ICNEG1]
PORTB = 0b00000101;
_delay_us(dt1);
// 6th segment
PORTD = 0b00000001; // X1(Y1) [ICNEGO or ICNEG1]
PORTB = 0b00000001; // Demultiplexer: Sampling X1
_delay_us(dt1);
// 7th segment
PORTD = 0b00000001; // X1(Y1) [ICNEGO or ICNEG1]
PORTB = 0b00000001; // Demultiplexer: Sampling X1
_delay_us(dt1);
// 8th segment
PORTD = 0b00000001; // X1(Y1) [ICNEGO or ICNEG1]
PORTB = 0b00000101;
_delay_us(dt1);

// Third Period (Dark)
// 9th segment
PORTD = 0b00000010; // X2(Y2) [AGROUND]
PORTB = 0b00000110;
_delay_us(dt1);
// 10th segment
PORTD = 0b00000010; // X2(Y2) [AGROUND]
PORTB = 0b00000010; // Demultiplexer: Sampling X2
_delay_us(dt1);
// 11th segment
PORTD = 0b00000010; // X2(Y2) [AGROUND]
PORTB = 0b00000010; // Demultiplexer: Sampling X2
_delay_us(dt1);
// 12th segment
PORTD = 0b00000010; // X2(Y2) [AGROUND]

```

---

```
PORTB = 0b00000110;  
_delay_us(dt1);  
}  
}
```

# Appendix B

## NIRO 200NX Specifications

<b>Measured Data</b>	Oxygenated haemoglobin changes ( $\Delta\text{HbO}_2$ ) Deoxygenated haemoglobin changes ( $\Delta\text{HHb}$ ) Total haemoglobin changes ( $\Delta\text{tHb}$ ) Tissue Oxygenation Index (TOI) Normalised Tissue Haemoglobin Index (nTHI)
<b>Signal Processing</b>	Modified Beer-Lambert law ( $\Delta\text{HbO}_2$ , $\Delta\text{HHb}$ , and $\Delta\text{tHb}$ ) Spatially Resolved Spectroscopy (TOI, nTHI)
<b>Light source</b>	Light Emitting Diodes Wavelengths: 735, 810, and 850 nm Output power: less than 2 mW Pulse frequency: 1.7 kHz Spectrum width: < 60 nm
<b>Detection</b>	PIN - Si (Silicon) photodiodes
<b>Probe separation distance</b>	3 or 4 cm centre-to-centre distance
<b>Analogue outputs</b>	Connector: D-Sub-9-pin (female) TOI: 0 V to 1 V (corresponding to 0 % and 100 %) nTHI: 0 V to 5 V (corresponding to 0 and 5 A.U.) $\Delta\text{HbO}_2$ and $\Delta\text{HHb}$ : -5 V to +5 V (corresponding to -1000 $\mu\text{M} \cdot \text{cm}$ and +1000 $\mu\text{M} \cdot \text{cm}$ )

## References

- [1] J. Allen, "Photoplethysmography and its application in clinical physiological measurement," *Physiological Measurements*, vol. 28, pp. R1–R39, 2007.
- [2] A. A. Kamal, J. B. Harness, G. Irving, and A. J. Mearns, "Skin photoplethysmography - a review," *Computer Methods and Programs in Biomedicine*, vol. 28, no. 4, pp. 257–269, 1989.
- [3] P. A. Kyriacou, "Pulse oximetry in the oesophagus," *Physiological Measurement*, vol. 27, no. 1, pp. R1–R35, 2006.
- [4] Y. Mendelson, "Pulse oximetry: theory and applications for noninvasive monitoring." *Clinical chemistry*, vol. 38, no. 9, pp. 1601–1607, 1992.
- [5] T. Aoyagi, "Pulse oximetry: its invention, theory, and future," *Journal of anaesthesia*, vol. 17, no. 4, pp. 259–266, 2003.
- [6] J. T. Moyle, C. Hahn, and A. P. Adams, *Pulse oximetry*. JSTOR, 2002.
- [7] J. A. Pologe, "Pulse oximetry: technical aspects of machine design." *International anesthesiology clinics*, vol. 25, no. 3, pp. 137–153, 1987.
- [8] J. G. Webster, *Design of Pulse Oximeters*. Bristol,: Institute Of Physics (IOP) Publishing, 1997.
- [9] K. Shelley, "Photoplethysmography: Beyond the calculation of arterial oxygen

- saturation and heart rate,” *Anaesthesia & Analgesia*, vol. 105, no. 6, pp. S31 – S36, 2007.
- [10] D. Meredith, D. Clifton, P. Charlton, J. Brooks, C. Pugh, and L. Tarassenko, “Photoplethysmographic derivation of respiratory rate: a review of relevant physiology,” *Journal of medical engineering & technology*, vol. 36, no. 1, pp. 1–7, 2012.
- [11] P. Rolfe, “In vivo near-infrared spectroscopy,” *Annual review of biomedical engineering*, vol. 2, no. 1, pp. 715–754, 2000.
- [12] H. Owen-Reece, M. Smith, C. Elwell, and J. Goldstone, “Near infrared spectroscopy.” *British journal of anaesthesia*, vol. 82, no. 3, pp. 418–426, 1999.
- [13] M. Ferrari, L. Mottola, and V. Quaresima, “Principles, techniques, and limitations of near infrared spectroscopy,” *Canadian journal of applied physiology*, vol. 29, no. 4, pp. 463–487, 2004.
- [14] G. J. Tortora and B. H. Derrickson, *Principles of anatomy and physiology*. John Wiley & Sons, 2009.
- [15] V. C. Scanlon and T. Sanders, *Essentials of anatomy and physiology*. FA Davis, 2007.
- [16] K. E. Barrett, S. M. Barman, S. Boitano *et al.*, *Ganong’s review of medical physiology*. New Delhi: McGraw Hill, 2010, 2010.
- [17] W. G. Zijlstra, A. Buursma, and O. W. van Assendelft, *Visible and Near Infrared Absorption Spectra of Human and Animal Haemoglobin*. CRC Press, 2000.
- [18] C. Guyton Arthur and E. Hall Jhon, *Textbook of medical physiology*. Prism Books Pvt Limited, 2006.
- [19] J. B. West, *Respiratory physiology: the essentials*. Lippincott Williams & Wilkins, 2008.
- [20] K. M. V. D. Graaff, W. R. Rhees, and S. Palmer, *Human Anatomy and Physiology*. USA,: McGraw-Hill Companies, Inc., 2010.

- 
- [21] F. F. Jobsis, “Noninvasive, infrared monitoring of cerebral and myocardial oxygen sufficiency and circulatory parameters,” *Science*, vol. 198, no. 4323, pp. 1264–1267, 1977.
- [22] J. Murkin and M. Arango, “Near-infrared spectroscopy as an index of brain and tissue oxygenation,” *British journal of anaesthesia*, vol. 103, no. suppl 1, pp. i3–i13, 2009.
- [23] A. Pellicer and M. del Carmen Bravo, “Near-infrared spectroscopy: a methodology-focused review,” in *Seminars in Fetal and Neonatal Medicine*, vol. 16, no. 1. Elsevier, 2011, pp. 42–49.
- [24] T. Jue, K. Masuda *et al.*, *Application of near infrared spectroscopy in biomedicine*. Springer, 2013.
- [25] T. Scheeren, P. Schober, and L. Schwarte, “Monitoring tissue oxygenation by near infrared spectroscopy (nirs): background and current applications,” *Journal of clinical monitoring and computing*, vol. 26, no. 4, pp. 279–287, 2012.
- [26] M. S. Thorniley, J. Sinclair, N. Barnett, C. Shurey, and C. Green, “The use of near-infrared spectroscopy for assessing flap viability during reconstructive surgery,” *British journal of plastic surgery*, vol. 51, no. 3, pp. 218–226, 1998.
- [27] A. Repež, D. Oroszy, and Z. M. Arnež, “Continuous postoperative monitoring of cutaneous free flaps using near infrared spectroscopy,” *Journal of Plastic, Reconstructive & Aesthetic Surgery*, vol. 61, no. 1, pp. 71–77, 2008.
- [28] C. M. Choi and R. G. Bennett, “Laser dopplers to determine cutaneous blood flow,” *Dermatologic surgery*, vol. 29, no. 3, pp. 272–280, 2003.
- [29] M. Leahy, F. De Mul, G. Nilsson, and R. Maniewski, “Principles and practice of the laser-doppler perfusion technique,” *Technology and health care*, vol. 7, no. 2-3, pp. 143–162, 1999.
- [30] N. Vongsavan and B. Matthews, “Some aspects of the use of laser doppler flow meters for recording tissue blood flow,” *Experimental physiology*, vol. 78, no. 1,

- pp. 1–14, 1993.
- [31] H. C. Eun, “Evaluation of skin blood flow by laser doppler flowmetry,” *Clinics in Dermatology*, vol. 13, no. 4, pp. 337–347, 1995.
- [32] Y. Watanabe and E. Okada, “Influence of perfusion depth on laser doppler flow measurements with large source-detector spacing,” *Applied optics*, vol. 42, no. 16, pp. 3198–3204, 2003.
- [33] I. Fredriksson, M. Larsson, and T. Strömberg, “Measurement depth and volume in laser doppler flowmetry,” *Microvascular research*, vol. 78, no. 1, pp. 4–13, 2009.
- [34] A. Lima and J. Bakker, “Noninvasive monitoring of peripheral perfusion,” *Intensive care medicine*, vol. 31, no. 10, pp. 1316–1326, 2005.
- [35] J. C. Yuen and Z. Feng, “Monitoring free flaps using the laser doppler flowmeter: five-year experience.” *Plastic and reconstructive surgery*, vol. 105, no. 1, pp. 55–61, 2000.
- [36] J. M. Smit, C. J. Zeebregts, R. Acosta, and P. M. Werker, “Advancements in free flap monitoring in the last decade: a critical review,” *Plastic and reconstructive surgery*, vol. 125, no. 1, pp. 177–185, 2010.
- [37] U. Dirnagl, B. Kaplan, M. Jacewicz, and W. Pulsinelli, “Continuous measurement of cerebral cortical blood flow by laser-doppler flowmetry in a rat stroke model,” *Journal of Cerebral Blood Flow & Metabolism*, vol. 9, no. 5, pp. 589–596, 1989.
- [38] J. Klaessens, R. Kolkman, J. Hopman, E. Hondebrink, K. Liem, W. Steenberg, F. de Mul, and J. Thijssen, “Monitoring cerebral perfusion using near-infrared spectroscopy and laser doppler flowmetry,” *Physiological measurement*, vol. 24, no. 4, p. N35, 2003.
- [39] J. Kaneko, Y. Sugawara, Y. Matsui, H. Sakata, and N. Kokudo, “Comparison of near-infrared spectroscopy and laser doppler flowmetry for detecting decreased hepatic inflow in the porcine liver,” *Journal of Investigative Surgery*, vol. 22, no. 4, pp. 268–274, 2009.

- 
- [40] A. Obeid, N. Barnett, G. Dougherty, and G. Ward, “A critical review of laser doppler flowmetry,” *Journal of medical engineering & technology*, 2009.
- [41] T. J. Galla, D. Hellekes, and A. M. Feller, “Differentiation between arterial and venous vessel occlusion by simultaneous measurement with laser doppler flowmetry and photoplethysmography,” *Journal of Reconstructive Microsurgery*, vol. 15, no. 1, pp. 67–72, 1999.
- [42] P. R. Hoskins, K. Martin, and A. Thrush, *Diagnostic ultrasound: physics and equipment*. Cambridge University Press, 2010.
- [43] J. Webster, *Medical instrumentation: application and design*. John Wiley & Sons, 2009.
- [44] C.-K. Perng, “Recent advances in postoperative free microvascular flap monitoring,” *Formosan Journal of Surgery*, vol. 46, no. 5, pp. 145–148, 2013.
- [45] J. Naqvi, K. H. Yap, G. Ahmad, and J. Ghosh, “Transcranial doppler ultrasound: a review of the physical principles and major applications in critical care,” *International journal of vascular medicine*, vol. 2013, 2013.
- [46] M. Siegemund, J. Van Bommel, and C. Ince, “Assessment of regional tissue oxygenation,” *Intensive care medicine*, vol. 25, no. 10, pp. 1044–1060, 1999.
- [47] Y. Sakr, “Techniques to assess tissue oxygenation in the clinical setting,” *Transfusion and Apheresis Science*, vol. 43, no. 1, pp. 79–94, 2010.
- [48] A. T. Maciel, J. Creteur, and J.-L. Vincent, “Tissue capnometry: does the answer lie under the tongue?” *Intensive care medicine*, vol. 30, no. 12, pp. 2157–2165, 2004.
- [49] M. Buise, J. Van Bommel, and C. Ince, “Reflectance spectrophotometry and tissue oxygenation in experimental and clinical practice,” in *Intensive Care Medicine*. Springer, 2003, pp. 553–563.
- [50] K. Frank, M. Kessler, K. Appelbaum, and W. Dummler, “The erlangen micro-

- lightguide spectrophotometer emphasis,” *Physics in medicine and biology*, vol. 34, no. 12, p. 1883, 1989.
- [51] S. Friedland, D. A. Benaron, I. H. Parachikov, and R. Soetikno, “Measurement of mucosal capillary hemoglobin oxygen saturation in the colon by reflectance spectrophotometry,” in *Biomedical Optics 2003*. International Society for Optics and Photonics, 2003, pp. 405–412.
- [52] A. Figus, A. Mosahebi, and V. Ramakrishnan, “Microcirculation in diep flaps: a study of the haemodynamics using laser doppler flowmetry and lightguide reflectance spectrophotometry,” *Journal of Plastic, Reconstructive & Aesthetic Surgery*, vol. 59, no. 6, pp. 604–612, 2006.
- [53] M. B. Wallace, A. Wax, D. N. Roberts, and R. N. Graf, “Reflectance spectroscopy,” *Gastrointestinal endoscopy clinics of North America*, vol. 19, no. 2, pp. 233–242, 2009.
- [54] P. M. Fox, K. Zeidler, J. Carey, and G. K. Lee, “White light spectroscopy for free flap monitoring,” *Microsurgery*, vol. 33, no. 3, pp. 198–202, 2013.
- [55] A. Mayevsky and G. G. Rogatsky, “Mitochondrial function in vivo evaluated by nadh fluorescence: from animal models to human studies,” *American journal of physiology-Cell physiology*, vol. 292, no. 2, pp. C615–C640, 2007.
- [56] W. Groner, J. W. Winkelman, A. G. Harris, C. Ince, G. J. Bouma, K. Messmer, and R. G. Nadeau, “Orthogonal polarization spectral imaging: a new method for study of the microcirculation,” *Nature medicine*, vol. 5, no. 10, pp. 1209–1212, 1999.
- [57] S. Eriksson, J. Nilsson, and C. Stureson, “Non-invasive imaging of microcirculation: a technology review,” *Medical devices (Auckland, NZ)*, vol. 7, p. 445, 2014.
- [58] P. Goedhart, M. Khalilzada, R. Bezemer, J. Merza, and C. Ince, “Sidestream dark field (sdf) imaging: a novel stroboscopic led ring-based imaging modality for clinical assessment of the microcirculation,” *Optics express*, vol. 15, no. 23,

- pp. 15 101–15 114, 2007.
- [59] J. D. Briers, “Laser doppler, speckle and related techniques for blood perfusion mapping and imaging,” *Physiological measurement*, vol. 22, no. 4, p. R35, 2001.
- [60] H. Hoeksema, K. Van de Sijpe, T. Tondu, M. Hamdi, K. Van Landuyt, P. Blondeel, and S. Monstrey, “Accuracy of early burn depth assessment by laser doppler imaging on different days post burn,” *Burns*, vol. 35, no. 1, pp. 36–45, 2009.
- [61] M. E. van Genderen, J. van Bommel, and A. Lima, “Monitoring peripheral perfusion in critically ill patients at the bedside,” *Current opinion in critical care*, vol. 18, no. 3, pp. 273–279, 2012.
- [62] D. De Backer, G. Ospina-Tascon, D. Salgado, R. Favory, J. Creteur, and J.-L. Vincent, “Monitoring the microcirculation in the critically ill patient: current methods and future approaches,” pp. 263–275, 2012.
- [63] A. Pickard, W. Karlen, and J. M. Ansermino, “Capillary refill time: is it still a useful clinical sign?” *Anesthesia & Analgesia*, vol. 113, no. 1, pp. 120–123, 2011.
- [64] B. Anderson, A.-M. Kelly, D. Kerr, M. Clooney, and D. Jolley, “Impact of patient and environmental factors on capillary refill time in adults,” *The American journal of emergency medicine*, vol. 26, no. 1, pp. 62–65, 2008.
- [65] L. Blaxter, D. Morris, J. Crowe, C. Henry, S. Hill, D. Sharkey, H. Vyas, and B. Hayes-Gill, “An automated quasi-continuous capillary refill timing device,” *Physiological measurement*, vol. 37, no. 1, p. 83, 2015.
- [66] A. B. Hertzman, “The blood supply of various skin areas as estimated by the photoelectric plethysmograph,” *American Journal of Physiology–Legacy Content*, vol. 124, no. 2, pp. 328–340, 1938.
- [67] J. Dorlas and J. Nijboer, “Photo-electric plethysmography as a monitoring device in anaesthesia application and interpretation,” *British journal of anaesthesia*, vol. 57, no. 5, pp. 524–530, 1985.

- 
- [68] A. Reisner, P. A. Shaltis, D. McCombie, and H. H. Asada, "Utility of photoplethysmography in circulatory monitoring," *Anesthesiology*, vol. 108, no. 5, pp. 950–958, 2008.
- [69] K. Bendjelid, "The pulse oximetry plethysmographic curve revisited," *Current opinion in critical care*, vol. 14, no. 3, pp. 348–353, 2008.
- [70] A. A. Alian and K. H. Shelley, "Photoplethysmography: Analysis of the pulse oximeter waveform," in *Monitoring technologies in acute care environments*. Springer, 2014, pp. 165–178.
- [71] Y. Mendelson and B. D. Ochs, "Noninvasive pulse oximetry utilizing skin reflectance photoplethysmography," *IEEE Transactions on Biomedical Engineering*, vol. 35, no. 10, pp. 798–805, 1988.
- [72] L. Nilsson, T. Goscinski, S. Kalman, L.-G. Lindberg, and A. Johansson, "Combined photoplethysmographic monitoring of respiration rate and pulse: a comparison between different measurement sites in spontaneously breathing subjects," *Acta Anaesthesiologica Scandinavica*, vol. 51, no. 9, pp. 1250–1257, 2007.
- [73] M. Grubb, J. Carpenter, J. A. Crowe, J. Teoh, N. Marlow, C. Ward, C. Mann, D. Sharkey, and B. R. Hayes-Gill, "Forehead reflectance photoplethysmography to monitor heart rate: preliminary results from neonatal patients," *Physiological measurement*, vol. 35, no. 5, p. 881, 2014.
- [74] K. H. Shelley, D. H. Jablonka, A. A. Awad, R. G. Stout, H. Rezkanna, and D. G. Silverman, "What is the best site for measuring the effect of ventilation on the pulse oximeter waveform?" *Anesthesia & Analgesia*, vol. 103, no. 2, pp. 372–377, 2006.
- [75] D. Lawson, I. Norley, G. Korbon, R. Loeb, and J. Ellis, "Blood flow limits and pulse oximeter signal detection," *The Journal of The American Society of Anesthesiologists*, vol. 67, no. 4, pp. 599–603, 1987.
- [76] P. A. Kyriacou, K. Shafqat, and S. K. Pal, "Pilot investigation of photoplethysmographic signals and blood oxygen saturation values during blood pressure cuff-

- induced hypoperfusion,” *Measurement*, vol. 42, no. 7, pp. 1001–1005, 2009.
- [77] M. Shafique, P. A. Kyriacou, and S. K. Pal, “investigation of photoplethysmographic signals and blood oxygen saturation values on healthy volunteers during cuff-induced hypoperfusion using a multimode ppg/spo2 sensor,” *Medical and Biological Engineering and Computing*, vol. 50, no. 50, pp. 575–583, 2012.
- [78] A. B. Hertzman and J. B. Dillon, “Distinction between arterial, venous and flow components in the photoelectric plethysmography in man,” *American Journal of Physiology—Legacy Content*, vol. 130, no. 1, pp. 177–185, 1940.
- [79] N. E. Almond, D. P. Jones, and E. D. Cooke, “Noninvasive measurement of the human peripheral circulation: relationship between laser doppler flowmeter and photoplethysmograph signals from the finger,” *Angiology*, vol. 39, no. 9, pp. 819–829, 1988.
- [80] A. P. Lima, P. Beelen, and J. Bakker, “Use of a peripheral perfusion index derived from the pulse oximetry signal as a noninvasive indicator of perfusion,” *Critical care medicine*, vol. 30, no. 6, pp. 1210–1213, 2002.
- [81] P. Zaramella, F. Freato, V. Quaresima, M. Ferrari, A. Vianello, D. Giongo, L. Conte, and L. Chiandetti, “Foot pulse oximeter perfusion index correlates with calf muscle perfusion measured by near-infrared spectroscopy in healthy neonates,” *Journal of Perinatology*, vol. 25, no. 6, pp. 417–422, 2005.
- [82] M. E. van Genderen, S. A. Bartels, A. Lima, R. Bezemer, C. Ince, J. Bakker, and J. van Bommel, “Peripheral perfusion index as an early predictor for central hypovolemia in awake healthy volunteers,” *Anesthesia & Analgesia*, vol. 116, no. 2, pp. 351–356, 2013.
- [83] C. Felice, G. Latini, P. Vacca, and R. J. Kopotic, “The pulse oximeter perfusion index as a predictor for high illness severity in neonates,” *European journal of pediatrics*, vol. 161, no. 10, pp. 561–562, 2002.
- [84] R. F. Brodman, L. E. Hirsh, and R. Frame, “Effect of radial artery harvest on collateral forearm blood flow and digital perfusion,” *The Journal of thoracic and*

- cardiovascular surgery*, vol. 123, no. 3, pp. 512–516, 2002.
- [85] B. P. Imholz, W. Wieling, G. A. van Montfrans, and K. H. Wesseling, “Fifteen years experience with finger arterial pressure monitoring,” *Cardiovascular research*, vol. 38, no. 3, pp. 605–616, 1998.
- [86] C. Jeleazcov, L. Krajinovic, T. Münster, T. Birkholz, R. Fried, J. Schüttler, and J. Fechner, “Precision and accuracy of a new device (cnap) for continuous non-invasive arterial pressure monitoring: assessment during general anaesthesia,” *British journal of anaesthesia*, vol. 105, no. 3, pp. 264–272, 2010.
- [87] J. R. Martina, B. E. Westerhof, J. van Goudoever, E. M. H. de Beaumont, J. Truijen, Y.-S. Kim, R. V. Immink, D. A. Jöbsis, M. W. Hollmann, J. R. Lahpor *et al.*, “Noninvasive continuous arterial blood pressure monitoring with nexfin®,” *The Journal of the American Society of Anesthesiologists*, vol. 116, no. 5, pp. 1092–1103, 2012.
- [88] K. H. Shelley, W. B. Murray, and D. Chang, “Arterial–pulse oximetry loops: a new method of monitoring vascular tone,” *Journal of clinical monitoring*, vol. 13, no. 4, pp. 223–228, 1997.
- [89] J. Allen and A. Murray, “Age-related changes in peripheral pulse timing characteristics at the ears, fingers and toes,” *Journal of human hypertension*, vol. 16, no. 10, pp. 711–717, 2002.
- [90] A. Alian, G. Atteya, D. Gaal, T. Golembeski, B. Smith, F. Dai, D. Silverman, and K. Shelley, “Ventilation-induced modulation of pulse oximeter waveforms: A method for the assessment of early changes in intravascular volume during spinal fusion surgery in pediatric patients.” *Anesthesia and analgesia*, 2016.
- [91] G. Natalini, A. Rosano, M. Taranto, B. Faggian, E. Vittorielli, and A. Bernardini, “Arterial versus plethysmographic dynamic indices to test responsiveness for testing fluid administration in hypotensive patients: a clinical trial,” *Anesthesia & Analgesia*, vol. 103, no. 6, pp. 1478–1484, 2006.
- [92] P. A. Kyriacou, S. Powell, R. M. Langford, and D. P. Jones, “Esophageal pulse

- oximetry utilizing reflectance photoplethysmography,” *IEEE Transactions on Biomedical Engineering*, vol. 49, no. 11, pp. 1360–1368, 2002.
- [93] K. Budidha and P. Kyriacou, “The human ear canal: investigation of its suitability for monitoring photoplethysmographs and arterial oxygen saturation,” *Physiological measurement*, vol. 35, no. 2, p. 111, 2014.
- [94] —, “Investigation of photoplethysmography and arterial blood oxygen saturation from the ear-canal and the finger under conditions of artificially induced hypothermia,” in *Engineering in Medicine and Biology Society (EMBC), 2015 37th Annual International Conference of the IEEE*. IEEE, 2015, pp. 7954–7957.
- [95] W. H. Pearce, D. N. Jones, G. H. Warren, E. J. Bartle, T. A. Whitehill, and R. B. Rutherford, “The use of infrared photoplethysmography in identifying early intestinal ischemia,” *Archives of Surgery*, vol. 122, no. 3, pp. 308–310, 1987.
- [96] M. Hickey, N. Samuels, N. Randive, R. M. Langford, and P. A. Kyriacou, “An in vivo investigation of photoplethysmographic signals and preliminary pulse oximetry estimation from the bowel using a new fiberoptic sensor,” *Anesthesia & Analgesia*, vol. 112, no. 5, pp. 1104–1109, 2011.
- [97] A. J. Avino, W. A. Oldenburg, P. Gloviczki, V. M. Miller, L. J. Burgart, and E. J. Atkinson, “Inferior mesenteric venous sampling to detect colonic ischemia: A comparison with laser doppler flowmetry and photoplethysmography,” *Journal of vascular surgery*, vol. 22, no. 3, pp. 271–279, 1995.
- [98] J. Phillips, R. Langford, P. Kyriacou, and D. Jones, “Preliminary evaluation of a new fibre-optic cerebral oximetry system,” *Physiological measurement*, vol. 29, no. 12, p. 1383, 2008.
- [99] F. L. THORNE, N. G. CEORCIAUK, W. F. WHKKLER, and R. A. MLADICK, “Photoplethysmography as an aid in determining the viability of pedicle flaps.” *Plastic and reconstructive surgery*, vol. 44, no. 3, pp. 279–284, 1969.
- [100] B. C. Stack, N. D. Futran, M. J. Shohet, and J. E. Scharf, “Spectral analysis of photoplethysmograms from radial forearm free flaps,” *The Laryngoscope*, vol.

- 108, no. 9, pp. 1329–1333, 1998.
- [101] B. C. Stack Jr, N. D. Futran, B. Zang, and J. E. Scharf, “Initial experience with personal digital assistant-based reflectance photoplethysmograph for free tissue transfer monitoring,” *Annals of plastic surgery*, vol. 51, no. 2, pp. 136–140, 2003.
- [102] T. Zaman, P. Kyriacou, and S. Pal, “Free flap pulse oximetry utilizing reflectance photoplethysmography,” in *2013 35th Annual International Conference of the IEEE Engineering in Medicine and Biology Society (EMBC)*. IEEE, 2013, pp. 4046–4049.
- [103] W. Verkruysse, L. O. Svaasand, and J. S. Nelson, “Remote plethysmographic imaging using ambient light.” *Optics express*, vol. 16, no. 26, pp. 21 434–21 445, 2008.
- [104] A. A. Kamshilin, E. Nippolainen, I. S. Sidorov, P. V. Vasilev, N. P. Erofeev, N. P. Podolian, and R. V. Romashko, “A new look at the essence of the imaging photoplethysmography,” *Scientific reports*, vol. 5, 2015.
- [105] M. W. Wukitsch, M. T. Petterson, D. R. Tobler, and J. A. Pologe, “Pulse oximetry: analysis of theory, technology, and practice,” *Journal of Clinical Monitoring*, vol. 4, no. 4, pp. 290–301, 1988.
- [106] J. E. Sinex, “Pulse oximetry: principles and limitations,” *The American journal of emergency medicine*, vol. 17, no. 1, pp. 59–66, 1999.
- [107] J. F. Biebuyck, J. W. Severinghaus, and J. F. Kelleher, “Recent developments in pulse oximetry,” *The Journal of the American Society of Anesthesiologists*, vol. 76, no. 6, pp. 1018–1038, 1992.
- [108] A. Jubran, “Pulse oximetry,” pp. 45–48, 2009.
- [109] A. B. Hertzman and L. W. Roth, “The absence of vasoconstrictor reflexes in the forehead circulation. effects of cold,” *American Journal of Physiology–Legacy Content*, vol. 136, no. 4, pp. 692–697, 1942.

- 
- [110] P. D. Mannheimer, M. P. O’Neil, and E. Konecny, “The influence of larger subcutaneous blood vessels on pulse oximetry,” *Journal of clinical Monitoring and Computing*, vol. 18, no. 3, pp. 179–188, 2004.
- [111] K. H. Shelley, D. Tamai, D. Jablonka, M. Gesquiere, R. G. Stout, and D. G. Silverman, “The effect of venous pulsation on the forehead pulse oximeter wave form as a possible source of error in spo2 calculation,” *Anesthesia & Analgesia*, vol. 100, no. 3, pp. 743–747, 2005.
- [112] W. Verkruysse, M. Bartula, E. Bresch, M. Rocque, M. Meftah, and I. Kirenko, “Calibration of contactless pulse oximetry.” *Anesthesia and analgesia*, vol. Epub ahead of print, 2016.
- [113] D. Shao, C. Liu, F. Tsow, Y. Yang, Z. Du, R. Iriya, H. Yu, and N. Tao, “Noncontact monitoring of blood oxygen saturation using camera and dual-wavelength imaging system,” *IEEE Transactions on Biomedical Engineering*, vol. 63, no. 6, pp. 1091–1098, 2016.
- [114] M. Nitzan, A. Romem, and R. Koppel, “Pulse oximetry: fundamentals and technology update,” *Medical Devices (Auckland, NZ)*, vol. 7, p. 231, 2014.
- [115] Z. D. Walton, P. A. Kyriacou, D. G. Silverman, and K. H. Shelley, “Measuring venous oxygenation using the photoplethysmograph waveform,” *Journal of clinical monitoring and computing*, vol. 24, no. 4, pp. 295–303, 2010.
- [116] K. Shafqat, R. Langford, and P. Kyriacou, “Estimation of instantaneous venous blood saturation using the photoplethysmograph waveform,” *Physiological Measurement*, vol. 36, no. 10, p. 2203, 2015.
- [117] E. D. Chan, M. M. Chan, and M. M. Chan, “Pulse oximetry: understanding its basic principles facilitates appreciation of its limitations,” *Respiratory medicine*, vol. 107, no. 6, pp. 789–799, 2013.
- [118] G. G. Hallock and D. C. Rice, “A comparison of pulse oximetry and laser doppler flowmetry in monitoring sequential vascular occlusion in a rabbit ear model,” *The Canadian Journal of Plastic Surgery*, vol. 11, no. 1, pp. 11–14, 2003.

- 
- [119] D. Delpy and M. Cope, "Quantification in tissue near-infrared spectroscopy," *Philosophical Transactions of the Royal Society of London B: Biological Sciences*, vol. 352, no. 1354, pp. 649–659, 1997.
- [120] P. Van der Zee, M. Cope, S. Arridge, M. Essenpreis, L. Potter, A. Edwards, J. Wyatt, D. McCormick, S. Roth, E. Reynolds *et al.*, "Experimentally measured optical pathlengths for the adult head, calf and forearm and the head of the newborn infant as a function of inter optode spacing," in *Oxygen transport to tissue XIII*. Springer, 1992, pp. 143–153.
- [121] A. Duncan, J. H. Meek, M. Clemence, C. E. Elwell, L. Tyszczuk, M. Cope, and D. Delpy, "Optical pathlength measurements on adult head, calf and forearm and the head of the newborn infant using phase resolved optical spectroscopy," *Physics in medicine and biology*, vol. 40, no. 2, p. 295, 1995.
- [122] A. Torricelli, D. Contini, A. Pifferi, M. Caffini, R. Re, L. Zucchelli, and L. Spinelli, "Time domain functional nirs imaging for human brain mapping," *Neuroimage*, vol. 85, pp. 28–50, 2014.
- [123] D. T. Delpy, M. Cope, P. van der Zee, S. Arridge, S. Wray, and J. Wyatt, "Estimation of optical pathlength through tissue from direct time of flight measurement," *Physics in medicine and biology*, vol. 33, no. 12, p. 1433, 1988.
- [124] S. Suzuki, S. Takasaki, T. Ozaki, and Y. Kobayashi, "Tissue oxygenation monitor using nir spatially resolved spectroscopy," in *BiOS'99 International Biomedical Optics Symposium*. International Society for Optics and Photonics, 1999, pp. 582–592.
- [125] P. G. Al-Rawi, P. Smielewski, and P. J. Kirkpatrick, "Evaluation of a near-infrared spectrometer (niro 300) for the detection of intracranial oxygenation changes in the adult head," *Stroke*, vol. 32, no. 11, pp. 2492–2500, 2001.
- [126] M. Niwayama, L. Lin, J. Shao, N. Kudo, and K. Yamamoto, "Quantitative measurement of muscle hemoglobin oxygenation using near-infrared spectroscopy with correction for the influence of a subcutaneous fat layer," *Review of Scientific Instruments*, vol. 71, no. 12, pp. 4571–4575, 2000.

- 
- [127] M. Van Beekvelt, M. Borghuis, B. Van Engelen, R. Wevers, and W. Colier, "Adipose tissue thickness affects in vivo quantitative near-ir spectroscopy in human skeletal muscle," *Clinical science*, vol. 101, no. 1, pp. 21–28, 2001.
- [128] R. Boushel, H. Langberg, J. Olesen, J. Gonzales-Alonzo, J. Bülow, and M. Kjaer, "Monitoring tissue oxygen availability with near infrared spectroscopy (nirs) in health and disease," *Scandinavian journal of medicine & science in sports*, vol. 11, no. 4, pp. 213–222, 2001.
- [129] K. R. Ward, R. R. Ivatury, R. W. Barbee, J. Turner, R. Pittman, I. P. Torres Filho, and B. Spiess, "Near infrared spectroscopy for evaluation of the trauma patient: a technology review," *Resuscitation*, vol. 68, no. 1, pp. 27–44, 2006.
- [130] P. G. Al-Rawi and P. J. Kirkpatrick, "Tissue oxygen index thresholds for cerebral ischemia using near-infrared spectroscopy," *Stroke*, vol. 37, no. 11, pp. 2720–2725, 2006.
- [131] N. Hampson, E. Camporesi, B. Stolp, R. Moon, J. Shook, J. Griebel, and C. Piantadosi, "Cerebral oxygen availability by nir spectroscopy during transient hypoxia in humans," *Journal of Applied Physiology*, vol. 69, no. 3, pp. 907–913, 1990.
- [132] A. Petrova and R. Mehta, "Near-infrared spectroscopy in the detection of regional tissue oxygenation during hypoxic events in preterm infants undergoing critical care," *Pediatric Critical Care Medicine*, vol. 7, no. 5, pp. 449–454, 2006.
- [133] M. Wolf, K. von Siebenthal, M. Keel, V. Dietz, O. Baenziger, and H. Bucher, "Tissue oxygen saturation measured by near infrared spectrophotometry correlates with arterial oxygen saturation during induced oxygenation changes in neonates," *Physiological measurement*, vol. 21, no. 4, p. 481, 2000.
- [134] C. Elwell, M. Cope, A. Edwards, J. Wyatt, D. Delpy, and E. Reynolds, "Quantification of adult cerebral hemodynamics by near-infrared spectroscopy," *Journal of Applied Physiology*, vol. 77, no. 6, pp. 2753–2760, 1994.
- [135] F. Molinari, W. Liboni, G. Grippi, and E. Negri, "Relationship between oxygen

- supply and cerebral blood flow assessed by transcranial doppler and near-infrared spectroscopy in healthy subjects during breath-holding,” *Journal of neuroengineering and rehabilitation*, vol. 3, no. 1, p. 1, 2006.
- [136] K. Kurihara, A. Kikukawa, and A. Kobayashi, “Cerebral oxygenation monitor during head-up and-down tilt using near-infrared spatially resolved spectroscopy,” *Clinical physiology and functional imaging*, vol. 23, no. 4, pp. 177–181, 2003.
- [137] H. Obrig, M. Neufang, R. Wenzel, M. Kohl, J. Steinbrink, K. Einhäupl, and A. Villringer, “Spontaneous low frequency oscillations of cerebral hemodynamics and metabolism in human adults,” *Neuroimage*, vol. 12, no. 6, pp. 623–639, 2000.
- [138] I. Tachtsidis, C. E. Elwell, T. S. Leung, C.-W. Lee, M. Smith, and D. T. Delpy, “Investigation of cerebral haemodynamics by near-infrared spectroscopy in young healthy volunteers reveals posture-dependent spontaneous oscillations,” *Physiological measurement*, vol. 25, no. 2, p. 437, 2004.
- [139] C. Zweifel, G. Castellani, M. Czosnyka, E. Carrera, K. M. Brady, P. J. Kirkpatrick, J. D. Pickard, and P. Smielewski, “Continuous assessment of cerebral autoregulation with near-infrared spectroscopy in adults after subarachnoid hemorrhage,” *Stroke*, vol. 41, no. 9, pp. 1963–1968, 2010.
- [140] N. B. Hampson and C. A. Piantadosi, “Near infrared monitoring of human skeletal muscle oxygenation during forearm ischemia,” *Journal of Applied Physiology*, vol. 64, no. 6, pp. 2449–2457, 1988.
- [141] B. Shadgan, W. D. Reid, R. Gharakhanlou, L. Stpublisher-ids, and A. J. Macnab, “Wireless near-infrared spectroscopy of skeletal muscle oxygenation and hemodynamics during exercise and ischemia,” *Journal of Spectroscopy*, vol. 23, no. 5-6, pp. 233–241, 2009.
- [142] C. Zysset, N. Nasser, L. Büthe, N. Münzenrieder, T. Kinkeldei, L. Petti, S. Kleiser, G. A. Salvatore, M. Wolf, and G. Tröster, “Textile integrated sensors and actuators for near-infrared spectroscopy,” *Optics express*, vol. 21, no. 3, pp. 3213–3224, 2013.

- 
- [143] N. Everdell, D. Airantzis, C. Kolvyra, T. Suzuki, and C. Elwell, "A portable wireless near-infrared spatially resolved spectroscopy system for use on brain and muscle," *Medical engineering & physics*, vol. 35, no. 11, pp. 1692–1697, 2013.
- [144] R. A. De Blasi, M. Cope, C. Elwell, F. Safoue, and M. Ferrari, "Noninvasive measurement of human forearm oxygen consumption by near infrared spectroscopy," *European Journal of Applied Physiology and Occupational Physiology*, vol. 67, no. 1, pp. 20–25, 1993.
- [145] R. Belardinelli, T. J. Barstow, J. Porszasz, and K. Wasserman, "Changes in skeletal muscle oxygenation during incremental exercise measured with near infrared spectroscopy," *European journal of applied physiology and occupational physiology*, vol. 70, no. 6, pp. 487–492, 1995.
- [146] T. Hamaoka, H. Iwane, T. Shimomitsu, T. Katsumura, N. Murase, S. Nishio, T. Osada, Y. Kurosawa, and B. Chance, "Noninvasive measures of oxidative metabolism on working human muscles by near-infrared spectroscopy," *Journal of Applied Physiology*, vol. 81, no. 3, pp. 1410–1417, 1996.
- [147] M. C. Van Beekvelt, W. Colier, R. A. Wevers, and B. G. Van Engelen, "Performance of near-infrared spectroscopy in measuring local  $\dot{V}O_2$  consumption and blood flow in skeletal muscle," *Journal of Applied Physiology*, vol. 90, no. 2, pp. 511–519, 2001.
- [148] R. A. De Blasi, N. Almenrader, P. Aurisicchio, and M. Ferrari, "Comparison of two methods of measuring forearm oxygen consumption ( $\dot{V}O_2$ ) by near infrared spectroscopy," *Journal of biomedical optics*, vol. 2, no. 2, pp. 171–175, 1997.
- [149] R. Boushel and C. A. Piantadosi, "Near-infrared spectroscopy for monitoring muscle oxygenation," *Acta Physiologica Scandinavica*, vol. 168, no. 4, pp. 615–622, 2000.
- [150] J. R. Wilson, D. Mancini, K. McCully, N. Ferraro, V. Lanocce, and B. Chance, "Noninvasive detection of skeletal muscle underperfusion with near-infrared spectroscopy in patients with heart failure." *Circulation*, vol. 80, no. 6, pp. 1668–1674, 1989.

- 
- [151] D. M. Mancini, L. Bolinger, H. Li, K. Kendrick, B. Chance, and J. R. Wilson, "Validation of near-infrared spectroscopy in humans," *Journal of Applied Physiology*, vol. 77, no. 6, pp. 2740–2747, 1994.
- [152] K. Katayama, Y. Yoshitake, K. Watanabe, H. Akima, and K. Ishida, "Muscle deoxygenation during sustained and intermittent isometric exercise in hypoxia," *Med Sci Sports Exerc*, vol. 42, no. 7, pp. 1269–1278, 2010.
- [153] M. Ferrari, M. Muthalib, and V. Quaresima, "The use of near-infrared spectroscopy in understanding skeletal muscle physiology: recent developments," *Phil. Trans. R. Soc. A*, vol. 369, no. 1955, pp. 4577–4590, 2011.
- [154] B. Grassi, V. Quaresima, C. Marconi, M. Ferrari, and P. Cerretelli, "Blood lactate accumulation and muscle deoxygenation during incremental exercise," *Journal of Applied Physiology*, vol. 87, no. 1, pp. 348–355, 1999.
- [155] T. Hamaoka, K. K. McCully, M. Niwayama, and B. Chance, "The use of muscle near-infrared spectroscopy in sport, health and medical sciences: recent developments," *Phil. Trans. R. Soc. A*, vol. 369, no. 1955, pp. 4591–4604, 2011.
- [156] M. Girardis, L. Rinaldi, S. Busani, I. Flore, S. Mauro, and A. Pasetto, "Muscle perfusion and oxygen consumption by near-infrared spectroscopy in septic and non-septic-shock patients," *Intensive Care Medicine*, vol. 29, pp. 1173–1176, 2003.
- [157] H. Gomez, A. Torres, P. Polanco, H. K. Kim, S. Zenker, J. C. Puyana, and M. R. Pinsky, "Use of non-invasive nirs during a vascular occlusion test to assess dynamic tissue o2 saturation response," *Intensive Care Medicine*, vol. 34, no. 9, pp. 1600–1607, 2008.
- [158] G. J. Beilman, K. E. Groehler, V. Lazon, and J. P. Ortner, "Near-infrared spectroscopy measurement of regional tissue oxyhemoglobin saturation during hemorrhagic shock," *Shock*, vol. 12, no. 3, pp. 196–200, 1999.
- [159] M. Irwin, M. Thorniley, C. Dore, and C. Green, "Near infra-red spectroscopy: a non-invasive monitor of perfusion and oxygenation within the microcirculation of limbs and flaps," *British journal of plastic surgery*, vol. 48, no. 1, pp. 14–22,

- 1995.
- [160] M. Ferrari and V. Quaresima, “A brief review on the history of human functional near-infrared spectroscopy (fnirs) development and fields of application,” *Neuroimage*, vol. 63, no. 2, pp. 921–935, 2012.
- [161] M. Wolf, M. Ferrari, and V. Quaresima, “Progress of near-infrared spectroscopy and topography for brain and muscle clinical applications,” *Journal of biomedical optics*, vol. 12, no. 6, pp. 062 104–062 104, 2007.
- [162] M. Ferrari and V. Quaresima, “Near infrared brain and muscle oximetry: from the discovery to current applications,” *J. Near Infrared Spectrosc*, vol. 20, no. 1, pp. 1–14, 2012.
- [163] D. A. Boas, T. Gaudette, G. Strangman, X. Cheng, J. J. Marota, and J. B. Mandeville, “The accuracy of near infrared spectroscopy and imaging during focal changes in cerebral hemodynamics,” *Neuroimage*, vol. 13, no. 1, pp. 76–90, 2001.
- [164] A. Macnab and R. Gagnon, “Phantom testing of two clinical spatially-resolved nirs instruments,” *Journal of Spectroscopy*, vol. 19, no. 3, pp. 165–169, 2005.
- [165] S. Hyttel-Sorensen, L. C. Sorensen, J. Riera, and G. Greisen, “Tissue oximetry: a comparison of mean values of regional tissue saturation, reproducibility and dynamic range of four nirs-instruments on the human forearm,” *Biomedical optics express*, vol. 2, no. 11, pp. 3047–3057, 2011.
- [166] S. Hyttel-Sorensen, S. Kleiser, M. Wolf, and G. Greisen, “Calibration of a prototype nirs oximeter against two commercial devices on a blood-lipid phantom,” *Biomedical optics express*, vol. 4, no. 9, pp. 1662–1672, 2013.
- [167] A. Moerman and P. Wouters, “Near-infrared spectroscopy (nirs) monitoring in contemporary anesthesia and critical care,” *Acta Anaesthesiol Belg*, vol. 61, no. 4, pp. 185–194, 2010.
- [168] A. Ghosh, C. Elwell, and M. Smith, “Cerebral near-infrared spectroscopy in

- adults: a work in progress,” *Anesthesia & Analgesia*, vol. 115, no. 6, pp. 1373–1383, 2012.
- [169] C. Schubert, M. C. van Langeveld, and L. A. Donoso, “Innovations in 3d printing: a 3d overview from optics to organs,” *British Journal of Ophthalmology*, pp. bjophthalmol–2013, 2013.
- [170] J. G. Graeme, *Photodiode Amplifiers*. McGraw-Hill, 1996.
- [171] T. Instrument, “An-1803 design consideration for a transimpedance amplifier,” Texas Instruments, Application Report SNOA515A, February 2008. [Online]. Available: <http://www.ti.com/lit/an/snoa515a/snoa515a.pdf>.
- [172] D. Westerman, “Understand and apply the transimpedance amplifier,” National Semiconductor Corp., Tech. Rep., August 2007. [Online]. Available: [http://www.eetindia.co.in/STATIC/PDF/200708/EEIOL\\_2007AUG08\\_RFD\\_NETD\\_SIG\\_TA\\_01.pdf?SOURCES=DOWNLOAD](http://www.eetindia.co.in/STATIC/PDF/200708/EEIOL_2007AUG08_RFD_NETD_SIG_TA_01.pdf?SOURCES=DOWNLOAD).
- [173] R. Bitter, T. Mohiuddin, and M. Nawrocki, *LabVIEW: Advanced programming techniques*. CRC Press, 2007.
- [174] J. B. Olansen and E. Rosow, *Virtual bio-instrumentation: biomedical, clinical, and healthcare applications in LabVIEW*. Pearson Education, 2001.
- [175] L. Tan and J. Jiang, *Digital signal processing: fundamentals and applications*. Academic Press, 2013.
- [176] K. K. Tremper, “Pulse oximetry.” *Chest Journal*, vol. 95, no. 4, pp. 713–715, 1989.
- [177] S. Lu, H. Zhao, K. Ju, K. Shin, M. Lee, K. Shelley, and K. H. Chon, “Can photoplethysmography variability serve as an alternative approach to obtain heart rate variability information?” *Journal of clinical monitoring and computing*, vol. 22, no. 1, pp. 23–29, 2008.
- [178] H. Gehring, “Pulse oximeter in a comparative test,” *Intensive care medicine*, vol. 32, no. 9, pp. 1287–1289, 2006.

- 
- [179] J. C. Yuen and Z. Fend, “Distinguishing laser doppler flowmetric responses between arterial and venous obstructions in flaps,” *Journal of Reconstructive Microsurgery*, vol. 16, no. 8, pp. 629–635, 2000.
- [180] T. Jarm, R. Kragelj, A. Liebert, P. Lukasiewicz, T. Erjavec, M. Preseren-Strukelj, R. Maniewski, P. Poredos, and D. Miklavcic, *Postocclusive reactive hyperemia in healthy volunteers and patients with peripheral vascular disease measured by three noninvasive methods*. Springer US, 2003, pp. 661–669.
- [181] M. Bergkvist, J. Henricson, F. Iredahl, E. Tesselaar, F. Sjöberg, and S. Farnebo, “Assessment of microcirculation of the skin using tissue viability imaging: A promising technique for detecting venous stasis in the skin,” *Microvascular research*, vol. 101, pp. 20–25, 2015.
- [182] H. Photonics, *NIRO 200NX Instruction Manual*, ver.1.50e ed., Hamamatsu Photonics, August.
- [183] M. Instruments, *moorVMS-LDF User Manual*, version 2.0 ed., Moor Instruments Limited, Millwey, Axminster, Devon, EX13 5HU, UK, January 2009.
- [184] L. A. Critchley, A. Lee, and A. M.-H. Ho, “A critical review of the ability of continuous cardiac output monitors to measure trends in cardiac output,” *Anesthesia & Analgesia*, vol. 111, no. 5, pp. 1180–1192, 2010.
- [185] J. M. Bland and D. Altman, “Statistical methods for assessing agreement between two methods of clinical measurement,” *The lancet*, vol. 327, no. 8476, pp. 307–310, 1986.
- [186] J. M. Bland and D. G. Altman, “Measuring agreement in method comparison studies,” *Statistical methods in medical research*, vol. 8, no. 2, pp. 135–160, 1999.
- [187] T. Binzoni, T. Leung, M. Seghier, and D. Delpy, “Translational and brownian motion in laser-doppler flowmetry of large tissue volumes,” *Physics in medicine and biology*, vol. 49, no. 24, p. 5445, 2004.
- [188] G. S. Agashe, J. Coakley, and P. D. Mannheim, “Forehead pulse oximetry-

- headband use helps alleviate false low readings likely related to venous pulsation artifact,” *The Journal of the American Society of Anesthesiologists*, vol. 105, no. 6, pp. 1111–1116, 2006.
- [189] A. Casati, G. Squicciarini, M. Baciarello, M. Putzu, A. Salvadori, and G. Fanelli, “Forehead reflectance oximetry: a clinical comparison with conventional digit sensors during laparotomic and laparoscopic abdominal surgery,” *Journal of clinical monitoring and computing*, vol. 21, no. 5, pp. 271–276, 2007.
- [190] L. Schallom, C. Sona, M. McSweeney, and J. Mazuski, “Comparison of forehead and digit oximetry in surgical/trauma patients at risk for decreased peripheral perfusion,” *Heart & Lung: The Journal of Acute and Critical Care*, vol. 36, no. 3, pp. 188–194, 2007.
- [191] K. H. Shelley, M. Dickstein, and S. M. Shulman, “The detection of peripheral venous pulsation using the pulse oximeter as a plethysmograph,” *Journal of clinical monitoring*, vol. 9, no. 4, pp. 283–287, 1993.
- [192] K. Budidha and P. A. Kyriacou, “Development of an optical probe to investigate the suitability of measuring photoplethysmographs and blood oxygen saturation from the human auditory canal,” in *Engineering in Medicine and Biology Society (EMBC), 2013 35th Annual International Conference of the IEEE*. IEEE, 2013, pp. 1736–1739.
- [193] A. Lima and J. Bakker, “Clinical monitoring of peripheral perfusion: there is more to learn,” *Critical Care*, vol. 18, no. 1, p. 1, 2014.